Characterising Saharan Dust Sources and Export using Remote Sensing and Regional Modelling

Dissertation
zur Erlangung des Doktorgrades
der Mathematisch-Naturwissenschaftlichen Fakultät
der Christian-Albrechts-Universiät
zu Kiel

vorgelegt von

Kerstin Schepanski

IFM-GEOMAR

Kiel, Dezember 2008

Referent: Prof. Dr. A. Macke
Koreferent/in: Dr. I. Tegen
Tag der mündlichen Prüfung: 26. Januar 2009
Zum Druck genehmigt: Kiel, 26. Januar 2009

Zusammenfassung

Die vorliegende Doktorarbeit beschäftigt sich mit dem atmosphärischen Kreislauf von nordafrikanischem Wüstenstaub. Dabei wird die Ausprägung der einzelnen Stufen Emission, Transport und Deposition während verschiedener Jahreszeiten anhand von Satellitenbeobachtungen und Modellsimulationen diskutiert.

Satellitengestützte Messungen im infra-roten (IR) Bereich des Wellenlängenspektrums sind für die Erkennung von atmosphärischem Mineralstaub über im sichtbaren stark reflektierenden Flächen wie Wüsten sehr gut geeignet. Im Rahmen der vorliegenden Arbeit wurde ein Staubindex basierend auf Messungen des SEVIRI (Spinning Enhanced Visible and InfraRed Imager) Instruments auf dem geostationären Meteosat Second Generation (MSG) Satelliten im IR Wellenlängenbreich verwendet. Basierend auf den 15-minütigen Staubindexbildern wurde eine Karte der Staubquellregionen für den Zeitraum ab 03/2006 erarbeitet. Neben der räumlichen Information mit einer $1^\circ \times 1^\circ$-Auflösung ist die Uhrzeit des Zeitpunktes der ersten Staubmobilisierung in 3-stündlichen Intervallen gespeichert.

Die raum-zeitliche Information über afrikanische Mineralstaubquellen nördlich 5° N wurden hinsichtlich saisonaler Variabilität mit Blick auf räumliche und (tages)zeitliche Variabilitäten untersucht. Saisonale Verlagerungen von Regionen häufiger Staubquellen verdeutlichen den Zusammenhang zwischen jahreszeitlich unterschiedlicher Ausprägung atmosphärischer Zirkulationsmuster und Bodenbeschaffenheiten. Die örtlichen Morgenstunden weisen mit 65 % den größten Anteil an beobachteter einsetzender Staubmobilisierung (2006/03–2008/08) auf. Einsetzende Staubemission während dieser Tageszeit deutet auf den Einfluss des bis in die bodennahen Troposphärenschichten heruntergemischten Grenzschichtstrahlstroms (engl. low-level jet (LLJ)) und der damit zusammenhängenden, kurzfristig einsetzenden Zunahme der Windgeschwindigkeit. Im Rahmen der vorliegenden Arbeit wurde die Bedeutung des LLJ für die Staubmobilisierung anhand von Beobachtungsdaten, regionaler und globaler Modellsimulierung untersucht. Modellsimulationen wurden mit dem Regionalmodell LM-MUSCAT, bestehend aus dem meso-scaligen Atmosphärenmodell Lokalmodell (LM) des Deutschen Wetterdienstes (DWD), und dem Aerosolmodul MUSCAT (MUlti-Scale Chemistry Aerosol Transportmodell) erstellt.

Mit Fokus auf Staubexport und Depositionsflüsse über der Atlantikregion wurden drei jeweils einen Monat umfassende Fallstudien gerechnet. Dabei wurden die Monate (März, Juli und Januar) so gewählt, dass sie saisonal unterschiedliche atmosphärische Gegebenheiten widerspiegeln. Im Winter wird Wüstenstaub aus der Sahara in südwestliche Richtungen und in niedrigen Troposphärenschichten transportiert, im Sommer hingegen als abgehobene Schicht in westliche Richtung. Diese saisonalen Unterschiede zeichnen sich auch in den Depositionsflüssen ab.

Abstract

The present PhD thesis aims to characterise the Saharan dust cycle at different seasons using satellite remote sensing techniques and regional modelling studies. The dust cycle consits of (1.) dust entrainment into the atmosphere, (2.) dust transport, and (3.) dust deposition.

Satellite remote sensing techniques applied to the infrared (IR) spectrum are suitable to detect airborne dust over surfaces like deserts that are highly reflecting at visible wavelength. Here, a dust index based on 15-minute IR measurements provided by the SEVIRI (Spinning Enhanced Visible and InfraRed Imager) flying on-board of the geostationary Meteosat Second Generation (MSG) satellite is used to infer spatio-temporal characteristics of dust sources north of 5°N over Africa since March 2006. The time and location of individual dust source activations are compiled in a $1^\circ \times 1^\circ$ map in 3-hour time intervals.

Dust source activation frequencies are used to investigate the spatio-temporal distribution of active Saharan dust sources. Seasonally changing pattern of high frequencies of activated dust sources are evident, linking changing atmospheric conditions to soil conditions suitable for dust mobilisation. The spatial distribution of dust sources points towards the importance of endorheic drainage systems in mountain areas. Most of North African dust sources are situated in the foothills. The frequency distribution of the time-of-day when dust entrainment starts points towards the importance of different meteorological features forcing frequently recurring dust source activation. 65 % of dust source activation events during 2006/03–2008/08 observed over North Africa occur during 06-09 UTC, emphasing the importance of the nocturnal LLJ break-down as most important meteorlogical process for dust source activation.

Details of the role and ability of the LLJ break-down for dust entrainment were studied using wind speed observations at synoptic stations, regional and global atmospheric simulations in addition to the satellite based dust source activation observations. The ability of global and regional models is tested to represent this as an important feature for dust mobilisation with the observed frequency.

To study transport of airborne dust and removal of airborne dust from the atmosphere, three case studies are performed using the regional dust emission, transport and deposition model system LM-MUSCAT consisting of the atmospheric meso-scale model *Lokalmodell* LM (now renamed to COSMO) provided by the German weather service (DWD) and the *MUlti-Scale Chemical Aerosol Transport* model MUSCAT. Each case study comprises one month representing spring, summer and winter, respectively. The model results are used to describe seasonal differences concerning dust export towards the eastern North Atlantic, transport height, transport direction and deposition, showing strong seasonal differences. In winter, the dust layer is situated at lower tropospheric levels and transported in south-westward direction. In summer, the dust layer is found as an elevated layer, moving in westward direction.

Contents

Preface

This thesis is written cumulative and includes three scientific publication:

K. Schepanski, I. Tegen, B. Laurent, B. Heinold, and A. Macke (2007), *A new Saharan dust source activation frequency map derived from MSG-SEVIRI IR-channels*, Geophys. Res. Lett., 34, L18803, doi:10.1029/2007GL030168.

K. Schepanski, I. Tegen, M. C. Todd, B. Heinold, G. Bönisch, B. Laurent and A. Macke (2008), *Meteorological processes forcing Saharan dust emission inferred from MSG-SEVIRI observations of sub-daily dust source activation*, J. Geophys. Res., revised.

K. Schepanski, I. Tegen and A. Macke (2008), *Saharan Dust Transport and Deposition towards the Tropical Northern Atlantic*, Atmos. Chem. Phys. Discuss., 8, 16061-16096, SRef-ID: 1680-7375/acpd/2008-8-16061.

The latter publication is submitted to the journal *Atmosphere Chemistry Physics*, the last stage of the peer-review publishing process for this interactive open-access journal.

Chapter 1 will introduce the reader into the scientific topic of airborne mineral dust, Chapter 6 will give a short overview on the publications. The interested reader is referred to Chapter 2 – Chapter 5, which can be seen as additional information and give a more detailed background as it is possible in these scientific publications. However, these chapters are not essential to understand the work.

Chapter 1

Introduction on Mineral Dust

Desert areas are the main sources of atmospheric mineral dust. Worldwide, global modelling studies estimate a dust emission of 1100-5000 Tg per year (*Engelstaedter et al.*, 2006), whereby the estimates of individual studies vary strongly. According to these model estimates, around 40-70% of the global dust emission is occurring in North African deserts. Strong and frequently activated sources for mineral dust are mainly situated at subtropical latitudes, where the availability of water is limited (especially west parts of continents). There the vegetation cover is sparse and gives the impression of a dust belt. As water is one of the main limiting factors for vegetation, the arid and hyperarid climate of desert areas is commonly classified by the ratio of the mean annual precipitation and the mean annual evapotranspiration. Around 7.5% of the World's total land surface is classified as hyperarid area, around 12% is classified as arid area [UNEP Report: Dust Global Outlook, available at www.unep.org]. The Sahara desert that is strongest dust source worldwide shows highest aridity next to the Chilean-Peruvian desert.

The entrainment of mineral dust to the atmosphere is linked to the surface. Wind erosion and mobilisation of soil particles is a threshold problem, whereby wind velocity and turbulent fluxes are necessary to mobilise soil particles. This erosion process depends strongly on surface conditions. Vegetation, crusting and snow cover inhibit particle mobilisation. Consequently, for dust emission, two major conditions have to be fulfilled: (1.) Soil surface conditions suitable for dust mobilisation and (2.) appropriately high wind velocities.

Mineral dust aerosol, defined as a suspension of soil particles in a gaseous medium as the atmosphere (*Pye*, 1987) plays an important role in the weather and climate system (*IPCC*, 2007). Mineral dust is the major contributor to atmospheric aerosol (*Shao*, 2000). The atmospheric radiation budget is directly and indirectly influenced by dust particles (e.g. *Miller and Tegen*, 1999; *Sokolik and Toon*, 1996; *Tegen and Lacis*, 1996). Due to their physical, optical, chemical, and mineralogical properties mineral dust particles absorb and scatter shortwave as well as they absorb, scatter and re-emit longwave radiation at characteristic wavelengths of the radiation spectrum and consequently effect the atmospheric radiation budget directly (e.g. *Sokolik et al.*, 2001). Furthermore, atmospheric dust layers shadow the Earth's surface by scattering and absorbing solar radiation. Less solar radiation reaches the surface leading to lower surface temperatures but the radiation absorbed by the dust layer leads to a heating within the dust layer due to thermal re-emission. Hence a redistribution of the radiative energy is evident (*Perlwitz et al.*, 2001), resulting in a stabilised vertical atmospheric column (e.g. *Heinold et al.*, 2008b; *Miller and Tegen*, 1999). In particular over dust source areas where the break-down of the low-level jet (LLJ) forces dust mobilisation frequently (*Schepanski et al.*, 2008b), the enhanced atmospheric stability inhibits the downward transport of momentum from the LLJ and therefore dust mobilisation (*Heinold et al.*, 2008b). The stability affects vertical transport and exchange processes like e.g. convection, turbulence, and baroclitiy. Furthermore, airborne dust acting as an elevated heat source is able to change the surface pressure gradient. Hence, dust aerosol impacts on atmosphere dynamics and cloud formation processes (e.g. *Hoose et al.*, 2008; *Lohmann*, 2002). Size and number distribution of cloud condensation nuclei (CCN) are limiting factors for optical properties of clouds and precipitation rates (*DeMott et al.*, 2003; *Levin et al.*, 1996; *Rosenfeld et al.*, 2001; *Sassen et al.*, 2003; *Wurzler et al.*, 2000). Mineral dust aerosol is assumed to affect this distribution by changing cloud properties. As clouds play an important role for Earth's radiation budget, dust aerosol plays an important role in this context as well.

Besides radiative effects, deposited dust provides nutrients for terrestrial and oceanic ecosystems (e.g. *Mahowald et al.*, 2005). The fertilisation efficiency of dust depends on the bio-availability of micro-nutrients provided by the particles, mainly controlled by mineralogical and chemical properties as well as by processes on the particle surface during transport (*Goudie and Middleton*, 2001; *Journet et al.*, 2008; *Luo et al.*, 2003). Mineral dust as lithogenic soil particle is characterised by the same chemical and mineralogical composition as the source area. A study on soil composition by *Wedepohl* (1995) indicate an iron content of around 4 % for North Africa, so mineral dust can be considered as a transport medium for the micro-nutrient iron (*Fung et al.*, 2000; *Jickells et al.*, 2005; *Sarthou et al.*, 2003). Additionally, lithogenic dust particles originating from the soil of its place of origin represent the mineralogical source characteristics. Hence geomorphology of source areas provides the mineralogical characteristics of the soil dust particles and therefore their efficiency for fertilisation, as well as their role as CCN and their radiative behaviour. Thus, the knowledge of dust source areas concerning location, activity and geomorphology are a necessary prerequiste for an accurate estimation of dust impact on weather, climate and ecosystems.

Increasing diseases of asthma, infections, meningitis (*Griffin and Kellogg*, 2004; *Sultan et al.*, 2005) and valley fever seem to be related to dust outbreaks. Sampled dust aerosols are often accompanied by viable fungi and bacteria which my cause allergic reactions or asthma (*Griffin and Kellogg*, 2004; *Prospero et al.*, 2005). Furthermore, dust in general impact on air quality (*Gatz and Prospero*, 1996; *Prospero*, 1999) which today comes increasing in governmental focus. From economic considerations, dust impacts on aviation and ground transportation (e.g. affected by drifting sand) (*Criado and Dorta*, 2003).

Dust is observed to be transported over long distances. North Africa as strongest source area provides largest contributions to the global atmospheric dust content. Saharan dust is transported over the Atlantic Ocean (e.g. *Chiapello et al.*, 1995; *Ellis and Merrill*, 1995; *Gatz and Prospero*, 1996; *Perry et al.*, 1997; *Prospero and Lamb*, 2003; *Prospero et al.*, 1996; *Swap et al.*, 1992), towards the Mediterranean Sea (e.g. *Avila and Penuelas*, 1999; *Moulin et al.*, 1998), and farther east (e.g. *Ganor*, 1994; *Israelevich et al.*, 2002; *Kubilay et al.*, 2000). Frequently, dust is transported towards Southern Europe (e.g. *Lyamani et al.*, 2005; *Mattsson and Nihlen*, 1996; *Rogora et al.*, 2004) and farther north towards Central and North Europe (e.g. *Bücher and Dessens*, 1992; *Coen et al.*, 2004; *Psenner*, 1999; *Ryall et al.*, 2002; *Schwikowski et al.*, 1995; *Thomas*, 1982).

Besides dust export towards the Atlantic, Mediterranean and Red Sea regions, inter-hemispheric transport of Saharan dust is documented in the literature. *Koren et al.* (2006) and *Boy and Wilke* (2008) describe Saharan dust transport towards the Amazonian rain forest and the Andes, respectively. In ocean ecosystems, iron acts as controlling factor for marine life (e.g. phytoplankton growth) in high-nitrate, low chlorophyll (HNLC) regions (*Mahowald et al.*, 2005; *Moore et al.*, 2006; *Neuer et al.*, 2004; *Sarthou et al.*, 2007). Furthermore, iron supplied by mineral dust is assumed to enhance nitrogen fixation. Both, fertilisation and nitrogen fixation due to dust deposition ultimately influence the CO_2-cycle coupled to the climate system (*Gao et al.*, 2001; *IPCC*, 2007; *Moore et al.*, 2006, and references therein).

Over Asia, dust frequently emitted in the Taklamakan and Gobi deserts is often transported in eastward direction towards the Pacific Ocean and farther east to North America (e.g. *Jaffe et al.*, 2003; *McKendry et al.*, 2001; *Tsai et al.*, 2008; *VanCuren*, 2003; *Wilkening et al.*, 2000; *Zhang et al.*, 2003; *Zhao et al.*, 2006). Dust emission over Asia is mostly related to troughs and strong, active cold fronts (e.g. *Goudie and Middleton*, 1992; *Littmann*, 1991; *Liu et al.*, 2004; *Qian et al.*, 2002).

The atmospheric fraction of mineral dust is investigated and observed on several ways. Measurements of atmospheric dust are performed using ground and space-borne remote sensing techniques like sun-photometer, Lidar and satellite instruments. Sampling techniques (*Prospero et al.*, 1996), deposition measurements using sediment traps or ice core records (*Kohfeld and Harrison*, 2001, and related references) are used to describe dust deposition fluxes.

The AERONET (AErosol RObotic NETwork, *Holben et al.* (1998)) sun-photometer network is a good example for a long-term global network characterising atmospheric total column aerosol. But as only total column information can be retrieved, no information is gained on emission and deposition fluxes. The observations characterise transport with regard to a single station. Furthermore, weather observation stations provide information on the presence of atmospheric dust in addition to information of the general state of the atmosphere like wind, temperature, dew-point, pressure, precipitation and visibility. As dust reduces horizontal visibility, long-term station observations have been used to conclude to dust storm activity over North Africa (*Mbourou et al.*, 1997) but also worldwide (*Mahowald et al.*, 2007). Additionally, radio sonds and drop sonds (from air planes) provide information on the height of dust layers (e.g. *McConnell et al.*, 2008; *Ott et al.*, 1991)

The dust cycle consisting of entrainment (dust emission), transport path (height and direction) and deposition (dust removal from the atmosphere) strongly depends on atmospheric conditions during each step of the cycle. Local wind regimes force dust emission if the local threshold wind speed is exceeded and determines the dust flux into the atmosphere (*Marticorena and Bergametti*, 1995; *Shao*, 2001). Local and regional atmospheric conditions like stability and wind impact on vertical mixing, transport height and direction of the emitted dust particles. Atmospheric large-scale circulation transports the dust away from source regions. Thus, stability, transport height, size distribution of the airborne dust, clouds and precipitation are major factors for dust removal from the atmosphere, also affecting the location of deposition.
Dust emission does not occur as continuous process. It rather starts and stops when the surface winds exceed threshold conditions and fall short again. Observations show an intermittent characteristic. Airborne dust does not appear as a homogeneously distributed aerosol, although a background level of dustiness is obvious at stations downwind of desert areas (e.g. *Carlson*, 1979). Sometimes it occurs as dense dust plume, sometimes as slight dust haze at varying locations which makes it difficult to estimate dust feedback on e.g. radiation budget, cloud, precipitation and ecosystems.

For an adequate estimation of dust impacts on atmospheric processes and processes of the ecosystem, an as accurate as possible description of potential dust source areas with regard to geomorphology is necessary. Furthermore, the understanding of meteorological situations leading to frequent dust emission will help to relate dust storms to typical weather conditions and improve the adjustment of e.g. land-use in a changing environment. An improved dust forecast will also help to prevent health of millions of people living in desert areas.

To characterise dust cycle and to estimate dust feedbacks, modelling and measurement approaches have been performed during the last decades. Dust schemes have been implemented in global (e.g. GOCART (Global Ozone Chemistry Aerosol Radiation Transport) model, (*Ginoux et al.*, 2001), DEAD (Dust Entrainment And Deposition) module (*Zender et al.*, 2003)) and regional scale atmospheric models (e.g. DREAM (Dust REgional Atmospheric Model) (*Nickovic et al.*, 2001; *Pérez et al.*, 2003), CHIMERE-Dust model (*Menut et al.*, 2007), LM-MUSCAT (*Heinold et al.*, 2007)) to estimate the amount of dust emission, major dust transport paths, dust residence time within the atmosphere and deposition fluxes (e.g. *Ginoux et al.*, 2001; *Tegen and Fung*, 1994; *Weaver et al.*, 2001). The radiative feedback of dust leading to either warming or cooling of the net effect is estimated in recent literature, using global (e.g. *Perlwitz et al.*, 2001; *Tegen and Lacis*, 1996) and regional scale models (e.g. *Heinold et al.*, 2007; *Pérez et al.*, 2003). Such models must be validated against a range of observational data.

To improve our understanding of dust feedback to the environment, several measurement campaigns have been performed during the last decades. E.g., the BODEX (BODélé EXperiment) in 2005 studied on the process of dust entrainment. It carried out at the Bodélé Depression in Chad, often referred as “World's dustiest place” (*Todd et al.*, 2007, 2008; *Washington and Todd*, 2005; *Washington et al.*, 2006a,b). The AMMA (African Monsoon Multidisciplinary Analysis, *Redelsperger et al.* (2006)) campaign investigates dust and monsoon relations using a wide field of measurement set-ups, modelling and remote sensing techniques with the aim to improve the knowledge on West African Monsoon circulation and its influence on a regional and global environment. Besides the SHADE (SAHaran Dust Experiment, *Haywood et al.* (2003)) campaign in September 2000, the SAMUM (SAharan Mineral dUst experiMent, Tellus Special Issue, 61B(1), 2009) project focuses on the optical properties and radiative impact of Saharan dust particles. Thereby, the SAMUM-I campaign in May 2006 in Morocco determines optical and mineralogical properties of dust particles at near source regions. SAMUM-II in January/February 2008 was located at the Cape Verde Islands, suitable to study aged dust in an environment polluted with soot from biomass burning. The mixing of dust and biomass burning aerosol was also a topic of DABEX (Dust And Biomass EXperiment, *Johnson et al.* (2008)). Thereby, measurements have been performed during January and February 2006 near Niamey over the Sahel. The DODO-Experiment (Dust Outflow and Deposition to the Ocean) investigates Saharan dust export and deposition to the Atlantic using aircraft measurements based in Dakar, Senegal (*McConnell et al.*, 2008). In addition to studies on optical properties, the role of dust within the oceanic ecosystem is investigated by the SOPRAN (Surface Ocean PRocess in the Anthroprocene, http://sopran.pangaea.de) project embedded to the SOLAS (Surface Ocean – Lower Atmosphere Study, http://www.uea.ac.uk/env/solas) project frame. Besides African dust, Asian dust is in the focus of recent experiments like the ACE-Asia (Aerosol Characterization Experiment) project in 2001 and the PACDEX campaign (PACific Dust EXperiment, http://www.eol.ucar.edu/projects/pacdex/), which investigate Asian dust and pollutants transported to the Pacific. Such field studies provide information on specific short-term dust events.

Remote sensing methods are used to characterise atmospheric dust, but also to localise dust source areas over arid and semi-arid terrain (e.g. *Prospero et al.*, 2002; *Schepanski et al.*, 2007; *Zender and Newman*, 2003) following different approaches. Spectrometers onboard low orbiting space crafts like the Franco-American A-Train chain of sun-synchronous orbiting Earth observation satellites (in 2008 consisting of Aqua, Aura, Parasol, CALIPSO and CloudSat) show high spatial resolution of a single sample, but due to its relative narrow viewing field (13 km × 25 km for OMI (Ozone Monitoring Instrument) on-board NASA Aura space craft), at least one day is needed to cover the whole Earth by composing the meridional swathes (paths) of the satellites. Compared to single-viewing instruments like OMI, MODIS (MODerate resolution Imaging Spectrometer) or SEVIRI (Spinning Enhanced VIsible InfraRed Imager), multi-viewing instruments such as MISR (Multi-angle Imaging SpectroRadiometer) or MERIS (MEdium Resolution Imaging Spectrometer) are limited for dust retrievals by a relative coarse resolution (*Kahn et al.*, 2007).

To retrieve information on the vertical structure of atmospheric dust plumes, the vertical atmospheric column can be remotely observed by e.g. sondes or LIDAR instruments. Since 2006, CALIOP (Cloud-Aerosol Lidar with Orthogonal Polarization) is flying onboard CALIPSO (Cloud Aerosol Lidar and Infrared Pathfinder Satellite Observation) measuring vertical atmospheric profiles. This profiles containing information on vertical dust distribution are also used to assimilate models or to reduce the height dependency in aerosol retrievals. Furthermore, dust export paths e.g. from the Sahara towards the Atlantic are estimated (*Liu et al.*, 2008). But for spatio-temporal dust source characterisation, CALIPSO measurements are not suitable due to its narrow viewing-field and the resulting low spatio-temporal resolution. For dust source observation covering continental scale areas, relatively high spatial and temporal resolutions are required.

Aerosol optical thickness (AOT) retrievals applied to the visible part of the spectrum cannot be used for dust source determination over bright surfaces like in arid and hyperarid areas. For dust source analysis based on space-borne dust detection, dust aerosol algorithms as the OMI Aerosol index (AI), Deep Blue and infrared (IR) techniques are applicable. But due to their daily (or less) resolution the diurnal characteristic from polar-orbiting instruments like OMI and MODIS and accurate location of dust sources is difficult for an area like the Saharan desert, where dust source activations occur during the morning hours (*Schepanski et al.*, 2008b) and the sun-synchronous orbiting satellite overpasses around noon. Daily maps of airborne dust index like the TOMS/OMI AI are often used to retrieve dust source areas (e.g. *Prospero et al.*, 2002). *Prospero et al.* (2002) and *Washington et al.* (2003) relate high frequencies of high dust index values to the location of dust source areas. *Brooks and Legrand* (2000) follow a similar approach relating high mean values of the daily Infrared Difference Dust Index (IDDI) to dust source areas. *Grini et al.* (2005) assume relation between surface reflectivity and soil types suitable to act as dust source. All these approaches are applied to satellite retrievals that are available at daily resolution at best. Furthermore, the accuracy of the applied dust detection algorithms is limited by the ability of the space-borne instrument, which is characterised by sampling interval, orbital parameter and wavelength spectrum. Therefore, daily products are used and applied to statistical methods. Sub-daily processes as dust mobilisation and variabilities in transport cannot be resolved by applying daily retrievals. To have a more detailed understanding in dust source areas and mobilisation processes, observations on a higher temporal resolution are required. When comparing to sub-daily dust index products, a strong transport component in wind direction is evident, biasing the retrieved location of assumed dust sources (*Schepanski et al.*, 2007).

Geostationary satellites provide observations on a high temporal resolution such as the European Meteosat Second Generation (MSG) satellite. Due to its geostationary location, measurements are provided for the whole viewing field at one scanning sequence. The viewing field of the MSG SEVIRI (Spinning Enhanced Visible and InfraRed Imager (*Schmetz et al.*, 2002)) instrument covers the Arabian Peninsula, the Middle East, Africa, Europe, Eurasia and the Atlantic Ocean.

The high spatio-temporal resolution of MSG SEVIRI observations motivates an analysis of Saharan dust source activity (*Schepanski et al.*, 2007). A detailed characterisation of dust source activity improves the understanding of dust source distributions. Furthermore the knowledge on temporal distribution of dust source activity helps to identify meteorological situations that may provide atmospheric conditions suitable for dust mobilisation (*Schepanski et al.*, 2008b). Satellite observations are not able to quantify dust emission process itself. Only the fact, that dust was mobilised can be indicated by satellite indices. Monitoring times-of-day when dust mobilisation starts for each source location indicate recurring atmospheric conditions leading to dust source activations at this location. To investigate such recurring meteorological conditions, meso-scale model studies are a good enhancement (*Schepanski et al.*, 2008b).

Neither ground-based measurements, remote sensing nor modelling are able to describe all aspects of the dust cycle by itself. But in combination the information from each approach can complement each other and lead to a more accurate understanding and description of the global dust cycle. In the present work, the Saharan dust cycle is described using satellite remote sensing techniques, sun-photometer data, observations of weather stations and regional modelling. The work was performed in the frame of the network project TRACES (Ocean – Atmosphere – Land Impacts on TRopical AtlantiC EcoSystems) funded by the Wissenschaftsgemeinschaft Gottfried Willhelm Leibniz. The project investigates the transport of soil lithogenic matter towards the tropical Atlantic and its role in the ecosystem.

The present thesis is structured as following: First an overview on the Saharan dust cycle in Chapter 2 including dust emission, transport and deposition processes, and an introduction in the meteorological aspects forcing mineral dust emission in Chapter 3 will be given. Then Chapter 4 and Chapter 5 and will describe the methods used in this work: Satellite remote sensing and regional modelling. Results of this work will be given in Chapter 6 by three scientific publications, comprising the third part of the thesis. This thesis will conclude with an outlook given in Chapter 7.

Following scientific papers are published in the frame of this thesis:

K. Schepanski, I. Tegen, B. Laurent, B. Heinold, and A. Macke (2007), A new Saharan dust source activation frequency map derived from MSG-SEVIRI IR-channels, Geophys. Res. Lett., 34, L18803, doi:10.1029/2007GL030168.

> This publication presents a newly developed map of Saharan dust source areas inferred from 15-minute MSG SEVIRI IR dust index observations. The dust index is validated in terms of its sensitivity to detect airborne dust. A comparison of the newly derived dust sources with the commonly used approach that relates high frequencies of a dust-indicating aerosol index to dust source areas is performed showing a strong impact of dust wind transport component in

> dust source areas derived from daily dust retrievals. In addition, the new compiled map of dust sources is used in simulations of dust emission and transport with the regional model system LM-MUSCAT. An improvement of dust distribution can be shown when utilising the new map compared to earlier results.

K. Schepanski, I. Tegen, M. C. Todd, B. Heinold, G. Bönisch, B. Laurent and A. Macke (2008), Meteorological processes forcing Saharan dust emission inferred from MSG-SEVIRI observations of sub-daily dust source activation, J. Geophys. Res., revised.

> Dust entrainment to the atmosphere can be considered as a wind threshold problem, linking atmospheric and soil conditions. In this publications, the meteorological role for frequent dust mobilisation is investigated using spatio-temporal dust source analysis as introduced in *Schepanski et al.* (2007), wind measurements performed at synoptic stations, global and regional scale modelling. 65 % of Saharan dust source activation events are obseved during the local morning hours, pointing towards the frequent recurring meteorological process of the break-down of the low-level jet (LLJ). Here, the ability of the LLJ break-down as mechanism for frequent dust emission is the major focus.

K. Schepanski, I. Tegen and A. Macke (2008), Saharan dust transport and deposition towards the Tropical Northern Atlantic, Atmos. Chem. Phys. Discuss., 8, 16061-16096, SRef-ID: 1680-7375/acpd/2008-8-16061.

> A modelling study using the meso-scale dust emission and transport model LM-MUSCAT is performed to characterise seasonally changing strength and extension of the Saharan dust cycle. Three case studies are computed, each comprising an one month period representing different seasons (spring, summer, winter). Horizontal and vertical distributions of atmospheric dust concentrations indicate a clear seasonality concerning height and direction of dust transport. Furthermore, the contribution of dust originating from the Bodélé depression, the strongest emitting Saharan dust source area, is estimated.

The latter publication is submitted to the journal *Atmosphere Chemistry Physics*, the last stage of the peer-review publishing process for this interactive open-access journal.

Moreover, during the here presented work several publications have been written in collaboration with members of working groups at different institutes. In the following, this peer-review publications will be listed, but not discussed in detail.

W. Birmili, **K. Schepanski**, A. Ansmann, G. Spindler, I. Tegen, B. Wehner, A. Novak, E. Reimer, I. Mattis, K. Müller, E. Brüggemann, T. Gnauk, H. Herrmann, A. Wiedensholer, D. Althausen, A. Schladitz, T. Tuch, G. Löschau (2008), A case of extreme particulate matter concentrations over Central Europe caused by dust emitted over the southern Ukraine, Atmos. Chem. Phys., 8, 997-1016.

C. Cavazos, M. C. Todd, **K. Schepanski** (2008), Numerical model simulation of the Saharan dust event of March 2006, J. Geophys. Res., revised.

B. Heinold, I. Tegen, **K. Schepanski**, O. Hellmuth (2008), Dust Radiative Feedback on Saharan Boundary Layer Dynamics and Dust Mobilization, Geophys. Res. Lett., 35, L20817, doi:10.1029/2008GL035319.

L. Klüser and **K. Schepanski** (2008), Remote sensing of mineral dust with MSG inferred channels: A new Bitemporal Mineral Dust Index, submitted to Remote Sens. Environ.

F. Reinfried, I. Tegen, B. Heinold, O. Hellmuth, **K. Schepanski**, U. Cubasch, H. Huebener, P. Knippertz, Simulations of convectively-driven density currents in the Atlas region using a regional model: Impacts on dust emission and sensitivity to horizontal resolution and convection schemes, J. Geophys. Res., revised.

R. Washington, C. Bouet, G. Cautenet, E. Mackenzie, I. Ashpole, S. Engelstaedter, G. Lizcano, G. Henderson, **K. Schepanski**, I. Tegen (2008), Dust as a Tipping Element: The Bodélé Depression, Chad, PNAS, revised.

B. Heinold, I. Tegen, M. Esselborn, K. Kandler, P. Knippertz, D. Müller, A. Schladitz, M. Tesche, B. Weinzierl, A. Ansmann, D. Althausen, B. Laurent, A. Massling, T. Müller, **K. Schepanski**, A. Wiedensohler (2009), Regional Saharan Dust Modeling during the SAMUM 2006 Campaign, Tellus, 61B(1), in press.

P. Knippertz, A. Ansmann, D. Althausen, D. Müller, M. Tesche, E. Bierwirth, T. Dinter, T. Müller, W. von Hoyningen-Huene, **K. Schepanski**, M. Wendisch, B. Heinold, K. Kandler, A. Petzold, L. Schütz, I. Tegen (2009), Dust Mobilization and Transport in the Northern Sahara during SAMUM 2006 – A Meteorological Overview, Tellus 61B(1), in press.

Chapter 2

Saharan Dust Cycle

2.1 Dust Mobilisation: A Threshold Phenomenon

Dust mobilisation is limited by surface characteristics and surface wind velocity. Observations and laboratory experiments show a non-linear relation between the number and size distribution of mobilised dust and the surface wind velocity (*Bagnold*, 1941). Furthermore, dust mobilisation only occurs for wind velocities higher than a certain local threshold.

Physically, dust mobilisation is described by processes setting soil particles in motion, either in horizontal or vertical direction. Therefore, momentum is transferred due to wind or collision with adjacent particles. The magnitude of transferred momentum, particle gravitation and interparticle cohesion forces comprising van der Waals, electrostatic, capillary and chemical binding forces are factors limiting whether a particle starts moving or remains at rest. In general, dust emission can be determined by the balance of gravitational, cohesive and aerodynamic forces (*Shao*, 2001). As particle mobilisation depends on the momentum transfer from the air to the erodible soil elements, energy transfer can be described by the surface wind shear stress $[kg\, m^{-1} s^{-2}]$,

$$\tau = \rho_a u_\star^2, \tag{2.1}$$

with ρ_a being the air density $[kg\, m^{-3}]$ and $u_\star$ the wind friction velocity $[m\, s^{-1}]$,

$$u^\star = U_0 \kappa \ln \left(\frac{z}{z_0} \right)^{-1}, \tag{2.2}$$

with the von Karman constant κ, the roughness length z $[m^{-1}]$, the surface roughness length z_0 $[m^{-1}]$ and the surface wind velocity U_0 $[m\, s^{-2}]$. This relationship is valid for neutral stability conditions. The threshold wind friction velocity $u_{\star,t}$ $[m\, s^{-1}]$ be exceeded for dust particle mobilisation depends on particle diameter D_p $[m]$ (Figure 2.1), particle density ρ_p and air density ρ_a, according to the equation

$$u_{\star,t} = A \sqrt{\frac{\rho_p g D_p}{\rho_a}}, \tag{2.3}$$

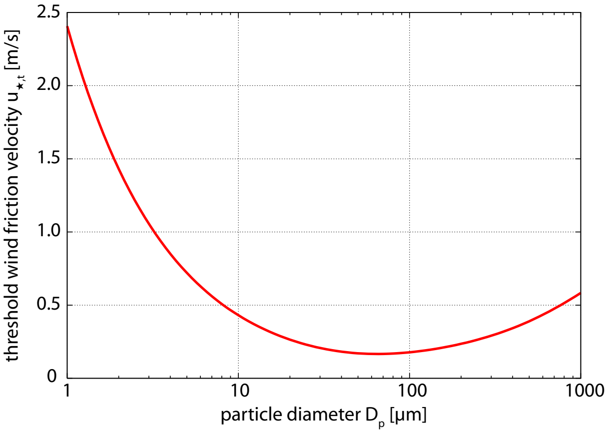

Figure 2.1: *Threshold wind velocity for particle mobilisation depending on particle size. For small particles cohesive forces are dominant and inhibit particle mobilisation for low wind friction velocities. For large particles the threshold wind friction velocity increases again due to increasing gravitational forces. After Marticorena and Bergametti (1995).*

with the gravitational constant g $[m\,s^{-2}]$ and a threshold parameter A depending on the friction Reynolds number (*Marticorena and Bergametti*, 1995). $u_{\star,t}$ is small for dry and sparse vegetated sandy surfaces. Therefore, the most important dust sources are situated over such areas. Over semi-arid and arid areas wind velocities of at least around $6\,m\,s^{-1}$ are necessary to mobilise dust particles (*Bouet et al.*, 2007; *Tegen and Lacis*, 1996; *Todd et al.*, 2007). As wind provides momentum, and soil characteristics require a minimum of transferred energy for mobilisation, both, wind and soil characteristics are the main limiting factors to describe dust mobilisation. Both, $u_{\star,t}$ and $u_\star$ depend on several factors such as atmospheric conditions, soil type, soil texture, and topographical forcing e.g. turbulence by windbreaks (*Shao*, 2000).

The soil surface can be described by vegetation cover, roughness elements (e.g. rocks, stones, pebbles), soil texture (e.g. coarse, medium, fine sand, silt, clay) and soil moisture content. On the one hand these parameters limit the erodibility of the surface and on the other hand the momentum flux required for particle mobilisation is a limiting factor (*Gillette*, 1979; *Marticorena and Bergametti*, 1995). Soil surfaces are a mixture of different-sized particles following a size distribution according to the local geomorphological conditions. Both, gravitational and cohesion forces are size-dependent and are described by the soil surface characteristics. Cohesion forces depend on mineralogical composition of the soil. E.g., clay particles show higher cohesion forces than quartz particles in the same size range. The progress of mobilised particles depends on buoyancy and gravitational forces, influenced by particle weight and aerodynamic drag. To describe the momentum flux from the atmosphere to the soil, relations between wind friction velocity and dust flux have been assumed. A relation between wind friction velocity and size distribution of mobilised particles is obvious (*Marticorena and Bergametti*, 1995).

Bagnold (1941) proposed to classify three main types of particle motion (Figure 2.2): *suspension* for the finest particles with diameters smaller than 60 μm, *saltation* for particles

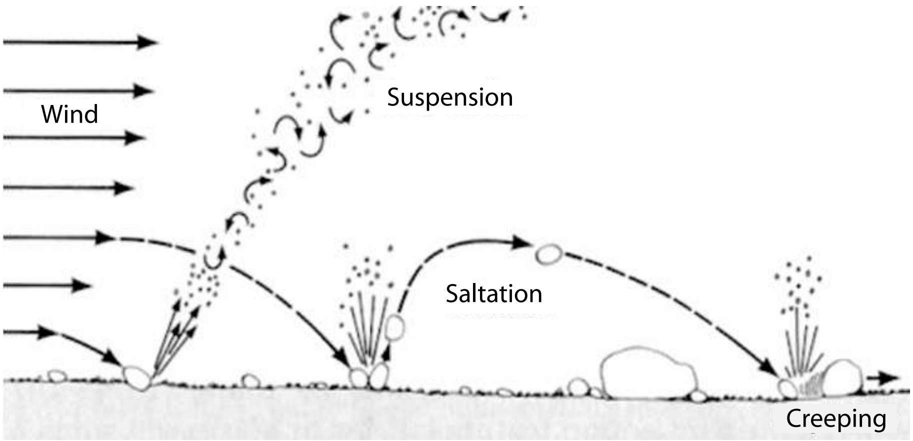

Figure 2.2: *Classification of particle motion (Bagnold, 1941), modified from http://www.lmfa.ec-lyon.fr*

larger than 60 μm but smaller than 2000 μm and *creeping* for particle elements larger than 2000 μm. Depending on particle size and factors like wind, stability, and precipitation rate, a certain residence time for dust particles can be assumed (*Duce*, 1995).

Suspension or aerodynamic entrainment
Finest particles ($< 60\,\mu$m) are small enough to be transported upward by turbulent eddies and aerodynamic forces (*Shao*, 2001). Gravity forces diminish mobilisation of particles larger than 2000 μm. Fine particles are difficult to mobilise due to interparticle cohesive forces. Dust flux due to direct aerodynamic entrainment is low (*Loosmore and Hunt*, 2000). Once mobilised, fine particles are able to remain in the atmosphere for long times and can be transported over long distances far away from their source regions by large scale circulation pattern (e.g. *Mahowald et al.*, 2003; *Prospero et al.*, 1981, 1996; *Riemer et al.*, 2006). Desert dust, associated with particle diameters smaller than 60 μm are observed to cross the oceans within elevated air layers (e.g. *Arimoto et al.*, 1997; *Barkan et al.*, 2004; *Goudie and Middleton*, 2001; *Prospero et al.*, 1981, 1996).

Saltation (bombardment)
Due to the sandblasting behaviour, a disaggregation of fine and coarse particles can be observed (*Zender et al.*, 2003). Particles with diameters in the range of 60 to 100 μm are most suitable for mobilisation (*Bagnold*, 1941; *Iversen and White*, 1982). But due to gravitational forces, the particles settle down within a few minutes or hours (*Duce*, 1995). Saltation is the main and most efficient process for dust mobilisation and due to its sandblasting behaviour also fine particles are emitted (e.g. *Grini et al.*, 2002; *Marticorena and Bergametti*, 1995; *Shao et al.*, 1993, 1996).
Particles lifted by surface winds with diameters in the rage of 60 to 2000 μm reach heights of a few decimetre up to 1-2 m (*Marticorena and Bergametti*, 1995; *Pacyna*, 1995). To remain in the atmosphere, gravitational forces related to the particle weight, and buoyancy forces impacted by upward motion and aerodynamic drag, have to be at least in

an equilibrium. Particles larger than 60 μm fall back to the ground near the source area. Momentum from the air is transferred to soil particles that are lifted and deposited down again by gravitational settling, where it may mobilise smaller particles by impaction.

Creeping
Soil particles larger than 2000 μm were too heavy for up-lifting, but wind momentum is able to set these particles in horizontal motion by shear forces. This motion is called creeping.

In the recent literature several formulations and approaches describing dust mobilisation processes mathematically exists (e.g. *Marticorena and Bergametti*, 1995; *Shao*, 2001; *Zender et al.*, 2003). Commonly, the dust flux F is separated into a horizontal and vertical component. Taking sandblasting linking the horizontal dust flux F_h $[kg\,m^{-1}\,s^{-1}]$ to the vertical flux F_v $[kg\,m^{-2}\,s^{-1}]$ into account, the dust flux can be approximated by Equation 2.4 and 2.5, representing the non-linear relation between dust flux and wind velocity (Figure 2.3). Here, the sandblasting efficiency is expressed by the soil type depending factor α $[m^{-1}]$.
Vertical dust flux:

$$F_v = \alpha F_h, \tag{2.4}$$

Horizontal dust flux:

$$F_h = \frac{\rho_a}{g} u_\star^3 \left(1 + \frac{u_{\star,t}(D_p)}{u_\star}\right)\left(1 - \frac{u_{\star,t}^2(D_p)}{u_\star^2}\right) \tag{2.5}$$

Beside $u_\star$ and $u_{\star,t}$, the dust flux is determined by the effective surface area covered by vegetation and snow and the surface soil moisture content. Vegetation and snow cover prevent dust mobilisation.
The amount of particles set into motion due to sandblasting depends on particle size distribution and the mineralogical composition. Consequently, different sandblasting efficiencies have to be assumed for different soil types as shown by wind tunnel experiments (e.g. *Gillette*, 1978) and field experiments (e.g. *Shao et al.*, 1996). Dust emission occurs when all limiting factors allow for wind erosion. However, it can be imagined that spatial and temporal variability in dust source areas is evident, mainly related to varying local soil characteristics (i.e. vegetation cover in semi-arid areas) and atmospheric conditions.

2.2 Dust Transport

Dust mixed up into the atmosphere is transported within local wind regimes, regional- and large-scale circulation pattern. Dust transport depends on, the height up to which the dust is mixed. Dust particles larger than 60 μm are removed from the atmosphere by dry deposition in less than one day (*Duce*, 1995) in the absence of precipitation and cloud interactions. Larger particles (60 - 2000 μm) fall out near the source area and particles are situated at lower tropospheric levels. Only small particles ($<$ 60 μm) can be mixed

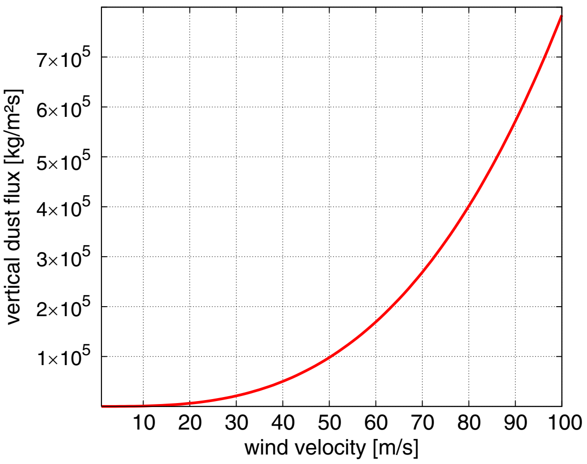

Figure 2.3: *Relation of vertical dust flux and surface wind velocity, after Marticorena and Bergametti (1995).*

over the entire boundary layer depth due to turbulent fluxes and can remain within the atmosphere for several days (*Duce*, 1995). During this time, the dust aerosol is embedded in the transport of the air mass. Vertical turbulent fluxes determine the mixing height and therefore the vertical extent of the dust layer. Local wind regimes, impacted by surface conditions like topography and roughness elements (e.g. vegetation, rocks, stones) transport the dusty air layers away from the source area. On a larger scale, local wind regimes are impacted by regional and large-scale circulation pattern, which gain influence on the dust transport. During transport, the height of the dust layer changes due to air mass properties. This leads either to elevation or subsidence, which in terms determines whether the dust layer is more impacted by larger-scale circulation pattern or local scale conditions. Particles being mixed into upper tropospheric levels are able to remain within the atmosphere for 1-2 weeks (*Duce*, 1995) and will be influenced by general circulation regimes of the atmosphere (e.g. *Mahowald et al.*, 2003; *Prospero et al.*, 1996; *Riemer et al.*, 2006).

The Sahara as World's largest dust source contributes the largest fraction to the atmospheric dust content and shows seasonal varying transport pattern with regard to amount and pathway. The wind regimes are important for transport directions, air mass characteristics like moisture content and temperature are important especially for transport height. Additionally, the seasonality of the dust source activity affects the dust export as it adjusts the local and temporal distribution of source areas and the emitting dust flux. Saharan dust export towards the tropical and subtropical North Atlantic is mainly influenced by

1. spatial distribution of activated dust source areas,
2. predominant regional wind regimes,
3. boundary layer heights, and
4. precipitable clouds controlling atmospheric wash-out and rain-out of dust.

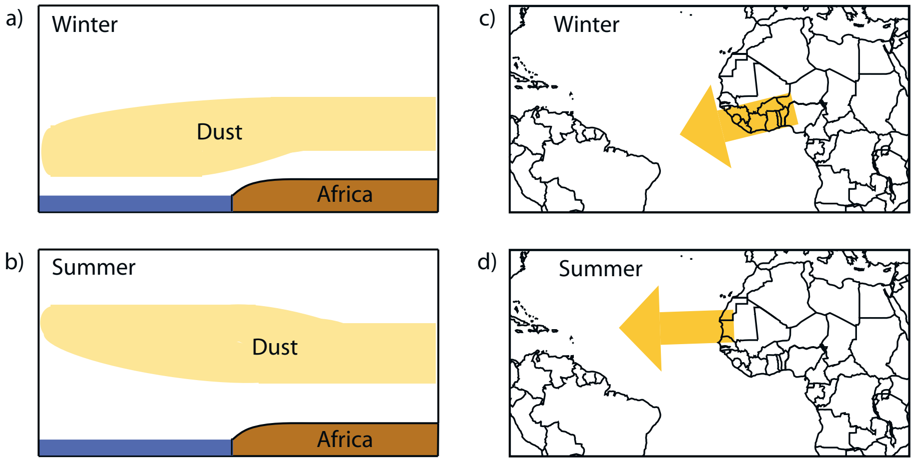

Figure 2.4: *Schematics of Sahran dust export towards the tropical North Atlantic with regard to main transport height and direction. The image is taken from Schepanski et al. (2008a). In winter, a south-westward wind regime is dominant and transport dust towards South America. In summer, westward winds transport dust towards the Caribbean. Additionally, dust source activity changes with seasons. In winter, the Bodélé area is the most activ dust source area, while West African dust sources are dominant in summer (Schepanski et al., 2007).*

After dust mobilisation, upward mixing leads to a specific vertical distribution of atmospheric dust, influenced e.g by particle size distribution and atmospheric stability. Boundary layer dynamic is responsible for the (homogeneous) vertical distribution of dust and the height of the top of the dust layer which is important for transport. First, a new dust layer is transported by local wind regimes within the boundary layer (BL) because the inversion at the top of the daytime boundary layer inhibits a vertical mixing over the entire troposphere. During night, convective turbulence due to insolation creases and a shallow boundary layer develops within the height of the former daytime boundary layer. The layer between the former top of the daytime boundary layer and the top of the nocturnal boundary layer is called residual boundary layer. In case of a strong vertical mixing during daytime and consequently a deeper daytime boundary layer, dust is trapped within the residual layer (*Kalu*, 1979). During night, a nocturnal low-level jet (LLJ) can develop under suitable conditions, at the top of the nocturnal boundary layer. This low-level wind speed maximum transports the dust layer away from the source region (e.g. *Westphal et al.*, 1987). When a strong daytime boundary layer develops dust again is mixed down from the former residual layer. Otherwise, the dust remains as an enclosed layer within the atmosphere. On the one hand, during step-wise coupling dust layer to the daytime boundary layer and decoupling to a residual layer, a dust layer can either lost dust load due to daytime turbulent downward mixing. On the other hand, it can be rapidly transported during night within the nocturnal LLJ. By reaching areas with daytime boundary layer depth below the level height of the dust layer, dust can become detached and remains for a long time in the atmosphere, and thus can be transported over long distances. Depending on the seasons, boundary layer depths change and so does the transport height of dust layers entering the tropical North Atlantic (Figure 2.4). Consequently, transport paths of Saharan dust layers towards the Atlantic depend on the seasons (Figure 2.4), mainly related to the position of the inter-tropical convergence zone (ITCZ) and of strength and direction of the trade winds (*Engelstaedter et al.*, 2006; *Mbourou et al.*, 1997; *Moulin et al.*, 1997).

Interannual variability of dust transport across the Atlantic is proposed to be related to the North Atantic Oscillation (NAO) (*Hurrell*, 1995; *Jones et al.*, 1997) and is investigated by several studies using satellite data (e.g. *Chiapello and Moulin*, 2002; *Chiapello et al.*, 2005; *Evan et al.*, 2006; *Moulin et al.*, 1997; *Riemer et al.*, 2006), in-situ measurements (e.g. *Mahowald et al.*, 2003; *Moulin et al.*, 1997) and global modelling (e.g. *Ginoux et al.*, 2004). The NAO is build up by two centrers of action, the Icelandic Low and the Azores High. To characterise the variability of the NAO, an index is defined by from the normalised difference between atmospheric pressure at sea-level at stations near to the two centres of action: Stykkisholmur, Iceland and Lisbon, Portugal (*Hurrell*, 1995). *Jones et al.* (1997) use the standardised pressure difference between Iceland and Gibraltar instead. A strengthening of the Azores high and thus a northward shift of the westerly winds occurs for positive phases of the NAO. The trade winds are strengthened and shifted (*Chiapello and Moulin*, 2002; *Chiapello et al.*, 2005), dryer conditions (*Moulin et al.*, 1997) and strong Harmattan surges due to a strong Azores high occur (*Knippertz and Fink*, 2006) leading to increased dust mobilisation over North Africa. Furthermore, patterns of wind and precipitation related to the NAO control dust transport across the Atlantic, especially during winter.

The variability of Saharan dust outbreaks towards the tropical Atlantic during northern hemispheric summer is assumed to be modulated by African Easterly Waves (AEW) (e.g. *Jones et al.*, 2003, 2004; *Prospero and Nees*, 1986; *Prospero et al.*, 1981). AEW are synoptic-scale disturbances of the middle-level African Easterly jet (AEJ), which is build up by the thermal gradient between high temperatures over the Sahara desert and lower temperatures over the Gulf of Guinea (e.g. *Thorncroft and Blackburn*, 1999).

Enclosed Saharan dust layers propagating towards the North Atlantic are often refereed to as Saharan Air Layer (SAL) (e.g. *Dunion and Velden*, 2004) and are observed to extend over a large area of the North Atlantic far west to the West Indies (*Carlson and Prospero*, 1972). The dusty air layer can be identified by very low relative humidity, high optical opacity and high potential temperatures. The layer is separated by a strong vertical inversion. During north hemispheric summer, the SAL is located above the trade wind layer at a height of up to 5–7 km (*Chiapello et al.*, 1997; *Dunion and Velden*, 2004; *Kalu*, 1979), during winter, the SAL is embedded in the trade wind layer at levels below 1.5–2 km (*Barkan et al.*, 2004; *Chiapello et al.*, 1997). In summer, the Saharan dusty air overlays the moist, denser monsoon air, reaches the Atlantic and crosses the ocean embedded within the westward winds as enclosed layer. The marine BL is relative shallow compared to the continental BL. When reaching the warm, West Atlantic, the SAL extends downward into the marine BL due to sedimentation of dust particles (*Karyampudi et al.*, 1999). Furthermore, deep moist convection strong enough to penetrate through the BL inversion and strong vertical wind shears due to the middle-level easterly jet is able to mix dust from

the SAL downwards (*Karyampudi et al.*, 1999). To cross the Atlantic, times of around one week (5-7 days) are derived from satellite imaginary (e.g. *Carlson and Prospero*, 1972; *Ott et al.*, 1991), dust plume tracking by atmospheric soundings, and the time of arrival of dust-laden air at different stations along the transport pathway (*Prospero et al.*, 1981).
Beside dust export towards the North Atlantic, Saharan dust is transported towards the Mediterranean Sea and farther to South, Central and North Europe (e.g. *D'Almeida*, 1986; *Franzen et al.*, 1994; *Guerzoni et al.*, 1997). The Sharav Cyclone, a lee-cyclone enhanced by baroclinity counts for several dust storms observed over the Mediterranean coast and Middle East (*Alpert and Ziv*, 1989; *Alpert et al.*, 1990).

Dust transport paths give information on areas where the dust can be expected to settle down, which is e.g. important for economical (e.g. aviation and ground transportation), governmental (e.g. air-quality restrictions), health and fertilisation aspects. During atmospheric transport, dust particle surface may change concerning physical, optical and chemical characteristics. (Photo)-chemical processes under dry or aqueous (e.g. in presence of clouds or moist air) conditions as well as reactions due to adsorption of soot and pollutants (e.g. sulphur) occurs, depending on the transport path in relation to clouds or emitted pollutants (e.g. biomass burning, industry, aviation, shipping) (e.g. *Erel et al.*, 2006; *Meskhidze et al.*, 2003). Changing particle characteristics may change particle–radiation interactions, the bio-availability of micro-nutrients delivered by dust or the hygroscopic properties important for particle–cloud interactions (e.g. *Fan et al.*, 2006; *Johansen et al.*, 2000; *Meskhidze et al.*, 2005).

2.3 Dust Deposition

The removal of dust from the atmosphere is described by the deposition, separated into dry and wet deposition. The former is related to turbulent diffusion and gravitational settling. The latter is described by scavenging processes like rain wash-out or in-cloud scavenging (removal of dust particles by cloud droplets).
Whether dust particles remain in the atmosphere or settle down can be described by the relation of particle upward and downward motions. Due to their weight, gravitational forces lead to a downward motion. Turbulent eddies as well as Brownian diffusion have either upward or downward components of vertical motions intensifying or diminishing buoyancy effects of drag forces. Turbulent transfer, Brownian diffusion, impaction, interception, gravitation and particle rebound have to be considered. A simple description of the forces acting on aerosol particles within a fluid like the atmosphere are given by Newton's gravitation law (left term of Equation 2.6) for friction consideration and the Stokes equation describing the flow within a viscose medium with relation to drag, viscosity and particle velocity (right term of Equation 2.6). Equilibrium between gravitational and frictional forces leads to the equation

$$\frac{g\pi D_p^3 \left(\rho_p - \rho_a\right) C_c}{6} = 3\pi\eta D_p v_g, \tag{2.6}$$

with the gravitational constant g $[m\,s^{-2}]$, particle diameter D_p $[m]$, particle density ρ_p $[kg\,m^{-3}]$, air density ρ_a $[kg\,m^{-3}]$, Cunningham slip correction factor C_c, dynamic viscosity of air η $[kg\,m^{-1}\,s^{-1}]$ and the gravitational settling velocity v_g $[m\,s^{-1}]$. Gravitational settling is commonly described by the terminal settling velocity v_g, derived from Equation 2.6 describing the terminal fall velocity of a particle

$$v_g = \frac{(\rho_p - \rho_a)\, g D_p^2 C_c}{18\eta}. \tag{2.7}$$

The Stokes law considers the velocity of the air surrounding the dust particles relative to the particle itself as zero. This assumption is correct in continuum but not for particles larger than the mean free path λ of air molecules. So the Cunningham slip correction factor C_c is used to apply the Stokes law for larger particles. The experimentally determined relation

$$C_c = 1 + \frac{2\lambda}{D_p}\left[1.142 + 0.558\exp\left(-\frac{0.4995 D_p}{\lambda}\right)\right] \tag{2.8}$$

is a function of the particle diameter D_p and the mean free path λ $[m]$ of air molecules and is proposed by *Allen and Raabe* (1982, 1985). The quotient $\frac{2\lambda}{D_p}$ expresses the Knudsen Number, a measure for the density of the flow. Mineral dust particles are the product of soil erodible processes and consequently non-spherical particles with irregular surface structures. To take different settling velocities of spherical and irregular particles into account, an equivalent aerodynamic diameter, Stokes diameter or volume equivalent diameter is defined, adjusted to Stokes Equation by a shape factor. The aerodynamic diameter is described by the diameter of a spherical particle with the density of $\rho_0 = 1000\,kg\,m^{-3}$. The artificially created particle is characterised by the same sedimentation velocity v_g as the particle of interest. The Stokes diameter denote the diameter of a spherical particle having the same density and sedimentation velocity as the particle of interest. Finally, the volume equivalent diameter indicates the diameter of a spherical particle with the same volume as the non-spheric particle of interest.

Dry deposition is separated for large particles ($\mathrm{D}_p > 2\,\mu$m) and small particles ($\mathrm{D}_p < 2\,\mu$m). Large particle deposition is dominated by the gravitational settling, small particles are additionally affected by the surface resistance R_s and aerodynamic resistance R_a accounting for turbulent deposition. The aerodynamic resistance determines the heat and water vapour transport due to evaporation from the surface into the air layers above the canopy layer, whereby neutral stability conditions are assumed. Transpiration by crops and evaporation by the soil surface both impact on the vapour flow and are described by the surface resistance depending on their part on the stomatal resistance and the sunlit leaf area index. Furthermore, to describe deposition accurately, turbulent transfer, Brownian diffusion, impaction, interception, gravitationally settling, and particle rebound have to be taken into account. Deposition is affected by particle size, density and meteorological condition as well. The dry deposition is commonly parametrised using the deposition velocity v_d $[m\,s^{-1}]$ following (*Zhang et al.*, 2001):

$$v_d = \frac{1}{R_a + R_s + R_a R_s v_g} + v_g \tag{2.9}$$

Especially for particles with diameters $D_p < 2\,\mu$m, atmospheric small-scale dynamics (e.g. turbulent elements) deflect particle deposition path. Close to the surface, roughness elements and vegetation effect the turbulent processes.

Wet deposition describes the particle removal by scavenging due to rain-out (sub-cloud scavenging by falling rain drops collecting dust particles) and wash-out (in-cloud scavenging either by nucleation scavenging by activation and growth of dust particles to cloud droplets or by collecting the non-activated fraction of a particle by coagulation with cloud droplets). The wet deposition rate is mainly controlled by the precipitation rate and the scavenging efficiency of the rain drops related to the rain-drop size distribution. Wet deposition by rain-out and wash-out can be parametrised following e.g. *Berge* (1997) and *Jacobson et al.* (1997).
The wet deposition rate Ω $[kg\,m^{-2}\,h^{-1}]$ is controlled by the precipitation rate Λ $[mm\,h^{-1}]$, the scavenging coefficient σ $[m^2\,kg^{-1}]$:

$$\Omega = -\sigma \cdot \Lambda \tag{2.10}$$

with

$$\sigma = \frac{A \cdot E}{v_r}. \tag{2.11}$$

The scavenging coefficient σ is related to the rain drop fall velocity v_r $[m\,s^{-1}]$, an empirical factor $A = 5.2\ m^3\,kg^{-1}\,s^{-1}$, and the collection efficiency of the rain drops E. Both factors A and E are related to the Marshall-Palmer size distribution (Equation 2.12), describing the best-fit exponential approximation of observed rain-drop size distributions (*Marshall and Palmer*, 1948),

$$N(D_r) = N_0 e^{-\Lambda D_r}, \tag{2.12}$$

with diameter D_r $[m]$. The slope factor of the fitted exponential function is found to be the precipitation rate Λ, the intercept parameter N_o can be given as constant $N_0 = 8 \cdot 10^6\,m^{-4}$ (*Marshall and Palmer*, 1948).
Dry and wet deposition show seasonal varying pattern, depending on the state of the atmosphere and transport path (*Schepanski et al.*, 2008a). Of course, the location of source areas also affect the deposition area, as it is the result of emission and transport path.

Dust deposition towards the oceans is estimated using global modelling (e.g. *Ginoux et al.*, 2001; *Luo et al.*, 2003; *Zender and Newman*, 2003). Different modelling studies estimate a deposition flux of 180-260 $\mathrm{Mt\,yr^{-1}}$ for the North Atlantic basin (*Mahowald et al.*, 2005).

Chapter 3

Meteorological Aspects of Saharan Dust Emission

For arid areas, where vegetation cover is sparse, meteorological conditions are the main factors determining whether a dust source becomes active or not. In the following, an introduction into the role of the boundary layer as interface between dust emitting surface and dust transporting free troposphere will be given.

3.1 The Atmospheric Boundary Layer

The atmospheric or planetary boundary layer (BL) is commonly defined as the lowest atmospheric air layer which is impacted by surface structure via friction, and heat fluxes (*Garratt*, 1992). Surface elements decelerate air flows close to the surface. Turbulence forced by thermal convection and mechanical turbulence due to wind shear characterise the nature of the BL. As the BL is coupled to the surface, exchange processes concerning the conserved quantities mass (e.g. precipitation and evaporation, emission and deposition of aerosols), energy (e.g. latent and sensible heat flux, radiation) and momentum (e.g. friction) between atmosphere and geosphere occur.

The inertial sublayer (Prandtl-Layer) is situated above the interfacial sublayer comprising the first few millimetres above the surface. This layer is characterised by a strongly increasing wind velocity and turning wind direction due to decreasing impact of the surface elements. In contrast to the interfacial sublayer, the flow above becomes turbulent and is often characterised by a Reynolds number (measure of the ratio of inertial and viscose forces) $Re > 5000$. Air flow within the inertial sublayer can be expressed by the equilibrium of pressure gradient force and turbulent friction force, often termed antitriptic wind. Wind, turbulence and turbulent exchange are closely related. So the vertical flux of momentum is described by the turbulent exchange coefficient K $[m^2\, s^{-1}]$ related to the turbulent viscosity and the vertical gradient of momentum. Prescribing a thermal neutral atmospheric stratification, the turbulent exchange coefficient K increases with height z $[m]$:

$$K = \kappa u_\star z, \tag{3.1}$$

with the empiric von Karman constant κ and the wind friction velocity $u_\star$ $[m\,s^{-1}]$. However, within the inertial sublayer, the vertical momentum flux is assumed to be constant with height. Consequently, the vertical momentum flux, the density of air and the von Karman constant κ can be considered as constant and for the vertical wind $v(z)$ profile $[m\,s^{-1}]$ follows:

$$v(z) = \frac{u_\star}{\kappa} \ln\left(\frac{z}{z_0}\right), \tag{3.2}$$

with the surface roughness length z_0 $[m^{-1}]$ and the vertical height z $[m]$.

For a logarithmic wind profile to occur, thermal neutral stratification of the atmosphere is one of the preconditions. In case of non-thermal neutral stratification, the wind shear dv/dz does not change with the reciprocal height z^{-1}. Furthermore, the decrease is empirically related to the Monin-Obukhov length $\mathrm{L}_\star$ $[m]$. The Monin-Obukhov length describes the height at which turbulence produced by vertical shear is balanced by negative buoyancy. In case of stably stratified atmosphere, the surface wind velocity is low and increases stronger than the logarithmic profile with height. For unstable atmospheric conditions, the surface wind velocity is higher than in the neutral case but the increase with height is weaker.

Above the inner region (interfacial and inertial sublayer) lies the outer region (*Garratt*, 1992). The transition from inner to outer region is characterised by an overlap region. Within the outer region, often referred to as Ekman layer, the air flow is just little affected by the surface characteristics and the impact to the Coriolis force due to the Earth's rotation is obvious. Mainly three forces determine the wind flow and its direction: the propulsive pressure force, the deflecting Coriolis force and the decelerating turbulent friction force. The equilibrium between these forces results in the geotriptic wind. A major characteristic of the Ekman layer is the turning wind direction with height and co-instantaneously increasing wind velocities due to decreasing deceleration effect of surface elements. Under ideal conditions (flat, homogeneous terrain, no advection, predominant mechanic turbulence (wind shear)), the hodograph of the wind vectors will show the so called Ekman spiral.

With regard to the vertical wind profile, the top of the Ekman layer is reached when the geotriptic wind equals the geostrophic wind, described by the equilibrium of pressure gradient force and Coriolis force.

The structure and height of the BL depends strongly on the turbulence development, mainly affected by diurnal heating and cooling of the surface (*Thorpe and Guymer*, 1977). During daytime, the BL is dominated by convective turbulence elements due to inhomogeneous heating and resulting buoyancy effects leading to thermal instability or convection. At near-surface layers, a super-adiabatic lapse-rate is observed. In this case of unstable BL condition, the outer region or Ekman layer is often termed mixed-layer in the literature. Under neutral atmospheric conditions, buoyancy effects that would be a prerequisite for convective turbulence are absent. Static stable conditions, typically occurring during night, are characterised by a surface inversion.

The top of the BL under convective conditions is often marked by a stably stratified layer, the so called capping inversion. This layer decouples the turbulence within the BL from

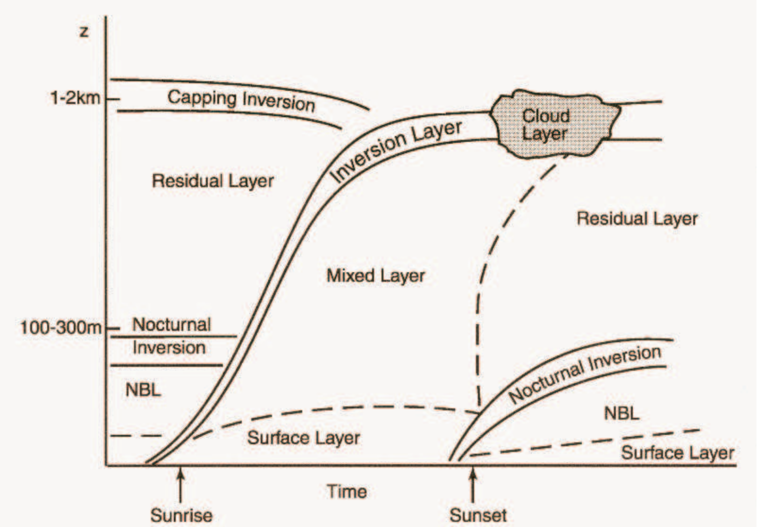

Figure 3.1: *Structrue of atmopsheric boundary layer development, Wyngaard 1992*

the free troposphere above. Turbulent motion and elements of raising air, e.g. thermal plumes and latent heat conversion, are able to erode this capping inversion layer. Over deserts, the BL regularly reaches depths around 5 km, but also depth up to 10 km have been observed over heated desert surfaces. Under stable condition, the top of the BL is not so well defined because the turbulence is weaker. Consequently the stable BL is shallow, often just a few hundred meters deep. Assuming an Ekman layer, wind speed should be zero at surface due to friction. But turbulent momentum mixing leading to a homogeneous BL causes sub-geostrophic wind speeds within the BL.

After sunset, surface heating stops and convective turbulence diminishes due to weakening buoyancy. As surface and lower atmosphere cool, the BL breaks down to a shallow nocturnal BL (NBL) within a stably stratified layer, and a surface temperature inversion develops. Above the surface inversion, a weak residual layer still exists as the rest of the daytime BL (*Garratt*, 1992).

The NBL is generally defined as a shallow, turbulent layer above which the mean shear stress and heat flux are negligibly small (e.g. *Garratt*, 1992; *Hoxit*, 1975; *Mahrt*, 1999; *Mauritsen and Svensson*, 2007).

The NBL depth is highest under clear-sky conditions with moderate to high wind speeds over horizontal terrain. The lower the surface wind speed, the shallower the NBL. In that case, intermittent turbulence occurs: turbulent mixing due to high wind shear at top of the NBL occurs abruptly and decreases the shear to a sub-critical value (*Van de Wiel et al.* (2003) and references therein, *Mahrt* (1985)). Mainly turbulent and radiative effects influence the temperature inversion and since turbulence is not a precondition, its height is mostly found to be higher than the NBL extension. In the upper part of the inversion, sharp density gradients can occur and gravity waves can be forced (*Garratt*, 1992; *Sorbjan*, 2006, and related references).

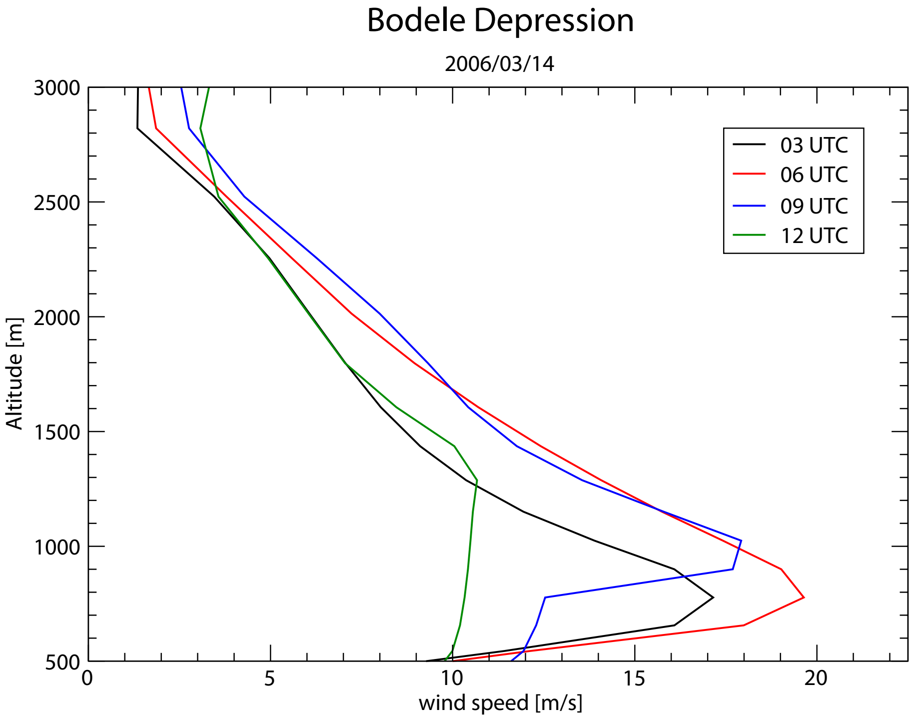

Figure 3.2: *Temporal evolution of the nocturnal low-level jet (LLJ) over the Bodélé depression on March 14 2006. The wind speed maximum of the nocturnal LLJ develops during 03-06 UTC and is present until the daytime BL depth reaches the height of the LLJ (morning hours after sunset). Then downward mixing of the momentum of the LLJ starts, indicated by increasing surface wind speeds and decreasing wind speed maximum.*

3.2 The Nocturnal Low-Level Jet

Examining the vertical wind profile (Figure 3.2), a low-level jet (LLJ) can be identified by a horizontal wind speed maximum occurring in the lowest few kilometres of the atmosphere (e.g. *Banta et al.*, 2006; *Blackadar*, 1957; *Holton*, 1967). It should not be confused with the jet streams at the top of the troposphere reaching length of thousands of kilometres, width of hundreds of kilometres and high wind speeds of about 100 $\mathrm{m\,s^{-1}}$ (*Davis*, 2000; *Lenschow and Stankov*, 1979; *Stensrud*, 1996).

Measurement campaigns like the CASES-99 (Cooperative Atmosphere-Surface Exchange Study-1999) campaign (*Poulos et al.*, 2002) and the Wangara experiment (south-east Australia) and model studies (e.g. *Brost and Wyngaard*, 1978; *Enger et al.*, 1993; *McNider et al.*, 1993; *Thorpe and Guymer*, 1977) have shown that there are several possible causes for the LLJs (e.g. *Blackadar*, 1957; *Bonner*, 1968; *Bonner and Paegle*, 1970; *Brost and Wyngaard*, 1978; *Chimonas*, 2005; *Davis*, 2000; *Enger et al.*, 1993; *Ha and Mahrt*, 2001; *Holton*, 1967; *Hoxit*, 1975; *Mahrt*, 1985; *Mahrt et al.*, 1998; *McNider and Pielke*, 1981; *Thorpe and Guymer*, 1977): synoptic-scale baroclinity associated with weather patterns, baroclinicity associated with sloping terrain, fronts, advective acceleration, splitting, ducting and confluence around mountain barriers, land and sea breezes, mountain and valley winds, and inertial oscillation (*Kraus et al.*, 1985). In general there are two different types of LLJs: on the one hand those which occur in disturbed conditions within the troposphere associated with stationary rain bands on a cold front (*Browning and Bryant*, 1975) as well as the East African jet (*Findlater*, 1972), and on the other hand those which are related to fine weather conditions with clear skies and low surface wind speeds over land (e.g. *Thorpe and Guymer*, 1977). The latter can be explained by frictional decoupling at night due to radiative cooling performing a nocturnal temperature inversion at the top of the static stably stratified layer of cooled air (e.g. *Banta et al.*, 2003, 2002; *Blackadar*, 1957; *Mahrt*, 1999; *Nappo*, 1991).

Within the residual layer above the nocturnal BL, the decoupled air accelerates due to geostrophy. As the degeneration of the BL to the NBL occurs relatively fast, the air aloft is accelerated to super-geostropic wind velocities and a LLJ can develop (Figure 3.2). During the next morning, turbulent processes couple the LLJ layer to the surface and momentum of the LLJ is mixed downward leading to suddenly increasing surface wind speeds frequently strong enough to mobilise dust. The LLJ often reaches super-geostrophic wind speeds, which are high enough to mobilise dust in case of downward mixing during the next morning (Figure 3.2). *Mahrt* (1999) has found a high night-to-night variability of height and strength of the nocturnal LLJ, but low variability within the same night. The characteristics of a LLJ can be observed over all continents (*Stensrud*, 1996, and related references). LLJs can occur during daytime and night time over flat and complex terrain and shows often length of tens to hundreds of kilometres (*Davis*, 2000).

To physically describe the retardation from the sub-geostrophic wind speeds during day to the super-geostrophic velocities during night, three present approaches have been proposed and will be presented in the following: inertial oscillation (*Blackadar*, 1957), thermal wind (*Holton*, 1967), and shallow baroclinity (*Stensrud*, 1996).

Inertial Oscillation

The first approach introduced by *Blackadar* (1957) can explain both diurnal variability of wind speed intensity (higher wind speed at night time) like an oscillation, their day-to-day and night-to-night variability, respectively, and the super-geostrophic velocities.

Near nightfall, the lowest air layers cool due to radiative cooling. Hence they become static stably stratified and turbulence is reduced except within the shallow NBL: a surface temperature inversion develops and decouples the air above the inversion from the surface layer (e.g. *Banta et al.*, 2006; *Nappo*, 1991). The decoupled air becomes nearly frictionless and turbulence free, and accelerates to geostrophic conditions. At the beginning, there is an imbalance between pressure gradient $\underline{F}_p = -\frac{1}{\rho}\nabla_h p$ and Coriolis forces $\underline{F}_c = f\underline{k} \times \underline{v}$, inducing an inertial oscillation ($\underline{F}_p$ pressure gradient force, ρ density, p pressure, $\underline{F}_c$ Coriolis force, $f = 2\Omega \sin\phi$ Coriolis parameter with Ω the angular speed of Earth' rotation and ϕ the latitude, $\underline{k}$ unit vector along z-axis, $\underline{v}$ wind vector)(Figure 3.3 and Equation 3.5). Applying the equation of horizontal motion ($\underline{v}_h$ denotes the horizontal wind vector and $\underline{F}_R$ the friction drag force)

$$\frac{\partial \underline{v}}{\partial t} + (\underline{v}_h \cdot \underline{\nabla}_h)\,\underline{v}_h + f\underline{k} \times \underline{v}_h = -\frac{1}{\rho}\nabla_h p + \underline{F}_R \tag{3.3}$$

to the conditions above the boundary layer where the horizontal pressure gradient $-\frac{1}{\rho}\nabla_h p$ can be assumed as zero, the horizontal motion as homogeneous (no advective acceleration $(\underline{v}_h \cdot \underline{\nabla}_h)\,\underline{v}_h$) and no turbulence (Reynold stress) is evident,

$$\frac{\partial \underline{v}}{\partial t} = -f\underline{k} \times \underline{v}_h \tag{3.4}$$

describes the geostrophic conditions above the boundary layer. To describe the inertial oscillation, the difference between occurring wind $\underline{v}$ and geostrophic wind $\underline{v}_g$, often termed as ageostrophic wind $\underline{v}_{ag} = \underline{v} - \underline{v}_g$ is considered. The differentiation with respect to time leads to the equation of oscillation:

$$\frac{\partial^2}{\partial t^2}\left(\underline{v}_{ag}\right) = f^2\left(\underline{v}_{ag}\right). \tag{3.5}$$

The solutions are sinusoidal oscillations with a frequency T $[s^{-1}]$ depending on latitude:

$$T = \frac{2\pi}{f} \tag{3.6}$$

Considering the geostrophic wind speed as stable case, turbulent mixing and friction cause sub-geostrophic wind speeds as during daytime. This oscillation between increase and decreases of wind speed from the sub-geostrophic case to the super-geostrophic case and back has a period of 15 hours at subtropic latitudes, 17 hours at mid-latitudes. Shortly after sunrise the BL develops exceeding the height of nocturnal surface inversion and the inertial oscillation breaks down. Finally the approach of an inertial oscillation relying on the retardation to sub-geostrophic wind speeds during daytime and a frictional decoupling during night time, explains the LLJ occurrence at synoptic scale conditions allowing surface inversions and its wind speed variations. Thus, a wind speed maximum will be generated at round about 8 hours after sunset (*Hoxit*, 1975). However, this approach does not take sloping terrain into account.

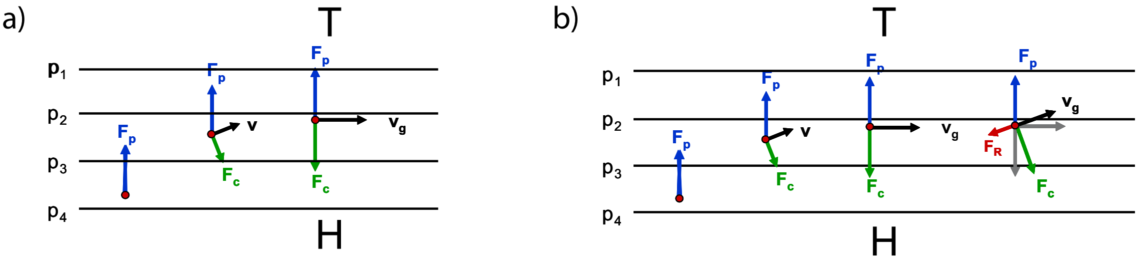

Figure 3.3: *Derivation of inertial oscillation from geostrophy. a) Describes the development of the geostropic state of equilibrium for an air parcel accelerated by the pressure gradient. In case of equilibrium, the air parcel is characterised by motion parallel to the isobars. The right-most vector diagram in b) shows the impact of frictional drag at surface reducing the wind velocity while backing wind direction and leading to sub-geostrophic wind velocities.* $\underline{F}_c$ *Coriolis force,* $\underline{F}_p$ *pressure gradient force,* $\underline{v}$ *wind,* $\underline{v}_g$ *geostrophic wind,* $\underline{F}_R$ *frictional drag force.*

Thermal Wind

The NBL is sensitive to some minor influences (*Sorbjan*, 2006) as terrain slopes (e.g. *Brost and Wyngaard*, 1978; *Holton*, 1967; *McNider and Pielke*, 1981) and heterogenities of surface characteristics (e.g. *Mahrt et al.*, 1998; *Nappo*, 1991). As the approach by *Blackadar* (1957) does not account for complex terrain, two more approaches have been proposed: first by *Holton* (1967) basing on thermal wind and second on *Stensrud* (1996) basing on shallow baroclinity. Diurnal heating and cooling of sloping terrain result in a periodic variation of thermal wind and consequently in wind speed oscillation (thermal wind + geostrophic wind on the one side and thermal wind - geostrophic wind on the other side) (e.g. *Bonner and Paegle*, 1970; *Holton*, 1967; *McNider and Pielke*, 1981). At daytime, solar radiation warms up the surface and a mixed layer with near-adiabatic laps rate develops. Considering a horizontal slice within sloping terrain, a temperature gradient $\underline{\nabla}_h T$ develops from warm surface to cool surrounding air at the same horizontal slice. This temperature gradient is evident at surface and at higher levels as well (Figure 3.4). Referring to the simplified thermal wind equation

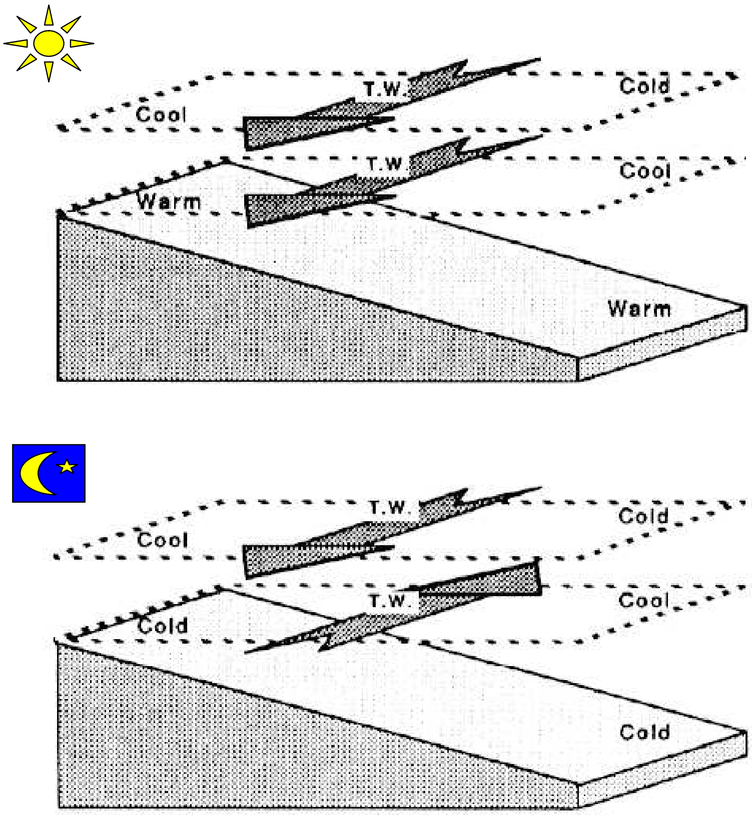

Figure 3.4: *Thermal wind (T. W.) and shallow baroclinity at mountain hills (Stull, 1988).*

$$\frac{\partial \underline{v}_g}{\partial z} = \frac{g}{fT}\underline{k} \times \underline{\nabla}_h T, \tag{3.7}$$

a balancing flow should occur. Turbulent mixing during daytime weakens this flow. At night time, the surface cools more quickly than the air. Hence considering a slice starting at near surface levels at one point, the temperature gradient is reversed compared to the daytime value. But considering a horizontal slice starting above the thermal inversion, the temperature gradient may be the opposite as below the inversion. The stably stratified layers below the inversion layer subpress motion so that calm or nearly calm conditions appear near the surface. Above the inversion, no friction retard the thermal wind and a jet can develop. The thermal wind is described by the equation 3.8 describing the change of the geostrophic wind components $\underline{v}_g$ with height. For a horizontal layer between two given geopontential levels Φ_0 and Φ_1, the thermal wind vector $\underline{v}_T$ is given by:

$$\underline{v}_T = \frac{1}{f}\underline{k} \times \underline{\nabla}(\Phi_1 - \Phi_0). \tag{3.8}$$

Summarising, the following equation system can be formed:

$$\text{day time}: \quad \frac{\partial T}{\partial x} \leq 0, \quad \frac{\partial \underline{v}_T}{\partial z} \leq 0 \tag{3.9}$$

$$\text{night time}: \quad \frac{\partial T}{\partial x} \geq 0, \quad \frac{\partial \underline{v}_T}{\partial z} \geq 0 \tag{3.10}$$

This approach alone cannot explain the super-geostrophic wind, but it may work together with the approach of inertial oscillation. Accordingly, both approaches together can explain the development and occurrence of nocturnal LLJ over sloping and complex terrain (*Holton*, 1967).

Furthermore, mountain sides can block and channel low-level flows of cold, stably stratified air mass to flow along the deepest path downward. Due to the high density of cold air, it is trapped in mountain valleys and forces a temperature gradient oriented normal to the mountains. This gradient can be assumed to be persistent during geostrophic balance of wind flows as described above, and a LLJ with mountain-parallel flow develops (*Stensrud*, 1996, and related references).

Shallow Baroclinity

This approach mainly takes horizontal differences due to surface variability into account (*Stensrud*, 1996). Significant changes in surface characteristics such as land-sea contrast in coastal regions, land/sea-ice contrasts or rock-sand contrasts leads to horizontal changes of sensible and latent heat fluxes (*Murphy et al.*, 1982). The resulting gradients produce strong low-level baroclinity within the BL and LLJs through strong geostrophic forcing, whereby the LLJ develops parallel to the low-level horizontal temperature gradient (*Stensrud*, 1996, and related references). Shallow baroclinity can explain constant LLJ occurrences throughout the day but, however, in regions where the surface fluxes have a diurnal component, significant diurnal changes in the strength of the LLJ occur.

LLJs produced by shallow baroclinity due to surface characteristic changes are observed in coastal region, the Antarctica, in shelf ice regions, in desert areas with sharp rock/sand or mountain/salt lake contrasts.

Topography influences the wind flow in direction and speed as it blocks and modifies the flow (*Peagle et al.*, 1984). Consequently, on a meso-scale, mountains can accelerate flows above a mountain ridge due to increasing transport through a horizontal slice, within a

valley due to channelling effect, and edging effect as sharp topographical gradients which forces development of eddies. On the lee-ward side of mountains, lee-waves can be generated and lead to turbulent mixing down of momentum resulting in gusts at surface level. On a large scale, lee-cyclones can develop and generate their own dynamic.
Over the Bodélé depression, located surrounded by the Tibesti Mountains in the North and the Ennedi Mountains in the East, a topographically forced LLJ occurs frequently (*Engelstaedter and Washington*, 2007; *Todd et al.*, 2008; *Washington and Todd*, 2005; *Washington et al.*, 2006a,b). Thereby, the mountains accelerate wind with south-westward direction and provide a LLJ. During daytime, convective turbulence mixes momentum downward and the LLJ disappears on most days, except the BL does not extend to the height of the LLJ. Then the LLJ remain above the daytime BL. After sunset, the LLJ develops fast. The Bodélé LLJ occurs very frequent and is able to explain the high frequency of dust events originating from the Bodélé depression.

Dust source observations indicate that 65% of all Saharan dust source activations occur during the morning hours (*Schepanski et al.*, 2008b). For dust mobilisation, the down-ward transport of the LLJ's momentum leads to high surface wind speeds (*Schepanski et al.*, 2008b), when the LLJ layer becomes coupled to the near-surface air layers by turbulence. As calm night-time BL conditions are required for LLJ development, the local frequency of LLJ occurrences also change with seasons (*Schepanski et al.*, 2008b).

3.3 Hadley Circulation

The Hadley circulation describes the distribution and location of high and low pressure systems forcing general atmospheric circulation patter over the tropics and subtropics. The variability of the Hadley circulation is linked to the variability of dust source areas and their activities because the Hadley circulation impacts on air mass circulation in which single synoptic scale atmospheric features are embedded. Also the LLJ development is effected by the strength and characteristic of the Hadley circulation because it affects BL dynamics.

Rather stationary high pressure systems are situated over the subtropical ocean on both hemispheres (Azores high, St. Helena high, Indic-Mascarean high and the high pressure system due to the Asian Ferrel-Circulation, Figure 3.5). Surface conditions, in particular ocean currents, determine the stability of these high pressure systems. Cold ocean currents caused by up-welling along the east shores of the oceans stabilise the lower troposphere leading to more stationary conditions. Along the oceans west shores, warm water currents destabilise the lower troposphere leading to frequent convective interruptions and thereby less stable conditions.

These high pressure systems are part of the Hadley circulation, describing the meridional circulation between the thermal equator and the subtropics. The Hadley cell consists of

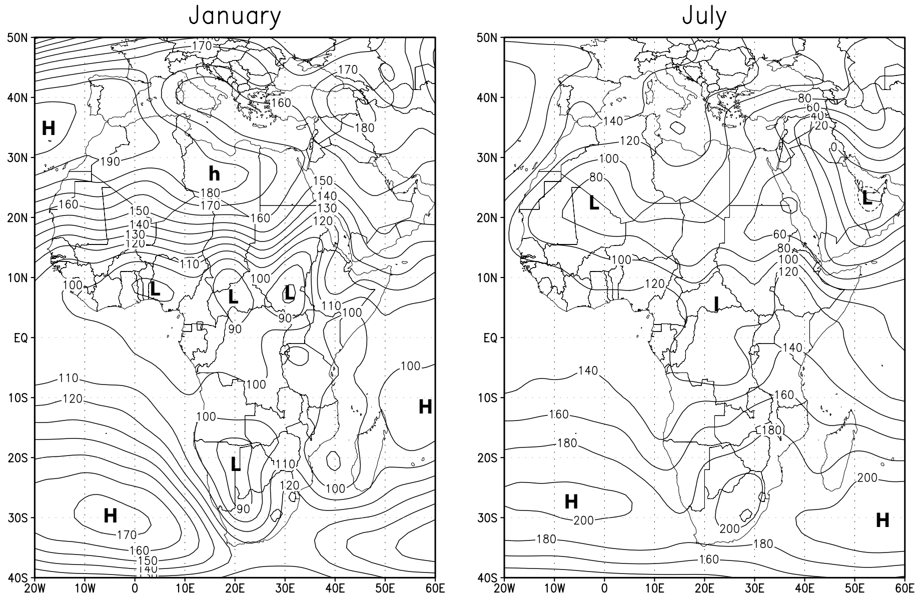

Figure 3.5: *CDAS-NCEP/NCAR Reanalysis geopotential [gpdm] at 1000 hPa level. Climatological mean of 1979-1995.*

the equatorial trough related to the thermal equator, where air masses heated by solar insolation ascend. Ascending air leads to low pressure at surface levels and high pressure zone in the upper troposphere. As consequence of the mass balance, upper tropospheric air masses spread out to the north and south (anti-trade winds). The air cools due to the conversion of latent heat, and descends leading to upper-tropospheric low pressure and an area of high pressure at surface levels: the subtropical high. Within the lower troposphere, an equilibrium air flow from the zone of high pressure to the equatorial trough occurs: the trade wind, over the Sahara often named Harmattan.

Due to significant seasonal changes in surface pressure distribution caused by changing solar inclination over the large continental area of the Sahara, the northern hemisphere has different high and low pressure distribution for summer and winter. At lower tropospheric levels, the Azores high over the subtropical North Atlantic shifts northward and the Saharan heat low (SHL) develops south of the Atlas Mountain chain. At the upper tropospheric levels, high pressure is evident over the SHL. Heat lows are normally related to strong precipitation events due to ascending air motions. But in case of the SHL, very dry desert air inhibits precipitation. Furthermore, the upper tropospheric high pressure area suppress the ascending motion of the SHL. Thus an inversion layer (trade wind inversion), is formed by descending air due to the subsiding branch of the Hadley circulation and the ascending air from the surface SHL. The height of the inversion layer increases from the SHL towards the equatorial trough, accompanied by deep convection, which is at maximum at the location of the inter-tropical convergence zone (ITCZ), located at around 10 to 15° N during northern hemispheric summer. From the centre of the SHL to the equatorial trough atmospheric moisture content increases inhomogeneously. A strong gradient of atmospheric moisture content occurs where dry desert air meets moist monsoon air at the inner-tropical discontinuity (ITD). The combination of a raising inversion layer height and an increasing atmospheric moisture content indicates convective clouds towards the equatorial trough. Figure 3.6 illustrates different air mass characteristics of desert and monsoon air between surface heat trough (SHL) and region of strongest precipitation (ITCZ).

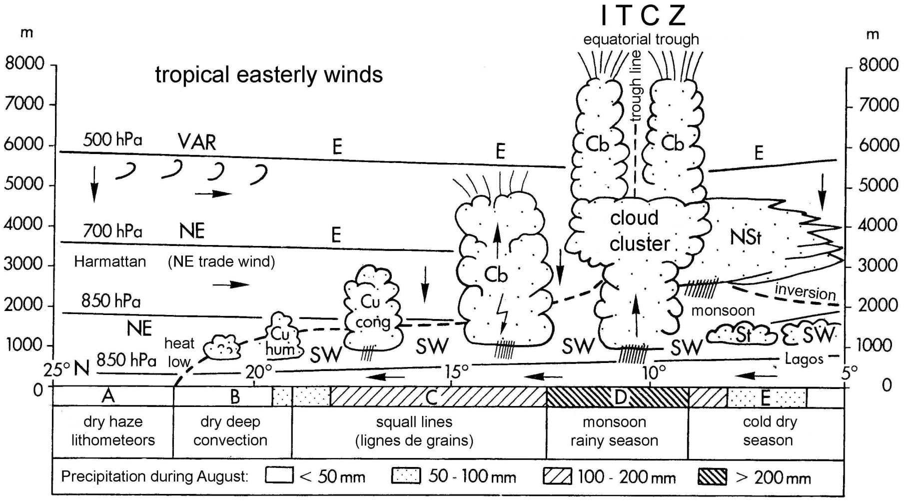

Figure 3.6: *Meridional transect of weathering zones over West Africa between the Sahel zone and the coast of Guinea, modified after Weischet and Endlicher (2000). Air mass characteristics and the trade wind inversion are illustrated. For a detailed explanation on the five weathering zones see text. Cu denotes cumulus, Cb cumulonimbus, and NSt nimbostratus*

Five weather zones are defined, originally based on studies of *Hamilton and Warchbold* (1945); *Leroux* (1983); *Solot* (1959); *Walker* (1958). *Zone A* located far north of the ITCZ is dominated by the Harmattan. The atmospheric conditions are stable and dry haze reduces the horizontal surface visibility. Here, stable atmospheric conditions are suitable for nocturnal LLJ development (*Schepanski et al.*, 2008b) providing sudden high surface wind velocities during the morning. *Zone B* is characterised by the ITD. As over the desert the Harmattan (north-east trade wind) is dominant and the monsoon air is transported by the south-west monsoon winds, the ITD is further characterised by a conversion of both wind regimes (Figure 3.7). There, the moisture gradient at surface levels is strongest, often dew-point difference of 15 K and more are observed accompanied by a strong shift in wind direction. Near the surface, the denser monsoon air is evident while at higher tropospheric levels the dry north-east trade winds are still dominant. Both, monsoon and trade wind layer are separated by the trade wind inversion. The height of the inversion increases with decreasing distance towards the ITCZ. Due to strong vertical wind shear within the trade wind inversion and the dry trade wind air mass, only shallow convective clouds can develop. Occasional convective events are able to penetrate the inversion layer. However, the evaporation rate is too high to allow for precipitation reaching the soil surface. Compared to zone B, *zone C* is characterised by a deeper monsoon air layer (1500-2000 m) allowing for deep moist convection and strong thunderstorms. Over this region, convective clouds are often observed to be characterised by an organised structure (e.g. *Houze et al.*, 1990; *Parker and Johnson*, 2000). This cloud complexes, so-called meso-scale convective systems (MCS) or meso-scale convective complex (MCC) show a longer life-time and a more complex dynamic than individual convective elements. MCSs are characterised by a contiguous precipitation area of more than 100 km and up to 500 km in at least one horizontal direction. They have life-times of about 20 hours. Horizontal extent and life-time of MCSs are limited by the Coriolis parameter and ageostrophic advection. MCSs are accompanied by strong rainfall events which are assumed to account for 75% of the annual sub-Saharan precipitation (*Laurent et al.*, 1998). Most precipitation evaporates before reaching the surface, and a pool of cold, dense air is generated sinking rapidly downwards. Such downward flow of cold air generated by evaporative cooling is often termed “gravity current” or “density current” (e.g. *Flamant et al.*, 2007). High surface wind speeds associated with such gravity currents reaching the surface are able to force dust emission. Dust storms, so called Haboobs, associated with such cold outflows develop and spread radially out (10-15 $m\,s^{-1}$) forming an arcus-like front-edge. Haboobs are a typical phenomenon for this region. *Zone D* marks the location of the ITCZ characterised by deep convection forming cloud clusters and strong precipitation. The depth of the monsoon air mass is deepest with 2.5-3 km. The trade wind inversion layer is not evident due to the missing presence of the subtropical high. Southward of the ITCZ, the vertical characteristics of the troposphere are impacted by the St. Helena high. Again, in upper tropospheric levels, subsidence dominates and reducing the level height of trade wind inversion. Besides the anti-cyclonic subsidence, the cold Benguela current stabilises the atmosphere as well. Furthermore, the transition of south-east trade winds to south west monsoon winds at near surface levels while the south-east trade winds are persistent at higher tropospheric levels leads to vertical wind shear, which prevents deep convection. Stratifom clouds with occasionally drizzle (nimbostratus) are evident.

The Hadley circulation is probably the major element of general atmospheric circulation impacting on the North African dust source activation during north-hemispheric summer. In winter, when the equatorial trough and thereby the axis of the Hadley circulation is shifted to the south, extra-tropical disturbances related to the southward shifted polar jet force cyclogenetic activities, which disturb the predominant Harmattan winds. Furthermore, all meteorological elements are embedded within the Hadley circulation on different scales. With regard to dust source activation, the strength and centre of the Hadley circulation effects the distribution of activated dust sources as well as the strength of occurring dust storms on the one hand, but decrease dust mobilisation by precipitation and increasing vegetation cover on the other hand (*Engelstaedter et al.*, 2006).

3.4 West African Monsoon Circulation

The West African Monsoon (WAM) circulation is a predominant characteristic over West Africa during the northern hemisphere summer. Due to its ageostrophic meridional flow it is associated with the advection of moist air from the Gulf of Guinea towards the Sahara (Figure 3.7, *Parker et al.* (2005); *Sultan et al.* (2006)). It is assumed to be affected by the combination of geostrophy and convection, both interacting on a diurnal time scale. Due to peaking solar inclination in northern hemisphere summer, the SHL south of the

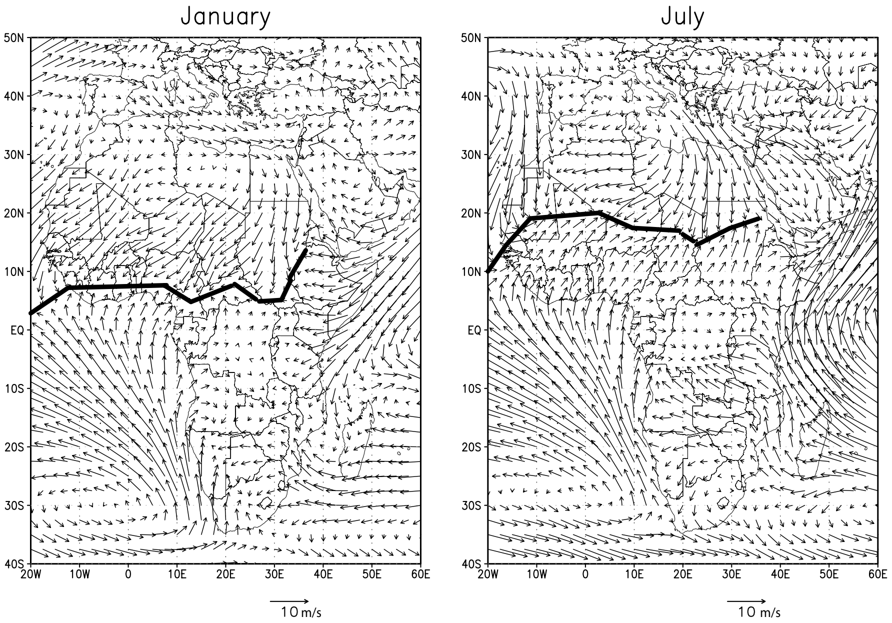

Figure 3.7: *CDAS-NCEP/NCAR Reanalysis climatological mean wind distribution at 1000 hPa for January and July 1979-1995. The convergence line of NE trade and SE monsoon flow is associated with the ITD over the North African continent (black line).*

Atlas Mountains develops (Figure 3.5). Moist air from the Gulf of Guinea is advected towards the Sahara. This transport is driven by the pressure gradient between the Gulf of Guinea and the SHL, supported by the temperature and moisture gradient between desert and monsoon region (Figure 3.7). However, the SHL is assumed to contribute to the strength of the WAM (*Drobinski et al.*, 2005; *Parker et al.*, 2005; *Ramel et al.*, 2006; *Sijikumar et al.*, 2006; *Sultan and Janicot*, 2003). In contrast to the pressure minimum of the SHL during afternoon due to maximum thermal heating, the wind velocity within the lower troposphere is observed to be lowest. With regard to atmospheric boundary layer dynamics, the afternoon wind velocity minimum can be explained by strong vertical mixing due to convective turbulence leading to a homogeneous vertical distribution of momentum. However, the ageostrophic wind (geostrophic wind adjusted by the surface friction drag) does not occur during day time. At dawn, insolation as driving factor for convective BL turbulence and therefore for the diminished ageostrophic wind, ceases and the pressure gradient force of the SHL becomes more dominant.

The WAM acts as major contributor to transport of moist air towards the Sahel, where it is involved into moist convection and the development of MCSs. Thus the WAM is one of the controlling processes for Sahel precipitation, a limiting factor for human agricultural activity in this region. Dust emission is influenced by the WAM in different ways. Besides triggering dust emission by forcing the development of strong surfaces winds in convective events (Haboobs), precipitation related to the WAM also inhibits dust mobilisation due to increasing soil moisture and vegetation cover. Furthermore, the geostrophic wind related to the WAM has a major contribution to the nocturnal LLJ development (e.g. *Parker et al.*, 2005) and therefore to morning time dust source activation (*Schepanski et al.*, 2008b).

Because of clouds, precipitation and evaporation the air temperature is relatively low over equatorial regions. Thus a strong temperature gradient between the Sahara and the equatorial area occurs (*Burpee*, 1972; *Cook*, 1999; *Thorncroft and Blackburn*, 1999). From this gradient an easterly thermal wind results leading to a strong wind speed maximum of 10-20 $m\,s^{-1}$ at around 650 hPa over 16° N in summer (August) (*Burpee*, 1972; *Parker et al.*, 2005). This mid-tropospheric wind speed maximum is termed African Easterly jet (AEJ). As the strength of the AEJ depends on the thermal and thereby on the moisture gradient between the Sahara and the coast of Guinea, seasonal variability occurs. The AEJ is located close to the ITD. Thus disturbances related to the flow dynamics of the AEJ, or initiated by hindrances like mountains, may lead to baroclinic or barotropic instabilities (*Burpee*, 1972, 1974). Co-located to the ITD, strong gradients with regard to moisture and temperature force the development of strong deep convection, which is able to organise itself as MCS. These convective elements lead to a synoptic-scale wave-like perturbation of the AEJ (e.g. *Berry and Thorncroft*, 2005). This wave-structures are the so-called African Easterly waves (AEW) are observed during summer (June to September) with wavelengths of 2000 to 4000 km (*Burpee*, 1972, 1974; *Carlson*, 1969) and a propagating velocity of about 8 $m\,s^{-1}$ in westward direction. AEWs are observed westward of 30° E and are assumed to modulate Sub-Saharan rainfall (e.g. *Payne and McGarry*, 1977).
African Easterly Waves are characterised by zones of convergence and divergence along a zonal flow, which can be identified well on isobaric weather charts. They are a common phenomenon during north-hemispheric summer over the African continent and the tropical North Atlantic (e.g. *Berry et al.*, 2007; *Burpee*, 1972). They are associated with Saharan dust outbreaks towards the tropical East Atlantic (e.g. *Jones et al.*, 2003, 2004; *Prospero and Nees*, 1986; *Prospero et al.*, 1981) that occur every 3-5 days (e.g. *Jones et al.*, 2003). Under suitable conditions like sea surface temperatures above 26-27°C and less horizontal wind shear, AEWs entered towards the tropical North Atlantic can act as seeding for strong gales (named as Cape Verde gale) or Hurricanes (e.g. *Thorncroft and Hodges*, 2001).

Chapter 4

Remote Sensing of Mineral Dust

In this thesis, infrared (IR) measurements taken from the geostationary MSG satellite are used to characterise Saharan dust emission areas and events in space and time. The Sahara desert is the World's most important dust source (e.g. *Goudie and Middleton*, 2001; *Middleton and Goudie*, 2001; *Prospero et al.*, 2002; *Washington et al.*, 2003). To study Saharan dust source location and characteristics with regard to time of activity, dust flux, and transport, remote sensing methods are required due to the spatial and temporal limits of ground-based observations. During previous studies, estimations on mineral dust sources have been made based on dust retrievals with at best daily resolution. In this chapter, the basics of the IR dust remote sensing technique and its limits of application will be discussed.

4.1 Meteosat Second Generation (MSG) Satellite

Low Earth orbiting meteorological satellites have a higher spatial resolution of their field-of-view due to lower orbital height, but their temporal resolution is, at best, daily. The field of view of geostationary satellites does not change with time as their orbit requires a similar angle velocity as the Earth. The temporal resolution of measurements taken by geostationary satellites is limited by the ability of the scanning interval of the instrument. The here used SEVIRI (Spinning and Enhanced Visible and InfraRed Imager) instrument on-board the Meteosat Second Generation (MSG) space craft is characterised by a return-interval of 15 minutes for single measurements on a resolution of 3×3 km at nadir (*Schmetz et al.*, 2002). The spatial resolution decreases with distance from the sub-satellite point due to the curvature of the earth surface (Figure 4.1). The satellite is located at 3.5° W over the equator (Gulf of Guinea), the images are entered at 0° longitude.

The SEVIRI instrument measures radiances at 11 different narrow-band wavelength (channels) covering the visible and IR spectrum between $0.6\,\mu$m and $13.4\,\mu$m and one high resolution broadband channel, listed in Tabel 4.1. As the instrument is designed for meteorological purpose, the channels fulfill different objectives in weather and climate monitoring. The atmosphere of the Earth shows different radiative characteristics at different wavelength of the solar and thermal spectrum. As it is not possible to measure at sin-

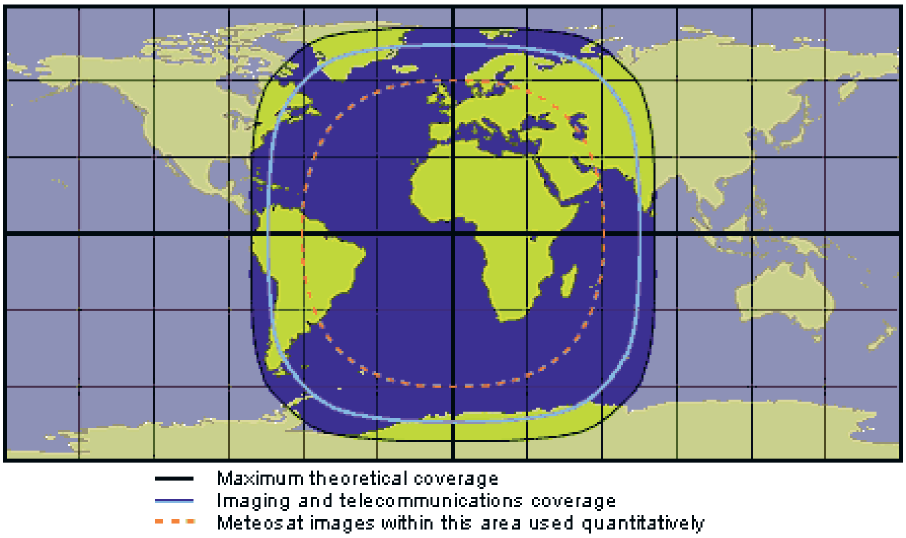

Figure 4.1: *Coverage area of MSG satellite (http://www.eumetsat.int).*

gle, discrete wave length, spectro-radiometer are designed to detect at narrow wavelength bands. Specific, wavelength dependent characteristics of atmospheric objects and the atmosphere itself can be remotely sensed at best with as narrow as possible wavelength bands. Then the spectral contribution of other atmospheric objects is lowest.

Channel	**Alternative Name**	**Central Wavelength**	**Primary Objectives**
Ch01	VIS 0.6	0.64 μm	surface, clouds, wind field
Ch02	VIS 0.8	0.81 μm	surface, clouds, wind field
Ch03	NIR 1.6	1.64 μm	surface, cloud phase
Ch04	IR 3.9	3.90 μm	surface, clouds, wind field
Ch05	WV 6.2	6.25 μm	water vapour, high-level clouds, atmospheric instability
Ch06	WV 7.3	7.35 μm	water vapour, atmospheric instability
Ch07	IR 8.7	8.70 μm	surface, clouds, atmospheric instability
Ch08	IR 9.7	9.66 μm	ozone
Ch09	IR 10.8	10.80 μm	surface, clouds, wind fields, atmospheric instability
Ch10	IR 12.0	12.00 μm	surface, clouds, atmospheric instability
Ch11	IR 13.4	13.40 μm	cirrus cloud height, atmospheric instability
Broadband:			
Ch12	HRV	0.4 - 1.1 μm	cirrus cloud height, atmospheric instability

Table 4.1: *MSG SEVIRI channels and its objectives, after EUMETSAT.*

The atmosphere is characterised by so-called atmospheric windows, wavelength bands at which the transmittance is highest and the atmosphere is relatively transparent. With regard to the wavelength spectrum remotely sensed by the MSG-SEVIRI, three major important windows exists (Figure 4.2): the visible window, the 3.7 μm window, the and the 8.5–12.5 μm IR-window (intermitted by the ozone (O_3) absorption band at 9.6 μm) (*Kidder and Vonder Haar*, 1995). The relatively high or low spectral transmittance of the atmosphere is due to absorption and emission characteristics of atmospheric gases, especially water vapour ($\mathrm{H_2O}$), carbon dioxide ($\mathrm{CO_2}$) and ozone ($\mathrm{O_3}$).

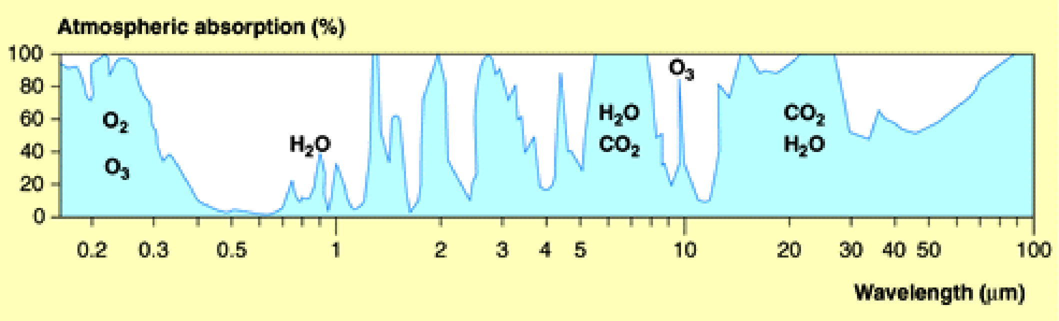

Figure 4.2: *Spectral distribution of atmospheric absorption [%]. High absorption means low transmittivity of radiation and thereby a strong impact of the atmosphere. Low absorption indicates a relatively low impact of the atmosphere. The image is taken from www.eduspace.esa.int.*

As the impact of the atmosphere is relatively low at the atmospheric window wavelength bands, non-gaseous atmospheric elements like clouds or dust can be remotely sensed. The combination of several wavelength band at which the element of interest shows spectral different characteristics, provides additional information. An example is the red-green-blue (RGB) composite technique (Figure 4.4 and 4.6).

4.2 Dust Detection Method

In case of airborne mineral dust, at visible wavelengths solar radiation is scattered back. Compared to ocean's surfaces, vegetated surfaces or generally dark surfaces, dust layers appear as bright area due to intense back-scattering (Figure 4.4a). Bare soil surfaces show high back-scattering rates and bright dust layers cannot be clearly distinguished from the surrounding over such high-reflecting surfaces. Thus, dust detection using visible wavelength bands shows good results over dark surfaces such as oceans, but is very difficult over bright surfaces like the Saharan desert (*Fraser*, 1997). Additionally, dust detection at the visible part of the spectrum is constricted to daylight and limited by sun-glint areas over the ocean.

Ackerman (1997) proposes a tri-spectral algorithm for dust detection using IR wavelength band centred at around 8.5 μm, 11 μm and 12 μm. The 11 and 12 μm wavelength bands are termed as “split-window” (e.g. *Chesters et al.*, 1983) as the brightness temperature differ-

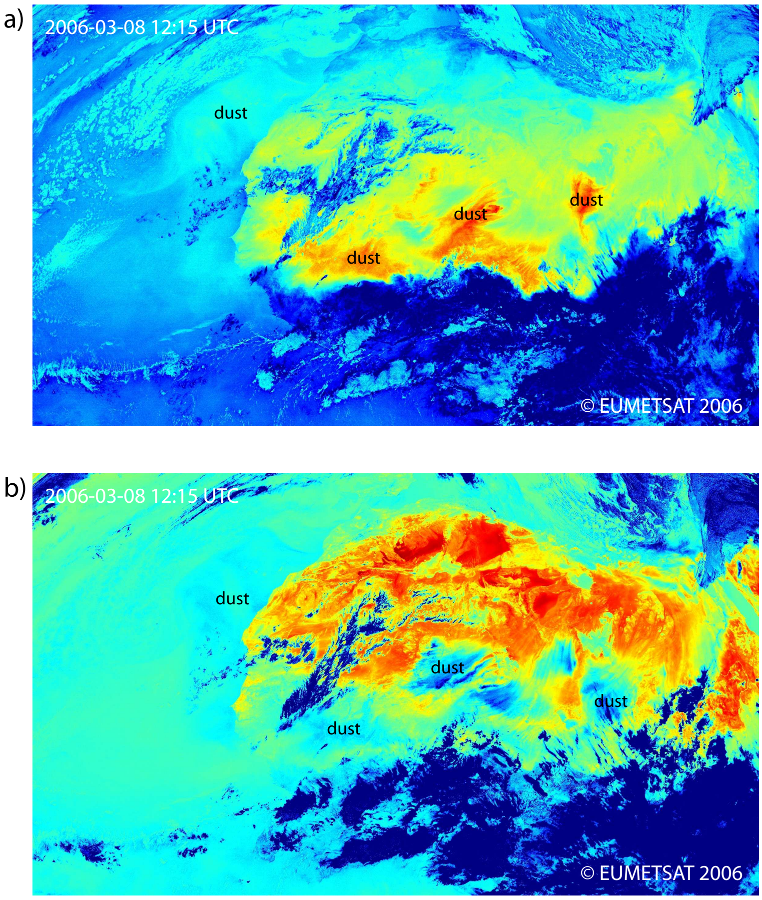

Figure 4.3: *a) The thermal signature of airborne mineral dust can be separated from the signature of the surface by applying the split-window technique. Thereby the BTD of the two adjacent wavelength channels entered at 10.8 and 12 μm is able to indicate the presence of airborne dust. b) Besides BTD of the split-window channels, BTD of 10.8 and 8.7 μm is able to indicate the presence of airborne dust as well. Both BTD imaginaries are shown for March 08 2006, 12:15 UTC. Compare also to Figure 4.4b.*

ence (BTD) of measurements at two adjacent wavelength channels can be used in order to separate atmospheric and surface signature. The split-window technique at IR wavelength has primarily been applied to remote sensing of volcanic ash aerosols (e.g. *Barton et al.*, 1992; *Prata*, 1989), but studies e.g. by *Shenk and Curran* (1974) and *Legrand et al.* (1989) pointed towards the potential of thermal IR split-window techniques for remote sensing of airborne dust, especially over land (Figure 4.3). Dust aerosol shows a strong variation in the 8-10 μm and 10-12 μm part of the spectrum, a wavelength region where the atmosphere is fairly transparent (*Ackerman*, 1997) (Figure 4.2).

For monochromatic radiation, transmittance due to the aerosol and transmittance due to the clean atmosphere lead to the transmittance of the real atmosphere. In case of mineral dust aerosol, the radiative absorption is strong for wavelength of 8-9 μm and 10-12 μm as well. At these wavelength regions, absorption due to atmosphere gases is weak (Figure 4.2). Thus the split-window technique is a potential tool to detect airborne dust by separating

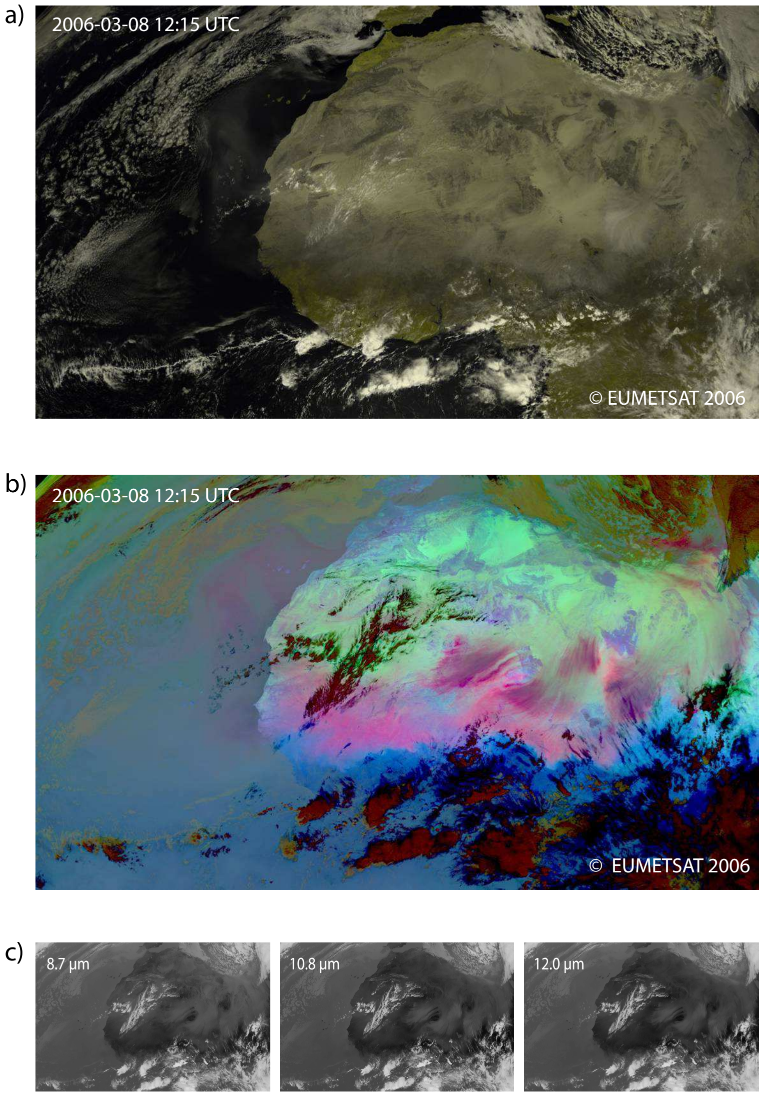

Figure 4.4: *Remote sensing of airborne dust: a) RGB-composite using VIS 0.6 VIS 0.8 and NIR 1.2 b) RGB composite images using tri-spectral BTD. In Figure 4.4b the magenta colour indicates airborne dust. c) Brightness temperature imaginary for the IR channels chosen for the tri-spectral composite image indicating airborne dust. All images are shown for March 08 2006, 12:15 UTC.*

the atmospheric (dust) and surface radiance contribution. Furthermore, applying different wavelengths account for the spectral radiative properties of dust particles.

To detect dust aerosol a few parameters have to be known (*Ackerman*, 1997): (1.) atmospheric structure, (2.) extinction coefficient (integrated over path it describes the optical depth, a measure for the attenuation of radiation by an aerosol volume), (3.) single-scattering albedo (1 for a non-absorbing medium and 0 for a fully absorbing and non-scattering medium) and (4.) phase function describing the direction of the scattered energy.

Both, real and imaginary part of the refractive index of dust particles show a strong

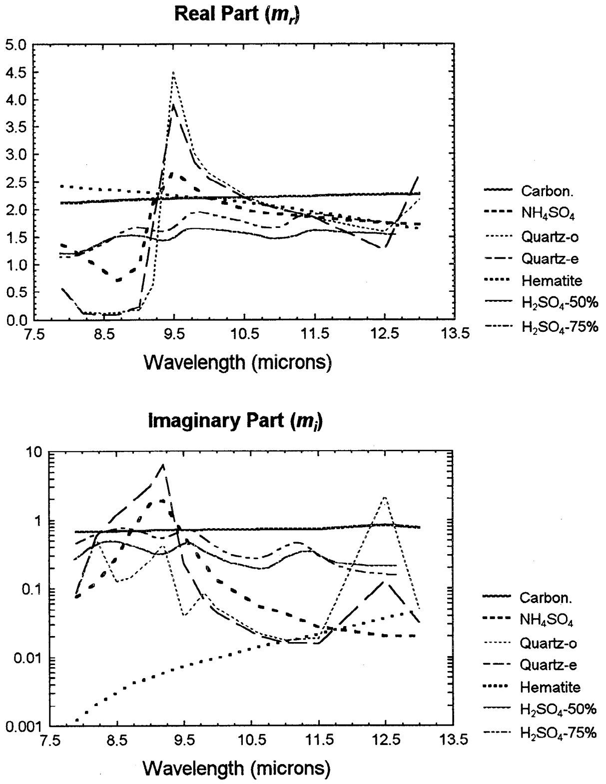

Figure 4.5: *Refractive index for the 8 to 12 µm wavelength region, shown for elemental components common in atmospheric aerosols. The figure is taken from Ackerman (1997).*

spectral dependency, encouraging the application of the split-window techniques (e.g. *Ackerman*, 1997; *Sokolik*, 2002; *Wald et al.*, 1998). As the refractive index for dust and ice or water clouds are different, multi-spectral IR techniques are a potential tool to separate dust plumes and clouds (*Ackerman*, 1997). Compared to clear-sky conditions, the presence of dust aerosol decrease the BTD between the 10.8 µm and the 12 µm wavelength band (BTD(10.8, 12)) (e.g. *Sokolik*, 2002).

Beside physical characteristics, mainly impacted by chemical and mineralogical constitution of the particle, size affects the radiative characteristic of a particle (*Ackerman*, 1997; *Wald et al.*, 1998). In addition to the spectral variability of dust and clear atmosphere, spectral particle size dependencies and temperature differences between desert surface and airborne dust provide additional a criterion for thermal dust detection. The thermal emissivity of airborne dust is less than the desert surface emissivity at wavelength around 11 µm (*Wald et al.*, 1998). This can be explained by the fact, that surface emissivities are decreased by particle size distribution (granulometry of soil aggregates) and packing effects (particle – particle distance). Considering wavelength around 8.5 µm, the emissivity increases for decreasing particle sizes.

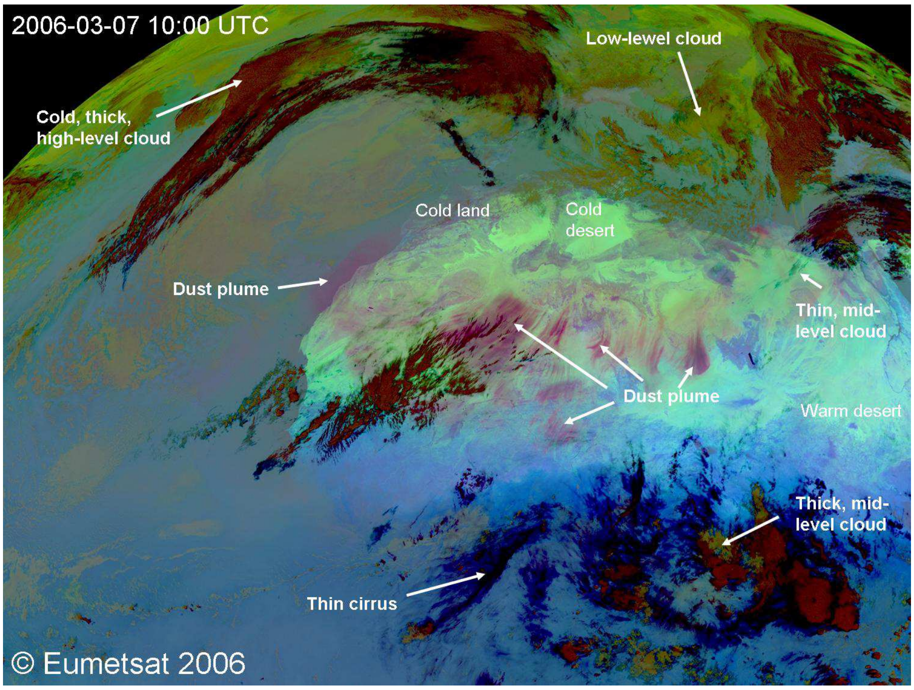

Figure 4.6: *MSG-SEVIRI tri-spectral thermal IR RGB-composite picture: red = 12 µm - 10.8 µm, green = 10.8 µm - 8.7 µm and blue = 8.7 µm. The composite image is shown for March 07 2006, 10:00 UTC.*

However, different spectral dependencies of absorption and emissivity due dust aerosol and surface, and high transmittance in case of pure atmosphere due to the atmospheric window characteristic, the thermal wavelength region 8-13 µm is well suitable for airborne dust detection as well as for applying the split-window technique to distinguish the spectral signature of airborne dust from the surface signature. According to the thermal channels provided by the MSG-SEVIRI instrument, in the context of this work a dust detection algorithm based on to brightness temperature (BT) converted radiances measured at the wavelength bands centred at 8.7 µm, 10.8 µm and 12 µm (Figure 4.4c) as provided by EUMETSAT is used. Due to applying BTs, the radiative signature of airborne dust and the surface can be separated, which is more difficult for BT of single wavelength channels (compare Figure 4.4b and c). The spectrally different characteristics of dust at 8.7 µm and 9.7 µm are quit significant, but due to the ozone absorption band at 9.7 µm, the IR9.7-channel is not suitable for dust detection.

Figure 4.6 shows a scene of MSG-SEVIRI dust index. This index is a colour index combining BTD(12, 10.8) (Figure 4.3a) for the red part, BTD(10.8, 8.7) (Figure 4.3b) for the green part and BT(8.7) for the blue part of the digital information. Atmospheric elements like clouds, dust plumes, and surfaces are represented by different colours indicating different spectral behaviours at the used wavelength bands. A similar index is applied to MODIS (Moderate-resolution Imaging Spectroradiometer) IR channels (*Zhang et al.*, 2006), that has been recently used to characterise Australian dust sources (*Bullard et al.*, 2008).

Thermal wavelength bands have been used for dust detection before. *Legrand et al.* (2001)

presented the IDDI (IR difference dust index) using first generation Meteosat measurements. Based on the broad-band IR channel (10.5-12.5 μm), a daily noon-time index for dust detection is designed by comparing cloud free noon-time scenes to a reference image build up on a 15-day reference period (*Brooks and Legrand*, 2000). Meteosat first generation (1977-2004, at 0° over the equator) does not provide the ability to apply the split-window technique. The comparison to a reference scene limits the index to a daily time resolution. Furthermore, the cloud free reference scene representing the highest BT values measured during the reference period is affected by long-lasting dust events (*King et al.*, 1999), persistent clouds, or by biomass burning aerosol (*Brooks and Legrand*, 2000).

4.3 Dust Detection Algorithm at UV and Visible Wavelengths

Dust detection algorithm also exists at other regions of the wavelength spectrum. Measurements at the short part of the visible spectrum like the deep-blue part or at the ultra-violet (UV) part of the spectrum are successfully applied to dust detection objectives, able to infer airborne dust over desert land surfaces.

Product	**Characteristic**						
	bright surf.	**global**	**long-term**	**night**	**sub-daily**	**height depend.**	**quant.**
VIS AOT		x	x		x		x
Deep Blue AOT	x	x					x
TOMS/OMI AI	x	x	x			x	
Meteosat IDDI	x		x			x	
MSG IR dust	x			x	x	x	

Table 4.2: *Characteristics of commonly used space-borne dust retrievals.*

Herman et al. (1997) defined an Absorbing Aerosol Index (AI) using the UV part of the spectrum measured by the Total Ozone Mapping Spectrometer (TOMS). TOMS was flying on-board several polar orbiting space crafts (Nimbus 7, ADEOS (Advanced Earth Observing Satellit), Meteor 3 and Earth-Probe) covering the measuring period 1979-2005. The AI algorithm is also applied to the Ozone Monitoring Instrument (OMI), since September 2004 on-board the low-orbiting Aura satellite (*Veihelmann et al.*, 2007). At UV wavelength, the surface reflectivity is low (*Eck et al.*, 1987) and UV-absorbing aerosols are detected due to their spectral contrast at 0.34 μm and 0.38 μm concerning backscattering effects (Mie-scattering) (*Herman et al.*, 1997). Since both mineral dust and soot are absobing at UV wavelength bands, the index does not distinguish between mineral dust aerosol and soot which becomes important especially over the Sahel and further south during the winter (*McConnell et al.*, 2008).

During the last years, *Hsu et al.* (2004) develop a new algorithm, Deep Blue, using a multiple narrow-channel technique applied to the deep-blue part of the shortwave spectrum (0.412, 0.47 and 0.65 μm for MODIS). The Deep Blue algorithm is able to detect absorbing aerosol over bright surfaces and provides information on the aerosol optical thickness (AOT). Compared to the IR aerosol detection algorithm, the Deep Blue algorithm uses look-up tables of a radiative transport model to retrieve aerosol information. At the moment, the retrieval is applied to MODIS on-board Terra spacecraft and SeaWiFS (Sea Wide Field-of-view Sensor) measurements, yielding to a daily resolution.

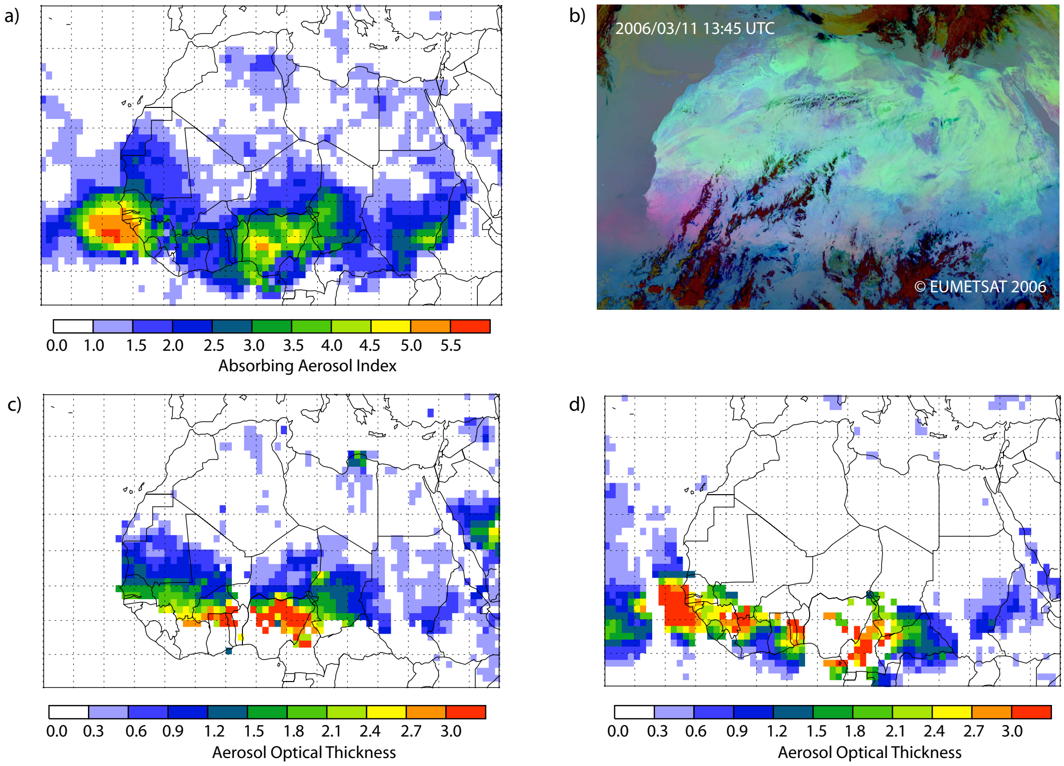

Figure 4.7: *Commonly used satellite retrievals to indicate the presence of airborne dust. All retrievals are applied to different wavelengths. a) OMI AI (UV, semi-quantitative index), b) MSG SEVIRI IR dust index (qualitative, magenta colour indicates airborne dust), c) MODIS Aqua Deep Blue AOT (deep-blue part of the visible spectrum, quantitative index) and d) MODIS Aqua AOT (visible wavelength, quantitative). All images are of the same event on March 11 2006 and taken at noon-time. The data for a), c) and d) are available at http://disc.sci.gsfc.nasa.gov/giovanni.*

A comparison of commonly used dust detection algorithms is shown in Table 4.2 with regard to dust source characterisation ability. Each algorithm is mainly limited by the measurement conditions provided by the used instrument. Instruments flying on-board a polar-orbiting satellite provide a low temporal resolution for a fixed surface location, but a high spatial resolution at each swath. Geostationary satellites are characterised by a high temporal resolution over an enlarged region compared to low, polar-orbiting satellites. Due to higher orbit level, spatial resolution is lower, but with e.g. 3 km at nadir for the MSG SEVIRI high enough to detect individual dust sources. Observations at wavelength of the

UV and IR are able to detect airborne dust over bright surfaces. Only IR based retrievals are able to detect airborne dust during day and night as thermal emittance is evident during all times. However, emissivity and scattering of airborne dust particles may change during transport (vertical and horizontal): The particles get cooler with increasing height and e.g. photo-chemical reactions or soot adsorption may change surface properties. Both affect the spectral signature of mineral dust particles at the measured radiance scene.

Figure 4.7 shows a comparison of results from commonly used retrievals to detect airborne dust, observed at noon time on March 11 2006. As discussed above, the retrievals are applied to different parts of the wavelength spectrum allowing dust retrieval over bright surfaces (e.g. AI, Deep Blue, IR retrievals) or not (e.g. MODIS VIS AOT). On March 05 a synoptic-scale density current was initiated along the Atlas Mountain chain by an upper-level disturbance. The density current, and dust emitted by high surface wind speeds, spread out radially and cross the entire Sahara towards the Sahel and the North Atlantic (*Tulet et al.*, 2008). The dust plume over the Sahel and West Africa shown by the scenes on Figure 4.7 is related to this extraordinary dust event. Thus the dust layer over the Sahel and southward is aged and mixed upward by boundary layer dynamics. All four aerosol indices show maximum dust concentrations over the Sahel and West Africa, but the images differ in detail. MODIS Deep Blue and VIS AOT retrieve high AOT values over Ghana, where OMI AI and MSG SEVIRI IR do not indicate high dust concentrations. Furthermore, MSG SEVIRI IR dust index does not indicate comparable high dust loadings over the Sahel and West Africa as it is indicated by the other retrievals. MSG SEVIRI IR dust index is based on thermal differences and thus is affected by the height and age of the dust plume, which limits the significance of this index to qualitative information on the presence of airborne dust. The MSG IR scene indicates active dust sources over the Akhdar Massif (Libya) and the Atlas mountains, both well represented by the MODIS Deep Blue retrieval. OMI AI shows some difficulties with regard to place of maximum (Atlas) and the maximum (Akhdra), which might be due to the height dependency of the retrieval leading to an underestimation of dust plumes at lower levels (*Israelevich et al.*, 2002).

OMI AI and former TOMS AI images have been used to identify dust sources (e.g. *Prospero et al.*, 2002). From this point of view of using airborne dust retrievals for dust source identification, the figure point towards difficulties in assuming high index values as being related to dust source areas. On the one hand, daily noon time images do not represent the place of origin as most dust plumes are initiated during the local morning hours (*Schepanski et al.*, 2007, 2008b). On the other hand, height dependencies strength aged, elevated dust plumes (*Israelevich et al.*, 2002). Hence high index values detected by those daily retrievals are the result of the strength of dust emission, the transport path affected by the present wind field, and the height of the dust layer. This have to be considered when relating high index values to dust source areas.

Beside radiances measurements performed by such single-viewing instruments, multi-viewing instruments like MISR are able to provide information on atmospheric dust content, including information on particle size and height of particle layer, also using visible wavelength (*Kahn et al.*, 2007). But the coverage of observations is lower than those provided by single-viewing instruments.

However, for dust source detection a high temporal resolution is a prerequisite. Therefore, the MSG IR technique on 15-minute time resolution are the best method to detect and study on individual dust sources.

Chapter 5

Meso-Scale Modelling

First three-dimensional (3D) global dust simulations comprising the whole dust cycle (emission, transport and deposition) have been computed at the beginning of the 1990s by *Joussaume* (1990), assuming the semi-arid, arid and hyper-arid areas as dust source. Earlier modelling studies used one-dimensional (1D) and two-dimensional (2D) mixed-layer models (*Berkofsky*, 1982; *Lee*, 1983), 2D steady state models (*Schütz*, 1980) or 2D time dependent grid point models (*Westphal et al.*, 1987) to simulate Saharan dust events.

Here, the meso-scale atmospheric model system LM-MUSCAT including a dust emission, transport and deposition scheme (*Heinold et al.*, 2007) is used to investigate meteorological features forcing dust emission (*Schepanski et al.*, 2008b) and to characterise Saharan dust export and deposition towards the tropical North Atlantic. In addition, the model is used to test the newly derived map of North African dust sources in the frame of the dust emission scheme implemented in the model system (*Schepanski et al.*, 2007).

The model system consists of the regional-scale meteorological model LM (LokalModell, now called COSMO, Version 3.19), provided by the Deutscher Wetterdienst (German Weather Service, DWD) *Steppler et al.* (2003)) and the MUlti-Scale Chemical Aerosol Transport model (MUSCAT, *Wolke et al.* (2004a)). In addition, a dust emission scheme based on *Tegen et al.* (2002) is implemented in MUSCAT.

5.1 Meteorological Part: Lokal-Modell

The LM as atmospheric frame component of the here used model system LM-MUSCAT computes meteorological and hydrological fields used for the simulation of dust emission, transport and deposition by the MUSCAT.

The non-hydrostatic meteorological model LM is developed as a "meso-to-micro scale prediction and simulation system" for tasks in scientific research and weather forecast (http://www.cosmo-model.org). The LM, since 2007 renamed as COSMO, is part of the national numerical weather prediction (NWP) system of the DWD, running operationally since 1999. The model is able to simulate atmospheric flow dynamics at the meso-γ (2 km – 20 km,), meso-β (20 km – 200 km), and meso-α (200 km – 2000 km), e.g. clouds, fog, frontal systems, meso-scale convective systems (MCS), small-scale weather events like cellular convection and thunderstorms and local wind systems due to e.g. orographic or thermic effects. Such as atmospheric, thermo-hydrodynamic processes are simulated solving the hydro-thermodynamical equations (*Steppler et al.*, 2003). The advantage of the usage of this dynamical equations are the possibility to describe compressible non-hydrostatic processes within the moist atmosphere without assumed scale approximations. Only the difference-fields between simulated and a reference state of the atmosphere are saved. As reference state of the atmosphere, a horizontal homogeneous, time-independent dry neutral atmosphere (vertically stratified, hydrostatic balanced) is assumed. For numerical computations with the finite difference method, the primitive equations are used in their advective form, the prognostic equation is used instead of the continuity equation. For time integration, the default Leapfrog (3 time-level) scheme is used, and modified by *Skammarock and Klemp* (1992). An Arakawa-C grid with a Lorenz vertical grid staggering is used, for spatial discretisation a second-order horizontal and vertical differencing is applied.

Processes which are not accurately resolved by either the equations or the spatio-temporal resolution have to be parametrised. The prognostic (time-dependent) and diagnostic (time-independent) variables computed by the LM are listed in Tabular 5.1.

Prognostic Variables	horizontal and vertical wind components (u, v, w) temperature (T) pressure perturbation (p'): deviation from the reference state specific humidity (q_v) specific cloud water content (q_c)
Diagnostic Variables	total air density precipitation flux of rain and snow
Parametrised Processes	grid-scale clouds and precipitation subgrid-scale clouds moist convection (following *Tiedtke* (1989)) radiation turbulent diffusion surface layer soil processes

Table 5.1: *Prognostic and diagnostic variables computed by the LM, (http://www.cosmo-model.org).*

Here, the LM runs on an artificial horizontal grid with a horizontal resolution of $28\,km \times 28\,km$ ($0.25° \times 0.25°$). For stereographic map projections, grid cells near the equator are approximately rectangular, grid-cell close to the poles are quite skewed due to the conformity. An artificial, rotated grid is defined for the model simulations to reduce that skewing. Therefore, new pole coordinates are defined in a way that maximises the rectangularity of most of the grid cells. That means, the equator of the artificial, rotated grid bisects the modelling domain. As the LM is a regional-scale model, its domain cov-

ers just a part of the global mesh. The vertical resolution is described by a generalised terrain-following height-coordinate grid (σ-p coordinate grid). Here, 40 σ-p levels are used to simulate meteorological process up to 23 km height. The first layer is situated at around 38 m above ground level.
Atmosphere and surface interact at diverse scales. So surface prescribing data sets, the so called “external data” are used for e.g. accurate parametrisation of physical processes. Table 5.2 refers to the external data sets required by the LM.

External Parameter	**Source**
mean topographical height	GTOPO30 data set (30” $\times$ 30”), USGS
roughness length	GTOPO30 and CORINE dataset
soil type	DSM data set (5’ $\times$ 5’) of FAO
vegetation cover	CORINE data set
land fraction	CORINE data set
root depth and leaf area index	CORINE data set

Table 5.2: *External parameters used by the LM, http://www.cosmo-model.org). CORINE stands for Coordination of information on the environment and was initiated in 1985 by the European Commission. GTOPO30 stands for a Global Topographical data set which is available at a horizontal resolution of 30”. It is provided by the United States Geological Survey, USGS. Information on soil type are given by the Digital Soil Mapping (DSM), provided by the Food and Agricultural Organisation (FAO), United Nations Educational.*

The external data are described on a higher-resolved grid than the model simulations will be done, so the external data are interpolated on the model grid. Thereby, fine elements are smoothed and the complexity of the topography is reduced.

5.2 Tracer Transport Model MUSCAT

The MUlti-Scale Chemical Aerosol Transport model MUSCAT (*Wolke et al.*, 2004a) is developed at the Leibniz Institute for Tropospheric Research (IfT) in Leipzig, Germany, with main focus on the simulation of emission, transport, and deposition processes of European aerosol species (*Wolke et al.*, 2004a,b). Adaptions made by *Heinold et al.* (2007) and the implementation of a dust emission scheme basing on *Tegen et al.* (2002) allow for the application of the model system LM-MUSCAT to simulate the mineral dust cycle (*Heinold et al.*, 2007, 2008a; *Schepanski et al.*, 2007, 2008a,b; *Tegen et al.*, 2006). Thereby, dust particles are transported as tracer at five independent size classes.

Dust emission depends on surface properties like vegetation cover, surface roughness, soil texture, and soil moisture content and atmospheric conditions like wind and stability. So dust emission can be described as threshold phenomenon, whereby the friction wind velocity has to exceed a certain, local threshold $u_\star \geq u_{\star,t}$ depending on local soil characteristics. The friction velocity threshold $u_{\star,t}$ is computed following the approach of *Iversen* *and White* (1982), modified by *Marticorena and Bergametti* (1995) (Equation 2.3). To compute the actual wind friction velocity $u_\star$ following Equation 2.2 wind fields provided by the LM are used and aerodynamic roughness length given by *Prigent et al.* (2005) for arid and semi-arid areas and *Marticorena et al.* (2004) for the Sahara domain. To consider soil characteristics strongly impacting on $u_\star$, soil data bases describing soil size distribution, soil texture and vegetation cover are required. The soil size distribution for the dust emission scheme implemented in the MUSCAT classifies four different soil size classes according to *Tegen et al.* (2002): clay, silt, medium/fine sand and coarse sand. As the size distribution does not follow the same proportion at each location, a local distribution is derived from a soil map including soil texture classes of the top 30 cm of the dominant soil type on a $0.5° \times 0.5°$ grid, provided by the Food and Agriculture Organization (FAO) (*Zobler*, 1986). Wind tunnel experiments show a particle size dependent sandblasting efficiency (*Gillette*, 1978). According to *Marticorena et al.* (1997) and *Tegen et al.* (2002) saltation efficiencies based on the wind tunnel experiments by *Gillette* (1978) have been assumed as $10^{-5}\,\mathrm{cm}^{-1}$ for silt, $10^{-6}\,\mathrm{cm}^{-1}$ for fine and medium sand and $10^{-7}\,\mathrm{cm}^{-1}$ for coarse sand (*Heinold et al.*, 2007). Beside the particle weight related to particle diameter as included in the soil size distribution, cohesion forces affect the sandblasting efficiency. Due to there mineralogical structure, clay shows high cohesion force between adjacent particles. An increasing clay content decreases the sandblasting efficiency. With regard to dust emission parametrisation, the sandblasting efficiency is set to $10^{-6}\,\mathrm{cm}^{-1}$ for clay content $< 45\,\%$ and $10^{-7}\,\mathrm{cm}^{-1}$ for a clay content $> 45\,\%$, taking the effect of variable clay contents for soils into account. The vegetation cover limits dust emission by decelerating surface wind velocities and therefore reducing the momentum transport from the air towards the soil particles, and by covering bare soils. Both limiting effects depend mainly on vegetation type and vegetation cover. E.g. a grass-like vegetation is assumed to be related to more effective dust sources than shrub-like vegetation. Shrub-like vegetation due to standing biomass elements lead a stronger decrease in surface wind velocity even if the leaf cover is low. For LM-MUSCAT, vegetation types are derived from simulations of the equilibrium terrestrial biogeography model BIOME4 (*Kaplan*, 2001). The simulation provides 27 potential vegetation types (biomes) on a $0.5° \times 0.5°$ grid. As dust emission occurs over non-forest areas, the following biomes are assumed to be important for dust mobilisation description: barren land, desert, tropical xerrophytic shrubland, temperate xerophytic shrubland, tropical grassland, temperate grassland, graminoid and forb tundra, erect dwarf-shrub tundra, prostrate dwarf-shrub tundra, and cushion-forb tundra. As mentioned above, vegetation cover is a limiting factor for dust emission beside the vegetation typ. The normalised difference vegetation index (NDVI) based on AVHRR (Advanced Very High Resolution Radiometer) difference reflectances R between $0.6\,\mu$m (visible) and $0.8\,\mu$m (near-IR) (Equation 5.1) describes the fraction of absorbed photosynthetically active radiation,

$$\mathrm{NDVI} = \frac{R_{0.8} - R_{0.6}}{R_{0.6} + R_{0.8}}. \tag{5.1}$$

Thereby high NDVI values indicate a high vegetation cover. Here, the GIMMS (Global Inventory Modelling and Mapping Studies) NDVI data set (*Pinzon*, 2002; *Pinzon et al.*, 2005; *Tucker et al.*, 2005) is used. For modelling, an empirical relationship between vegetation cover and dust emission following *Knorr and Heimann* (1995) is assumed. Therefore, an effective surface area is determined based on seasonal varying vegetation covers.

Soil moisture content reduces the soil erodibility as it impacts on cohesion forces between adjacent particles. So for a surface soil moisture content $> 99\,\%$, dust mobilisation is inhibited (*Heinold et al.*, 2007).

For modelling aspects, the emitted particles representing the original soil size spectrum with regard to surface wind velocities are distributed to five independent size bins with radii limiting at $0.1\,\mu$m, $0.3\,\mu$m, $0.9\,\mu$m, $2.6\,\mu$m, $8\,\mu$m and $24\,\mu$m (*Heinold et al.*, 2008a). These five independent size bins are transported as tracers described by the time-dependent, 3D advection-diffusion-reaction equation

$$\frac{dc}{dt} = \frac{\partial}{\partial w}\left(\rho_a K_z \frac{\partial v/\rho}{\partial w}\right) + Q(c) + D_s(c). \tag{5.2}$$

Thereby, the time-dependent dust concentration c is related to the vertical diffusion coefficient K_z, to the time-dependent emission term $Q(c)$, and to the deposition term D_s(c). Deposition, the removal of airborne dust particles from the atmosphere, is parametrised separately for dry and wet removal. The dry deposition is commonly parametrised using the deposition velocity v_d following *Zhang et al.* (2001). Wet deposition by rain-out and wash-out is parametrised following e.g. *Berge* (1997) and *Jacobson et al.* (1997) with details described in *Tsyro and Erdman* (2000).

5.3 Coupling: LM-MUSCAT

In the coupled model system LM-MUSCAT, the LM provides meteorological and hydrological fields, updated at every advection time step comprising 80 s. For radiative feedback considerations, the MUSCAT provides size-resolved dust concentration fields to the LM allowing on-line feedback mechanisms on e.g. temperature fields and atmospheric stability (*Heinold et al.*, 2007, 2008a). In MUSCAT, dust is transported as a tracer using meteorological fields up to 12 km height.

The spin-up period comprises 24 hours for the LM part, every 6 hours meteorological boundary conditions are updated using analysis field from the global weather forecast model (GME), provided by the DWD. After the spin-up period, the MUSCAT is coupled to the LM. A re-initialisation of the meteorological fields is done after a period of 24 hours.

Chapter 6

Publications

6.1 Summary of Publications

Within the present work seasonal changes of atmospheric Saharan dust cycle are characterised. Potential dust source areas and meteorological conditions suitable to force dust particle mobilisation are focussed. For this satellite remote sensing techniques (Spinning Enhanced VIsible and InfraRed Imager (SEVIRI) onboard the geostationary Meteosat Second Generation (MSG) satellite and atmospheric modelling (LM-MUSCAT, ECMWF ERA-40 reanalysis) are used. The transport of atmospheric dust depends on height, direction and atmospheric conditions during transport (e.g. the presence of clouds). The dust particles are finally removed from the atmosphere. Both, transport and deposition of mineral dust are investigated using results of the regional model system LM-MUSCAT. The model system consists of the meso-scale atmosphere model LM (Lokalmodell, *Steppler et al.* (2003)) provided by the German weather service DWD (Deutscher Wetterdienst) and the MUlti-Scale Chemistry Aerosol Transport model (MUSCAT, *Wolke et al.* (2004a)).

Modelling studies are limited by the accuracy of models, uncertainties due to parameterisation schemes and input parameters. Thus, observations are needed to improve our knowledge on processes as well as for model validation. Here, satellite remote sensing is used for observation of airborne dust as well as dust emission in terms of increasing dust indices. A $1^\circ \times 1^\circ$ map on dust source areas and the time-of-day of starting emission is compiled for the area covering Africa north of 5° N from MSG SEVIRI satellite data since March 2006. Thereby individual dust events are tracked back to the point of their first appearance (*Schepanski et al.*, 2007). The high temporal resolution at which the dust index is available is a prerequisite for this method. The movement of the dust index pattern enables distinctions from underground given in a similar colour. Additionally, dust mobilisation events directly linked to convective cloud dynamics are labelled. As dust events beneath clouds cannot be observed, only dust plumes leaving the area covered by the cloud can be detected.

Cloud cover is the main limit of this detection method. Additionally mobilisations along a dust plume track cannot be detected because of the overlying dust layer. As the dust source activation detection is done by visual observation, the dust detection is limited to the ability of the eyes to distinguish between the colour of the surface, impacted by the surface temperature and texture, and airborne dust. This is especially the case for diffuse dust plumes or over mountainous terrain and off the west coast of the Sahara where the warm ocean inhibit the application of the infrared (IR) dust index to thin dust plumes. Nevertheless, the estimated errors of this visual observations are lower than errors that would been made due to automatically assumed thresholds for dust presence. A comparison of dust indicating IR product and AErosol RObotic NETwork (AERONET, *Holben et al.* (1998)) aerosol optical thickness (AOT) at an African station (Banizoumbou, 13° 32' N; 2°39' E) is shown in Figure 6.1. The agreement between AOT measurements and the brightness temperature difference (BTD) used in the dust index supports the assumption that the dust index is a measure for the presence of dust.

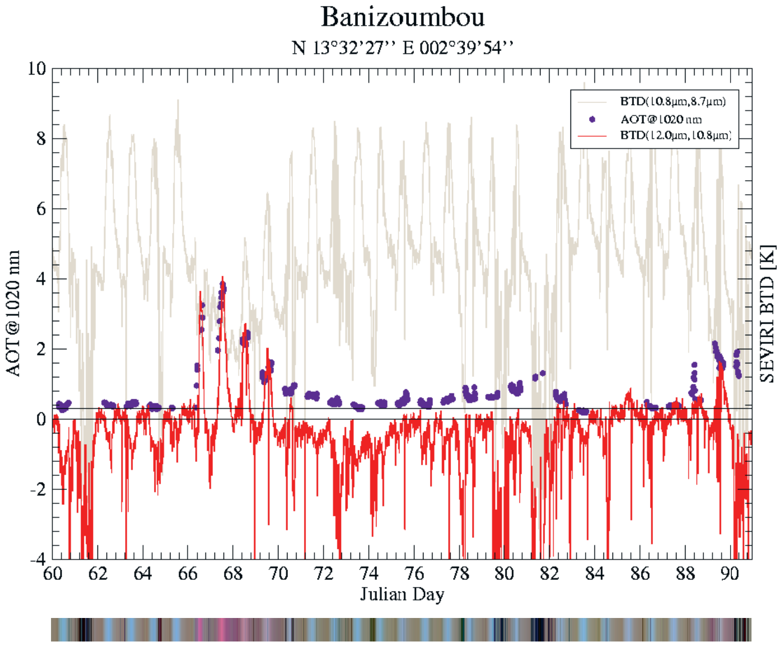

Figure 6.1: *Timeseries of AERONET AOT and MSG-SEVIRI BTD indicating dust. Bottom scale indicates the colour of the MSG-SEVIRI dust index. blue: daytime surface, gray: nighttime surface, magenta: dust, black: cloud.*

The new Saharan dust source map compiled from the dust index contains spatio-temporal information and enables for the first time the direct localisation of dust source areas, to characterise the sources by time-of-day of dust mobilisation and the frequency of dust source activation. Earlier remote sensing studies on Saharan dust sources based on daily dust retrievals, and were affected by dust transport due to the time-lag between dust source activation and dust detection. This map, named Dust Source Activation Frequency (DSAF), inferred from MSG observations is a new way to validate Saharan dust emissions computed by regional dust models. Alternatively, the map can be used as a mask for potential dust source areas in such models. The simulation of dust emission is only allowed where active dust sources have been observed by MSG-SEVIRI. No specific emission fluxes are prescribed. Atmospheric conditions determine the location of dust emission and its strength (dust emission flux) Seasonal changes in the pattern of active dust sources have to be represented by the dependence of dust emission and atmospheric conditions, e.g. wind fields. First studies show that the use of this mask improves the model performance when compared with an independent dataset (*Cavazos et al.*, 2008; *Schepanski et al.*, 2007, 2008b).

The DSAF dataset is used to investigate on the spatial distribution of dust source areas highlighting endorheic drainage systems like wadis located in the mountain foothills as frequent source areas. Furthermore, seasonally changing pattern of "hot spot" areas in terms of high frequencies of active dust sources are evident: During summer, the West Sahara becomes more active than in winter when the Bodélé depression is the most active dust source area. Beside spatial distribution and variability of dust source activation frequencies, the distribution of the time-of-day when dust emission starts is analysed. The morning hours between 06-09 UTC are characterised by the maximum dust source activation frequency, 65 % for the entire North African sector during an observation period of 2006/03–2008/08.

The time-of-day distribution of dust source activations has been used to relate dust entrainment to meteorological features (*Schepanski et al.*, 2008b). Thereby, two conditions were considered: (1.) The ability to provide atmospheric condition suitable for dust mobilisation (i.e. high wind speed) and (2.) the return frequency of such feature compared to the DSAF observations (Table 6.1). Wind speed observations provided by synoptic stations and modelling studies using LM-MUSCAT and global ERA-40 reanalysis fields were investigated because the dust emission process itself cannot be resolved by satellite

Time [UTC]	**Fraction of observed DSAF**	**Meteorological conditions**
00-03	2%	Haboob
03-06	5%	Haboob
06-09	65%	LLJ break-down
09-12	16%	LLJ break-down
12-15	8%	density currents in term of *Knippertz et al.* (2007), lee-cyclolysis like the Sharave-Cyclone
15-18	1%	density currents in term of *Knippertz et al.* (2007), Haboob
18-21	2%	Haboob
21-00	1%	Haboob

Table 6.1: *Attribution of time-of-day of observed DSAF [%] over the entire Saharan and Sahelian sector including Mahgreb, and probably most important meteorlogical situation forcing DSA (Schepanski et al., 2008b). Keep in mind, that over the entire desert from the Red Sea to the Atlantic a time difference of 4 hours.*

remote sensing. The break-down of the nocturnal LLJ is identified to account for most of dust source activations during the morning hours and can be seen as most important meteorological feature for dust emission over North Africa in terms of frequency of emissions.

Dust source activations occurring during the afternoon and evening hours are often related to gusts generated by dry or wet convection. Density currents (also termed gravity currents) and Haboobs are generated by evaporative cooling, occurring mostly during this time of day. The relatively low number of DSA occurring during afternoon and evenings point towards a lesser role of those convective events in terms of dust activation frequency, although the emission fluxes per event may be much higher than for the dust events occurring during morning hours.

Especially over the northern part of the Sahara and the Mediterranean coast, lee-cyclones (so called Saharav cyclone) develop on the lee-ward side of the Atlas Mountain chain especially during spring and early summer, enhanced by baroclinity. During noon and afternoon hours the convective activity and related gustiness of the wind is strongest. The active warm front of these cyclones is mostly accompanied by a dust storm moving in eastward direction.

Atmospheric conditions related to typical meteorological conditions do not occur with the same frequency for all areas. Seasonal changing meteorological conditions providing atmospheric conditions suitable for dust mobilisation are the main mechanism to force or inhibit the activation of individual dust sources over desert terrain.

Dust export form the Sahara becomes important especially for regions down-wind of dust sources because dust delivers micro-nutrients for terrestrial and oceanic ecosystems, and affects modern human life. Dust transport can be observed by satellite retrievals. To determine dust transport paths (height and direction), export and deposition fluxes, three case studies representing three different seasons (winter, spring and summer) have been performed using LM-MUSCAT. Strong seasonal variabilities regarding the amount of export and deposition, but also regarding transport height and transport direction influenced by atmospheric conditions such as wind regimes and air mass characteristics are shown by the simulations (*Schepanski et al.*, 2008a). In winter, dust is transported in near-surface levels in south-westward direction. In summer, dust transport shows a clear westward direction and takes place within elevated layers, mostly above the trade wind inversion. Nevertheless, emission, transport and deposition are linked to atmospheric conditions and circulation. Parameters like wind speed, stability, temperature and moisture impact on the vertical and horizontal distribution of the dust layer. The atmospheric circulation impacts on transport direction and velocity. Also the presence of clouds and the transport into cloudy regions, respectively, impact on deposition fluxes.

A new Saharan dust source activation frequency map derived from MSG-SEVIRI IR-channels

- Reproduced by permission of American Geophysical Union -

Geophysical Research Letters

K. Schepanski,[1,2] I. Tegen,[1] B. Laurent,[1] B. Heinold,[1] and A. Macke[2]

[1] Leibniz Institute for Tropospheric Research, Leipzig, Germany
[2] Leibniz Institute of Marine Science, IFM-GEOMAR, Kiel, Germany

Citation: Schepanski, K., I. Tegen, B. Laurent, B. Heinold, and A. Macke (2007), A new Saharan dust source activation frequency map derived from MSG-SEVIRI IR-channels, *Geophys. Res. Lett.*, 34, L18803, doi:10.1029/2007GL030168.

Abstract

We present a new dust source area map for the Sahara and Sahel region, derived from the spatiotemporal variability of composite images of Meteosat Second Generation (MSG) using the 8.7, 10.8 and 12.0μm wavelength channels for March 2006 - February 2007. Detected dust events have been compared to measured AOT and horizontal visibility observations. Furthermore the monthly source area map has been compared with the Ozone Monitoring Instrument aerosol index (AI). A spatial shift of the derived frequency patterns and the local maxima of AI-values can be explained by wind-transport of airborne dust implicitly included in the AI signal. To illustrate the sensitivity of a regional model using the new dust source mask, we present a case study analysis that shows an improvement in reproducing aerosol optical thickness in comparison to the original dust source parameterization.

1 Introduction

Soil dust aerosol plays an important role in the climate system (*IPCC*, 2007). Dust impacts the atmospheric radiation budget indirectly by influencing microphysical cloud processes and directly by scattering and absorbing shortwave radiation, and absorbing and re-emitting longwave radiation (*Sokolik et al.*, 2001). Furthermore, dust deposition provides nutrients for oceanic microorganisms, ultimately influencing the CO_2-cycle [e.g. *Jickells et al.*, 2005]. The atmospheric dust distribution itself is influenced by climate parameters like wind fields and precipitation.

The magnitude of the dust effects depends on the chemical, physical and optical properties of the particles, which vary due to different source areas and transport paths [e.g. *Koven* *and Fung*, 2006]. An adequate description of source areas is a prerequisite for estimates of the effects of dust aerosol, as well as for understanding the response of dust emissions to changing climate conditions.

Satellite remote sensing has previously been used to obtain information on dust sources. Daily maps of an absorbing aerosol index (AI), which is an indicator for the presence of dust aerosol over deserts, have been calculated from radiance measurements of the Total Ozone Mapping Spectrometer (TOMS) (*Herman et al.*, 1997), and since September 2004 from the Ozone Monitoring Instrument (OMI) (*Levelt*, 2002). Regions of maximum AI or high frequency of high AI occurrences are widely used as a proxy for dust source areas [e.g. *Prospero et al.*, 2002]. Recent applications in modeling the atmospheric dust cycle made use of the fact that the locations of maximum AI agree well with enclosed topographic depressions, and parameterize those as preferential dust sources [*Ginoux et al.*, 2001; *Tegen et al.*, 2002; *Zender and Newman*, 2003].

Beside the AI, a retrieval for aerosol properties over bright-reflecting surfaces exists considering the blue part of the shortwave spectrum ("Deep Blue" algorithm; (*Hsu et al.*, 2004)) using measurements by Sea-viewing Wide Field-of-view Sensor (SeaWiFS) and Moderate Resolution Imaging Spectroradiometer (MODIS). Furthermore a daily noon-time infrared difference dust index (IDDI) derived from Meteosat 1 has been used to detect dust source areas (*Brooks and Legrand*, 2000). All of these indices that provide information about aerosol over land are available at daily time resolution and do not resolve sub-daily processes like the daily cycle of dust emission.

Here we use the Meteosat Second Generation (MSG) Spinning Enhanced Visible and InfraRed Imager (SEVIRI) thermal IR radiance to identify dust source areas in the Sahara and Sahel region for applications in large-scale dust emission and transport models, making use of the high temporal and spatial resolution of the SEVIRI data (*Schmetz et al.*, 2002).

2 Satellite based dust retrieval from MSG

Atmospheric dust can be detected by MSG during daytime and nighttime at high temporal and spatial resolutions using IR wavelength channels. Here, the brightness temperature (BT) is used, and is calculated from narrowband radiances measured by the SEVIRI instrument onboard the geostationary MSG satellite located at 3.5°W above the equator. With a sampling rate of 15 minutes and a spatial resolution of 3km at nadir, SEVIRI BT are available at a high spatiotemporal resolution, which we use to identify activated dust sources (see *Schmetz et al.* (2002) for a detailed description of the SEVIRI instrument).

EUMETSAT offers a dust index product for MSG scenes on its website based on BT differences (BTD) (*http://www.eumetsat.int*). The same BTD and composite picture configuration is used for dust detection in this work. It is composed of the BTD at 12.0μm-10.8μm and 10.8μm-8.7μm, as well as 10.8μm. [e.g. *Ackerman*, 1997; *Sokolik*, 2002]. Several effects lead to dust detection in the thermal IR spectrum (*Ackerman*, 1997). The thermal emissivity of desert surface is low in the 8.7μm wavelength band compared to the 10.8μm wavelength band. Compared to clear sky conditions dust decreases the BTD between the 10.8μm and 12.0μm wavelength bands (BTD(12,10.8)), as it does for the 8.7μm and 10.8μm wavelength bands (BTD(10.8,8.7)).

According to *Wald et al.* (1998), thermal emissivities at the considered BTD(10.8,8.7) is more dependent on particle size than on temperature due to the opposite emissivity dependencies on particle size. A decrease in BTD for a dust loaded atmosphere in comparison to clear-sky conditions is also found in the BTD(12,10.8) [*Ackerman*, 1997; *Sokolik*, 2002]. Over dark surfaces (e.g. ocean) dust plumes can be clearly detected at visible wavelengths. Here, the BTD composite has been compared to the visible radiances that were showing enhanced reflection due to the presence of dust aerosols. In each case we detected co-location of the visible and IR detected aerosol plumes. Spatial correlations between BTD(12,10.8) resp. BTD(10.8,8.7) and radiances measured at 0.6μm for a 50×50-pixel offshore area on March 07, 2006 show a high dust pattern agreement (correlation coefficient of $|r|=0.79$ resp. $|r|=0.85$) for March 2006. Furthermore dust source activation occurs for some regions with a high frequency per month at nearly the same time of the day (e.g. in the Bodele Depression in December 2006 at 17 days at 7-9 am). For the case when the temperature of the surroundings is approximately constant, the regularity of dust emission for a known strong dust source (*Prospero et al.*, 2002) shows that the IR dust index used here indicates the presence of airborne dust.

To further evaluate the MSG dust index as an indicator for the presence of airborne dust, we perform correlations with aerosol optical thickness (AOT) sun-photometer measurements for some AErosol RObotic NETwork (AERONET) (*Holben et al.*, 1998) stations. To ensure that only the AOT affected by mineral dust are considered, we only use retrievals for AOT(1020nm) ≥ 0.3 and Angstroem coefficient $\alpha \leq 0.6$ (*Dubovik et al.*, 2002). The MSG dust index is dominated by the BTD(12,10.8)-signal. Peaking BTD(12,10.8) values and measured AOT show high correlations (Banizoumbou $|r|=0.73$, Cinzana $|r|=0.63$ and Dakar $|r|=0.55$). Furthermore correlations between the dust indicating composite color and measured AOT for significant dust events (AOT ≥ 1) have been computed for March 2006: Banizoumbou$|r|=0.77$, Cinzana $|r|=0.70$, and Dakar $|r|=0.66$.

MSG observed dust source activation events have also been compared to reduced horizontal visibility recorded at the WMO stations Faya-Largeau (17°56'N 19°08'E), Abeche (13°51'N 20°51'E), Bilma (18°41'N 12°55'E), Nguigmi (14°15'N 13°07'E), Agadez (16°58'N 7°59'E), Zinder (13°47'N 8°59'E) for the area (13-20°N 5-23°E) during March 2006 to February 2007. For the station observations, a dust event is defined for visibility below 5000m (*Mahowald et al.*, 2007), occurring at least once a day at one of the stations. Major dust events are well marked in both data sets. For the whole area, 68.7% of the time both MSG and station observations agree in indicating the presence or absence of dust events. Taking into account a one-day delay caused by the distance between dust source and station location, the agreement between MSG- and station observations reaches 74.9%.

Those tests support the premise that the MSG index shows the presence of dust. We do not attempt to derive quantitative optical thickness information from that index. Composite pictures using the BTD(12,10.8), BTD(10.8,8.7) and BT(10.8) are calculated for March

2006 to February 2007 for each 15-min SEVIRI scan [1]. Because of the high spatiotemporal resolution, dust source activation can be observed and localized by visual detection of tracing dust plume patterns back to their origin, in particular by inspecting consecutive images during dust mobilization and transport events. Dust emitting areas are visually determined and marked as dust source activation event on a 1° × 1° gridded map for the Saharan region between 5°N 20°W and 40°N 40°E. The monthly frequency of source activation events is calculated for each grid cell.

3 MSG Derived Dust Source Activation Frequency Map

For the one year of analysed data, the retrieved spatial dust source activation frequency (DSAF) pattern change with the seasons (Figure 1). The main source areas agree with source areas described by *D'Almeida* (1986) and *Prospero et al.* (2002). During December - February, the areas of most frequent dust emission events are located in the south-easterly part of the Sahara, mainly the Bodele Depression (16-19°N 16-19°E), where activation occurs at up to 65% of all days. The second most frequent source activation in this season is located in the southern foothills of Massif l'Air (15-18°N 5-9°E) with dust activations of up to 41% of days. During summer (June - August), dust is most frequently emitted in the western foothills of the Red Sea Mountains (16-19°N 34-36°E) (up to 27% of days), the foothills around Massif l'Air (17-20°N 6-8°E)(up to 26% of days), the area westerly of the Adrar Mountains (20-21°N 1-0°W) (up to 25% of days) and in the area of Sebkhas Mekherrane and Azzel Matti (25-27°N 0-3°E) (up to 20% of days). The temporal satellite observations indicate that catabatic flows like morning mountain winds and strong surface winds forced by convective clouds (squall lines), especially during the summer time in the Sahel region, are likely important for activating dust sources (*Engelstaedter and Washington*, 2007). Dust activation in the vicinity of mountainous areas occurs mostly during mornings and during afternoons and early evenings for dust events caused by strong winds in connection with convective clouds. Furthermore, the regional sea-land-wind circulation may activate dust sources in the north-eastern part of Libya. Seasonal changes in meteorological conditions cause changes in the spatial pattern of dust source activation.

4 Comparison of the MSG derived dust source areas to OMI Aerosol Index

A comparison of the new DSAF map derived from MSG with the OMI AI for the same period (here: July 2006) indicates that the maxima in AI retrievals are shifted downwind of the MSG derived source distribution (Figure 2). AI values have previously been used as proxy for dust source areas (*Prospero et al.*, 2002) and are available for each day. The regional shift between the patterns in the two datasets can be explained by the lower sampling rate of AI. OMI has its sun-synchronous overpass over the equator at 13:45

---

[1] On www.eumetsat.int/Home/Main/Image_Gallery/Satellite_Images_of_the_Month/Gallery/index.htm?l=en a video animation of the March 05 - March 10, 2006 dust event can be found.

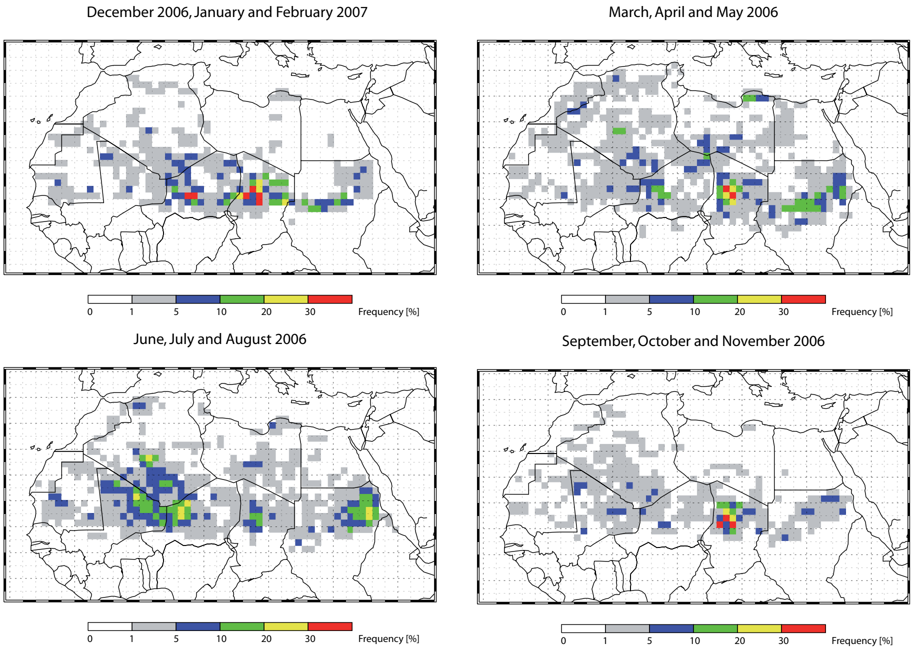

Figure 1: *Seasonal frequencies of dust source activation on a 1° × 1° grid, derived from MSG IR difference composite images for March 2006 to February 2007.*

local time (*Levelt*, 2002), but most dust sources are activated during mornings or during the afternoons and evenings (gusts in connection with convective clouds). Thus, at the OMI overpass time, the airborne dust has already been mixed up into the atmosphere and transported by local and regional wind systems, thus probably causing a bias in the OMI-retrieved source locations. Furthermore, dust detection by OMI below 1.5 km height is difficult (*Herman et al.*, 1997), so that mineral dust in proximity to its source may not be detected. Both effects result in a transport bias affecting the AI dataset when used as proxy for dust source determination, where in each case the differences between the present MSG results and the AI can be explained by downwind transport of the dust plumes at the time of the AI retrieval.

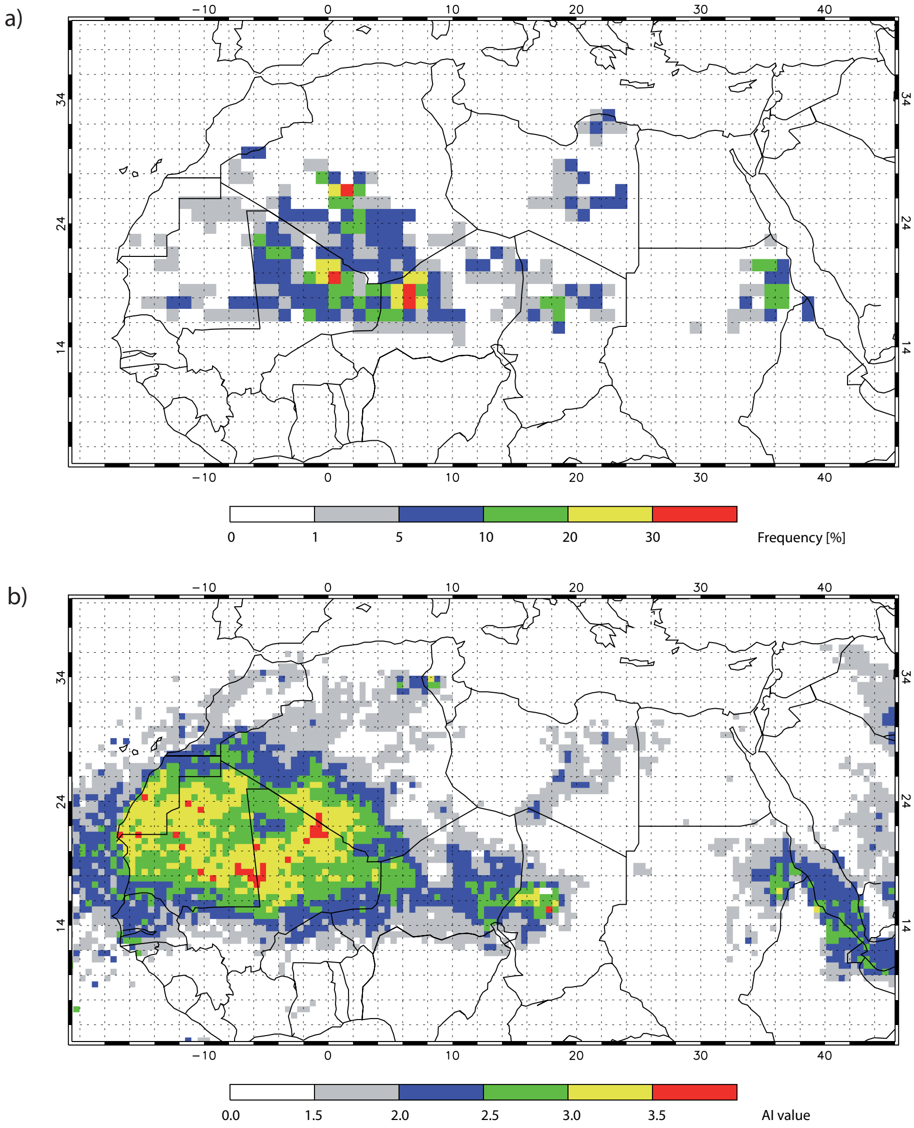

Figure 2: *Monthly frequency of dust source activation for July 2006, derived from MSG IR composite pictures (a) and averaged OMI AI for July 2006 (b).*

5 Model Application

While computations of the dependencies of dust emission fluxes on soil, surface properties, and friction wind velocity is meanwhile quite sophisticated in large-scale models [e.g. *Marticorena et al.*, 1997], the accuracy of such computations is limited by the available input data. The Saharan DSAF map provides a new mask for potential dust source areas useful for models of the Saharan dust cycle.

We use the new source area map as input field for the LM-MUSCAT regional dust transport model (*Heinold et al.*, 2007) to test how using the new sources changes the model results for a case study of a Saharan dust event from March 5-10, 2006. The model consists of the regional meteorological model Lokal-Modell (LM) from the Deutscher Wetterdienst (DWD) and the MUlti-Scale Chemical Aerosol Transport Model (MUSCAT), including a dust emission scheme based on *Tegen et al.* (2002). The model simulations were performed for an area covering 0.2°N 32.3°W - 41.3°N 33.3°E with a horizontal resolution of 28km and 40 vertical layers.

For a first test, dust emission was set to zero at those grid cells where source activation was observed less than 4 times a year in the MSG dataset. For Test case 1, soil texture was held at fixed values and the surface roughness was set to z_0=0.001cm for the entire model region. For Test case 2 the surface roughnesses used as input parameters in the dust emission code were set to satellite-derived values (*Laurent et al.*, 2005). The source activation and the magnitudes of emission fluxes are computed by LM-MUSCAT with the use of LM surface winds at each 80s time step. A simulation of the same period with the original model (*Heinold et al.*, 2007) was used as reference case. In the reference case, dust emission fluxes depend on soil texture, surface roughness, and surface wind speeds and topographic depressions are parameterized as hot spots of dust emission. Compared to AERONET's AOT the use of the new source area map clearly improves the modeled AOT for both test cases compared to the reference case, both in AOT magnitude and timing of dust events (Figure 3). At the location of the AERONET station Saada the AOT results of Test case 1 show best agreement with the observations, while at the other stations Test case 2 performs best. Correlations between modeled and observed AOT show high correlation coefficients for the Test cases 1 and 2 ($|r|$=0.9) and lower ones for the reference case ($|r|$=0.7).

These results using the new source area map as a mask for potential dust sources represent a first test; further refinements of the source formulation are needed. However, for this case study the implementation of the new derived dust source areas already show a promising improvement of the model performance.

6 Summary and Conclusion

We used three thermal IR wavelength channels of the SEVIRI instrument on board the geostationary MSG satellite to detect the present atmospheric dust over land. The high spatiotemporal resolution makes the detection of individual dust emission events possible. Using this information we compiled a new monthly 1° × 1° DSAF map for the Sahara and Sahel region from MSG IR composite pictures for the March 2006 - February 2007. The advantage of using measurements by a geostationary satellite is the improved detection of atmospheric dust close to its source due to the higher temporal resolution of the retrievals compared to daily retrievals from polar-orbiting instruments like OMI. In the presence of clouds, localization of dust emission is limited. Uncertainities in localization and missinterpretation of the MSG-signal are the main error sources. Results from the application of the DSAF map as a 'mask' to describe dust emission areas in a dust model indicate that this observation-based dust source distribution has the potential to improve the performance of regional scale Saharan dust transport models compared to earlier source area

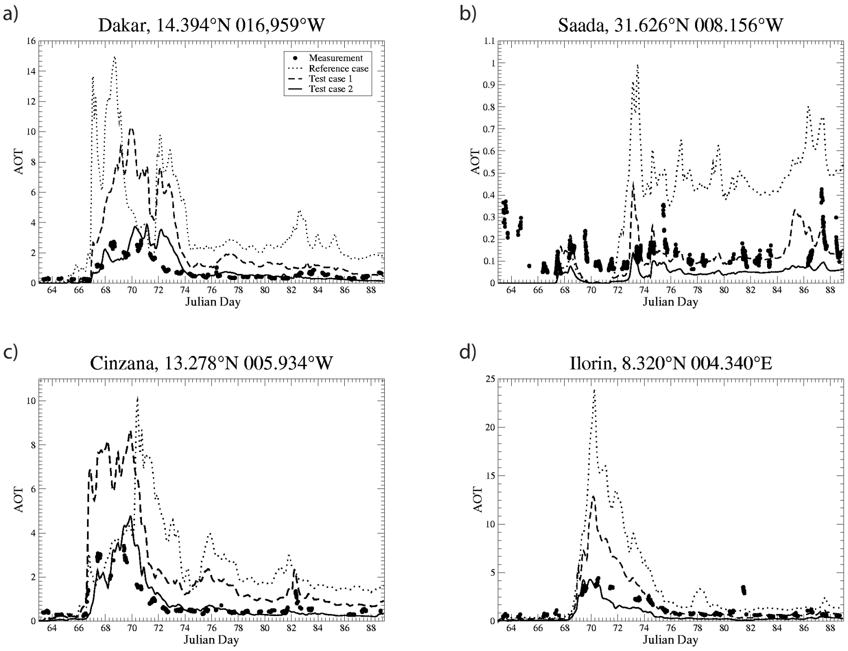

Figure 3: *Comparison of modeled (550 nm) and measured AOT(440 nm) at AERONET stations for (a) Dakar, (b) Saada, (c) Cinzana and (d) Ilorin for March 4^{th} - 29^{th} (shown as Julian Days).*

parameterizations.
The MSG dataset will be extended to include results for upcoming years, and additional case studies will be performed to test possible improvements in dust models from the use of the new source parameterization.

Acknowledgments

We acknowledge to the GES-DISC Interactive Online Visualization ANd aNalysis Infrastructure (Giovanni) as part of the NASA's Goddard Earth Science (GES) Data and Information Service Center (DISC) for the OMI AI data set. We thank B. Chatenet, B. Duchemin, B. Mougenot, R. Pinker and D. Tanre, for kindly providing AERONET data. We also thank the Deutscher Wetterdienst for good cooperation and support. We thank Natalie Mahowald and one anonymous reviewer for their comments, which helped to improve the paper.

References

Ackerman, S. A. (1997), Remote sensing aerosol using satellite infrared observations, *J. Geophys. Res.*, *102*(D14), 17,069–17,079.

Brooks, N., and M. Legrand (2000), Dust variability over northern Africa and rainfall in the Sahel, in *Linking Climate Change to Landsurface Change*, edited by S. J. McLaren and D. Kniveton, pp. 1–25, Kluwer Academic Publishers, Dordecht, The Netherlands.

D'Almeida, G. A. (1986), A Model for Saharan Dust Transport, *J. Climate Appl. Meteor.*, *25*, 903–916.

Dubovik, O., B. Holben, T. F. Eck, A. Smirnov, Y. J. Kaufman, M. D. King, D. Tanre, and I. Slutsker (2002), Variability of Absorption and Optical Properties of Key Aerosol Types Observed in Worldwide Locations, *J. Atmos. Sci.*, *59*, 590–608.

Engelstaedter, S., and R. Washington (2007), Atmospheric controls on the annual cycle of North African dust, *J. Geophys. Res.*, *112*, D03,103.

Ginoux, P., M. Chin, I. Tegen, J. M. Prospero, B. Holben, O. Dubovik, and S.-J. Lin (2001), Sources and distributions of dust aerosols simulated with the GOCART model, *J. Geophys. Res.*, *106*(D17), 20,255–20,273.

Heinold, B., J. Helmert, O. Hellmuth, R. Wolke, A. Ansmann, B. Marticorena, B. Laurent, and I. Tegen (2007), Regional Modeling of Saharan Dust Events using LM-MUSCAT: Model Description and Case Studies, *J. Geophys. Res.*, *112*, D11,204, doi: 10.1029/2006JD007443.

Herman, J. R., P. K. Bhartia, O. Torres, C. Hsu, C. Seftor, and E. Celarier (1997), Global distribution of UV-absorbing aerosols from Nimbus 7/TOMS data, *J. Geophys. Res.*, *102*(D14), 16,922–16,922.

Holben, B. N., et al. (1998), AERONET - A Federated Instrument Network and Data Archive for Aerosol Characterization, *Remote Sens. Environ.*, *66*, 1–16.

Hsu, N. C., s. C. Tsay, M. D. King, and J. R. Herman (2004), Aerosol Properties Over Bright-Reflecting Source Regions, *IEEE Trans. Geosci. Remote Sens.*, *42*(3), 557–569.

IPCC (2007), *Climate Change 2007: The Physical Science Basis.*, Contribution of Working Group I to the Forth Assessment Report of the Intergovernmental Panel on Climate Change, edited by S. Solomon and D. Quin and M. Manning and Z. Chen and M. Marquis and K.B. Averyt and M. Tignor and H.L. Miller, Cambridge, United Kingdom and New York, NY, USA.

Jickells, T. D., et al. (2005), Global Iron Connections Between Desert Dust, Ocean Biogeochemistry, and Climate, *Science*, *308*(5718), 67–71.

Koven, C. D., and I. Fung (2006), Inferring dust composition form wavelength-dependent absorption in Aerosol Robotic Network (AERONET) data, *J. Geophys. Res.*, *111*, D14,205, doi:10.1029/2005JD006678.

Laurent, B., B. Marticorena, G. Bergametti, P. Chazette, F. Maignan, and C. Schmechtig (2005), Simulation of the mineral dust emission frequencies from desert areas of China and Mongolia using an aerodynamic roughness length map derived from POLDER/ADEOS 1 surface products, *J. Geophys. Res.*, *110*, D18S04, doi: 10.1029/2004JD005013.

Levelt, R. F. (2002), *OMI Algorithm Theoretical Basis Document Volume 1: OMI Instrument, Level 0-1b processor, Calibration & Operations*, Technical Report.

Mahowald, N. M., J. A. Ballantine, J. Feddema, and N. Ramankutty (2007), Global trends in visibility: implications for dust sources, *Atmos. Chem. Phys.*, *7*, 3309–3339.

Marticorena, B., G. Bergametti, B. Aumont, Y. Callot, C. N'Doume, and M. Legrand (1997), Modeling the atmospheric dust cycle: 2. Simulation of Saharan dust sources, *J. Geophys. Res.*, *102*(D4), 4387.

Prospero, J. M., P. Ginoux, O. Torres, S. E. Nicholson, and T. E. Gill (2002), Environmental characterization of global sources of atmospheric soil dust identified with the Nimbus 7 Total Ozone Mapping Spectrometer (TOMS) absorbing aerosol product, *Rev. Geophys.*, *40*(1), 1002, doi:10.1029/2000RG000095.

Schmetz, J., P. Pili, S. Tjemkes, D. Just, J. Kerkmann, S. Rota, and A. Ratier (2002), An introduction to Meteosat Second Generation (MSG), *Bull. Amer. Meteor. Soc.*, *83*, 977–992.

Sokolik, I. N. (2002), The spectral radiative signature of wind-blown mineral dust: Implications for remote sensing in the thermal IR region, *Geophys. Res. Lett.*, *29*(24), 2154, doi:10.1029/2002GLR015910.

Sokolik, I. N., D. M. Winker, G. Bergametti, G. D. A, G. Carmichael, Y. J. Kaufman, L. Gomes, L. Schuetz, and J. E. Penner (2001), Introduction to special section: Outstanding problems in quantifying the radiative impacts of mineral dust, *J. Geophys. Res.*, *106*(D16), 18,015–18,027.

Tegen, I., S. P. Harrison, K. Kohfeld, and I. C. Prentice (2002), Impact of vegetation and preferential source areas on global dust aerosol: Results from a model study, *J. Geophys. Res.*, *107*(D21), 4576, doi:10.1029/2001JD000963.

Wald, A. E., Y. J. Kaufman, D. Tanre, and B.-C. Gao (1998), Daytime and nighttime detection of mineral dust over desert using infrared spectral contrast, *J. Geophys. Res.*, *103*(D24), 32,307–32,313.

Zender, C. S., and D. Newman (2003), Spatial heterogeneity in aeolian erodibility: Uniform, topographic, geomorphic, and hydrologic hypotheses, *J. Geophys. Res.*, *108*(D17), 4543, doi:10.1029/2002JD003039.

Meteorological processes forcing Saharan dust emission inferred from MSG-SEVIRI observations of sub-daily dust source activation

Journal of Geophysical Research, revised

- Reproduced by permission of American Geophysical Union -

K. Schepanski,[1,2] I. Tegen,[1] M. C. Todd,[3] B. Heinold,[1] G. Bönisch,[4] B. Laurent,[1]
and A. Macke[2]

[1] Leibniz Institute for Tropospheric Research, Leipzig, Germany
[2] Leibniz Institute of Marine Science, IFM-GEOMAR, Kiel, Germany
[3] Department of Geography, University College London, London, UK
[4] Max-Planck-Institute for Biogeochemistry, Jena, Germany

Citation: Schepanski, K., I. Tegen, M. C. Todd, B. Heinold, G. Bönisch, B. Laurent and A. Macke (2007), Meteorological processes forcing Saharan dust emission inferred from MSG-SEVIRI observations of sub-daily dust source activation, *J. Geophys. Res.*, revised.

Abstract

15-minute Meteosat Second Generation (MSG) infrared dust index images are used to identify dust source areas. The observations of dust source activation (DSA) frequencies are compiled in a 1° × 1 ° map for the Sahara and Sahel, including temporal information at 3-hourly resolution. Here, we use this dataset to identify the most active dust source areas and the time-of-day when dust source activation occurs most frequently. In the Sahara desert 65 % of DSA (2006/03-2008/02) occur during 06-09 UTC, pointing towards an important role of the break-down of the nocturnal low-level jet (LLJ) for dust mobilization. Other meteorological mechanisms may lead to dust mobilization including density currents initiated by deep convective systems which mobilize dust fronts (haboobs) occurring preferentially in the afternoon hours, and cyclonic activities. The role of the nocturnal LLJ for dust mobilization in the Sahara is corroborated by regional model studies and analysis of meteorological station data.
15-minute Meteosat Second Generation (MSG) infrared dust index images are used to identify dust source areas. The observations of dust source activation (DSA) frequencies are compiled in a 1° × 1 ° map for the Sahara and Sahel, including temporal information at 3-hourly resolution. Here, we use this dataset to identify the most active dust source areas and the time-of-day when dust source activation occurs most frequently. In the Sahara desert 65 % of DSA (2006/03-2008/02) occur during 06-09 UTC, pointing towards an important role of the break-down of the nocturnal low-level jet (LLJ) for dust mobilization.

Other meteorological mechanisms may lead to dust mobilization including density currents initiated by deep convective systems which mobilize dust fronts (haboobs) occurring preferentially in the afternoon hours, and cyclonic activities. The role of the nocturnal LLJ for dust mobilization in the Sahara is corroborated by regional model studies and analysis of meteorological station data.

1 Introduction

Airborne mineral dust particles impact on several atmospheric processes mainly related to radiation and cloud micro-physics (*IPCC*, 2007). The atmospheric radiation budget is influenced by airborne dust particles directly and indirectly [e.g. *Tegen and Lacis*, 1996, *Sokolik and Toon*, 1996, *Miller and Tegen*, 1999]. Beside impacts on physical processes controlled mainly by optical and physical characteristics, deposited mineral dust acts as nutrient to marine and terrestrial ecosystems due to its mineralogical composition [*Claquin et al.*, 1999]. As a source of iron, mineral dust provides nutrients for oceanic microorganisms and influences terrestrial ecosystems (*Mahowald et al.*, 2005). Ultimately dust influences the global CO_2-cycle [e.g. *Fung et al.*, 2000, *Jickells et al.*, 2005].

Consequently, an adequate description of source areas and meteorological processes controlling dust emission is a prerequisite for accurate estimations of dust aerosol effects, as well as for the understanding of the response of dust emission to changing climate conditions. The Sahara is the World's most important dust source area [e.g. *Prospero et al.*, 2002, *Washington et al.*, 2003, *Goudie and Middleton*, 2001, *Middleton and Goudie*, 2001] providing an estimated dust production of 40-70 % of the global annual total (*Engelstaedter et al.*, 2006). Physical, optical and mineralogical properties that are important for the climate impacts of dust are controlled by local geomorphology of dust source regions. As in-situ measurements at all of the important dust source locations are impossible, remote sensing must be used to provide a comprehensive dataset on Saharan dust sources.

Since remote sensing offers retrievals of airborne dust, several approaches for dust source determination have been developed. Most commonly data from low Earth orbiting satellites are used. Earlier attempts to derive the major dust source areas in the Sahara included the use of daily datasets of the absorbing Aerosol Index (AI) from radiance measurements of the Total Ozone Mapping Spectrometer (TOMS) (*Herman et al.*, 1997), since September 2004 from the Ozone Monitoring Instrument (OMI) (*Torres et al.*, 2007). As the index indicates airborne dust over the ocean as well as over land surfaces like desert areas, the AI has been used to determine dust source areas, characterized by high frequencies of high AI values [e.g. *Prospero et al.*, 2002, *Washington et al.*, 2003]. The main areas of high AI frequencies are located over topographic depressions, which were then parameterized as preferential dust sources for modeling applications [*Ginoux et al.*, 2001, *Tegen et al.*, 2002, *Zender and Newman*, 2003].

In addition to estimates based on satellite sensors measuring at ultra-violet (UV) wavelengths, visible wavelengths are also used. Notably Moderate Resolution Imaging Spectroradiometer (MODIS) and Sea-viewing Wide Field-of-view Sensor (SeaWiFS) measurements are used to derive aerosol properties over bright-reflecting surfaces like deserts from the deep-blue part of the shortwave spectrum using the “Deep Blue” algorithm (*Hsu et al.*, 2004). Also, a daily noon-time Infrared (IR) Difference Dust Index (IDDI) calculated from Meteosat measurements has been used to derive dust source areas (*Brooks and Legrand*, 2000).

Such results are useful, but the temporal resolution is limited to, at best, instantaneous observations at a fixed daytime slot. Dust mobilization is known to be forced by synoptic-scale, meso-scale and local-scale winds as well as near surface turbulent processes, which are highly variable in time and can usually not be resolved adequately from a single day sample. Therefore biases in estimates of mean aerosol properties may occur, especially near source regions. Here, we use 15-minute IR measurements by Meteosat Second Generation (MSG) Spinning Enhanced Visible and InfraRed Imager (SEVIRI) instrument to obtain dust source information for the Sahara (*Schepanski et al.*, 2007). In addition to the identification of areas that are of major importance for dust mobilization, the information of the time-of-day when the mobilization occurs reduces biases associated with poor temporal sampling and also provides information on possible meteorological processes responsible for dust emission. This paper aims to determine the diurnal cycle of dust emission in the Sahara inferred from satellite observations and to relate to associated meteorological controls able to force dust source activation (DSA). It is structured as following: Section 2 will give a short overview on meteorological features, which are related to dust source activation. Time-of-day distributions of observed dust source activation frequencies (DSAF) derived from the MSG dust product and their associated meteorological dynamics are analyzed in Section 3. The break-down of the nocturnal low-level jet (LLJ) appears to be an important feature for Saharan dust source activation (DSA) during the morning hours. This motivates to investigate the occurrence of the nocturnal LLJ and its morning time break-down with regard to a) their ability to force dust mobilization and b) their frequency of occurrence. Therefore, wind observations of synoptic weather stations, and fields of regional- and global-scale atmospheric models will be used (Section 4).

2 Meteorological Processes Leading to Dust Source Activation

For Saharan dust mobilization, atmospheric processes on synoptic-, regional-, local- as well as turbulent-scales can force emission and atmospheric mixing of dust particles. All atmospheric processes forcing dust mobilization must generate wind speeds exceeding the local threshold velocity depending on surface roughness length, soil structure and vegetation (*Marticorena and Bergametti*, 1995). In this section, important meteorological situations able to provide frequently atmospheric conditions suitable for dust mobilization are described. These include the turbulent mixing of momentum from nocturnal low-level jets (LLJ), the Mediterranean cyclone (*Alpert and Ziv*, 1989), and convective activity (*Flamant et al.*, 2007).

2.1 Nocturnal Low-Level Jet

LLJs are most commonly observed at nighttime and can occur over all continents above flat and complex terrain. They may extend over tens to hundreds of kilometers [*Davis*, 2000, *May*, 1995] and can, for example, be caused by baroclinity associated with sloping terrain, splitting, ducting and confluence around mountain barriers, mountain and valley wind, and inertial oscillation (*Kraus et al.*, 1985). Over the Sahara, LLJs occur under clear skies and low surface wind speed conditions [e.g. *Thorpe and Guymer*, 1977]. LLJs are characterized by a horizontal wind speed maximum in the lowest few kilometers of the atmosphere [e.g. *Blackadar*, 1957, *Holton*, 1967, *Banta et al.*, 2006]. LLJ development is explained by frictional decoupling at night due to radiative cooling causing nocturnal temperature inversion at the top of the stably stratified cold surface layer [e.g. *Banta et al.*, 2003, *Banta et al.*, 2002, *Nappo*, 1991, *Mahrt*, 1999, *Blackadar*, 1957]. Frequently, LLJs over the Sahara develop during the evening and nighttime hours after sunset when boundary layer dynamic ceases. In most cases they are persistent until boundary layer turbulence sets in after sunrise. As such they are driven by diurnally varying eddy viscosity causing an inertial oscillation phenomenon.

A precondition for the development of LLJ is the frictional decoupling of air layers above the near-surface layers [e.g. *Nappo*, 1991, *Banta et al.*, 2006]. This development is influenced by the remaining turbulence within the lower troposphere. Turbulence can be forced by insolation (causing convective turbulence) as well as wind shear. During calm nights with low surface wind speeds, near-surface air layers are well stratified and turbulence is suppressed. In such conditions, air layers above near-surface can be frictionally decoupled such that wind speed within this decoupled air layer is not influenced by surface friction [e.g. *Hoxit*, 1975, *Garratt*, 1992, *Mauritsen and Svensson*, 2007, *Mahrt*, 1999].

After sunrise, convective turbulence arises with the onset of solar heating. The decoupled air layer aloft becomes frictionally coupled to the surface, and LLJ momentum is mixed down [*Blackadar*, 1957, *Lenschow and Stankov*, 1979]. High surface wind speeds occur as a consequence until the LLJ is degraded. This process causes a characteristic phase lag between the diurnal cycle of LLJ wind speeds and those at the surface. The LLJ peaks at nighttime while surface wind peaks in mid-morning when LLJ momentum is mixed down to the surface [*Parker et al.*, 2005, *Washington et al.*, 2006, *Todd et al.*, 2008]. These surface winds can enhance dust mobilization if they exceed the threshold velocity and occur at a potential dust source area [e.g. *Westphal et al.*, 1988]. The importance of the LLJ in the Bodélé region for dust emission has been established by *Washington et al.* (2006). However, nocturnal LLJ features are common in other locations across North Africa (*Parker et al.*, 2005) and are likely to play an important role for dust emission.

2.2 Mediterranean Cyclone

Especially in spring season, the temperature contrast between the North African coast and the Mediterranean Sea enhances a boundary layer (BL) baroclinity [*Pedgley*, 1972, *Alpert and Ziv*, 1989, *Trigo et al.*, 2002]. Cyclones are observed in connection with this temperature induced BL baroclinity, most frequently in spring when temperature gradients are strongest. These typical spring cyclones are known as Sharav cyclone, Saharan depression or Khamsin depression. At least three mechanisms dominate the generation of such cyclones [e.g. *Thorncroft and Flocas*, 1997, *Alpert and Ziv*, 1989, *Prezerakos et al.*, 1990, *Dayan et al.*, 1991, *Pedgley*, 1972]: Large-scale interior baroclinity, BL baroclinity, and jet stream related circulations. The cyclone, characterized by an active warm front, is frequently associated with extremely high surface temperatures, heavy dust storms and low visibilities, and a shallow cold front, that is well defined at the surface by changes in temperature of 10-20 K. It moves quickly eastward (typically faster than 10 $m\ s^{-1}$) mostly following the North African coast [*Alpert et al.*, 1990, *Alpert and Ziv*, 1989]. Observations indicate a frequent occurrence of the cyclone on the leeward side east and south of the mountain ridge of the Atlas Mountains [*Barkan et al.*, 2005, *Prezerakos et al.*, 1990, *Alpert et al.*, 1990, *Alpert and Ziv*, 1989]. Hence, both lee-effect of the mountains and coastal thermal gradient effect can explain the spring cyclogenesis, initiated by the presence of an upper-level trough to the west [e.g. *Horvath et al.*, 2006, *Egger et al.*, 1995]. Dust source activations related to the dynamics of the lee-cyclone can generally be initiated during the whole day, but the surface heating will strengthen convection during day time [e.g. *Trigo et al.*, 2002].

2.3 Moist Convection

During northern hemispheric summer, a heat low commonly develops over North Africa with a mean position centered near 20° N; 0° E. The Intertropical Convergence Zone (ITCZ) in terms of maximum rainfall area extends to about 15° N [e.g. *Nicholson*, 2000]. Large-scale sinking of air associated with the Hadley circulation is weak and the BL deep. Due to solar heating and moist air transported from the Gulf of Guinea northward by the southwest monsoon flow, deep convection develops with maximum activity in the afternoon (*Peters and Tetzlaff*, 1988). Down-bursts of cold, humid air related to deep convection can occur causing high surface wind speeds. Such density currents can propagate many hundreds of kilometers from the convective system and cause dust emission referred to as 'haboob' events [*Sutton*, 1925, *Idso et al.*, 1972, *Droegemeier and Wilhelmso*, 1987, *Flamant et al.*, 2007, *Bou Karam et al.*, 2008]. As the occurrence of haboobs is related to the dynamics of moist convection, they are frequently observed during afternoons and evenings.

Deep moist convection also occurs in mountain areas, notably near by the Atlas Mountains, due to orographic effects and blocking situations. Large scale density currents have been observed with evaporative cooling of cloud particles or precipitation. This can lead to high surface wind speeds and dust emission [*Droegemeier and Wilhelmso*, 1987, *Knippertz and Martin*, 2005, *Knippertz et al.*, 2007]. During daytime, air can be cooled by evaporation. Cloud droplets blown out by high winds in cloud top levels evaporate in dry surroundings. Consequently temperature decreases: A dense air mass is generated and sinks down as far as the surrounding air density is lower. In case of mountain ridges located orthogonally to a strong general flow, convective clouds are formed on top of the mountain ridges and the foehn effect provides a dry and warm air mass on the leeward side of mountain ridge.

These conditions lead to a high density difference between air cooled by evaporation and the surrounding air. However, hydrostatic equilibrium forces a high vertical sinking velocity of this dense air mass, which in most cases reaches surface as strong gusts reaching high wind speeds sometimes propagating far in excess about the foothills causing dust mobilization [*Knippertz et al.*, 2007, *Knippertz et al.*, 2009, *Smith and Reeder*, 1988, *Charba*, 1974].

Density currents provided by blown-out clouds are limited to the mountain regions and occur most frequently during the afternoon when convection reaches maximum (*Knippertz et al.*, 2007). Over the Sahara, they can be observed most frequently in the Atlas Mountains due to transport of moist air towards the mountains within the generally westerly circulation.

Beside moist convection, dry convection occurring related to the Saharan heat low where low atmospheric moisture content inhibit cloud development is identified to account for dust source activation (*Engelstaedter et al.*, 2006).

3 Spatio-Temporal Dust Source Characteristics Inferred from Satellite Observations

Measurements provided by geostationary satellites are suitable to locate and characterize dust source activity due to their regional coverage observations with a relatively high temporal resolution. Furthermore, high frequencies of temporal varying dust source activities point towards recurring meteorological features able to provide suitable conditions for dust mobilization.

3.1 Dust Source Activation from MSG-SEVIRI

For dust source area detection we use the SEVIRI instrument on-board the geostationary MSG Satellite, located at 3.5° W above the equator (see *Schmetz et al.* (2002) for a detailed description). The instrument provides narrow-band visible and IR measurements at a sampling interval of 15 minutes with a spatial resolution of 3 $km \times 3$ km at nadir. This high spatio-temporal resolution motivates the use of a MSG IR dust index, calculated from SEVIRI IR channels centered at 8.7 μm, 10.8 μm and 12.0 μm, to obtain information on dust source locations and activation over the Saharan desert between 5° N - 40° N; 20° W - 45° E (for a detailed description see *Schepanski et al.*, 2007). The dust index may be biased by variations in brightness temperature differences for dust at different heights. Here only qualitative information on presence or absence of dust is used. Individual dust plumes were identified from the SEVIRI dust product and tracked back to their initial location. From this information a frequency count was derived for each location (dust source activation frequency, DSAF). The spatio-temporal information on dust sources are compiled in a $1° \times 1°$ gridded map, including information on the time of the beginning of dust mobilization at 3-hour intervals and about convective clouds close to dust source areas during activation time (*Schepanski et al.*, 2007). DSAs downwind within a developing dust storm are not considered, and neither can dust sources totally covered by clouds. Currently

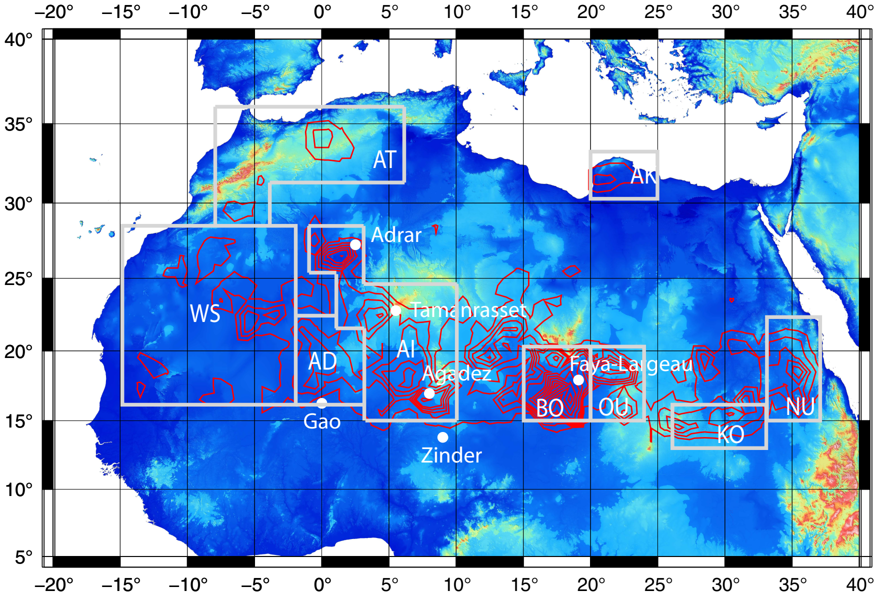

Figure 1: *Dust source activation frequency (DSAF) derived from MSG IR dust index (2006/03 - 2008/02 except 2007/08) is given in contour lines at 0.02 intervals. High DSAF in depression areas (Bodélé, sebkas, chotts) and the foothills of the Saharan mountain areas. DSAF lower than 0.02 are not shown. White dots represent the location of synoptic stations considered in this study. The boxes mark the predefined sub-areas for discussion on the sub-daily and monthly variability of observed DSA as shown in Figure 3. Colors indicate topography given by the GTOPO30 digital elevation data set provided by the U.S. Geological Survey.*

the dataset contains two years of observations between March 2006 and February 2008 (with August 2007 missing) with 3-hour temporal resolution. A separation is made between DSAs under clear skies and those connected with cloudy conditions. While DSA detection below clouds is impossible, DSA occurring close to cloud collars and related to gusts and down-burst due to convective activities are counted as “DSA under cloudy conditions” and included in the DSA dataset. The DSA therefore represents a frequency index for dust events, irrespective of their magnitude. It is the first available satellite based dataset to provide information on the diurnal cycle of dust emission. For the total Sahara we must emphasize that it is not a quantitative index of atmospheric dust burden. Instead it is a more direct measure of dust source activation and a more appropriate tool to study related emission processes compared to other satellite products based on retrievals at a specific time-of-day. MSG IR difference dust index images of airborne dust over the African continent northward of the equator were used to compile a mask of DSA areas in a 1° × 1° gridded map between 5° N and 40° N and 20° W and 45° E (*Schepanski et al.*, 2007). The comprehensive dataset described in *Schepanski et al.* (2007) allows a detailed analysis of DSA in time and space and the associated synoptic and meso-scale conditions likely to be forcing DSA.

3.2 Dust Source Analysis

3.2.1 Characteristics of Typical DSA Areas

Most active dust source areas according to this dataset are located in the foothills of the Saharan mountains (Figure 1). The areas are associated with endorheic water systems like wadis opening to alluvial fans, sebkhas and chotts in arid regions providing sediments due to fluvial abrasion, that can be lifted by strong winds [e.g. *Middleton and Goudie*, 2001, *Prospero et al.*, 2002, *Mahowald et al.*, 2003, *Zender and Newman*, 2003, *Engelstaedter et al.*, 2006, *Schepanski et al.*, 2007]. Dried-out lake beds like the area of the paleo-lake Mega-Chad also provide fine sediments and can be efficient dust sources [*Goudie and Middleton*, 2001, *Prospero et al.*, 2002, *Mahowald et al.*, 2003]. The two years of MSG DSA data show the highest frequency of DSA occurring during local morning hours (Figure 2 and 3, Table 1), especially in the mountainous areas of the Sahara (Hoggar, Adrar, Air, Tibesti, Ennedi, Highlands of Ouaddai, Highlands of Abessinia, Red Sea Mountains).

Several synoptic situations can lead to DSA. In the following section, relations between observed DSAF and recurrent meteorological features able to explain the observed frequency will be discussed concerning the time-of-day. To initiate dust emission the friction velocity of the surface wind has to exceed a threshold depending on surface roughness length, soil structure and vegetation (*Marticorena and Bergametti*, 1995). Most DSA occur during local morning hours in the Sahara (65 % during 06-09 UTC, see Table 1), frequently connected to the pronounced diurnal cycle of LLJs and the break down of the nocturnal stably boundary layer (BL) due to momentum mixing downwards after sunrise [e.g. *Lenschow and Stankov*, 1979, *Hoxit*, 1975]. Dust source activations are also frequently forced by gust fronts associated with density currents generated by moist convection which is likely to occur predominantly in the local afternoon and evening (*Yang and Slingo*, 2001). Assuming that DSA related to moist convection mostly occurs between 12 and 00 UTC, the percentage of DSA occurring during that time period may indicate the importance of convective cloud processes (Figure 2). The percentage of DSA occurrence during 12-00 UTC is higher in the spring and summer seasons when convective cloud systems occur (up to 25 % in April 2006), associated with upper-level disturbances due to troughs or moist convection during the monsoon period. In areas where the break-down of the nocturnal LLJ plays a minor role for DSA, the percentage of 12-00 UTC DSA can be more than 50 % as it does for the Akhdra area. There, especially orographically induced clouds, upper-level disturbances and density currents due to evaporation processes lead to wind speeds exceeding the threshold for DSA in mountain areas like the Atlas during the afternoon and evening [*Knippertz et al.*, 2007, *Knippertz et al.*, 2009].

Figure 2 shows DSAF during 03-09 UTC representing the morning hours over the entire Saharan domain, and 12-00 UTC for the four seasons. DSA during the morning hours are mostly related to the break-down of the LLJ. This is the time when DSA occur most frequently during all seasons. A seasonal variability is evident as consequence of changing meteorological conditions. During winter (DJF), the Bodélé is the most frequently activated source area. Source activation is mainly during the morning hours by the break-down of the Bodélé-LLJ (more than 30 % of all days). In summer (JJA), the observed

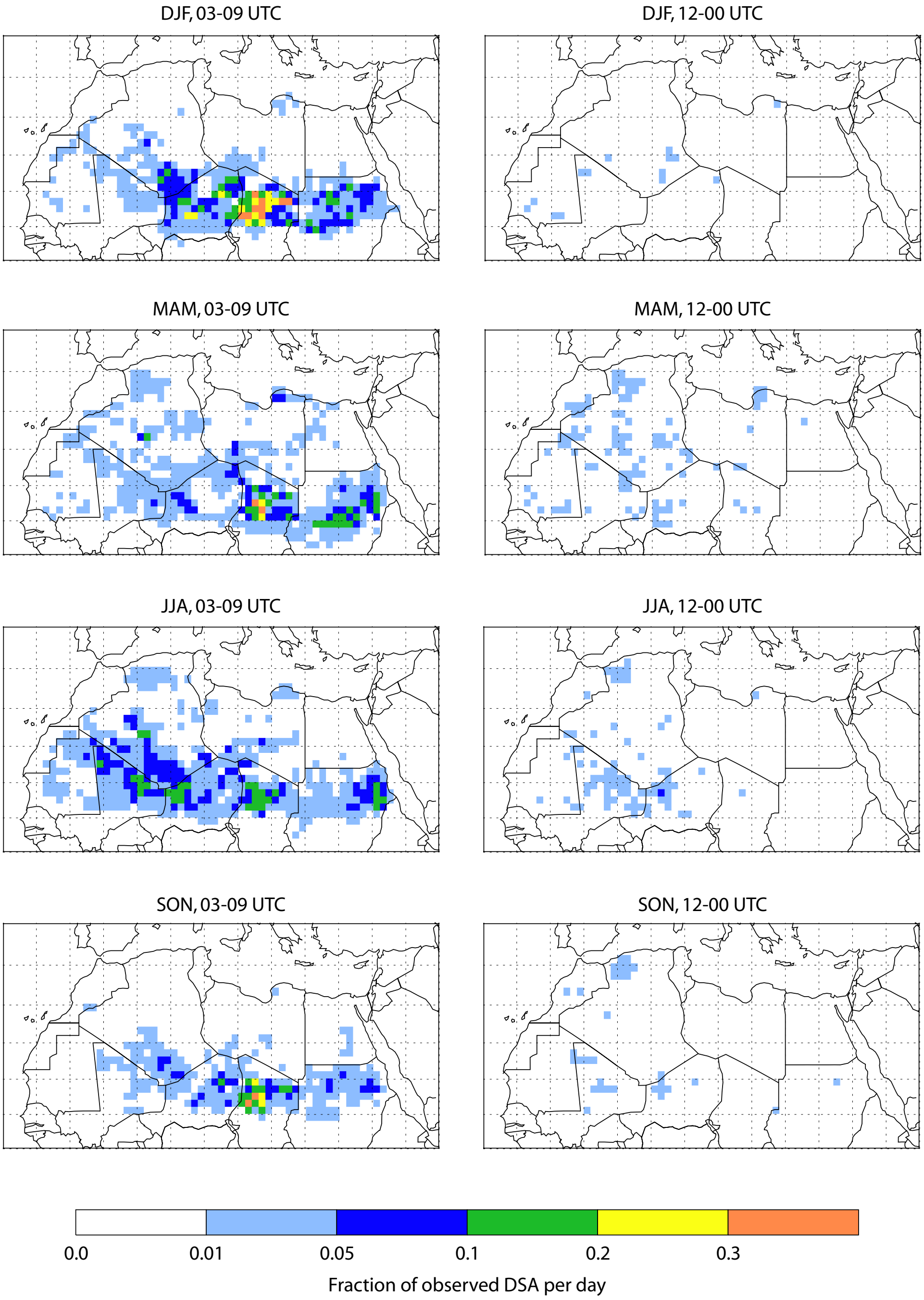

Figure 2: *Seasonal frequency of dust source activations (DSAFs) observed during 03-09 UTC (comprising local morning hours over the entire Saharan domain) (left column) and seasonal frequency of dust source activations observed during 12-00 UTC (right column). Morning time DSAs are mostly related to the break-down of the nocturnal LLJ. Afternoon to night DSAs are mostly related to convective events.*

frequency of morning DSA increases over the Western Sahara compared to winter (DJF) and autumn (SON) to frequencies up to 20 %. This is related to the West African Monsoon (WAM) circulation, which is identified to play a major role in forcing the nocturnal LLJ development over this area [e.g. *Parker et al.*, 2005, *Westphal et al.*, 1988]. During northern hemisphere summer the West African monsoon (WAM) plays an important role for regional low-tropospheric circulation pattern [e.g. *Parker et al.*, 2005]. The mean Saharan heat low has been shown to be a driver of the southwesterly monsoon flow over West Africa, transporting moisture from the Gulf of Guinea towards the Sahelian and South Saharan area. Furthermore, WAM provides moist air masses forcing deep moist convection with strong gusts able to mobilize dust (haboobs) [e.g. *Flamant et al.*, 2007]. During day time, convective turbulence within the boundary layer suppresses high wind speeds within the lower troposphere. Considering the diurnal cycle of lower tropospheric wind speeds, a minimum occurs during times when convective turbulence is evident [*Parker et al.*, 2005 and references therein]. During night, turbulence due to missing insolation ceases and a frictional decoupling of the near-surface air layer and the low-tropospheric air above develops. Then, the WAM flow accelerates and a low-level wind speed maximum occurs (LLJ). The DSAF observed during 12-00 UTC is low compared to frequencies observed during 03-09 UTC. Nevertheless, a season-to-season variability of DSAF of the 12-00 UTC time slot is evident, showing a strong relation to the occurrence of upper-level disturbances and the monsoon circulation.

Areas with similar topographic conditions and DSA behavior are compiled into nine main DSA areas (Figure 3 and 6). These are the Atlas Mountains (AT, 82 grid cells), Akhdar Mountains (AK, 15 grid cells), Western Sahara (WS, 156 grid cells), Air Mountains (AI, 72 grid cells), Adrar Mountains (AD, 28 grid cells), Bodélé depression (BO, 25 grid cells), Ouaddai Mountains (OU, 20 grid cells), Kordofan (KO, 21 grid cells) and the Red Sea and Nubian Mountains (NU, 28 grid cells). Note that the defined areas have different sizes. The DSAFs are not normalized to their size because of different distribution of local dust sources over the area. E.g. in the Bodélé depression area, all grid cells are able to be a dust source, which is not the case for the Atlas area. Each area is characterized by specific topographical and meteorological conditions and provides fine sediment due to geomorphological surface processes. Major DSA areas show typical seasonal and diurnal patterns (Figure 3). In Table 1, time-of-day and frequency of DSA for the different pre-defined areas are listed. The frequencies base on two years of observations, 2006/03-2008/02. In the following, the temporal DSA patterns are described in detail for the individual regions.

Atlas Mountains (AT)

The Atlas Mountains in northwestern Africa are situated like a barrier in the wind flow coming from the Atlantic ocean. Orographic clouds may develop during day time reaching maximum in the afternoon. This is also the case for lee-cyclones like the Sharav cyclone that develops especially in spring time. Both, orographic and baroclinic effects force strong surface wind speeds.

DSA in the Atlas area is most frequent during spring (Figure 3). Besides a minimum during winter, a second maximum occurs in autumn (September). Up to 30 % of the dust mobilization events occur during the afternoon (Table 1).

Time [UTC]	total*	AT	AK	WS	AI	AD	BO	OU	KO	NU
00-03	2 %	1 %	0 %	1 %	1 %	2 %	1 %	2 %	1 %	6 %
03-06	5 %	1 %	9 %	1 %	3 %	3 %	4 %	3 %	3 %	17 %
06-09	65 %	16 %	36 %	48 %	66 %	59 %	84 %	83 %	82 %	70 %
09-12	17 %	44 %	27 %	28 %	17 %	18 %	10 %	8 %	10 %	4 %
12-15	8 %	29 %	25 %	16 %	8 %	14 %	2 %	3 %	1 %	1 %
15-18	1 %	2 %	3 %	2 %	2 %	3 %	0 %	0 %	0 %	1 %
18-21	2 %	6 %	0 %	4 %	2 %	3 %	0 %	0 %	1 %	1 %
21-00	1 %	0 %	0 %	1 %	1 %	0 %	0 %	1 %	0 %	1 %

Table 1: *Temporal analysis of frequent DSA areas as defined in section 3.2.1: Frequency of DSA observed within a 3-hour period. Two-year period, 2006/03-2008/02. AT = Atlas, AK = Akhdra, WS = West Sahara, AI = Air, AD = Adrar, BO = Bodélé, OU = Ouaddai, KO = Kordofan, NU = Numbia.*
*total DSA observation area, northward of 5° N

Akhdar Mountains (AK)

The Akhdar Mountains located in the northeast of Libya with the Mediterranean Sea in the north and the Gulf of Sidra in the west are characterized by wadis and chotts on the Saharan side of the mountains. In the foothills on the Sahara side dust is most frequently activated during spring and early summer. Spring and early summer cyclones developing leeward of the Atlas track in eastward directions often cross the Libyan coast and cause strong wind speeds. Due to the thermal effect of insolation and heated surfaces, the development of cyclones occurs mostly during morning hours in the lee of the Atlas and reaches maximum during afternoon (*Trigo et al.*, 2002). Moving eastward, the cyclones cross the Akhdar domain mostly during afternoon to evening hours.

Beside DSA caused by cyclone activity, LLJs can develop and force high surface wind speeds in the vicinity of mountains situated parallel to the Mediterranean Sea but orthogonal to the coast to the Gulf of Sidra. As both processes are able to force DSA, time-of-day distribution of dust mobilization is variable, but morning hours (06-09 UTC) are dominant (Figure 3 and Table 1). The data shows a maximum occurrence of morning DSAs in winter and spring. However, as shown by the observations, the LLJ is not a very frequent phenomenon over the Akhdar area, indicated by relatively low total frequencies of occurrences (Figure 2).

Western Sahara (WS)

In the Western Sahara, Ergs and Hammadas as well as drainage systems and topographic gaps characterize the topography. DSA is most frequent during summer (Figure 3). In this season dust mobilization occurs at all times of the day, probably reflecting the occurrence of both a mean mid-morning peak in surface wind speeds associated with the downward mixing of the nocturnal LLJ and density currents associated with convective

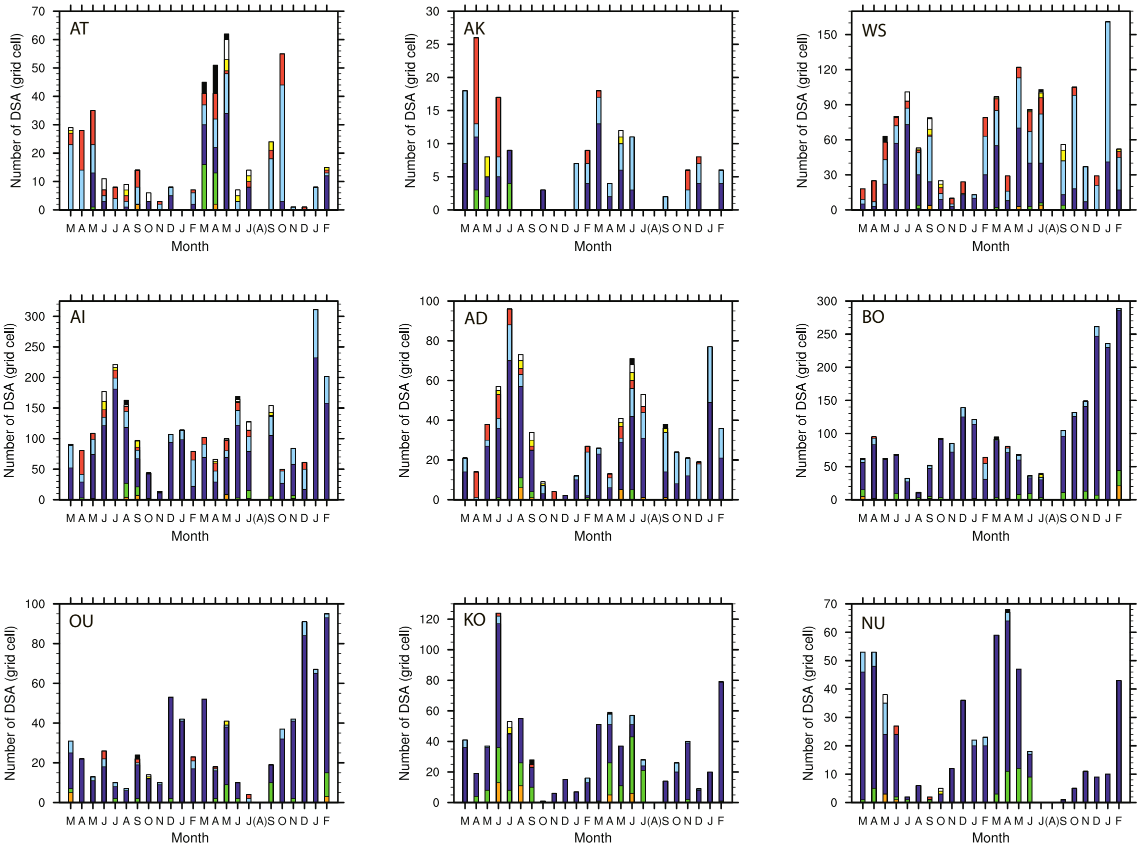

Figure 3: *Spatio-temporal analysis of the Saharan dust source activation distribution. Areas with high frequency of dust source activation (DSA) and characteristic topography or synoptic situations are analyzed concerning the DSA frequency and time of DSA. The Sahara is separated in the nine areas as shown in Figure 1. Orange: 00-03 UTC, light green: 03-06 UTC, blue: 06-09 UTC, light blue: 09-12 UTC, red: 12-15 UTC, yellow: 15-18 UTC, white: 18-21 UTC and black: 21-00 UTC.*

clouds, which tend to peak in the afternoon and evening. During the morning hours, DSAs are common in all seasons (Figure 3). During summer, a substantial proportion of DSA during local afternoon is observed, which point to DSA triggering deep convection, e.g. by density currents related to MSCs (Figure 3). As explained above, surface wind speeds peak in mid-morning when the LLJ momentum is mixed to the surface (*Parker et al.*, 2005) leading to DSA during morning hours in the vicinity of potential dust source areas.

Adrar Mountains and Air Mountains (AD and AI)

Both areas, Adrar and Air Mountains show similar temporal pattern of DSAF. DSAs are most frequent during local morning hours between 06 and 09 UTC in all seasons (up to 100 % of all DSA, see Figure 3). Comparing the strength of the seasonal cycle of DSAF over the area, the Adrar domain shows a more stressed cycle than the Air domain. For both areas the DSAFs are at a maximum during summer and a minimum during winter. For the rest of the year, the monthly distribution is more or less variable on a level above the autumn-minimum with a local maximum in winter and summer. During winter 2007/2008, a second maximum occurs related to generally high dust source activation frequency over the whole Sahara. The mountains are also affected by troughs and depressions crossing in winter and spring time as well as deep convection originating in the Sahel and moving north in summer. The down-mixing of the LLJ-momentum over potential dust source areas is a major cause for dust mobilization, in summer especially influenced by the WAM. However, down-bursts originating form deep moist convection also occur in summer, which play an important role for dust mobilization. However, the presence of sediments acting as dust sources are a necessary precondition.

Furthermore, the observations indicate a minimum of activity during autumn. For the rest of the year, the monthly distribution is more or less variable on a level above the autumn-minimum with a local maximum in winter and summer. This points towards the importance of the LLJ and the morning DSA respectively over this areas.

Bodélé Depression and Ouaddai Mountains (BO and OU)

The Bodélé is the single most active dust source area of the world [e.g. *Prospero et al.*, 2002] and characterized by a minimum activity during summer months. The LLJ is stronger and more frequent over the Bodélé than over any other location in North Africa (Figure 5-6 and 9). The Bodélé is surrounded by the Tibesti Mountains to the north, the Ennedi Mountains in the northeast and the Ouaddai Mountains in the east. The mountains evidently affect the general wind flow and accelerate the northeasterly LLJ by channeling and the Venturi effect, especially during winter months. *Todd et al.* (2008) estimate from model experiments that topography is responsible for up to 50 % of the peak LLJ wind speeds over the Bodélé. As the preconditions for wind acceleration due to channeling are often fulfilled, the LLJ develops frequently at night and forces high surface wind speeds the next day when turbulent mixing starts to mix momentum downward. Thus DSA in the Bodélé depression and the foothills of the adjacent mountains occurs very frequently after sunrise in the morning between 06 and 09 UTC (up to 85 %). During summer months, a minimum of DSAF occurs because of less frequent development of nocturnal LLJs (Figure 5 and Figure 9) and lower mean wind speeds (*Todd et al.*, 2008). This can be explained by the location of the inter-tropical discontinuity (ITD, conversion zone of the trade winds) related to weak geostrophic winds. Furthermore, during summer months wind direction is variable and topographic acceleration of air flow does not occur dominantly.

A strong seasonal cycle for DSA during the morning hours is observed (Figure 3, and Table 1) with a minimum in summer, especially in August. In addition, a strong amplitude between summer minimum and winter maximum is shown, pointing towards the importance of the LLJ in the seasonal cycle of DSA.

Kordofan (KO)

The topography of the Kordofan in the northern Sudan is mainly characterized by the mid-altitude Nubia Mountains with dense drainage likely to provide fluvial sediments. The hours between 03 and 09 UTC are again the most important time for DSA (see Figure 3

Time UTC	MAM $[m\ s^{-1}]$	JJA $[m\ s^{-1}]$	SON $[m\ s^{-1}]$	Annual $[m\ s^{-1}]$
00	E 6.7 (9.3)	E 6.7 (7.2)	E 5.7 (8.7)	E 6.2 (8.2)
03	E 6.7 (8.2)	E 6.7 (8.2)	E 5.7 (8.27)	E 8.2 (7.7)
06	E 6.2 (7.2)	E 6.45 (7.7)	E 5.1 (7.7)	E 5.7 (7.7)
09	E 9.3 (12.3)	SE 8.7 (11.3)	SE 6.95 (8.7)	E 8.7 (11.3)
12	W 6.7 (10.3)	E 9.8 (12.3)	E 7.7 (10.3)	E 8.2 (10.3)
15	W 11.05 (13.9)	E 8.7 (11.3)	NE 6.95 (10.8)	NE 6.7 (8.7)
18	W 7.95 (9.3)	E 9.0 (10.3)	NE 6.2 (9.8)	NE 6.2 (8.2)
21	NE 5.7 (6.2)	E 6.7 (7.7)	NE 5.1 (7.7)	E 5.1 (7.2)

Table 2: *Monthly median wind direction, median wind speed* $[ms^{-1}]$ *of wind direction and 75%-percentile of wind speed* $[ms^{-1}]$ *in parentheses, measured at Adrar (27°15'N; 2°31'E), 2006. MAM = March, April, May; JJA = June, July, August; SON = September, October, November. Wind directions: N = north, E = east, S = south, W = west.*

and Table 1), when solar heating starts and a convective BL develops which mixes down momentum of nocturnal LLJs (up to 100 % activation before 09 UTC). Note that local time here is UTC+2 hours, which explains the occurrence of DSA in the 03-06 UTC time slot. The DSAFs are lower during autumn and winter, higher in spring and summer (Figure 3).

Nubian Region (NU)

The area of high DSA in this region lies on the western foothills of the mountains, which separate the Nubian desert from the Red Sea. It is likely that sources of fine fluvial sediments are associated with wadis and endorheic drainage systems. Meteorological conditions force DSA mostly in spring and early summer. As for the Kordofan region to the south, the maximum DSAF occurs in the morning hours (up to 100 %) between 03 and 09 UTC (local time is UTC+2 hours). Again this indicates that the break-down of the nocturnal LLJ is the main mechanism to force DSA.

In general, dust source areas located in the western part of the Sahara are most active during summer months, in contrast to those in the eastern part of the Sahara which are most active during winter and spring months. A predominance of dust sources activated during the morning hours indicate the important role of the break-down of the nocturnal LLJ (e.g. Figure 2, 3 and Table 1). This points towards the important role of the LLJ for DSA over these areas. In seasons with weak or absent nocturnal LLJ development the percentage of DSAs occurring during morning shows a minimum. DSAs at noon and afternoon are often associated with gusts related to deep convection. Mainly in the Atlas Mountains gusts related to orographic influence, orographic clouds, and density currents force DSA in afternoon hours.

During winter (DJF) 2007/2008 DSAs occurred more frequently than during the same period 2006/2007. As DSA is mainly forced by atmospheric processes, detailed investigations of atmospheric conditions are necessary to explain this inter-annual variability and longer observation time series are required to decide whether the more recent high winter DSAFs constitute an unusual condition.

Time UTC	MAM $[m\ s^{-1}]$	JJA $[m\ s^{-1}]$	SON $[m\ s^{-1}]$	Annual $[m\ s^{-1}]$
00	SE 3.1 (4.1)	E 3.1 (4.6)	E 3.6 (5.1)	E 3.6 (7.2)
03	E 4.1 (5.7)	E 3.6 (6.7)	E 3.4 (5.7)	E 3.6 (8.2)
06	E 4.1 (7.2)	E 4.1 (6.7)	E 4.1 (6.2)	E 4.1 (8.7)
09	E 7.5 (9.3)	E 7.7 (9.8)	E 6.2 (7.7)	E 6.7 (11.3)
12	SE 5.1 (7.2)	SE 6.2 (7.2)	S 4.1 (6.7)	SE 5.1 (9.3)
15	NW 5.7 (7.2)	E 5.7 (7.7)	NW 4.1 (4.6)	NW 4.6 (8.7)
18	NW 5.1 (7.2)	E 6.2 (6.2)	S 3.6 (4.6)	NW 4.6 (8.2)
21	S 3.1 (3.6)	SE 3.1 (3.1)	SE 2.6 (3.1)	S 3.1 (5.1)

Table 3: *Monthly median wind direction, median wind speed $[m\ s^{-1}]$ of wind direction and 75%-percentile of wind speed $[m\ s^{-1}]$ in parentheses, easured at Tamanrasset (22° 47' N; 5° 31' E), 2006.*

4 LLJs and Surface Winds over North Africa

Occurrences of strong surface wind speeds are the main cause for dust mobilization. The predominance of satellite derived DSA during the morning hours (06-09 UTC) across the

North African domain are an indication that the diurnal phase-lag relationship of LLJ and surface winds is an important mechanism for dust emission in the region. To understand this further and the connection with strong surface wind speeds causing dust mobilization, observed surface station reports, regional model and ERA-40 reanalysis data were analyzed.

4.1 Wind Observations at Synoptic Stations

The observation of dust emission from remote sensing needs to be corroborated by ground measurements. Unfortunately, in the Sahara region the measurement network is sparse. Meteorological surface observation data are taken from the Integrated Surface Hourly (ISH) database (dataset 3505 (DSI 3505)), provided by the National Climatic Data Center (NCDC), Asheville, NC, USA. Here, quality-checked synoptic weather observations of surface wind speed and direction (3-hourly) from stations in the Sahara/Sahel sector are analyzed. Only stations with an acceptable number of observations for statistical consideration are chosen.

These surface wind speed measurements from meteorological stations can be used to test the occurrence of high wind speeds in the morning hours. Such direct observations provide a direct test of the diurnal cycle of local surface winds. Unfortunately, in this regions where dust emissions are observed, only few meteorological station data are available to provide information on long timescales. Results are shown for the stations Adrar (27°15' N; 2°31' E), Agadez (16°58' N; 7°59' E), Tamanrasset (22°47' N; 5°31' E), Gao (16°16' N; 0°03' W), Zinder (13°47' N; 8°59' E) and Faya-Largeau (17°56' N; 19°08' E), which have the most complete observation records. At other stations the numbers of observations at morning, especially between 06 and 12 UTC are too small to obtain meaningful results. Adrar is located westward of the Plateau de Tademait, Tamanrasset in the high Hoggar Mountains, Agadez in the southern foothills of the Air Mountains, Gao and Zinder in the Sahel/Savanna and Faya-Largeau in the North of the Bodélé depression (Figure 1). At some stations the suddenly increasing morning wind speeds are accompanied by a significant shift in wind directions. But at stations located in mountain areas close to mountain slopes, the wind direction may strongly be influenced by topography. However, all synoptic weather observation shown here indicate a significant increase in 10-m wind speeds during mid-morning hours (Tables 2-4 and Figure 4). At most stations the observed 10-m wind speed decreases during noon and afternoon due to BL development. The pattern of peaking wind speed occurs mostly after calm and clear sky nights, but also at stations with higher wind speeds during the night a morning increase in 10-m wind speed can be observed (e.g. Adrar) (Table 2, Figure 4).

Suddenly increasing surface wind speeds as well as shifting wind direction may be explained by down-mixing of momentum from aloft as provided by a nocturnal LLJ as explained in Section 2.1. Observations at 21, 00, 03 and 06 UTC might frequently indicate calm conditions in case of the nocturnal LLJ development. At 09 UTC, a significant increase in wind speed is observed due to break-down of nocturnal LLJ. At 12 UTC and later, the

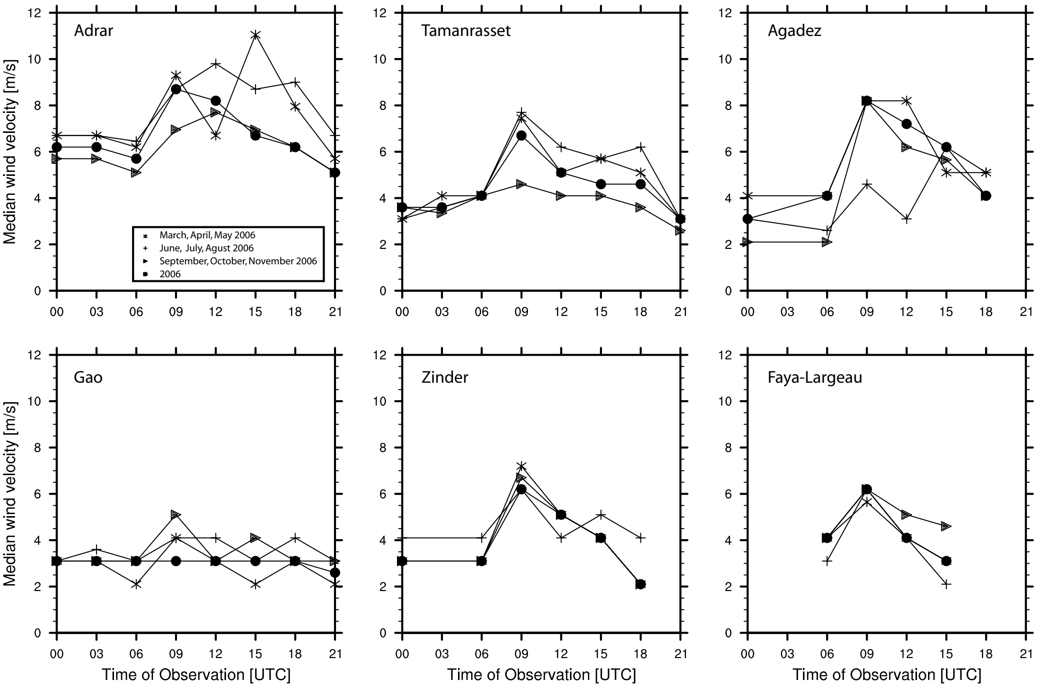

Figure 4: *Median wind speeds* [$m\ s^{-1}$] *for seasons MAM (March, April, May), JJA (June, July, August) and SON (September, October, November) 2006 at Adrar (27°15'N; 2°31'E), Tamanrasset (22°47'N; 5°31'E), Agadez (16°58'N; 7°59'E), Gao (16°16'N; 0°03'W), Zinder (13°47'N; 8°59'E) and Faya-Largeau (17°56'N; 19°08'E).*

wind moderates due to convective turbulence and the development of a deep, well mixed boundary layer. The observed variability during 24 hours are shown in Tables 2-4 as median wind speed and wind direction. The stations presented here are widely spread over the Sahara and Sahel sector. They indicate, that the break-down of the nocturnal LLJ, observed by increasing 10-m wind speeds, is a common phenomenon over North Africa and not limited to specific regions. The surface station data corroborate the explanation that nocturnal LLJ and its momentum down-mixing respectively are able to provide high wind speeds in a time period when DSA are observed frequently. However, this phenomenon is not ubiquitous in the Sahara region.

4.2 Large Scale Atmospheric Fields: ERA-40

To complete the impression of the LLJ feature given by the station data, the occurrence of LLJ has been analyzed from 10 years (1990-1999) of the 40 years global atmospheric ERA-40 reanalysis fields provided by ECMWF (*Uppala et al.*, 2005). The ERA-40 reanalysis data have a vertical resolution of 60 pressure levels up to 0.01 hPa and a horizontal resolution of 1° × 1° (T159). This analysis was conducted to (i) derive the spatial structure of LLJ frequency over the entire Sahara sector over an extended period of time, (ii) to determine the annual cycle of LLJ frequency for defined areas of frequent dust source activation observed by MSG (see Section 3.2.1) and (iii) to determine whether a global atmospheric model on a coarse horizontal and vertical resolution is able to reproduce the meteorological feature of the nocturnal LLJ. Reanalysis fields are commonly used to compute dust emission fields [e.g. *Laurent et al.*, 2008], therefore the presence of this feature in ERA 40 indicates to which extent ECMWF surface winds can represent the meteorological situation responsible for a large number of dust emission events in the Sahara. Information on the occurrence of LLJ phenomena for North Africa was derived from ERA-40 reanalysis data. Wind speed was obtained at 6 hourly intervals over the 10-year period 1990-1999 and the magnitude of the vertical wind shear calculated from wind speeds at 925 hPa and 770 hPa. The existence of a LLJ was then determined with respect to a threshold wind shear of 5 $m\ s^{-1}$. The threshold is chosen with respect to vertical wind profiles performed for several representative locations. While the vertical and temporal resolution of the ERA-40 data is not always sufficient to resolve the fine detail of LLJ features (*Todd et al.*, 2008) the data provide a good representation at the larger scale.

Time UTC	MAM $[m\ s^{-1}]$	JJA $[m\ s^{-1}]$	SON $[m\ s^{-1}]$	Annual $[m\ s^{-1}]$
00	E 4.1 (5.1)	E 3.1 (3.1)	E 2.1 (2.1)	E 3.1 (5.1)
06	E 4.1 (5.1)	NW 2.6 (2.1)	E 2.1 (2.1)	E 4.1 (7.2)
09	E 8.2 (11.8)	W 4.6 (5.1)	E 8.2 (8.7)	E 8.2 (11.8)
12	E 8.2 (8.7)	NW 3.1 (4.1)	E 6.2 (8.2)	E 7.2 (11.8)
15	E 5.1 (8.2)	SE 6.2 (6.2)	E 5.7 (7.2)	E 6.2 (9.8)
18	SE 5.1 (6.2)	SE 5.1 (6.2)	SE 4.1 (5.1)	SE 4.1 (8.2)

Table 4: *Monthly median wind direction, median wind speed* $[m\ s^{-1}]$ *of wind direction and 75%-percentile of wind speed* $[m\ s^{-1}]$ *in parentheses, easured at Agadez (16°58'N; 007°59'E), 2006.*

4.2.1 10-year LLJ Climatology

The mean frequency of nocturnal LLJs represented by the 06 UTC wind shear in ERA-40 data is shown in Figure 5. During the winter (Figure 5a) LLJs are widespread across the

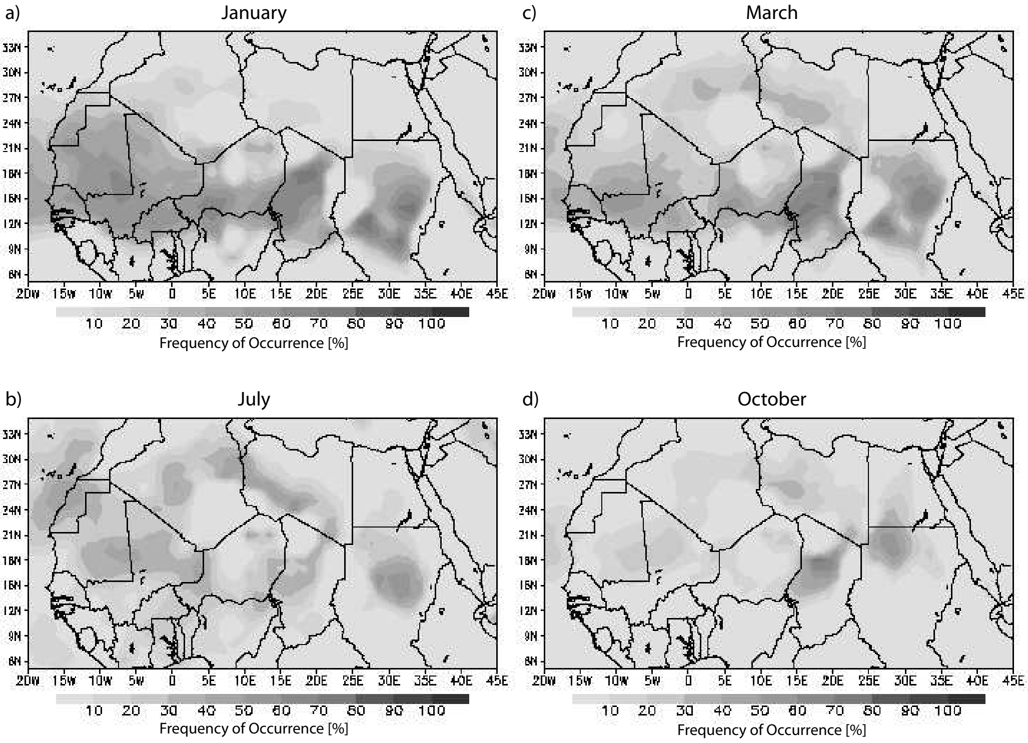

Figure 5: *ERA-40 climatology: Frequency of LLJ ($\Delta v \geq 5\ m\ s^{-1}$ between 925 hPa and 770 hPa p-level) during 10-year ERA-40 Reanalysis (1990-1999) at 06 UTC for January (a), March (b), July (c) and October (d).*

Sahel and southern Sahara occurring on 50 % of nights in a broad zone between 10-20° N extending almost the entire longitudinal extent of the continent. These LLJs occur within the mean northeasterly low level flow (the 'harmattan') which dominates North Africa in winter. LLJ frequency and magnitude is greatest where the large scale flow is influenced by topography, notably downwind of the Tibesti-Ennedi gap over the Bodélé depression of northern Chad, south of the Air Mountains in central Niger and to the west of the Ethiopian Highlands in eastern Sudan. During summer (Figure 5c) LLJ frequency is lower (by about 30-40 %) over the continent and the main axis shifts northwards such that the occurrence is focussed between about 15-30° N. This region encompasses the mean position of summer inter-tropical discontinuity, the divide between the dry northeasterly flow and the moist southwesterly monsoon flow. As such, nocturnal LLJ features occur in both circulations. Case studies of LLJs in both the northeasterly and southwesterly flow have been linked to dust emission [e.g. *Knippertz et al.*, 2009]. While it is clear that LLJs are enhanced close to regions of pronounced topography, it should be borne in mind that the results shown in Figure 5 are based on pressure level data, such that they do not represent the low level atmosphere over regions of high surface elevation. Satellite based datasets, however, indicate dust emission directly over mountain foothills, where wadis and drainage systems provide lot of fine, fluvial sediments [e.g. *Washington et al.*, 2003, *Schepanski et al.*, 2007].

ERA-40 10-yr LLJ for Defined Regions
In addition to the regional analysis of the DSAF, results of the seasonal cycle of LLJ occurrence in ERA-40 are shown for the individual areas in Figure 6. Over some areas, a weak seasonal cycle is shown by the ERA-40 analysis, e.g. the Atlas, and the Akhdra, whereby the observed DSAFs during the morning hours show a stronger season-to-season variability. The ERA-40 data show a mean of a 10-year period, so inter-annual variability in e.g. strength smooths the season-to-season variability. Generally, two different types of seasonal variability are evident following a semi-annual or an annual cycle. It depends on the seasonality of atmospheric circulation patterns forcing the LLJ development. Bodélé and the Ouaddai region for example show a strong winter maximum explained by a maximum frequency in LLJ development over that region. The Bodélé region itself shows the strongest impact of LLJ break-down for DSA by ERA-40 reanalysis and DSAF observations as well. Over the West Sahara, a second maximum during summer is evident, related to the forcing of the nocturnal LLJ development by the WAM. The Atlas and Akhdra region indicate the LLJ as a less important phenomenon shown by low occurrence frequencies retrieved from ERA-40 reanalysis (Figure 6) and the fraction of the morning time slot of the DSA observations (Figure 3).

Compared to the ERA-40 LLJ frequencies, the seasonal cycle of DSAF shows similar seasonal characteristics by the reanalysis data for most regions as summarized in Table 5. This points towards the important role of the LLJ for DSA over these areas. The ERA-40 data are based on pressure levels, such that the data might not be able to represent the low level atmosphere over high mountain regions which are dominant in this analyzed domain. LLJ occurrences from ERA might be underestimated by the global model due to smoothed topography and damped regional effects. To estimate the representation of the LLJ phenomenon within global scale models, more detailed studies have to be performed. Here, only the results of one global circulation model is presented and the results show promising similarities to regional modeling and observations. The ERA-40 reanalysis field indicate the importance of the LLJ feature over a 10-year period within the annual cycle. Furthermore it is shown, that a global general circulation model is able to capture such an important meteorological feature for DSA.

4.3 Regional Model LM-MUSCAT

In the following section the linkage of LLJ break-down and dust mobilization will be investigated using a regional-scale model in addition to the large-scale reanalysis. The role of LLJs in forcing DSA is tested by the regional dust emission and transport model LM-MUSCAT (*Heinold et al.*, 2007). The model consists of the meteorological regional

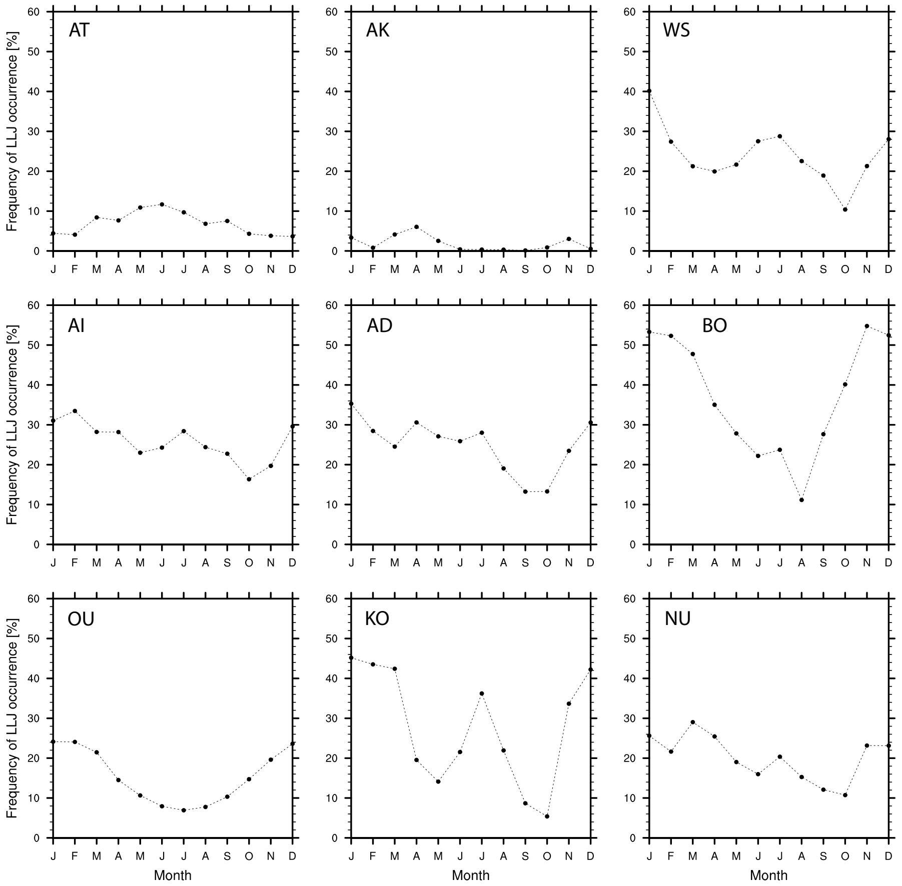

Figure 6: *Spatio-temporal analysis of the frequency of LLJ occurrence over the defined areas, based on ERA-40 reanalysis data (1990-1999). The areas are defined following high DSAF observations. The Sahara is separated in nine areas: Atlas Mountains (AT), Akhdar Mountains (AK), Western Sahara (WS), Air Mountains (AI), Adrar Mountains (AD), Bodéléle depression (BO), Ouaddai Mountains (OU), Kordofan (KO) and the Red Sea and Nubian Mountains (NU).*

model Lokal-Modell (LM) provided by the German Weather Service, Deutscher Wetterdienst (DWD) (*Steppler et al.*, 2003), and the MUlti-Scale Chemical Aerosol Transport Model (MUSCAT, *Wolke et al.* (2004b), *Wolke et al.* (2004a)), including a dust emission scheme based on work by *Tegen et al.* (2002). Dust emission, transport and deposition are simulated with MUSCAT using meteorological and hydrological fields that are computed by the LM and updated every advection time step comprising two LM time steps of 80 s. Local wind systems, clouds, precipitation, and meso-scale convection are simulated depending on topography. Sub-gridscale moist convection is parameterized following *Tiedtke* (1989). Soil erosion by wind mostly depends on the wind shear stress on the ground and occurs when the surface friction velocity increases above the threshold friction velocity, itself dependent on soil conditions of aerodynamic and smooth roughness length, dry soil size distribution. Dust emission fluxes are computed using LM surface winds and soil

	DSAF observations			10-year ERA-40			
Region	seasonality	max	min	seasonal cycle	max	min	LLJ
Atlas (AT)	annual	MAM	DJF	weak, annual	DJF	JJA	not domin.
Akhdra (AK)	annual	MAM	SON	weak, annual	MAM	JJA	not domin.
W-Sahara (WS)	semi-annual	JJA DJF	MAM SON	semi-annual	JJA DJF	MAM SON	important
Air (AI)	semi-annual	JJA DJF	SON	weak, semi-annual	JJA DJF	SON	important
Adrar (AD)	semi-annual	JJA DJF	SON	semi-annual	DJF JJA	SON	important
Bodélé (BO)	annual	DJF	JJA	annual	DJF	JJA	dominant
Ouaddai (OU)	annual	DJF	JJA	annual	DJF	JJA	dominant
Kordofan (KO)	annual	JJA	SON	semi-annual	DJF JJA	MAM SON	dominant
Numbia (NU)	annual	MAM	SON	annual	MAM	SON	important

Table 5: *Comparison of the seasonal variability of the ERA-40 10-year LLJ occurrence frequency and observed DSAFs for 2006/03-2008/02. See also Figures 3 and 6 for comparison. "Semi-annual" seasonal cycle indicates the presence of a secondary maximum in LLJ and/or DSAF, respectively. DJF = December, January, February, MAM = March, April, May, JJA = June, July, August, SON = September, October, November.*

moisture. In this study, dust emission in the model is only allowed in areas where dust source activation is observed on at least two days per year by the MSG-SEVIRI IR dust index during the observation period 2006/03-2007/02. Mobilized dust is transported as passive tracer in five independent size classes with radius limits at 0.1 μm, 0.3 μm, 0.9 μm, 2.6 μm, 8 μm, and 24 μm [*Heinold et al.*, 2007, *Heinold et al.*, 2009].

The model simulations were performed for an area covering the area 0.2° N - 32.3° W; 41.3° N - 33.3° E with a horizontal resolution of 28 km and 40 vertical layers. For analyzing meteorological conditions able to force dust mobilization, three case studies in different seasons have been computed: March 2006, July 2006, 20 December 2006 - 20 January 2007 (hereafter January 2007).

4.3.1 Linkage of LLJ Occurrence and Dust Mobilization: Regional Modeling Study

First, the ability of high surface wind speeds related to the break-down of the LLJ for dust mobilization will be discussed presenting an exemplary case study using the model system LM-MUSCAT. Furthermore, the median first-layer wind speed at days with modeled LLJ development and days without modeled LLJs will be compared to the medians of measured 10-m wind speeds (Figure 8). Then, the frequency of LLJ occurrence during the morning (06 UTC) retrieved from vertical wind shear simulated by the regional model

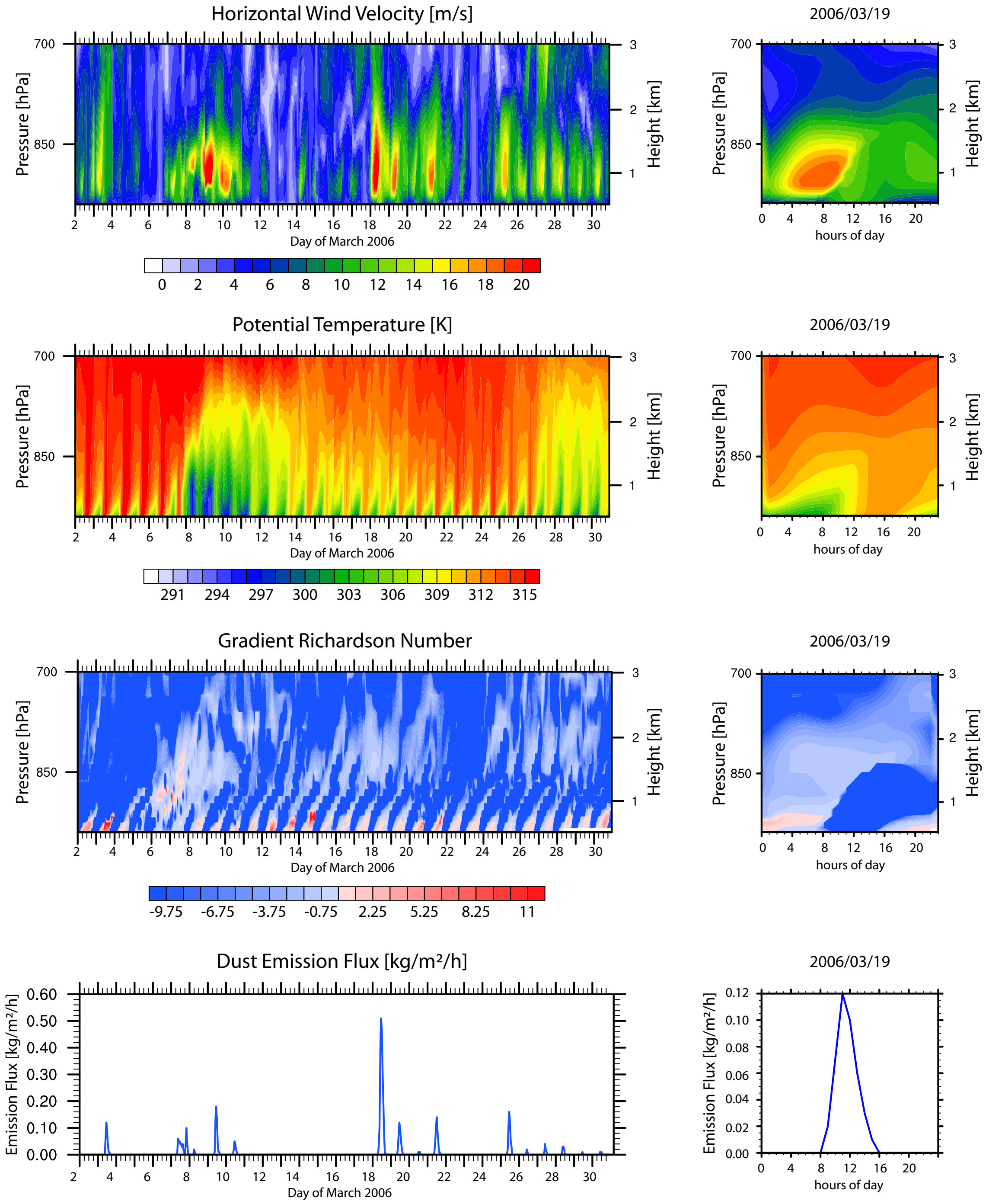

Figure 7: *Modeled time series of the vertical distribution of horizontal wind speed* $[m\ s^{-1}]$*, potential temperature [K], Richardson Number and dust emission flux* $[kg/m^2/h]$ *at Agadez (16° 58' N; 7° 59' E) for the month March 2006 (left) and exemplary for the 19 March 2006 (right).*

are shown.

Secondly, the model is used to investigate the connection between DSA during morning

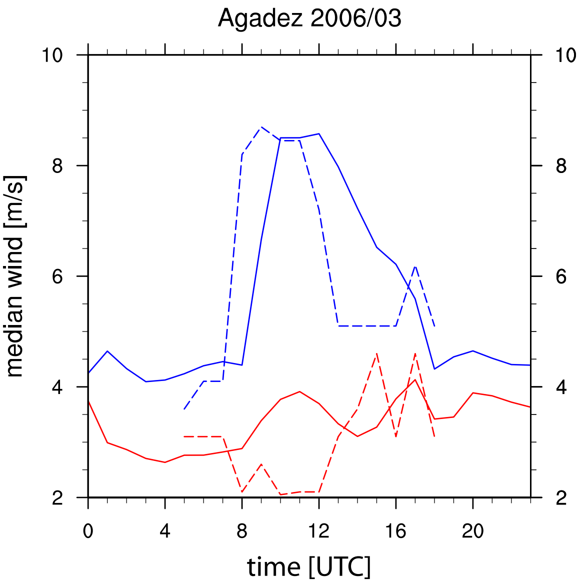

Figure 8: *Median wind speed for March 2006 at Agadez (16°58'N; 7°59'E). Solid lines show first layer wind simulations by the LM-MUSCAT, dashed lines synoptic observations of 10-m winds. Based on the occurrence of low-level wind speed maxima shown in Figure 7, days are separated in LLJ-days (blue) and days without LLJ development (red).*

hours and the occurrence of nocturnal LLJ over the Sahara. This is to show the extent to which the model is able to reproduce the LLJ feature related to morning time dust emission. To show the relation between LLJ occurrence and dust emission, vertical distribution of horizontal wind, potential temperature, gradient Richardson number and the surface dust emission flux is presented exemplary for Agadez for March 2006 (Figure 7). As indicated by Figure 7 (right side) for a 24-hour period, vertical and horizontal wind speed distribution show decreasing horizontal surface wind speeds during night but increasing wind speed at around 1 km height. In the early morning hours, high wind speeds from aloft propagate down and increase surface wind speeds (Figure 7). If the wind speed exceeds local threshold wind speed for dust mobilization dust emission depending on wind velocity occurs since the area is marked as potential dust source area. During day time, a well mixed boundary layer develops: Wind and potential temperature are well mixed within this layer. In contrast, at nighttime only a shallow nocturnal boundary layer (NBL) develops under stratified air layers characterized by vertical wind speed and potential temperature gradients (Figure 7).

Down-mixing of momentum as indicated by downward propagation of higher wind speeds is forced by turbulent mixing starting with solar heating after sunrise. Besides the vertical distribution of horizontal wind speed and potential temperature, the gradient Richardson Number Ri is an indicator for turbulent processes (*Reiter and Lester*, 1968) and is assumed for $Ri \leq Ri_c$. Turbulence might occur for $Ri_c = 1$, in weakly stratified layers for $Ri_c = 0.25$ [e.g. *Sorbjan*, 2006]. The Ri-Number is positive at night, when convective turbulence ceases due to missing insolation. The layer of positive Ri-Number grows from the near-surface layer, caused by stratification mainly due to radiative cooling. However, turbulent mixing processes are suppressed by the static stable layer, indicated by significant vertical potential temperature gradient as well as low wind speed. Furthermore, wind speeds within the lowest layers near the surface decrease after sunset and reach minimum before midnight. During the second half of the night, katabatic winds might disrupt the static stability and the surface wind speeds increase intermittently. Due to radiative cooling, a layer of cold and stratified air is built up reaching maximum depth shortly before dawn. Both vertical distributions of wind speed and potential temperature indicate the possibility of turbulence. Low surface wind speeds influence the magnitude of radiative cooling, which is strongest during calm, cloud-free nights. High vertical potential temperature gradients and low wind speeds suppressing vertical mixing and therefore turbulence, are indicated by positive Ri-Numbers. As shown in Figure 7, the vertical temperature gradients decrease with dawn, turbulence increases with decreasing Ri-Numbers and momentum is mixed down. During daytime, convective turbulence due to solar heating occurs and a well mixed BL develops and in case of dust mobilization, the particles will be mixed up. Accordingly, Ri-Number values remain negative indicating turbulence. For the March period in 2006 shown in Figure 7, periods of frequent nocturnal LLJ development and related dust emission during the next day and calm periods alter irregularly, reflecting the actual regional weather regime. The right column of Figure 7 presents a 24-hour period of a LLJ-day showing the above discussed relations between vertical distribution and evolution of horizontal wind speed, potential temperature, gradient Richardson number and dust emission flux. Thereby, the time of starting LLJ break-down (indicated by increasing first layer wind speeds and negative gradient Richardson numbers), coincides with dust emission (around 08 UTC on 19 March 2006). However, a good agreement between the occurrence of LLJs and dust emission during the day is evident, again showing the importance of the LLJ for dust emission.

The different time-of-day distribution of near-surface (first-layer, around 33 m above ground level (agl)) wind speeds on days with LLJ development (LLJ-days) and days without LLJ development is evident in the median wind speed distribution for both modeling results and synoptic observations (Figure 8) shown at Agadez. LLJ-days are identified by the occurrence of low-level wind speed maxima simulated by the LM-MUSCAT model (see Figure 7). We do not compare directly the modeled 10-m winds with the observations, as with a model grid resolution of 28 km perfect agreement cannot be expected in a mountainous region. On LLJ-days, the wind speed increases suddenly at around 08 UTC and decreases during the afternoon hours. During night, the wind speeds are lower than the threshold for dust emission (see Figure 7). Differences between model results and synoptic observations are evident due to sparse observations between the main observation times (00, 06, 12, 18 UTC), the height difference between 10-m wind measurements and model results given for the first model layer. On days without LLJ development, both model results and observations indicate low wind speeds. The temporal changes in wind speeds on LLJ-days and days without LLJ development indicate differences able to identify the break-down of the LLJ during the morning hours as main driver for dust emission (Figure 7 and 8).

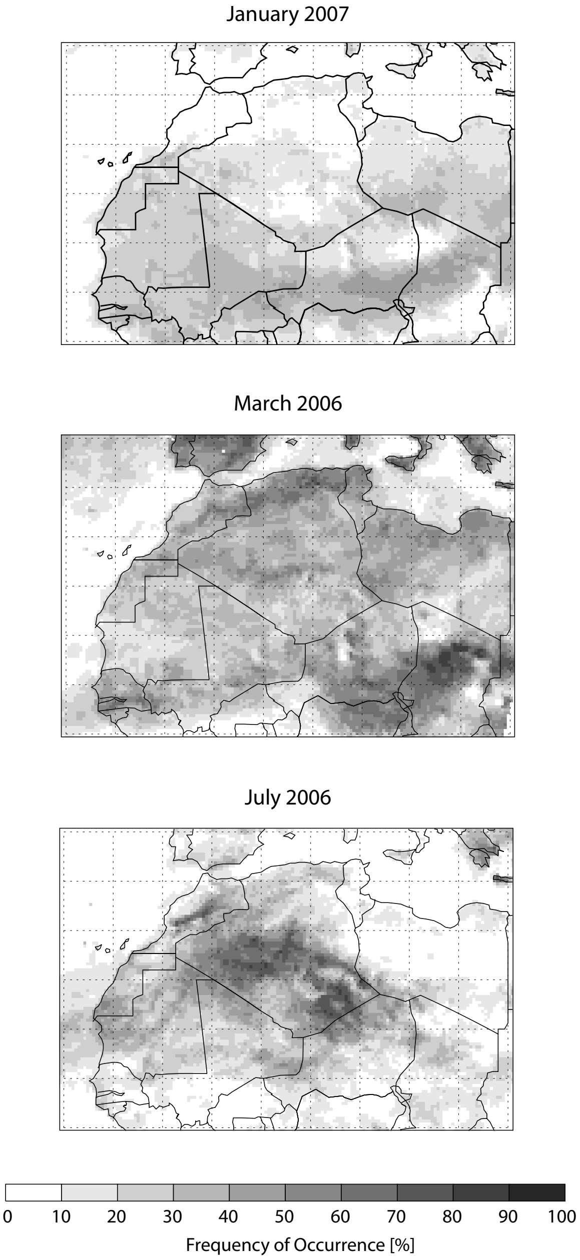

Figure 9: *Frequency [%] of LLJ ($\Delta v \geq 5\ m\ s^{-1}$ between level 60 m agl and 1000 m agl) occurrence at 06 UTC for January 2007, March 2006 and July 2006.*

As shown by the MSG DSA observations, the occurrence of nocturnal LLJs and their morning break-down plays an important role for generating wind speeds that exceed threshold for dust mobilization. To put these results in regional context, the local nocturnal LLJ occurrence frequency in the regional model is computed for the Sahara for different months (Figure 9). Nocturnal LLJ conditions are assumed if the wind speed difference $\Delta\ v$ between 60 m agl and wind speed at 1000 m agl exceeds 5 $m\ s^{-1}$. The threshold of

$5\ m\ s^{-1}$ for $\Delta\ v$ is empirically obtained by analyzing vertical profiles and allows to capture most of the LLJs. Single cyclonic disturbances over the Atlas and especially over the Mediterranean Sea and Southern Europe can also fulfill the conditions indicating LLJs due to their vertical wind speed profile. In Figure 9, the frequency of LLJ occurrence ($\Delta\ v\ \geq\ 5\ m\ s^{-1}$) at 06 UTC is shown for atmospheric winter conditions in January 2007 (2006/12/20 - 2007/01/20), for March 2006 representing atmospheric spring conditions and for July 2006 representing atmospheric summer conditions. The distribution as well as the frequency of LLJ occurrence change with season. During winter and spring, the Bodélé depression is characterized by a very high frequency of LLJ occurrence (up to 80 % and more). In January, a band-like pattern of high frequencies (over 75 %) occurs over the Sahel and South Sahara, which is the area where the LLJ is the most dominant. Further more north, the gap between the Tassili of Ajjer (directly north to the Hoggar) and the Tibesti shows high LLJ frequencies as well (up to 80 %). Beside the Saharan 'highlands', LLJs over the Ergs in the Western Sahara occur with a moderate frequency around 50-60 %. Over the Atlas and north Algeria, the LLJ frequency is low, mostly lower than 10 %. In spring, beside the dominant LLJ feature over the Bodélé depression, additional areas characterized by high frequencies of nocturnal LLJ occurrence are the Highlands of Chotts between the Tell-Atlas and the Saharan Atlas with frequencies between 60-70 % as well as the Akhadrar Mountains (around 50 %). Further south, the foothills of the Hoggar Mountains and the sebkhas westward of it show a local maximum of LLJ with frequencies around 40 %. While the areas of high nocturnal LLJ occurrence frequencies in March 2006 are mainly the Bodélé depression, the Highlands of Chotts, the Akhdrar Mountains and the foothills and sebkhas west of the Hoggar, in July 2006 the areas of high frequencies are mainly the Anti-Atlas (up 80 %) and the central and south Algerian mountains (up to 80 %).

Both the major patterns of high frequency in January 2007 and March 2006 computed with the regional model agree well with the 10-year climatology derived from the global atmospheric ERA-40 reanalysis fields (Figure 5). Thereby, agreements but also differences are evident. In July, the pattern of high LLJ occurrence frequencies do not agree in most areas for the regional model results and the reanalysis fields. The regional model LM-MUSCAT shows frequent LLJ occurrences over the Algeria, mainly over areas dominated by mountains (Hoggar, Air) and Algerian Ergs as well as over the Moroccan Atlas. In contrast, the ERA-40 reanalysis shows high LLJ frequencies around the Algerian mountains and over the Western Sahara during WAM period. Regional and global models are used to demonstrate, that both are able to reproduce such an important meteorological feature for dust emission as the LLJ with an acceptable agreement concerning seasonal changes and frequencies compared to satellite based observations. Differences between regional and global field are e.g. related to different horizontal and vertical resolutions and thereby to different representations of sub-grid scale features and topography.

5 Conclusion

This study presents the first comprehensive study of the diurnal characteristics of dust storm activation, based on a new dataset derived from MSG SEVIRI satellite data. Not only the temporal resolution of the SEVIRI data ensures that the DSAF dataset resolves the diurnal cycle of dust, but it allows back-tracking of dust plumes directly to source regions. In this way the DSAF is much more closely related to processes of dust emission than other satellite datasets, which provide some estimate of column integrated dust burden. The results here show that dust source activation in the Sahara is most commonly observed in the local early morning hours after sunrise. Such a condition can be explained by to the first order phase-lagged relationship between the nocturnal LLJ and surface winds. The downward mixing of nocturnal LLJs by turbulent mixing of momentum after sunrise leads to peak surface wind speeds and dust emission in the hours after sunrise. We can infer that this may be a dominant mechanism for DSA in the Sahara. The arid and stable climate over the Saharan desert provide preconditions for the development of nocturnal LLJs, which are a widespread phenomenon across the region.

Case study analysis with the LM-MUSCAT model (see Section 4.3.1) indicates that large scale dust storms are generally associated with synoptic scale variability resulting in large scale forcing of wind speeds. As such, it is the combination of the mean diurnal cycle in low level and surface winds with the day-to-day synoptic scale variability that explains much of the variability at diurnal timescales.

Of course there are many other meteorological conditions that lead to dust emission and some of these have been highlighted by the analysis of DSA. These include (i) down-bursts associated to moist convective dynamics during the monsoon period, (ii) orographic forced gusts due to orographic clouds and blocking situations, and (iii) cyclonic activity (mainly the Sharav cyclones during spring time over North Africa).

The DSAF dataset of the Sahara based on 15-minute MSG IR dust index retrievals is used to show the spatial and temporal distribution of DSA over the period of two years. During local morning hours, DSA in the foothills of the Saharan mountain areas occur most frequently (65 % between 06 and 09 UTC). For these cases, DSA is related to the break-down of the nocturnal LLJ as shown by measurements and model studies. Consequently, the foothills of the Saharan mountains are well suited as dust sources as they contain fine sediments due to fluvial erosion processes and by the frequently occurrence of high surface wind speed due to the break-down of nocturnal LLJ.

To test whether the break-down of the nocturnal LLJs is reproduced by a model, simulations with the LM-MUSCAT were performed leading to satisfying results. A comparison to a 10-year (1990-1999) climatology of ERA-40 reanalysis fields shows good agreements of the main pattern with high LLJ occurrence frequencies for winter (January) and spring (March), but shows differences for summer (July) especially over west Africa and high elevation surfaces. The differences over west Africa for the LM-MUSCAT are also evident in comparison to the MSG-SEVIRI DSAF observations, which show 48 % of the DSA during morning hours. For a comprehensive understanding of these differences, detailed investigations on summer meteorological conditions, especially in context of the WAM,

remain necessary.
The MSG-based analysis of DSAF gives only information on the frequency, not on the strength of such sources. While the LLJ lead to frequent occurrences of dust mobilization, the dust fluxes from these events are possibly smaller than those caused by convective activities. To clarify the role of LLJ for total dust emission fluxes, quantitative dust retrievals over desert surface will be needed.
Furthermore, the statistical analysis of DSAF shows a clear inter-annual variability. To explain this variability, longer time series and detailed investigations concerning inter-annual variability of major atmospheric conditions will be performed in the future.

ACKNOWLEDGMENTS
We thank the Deutscher Wetterdienst (DWD) for good cooperation and support. We also thank the U.S. Geological Survey's Earth Resources Observation and Science (EROS) data center for providing GTOPO30 digital elevation data set, available at http://www.edc.usgs.gov. Furthermore, we thank two anonymous reviewers for their helpful suggestions to improve the manuscript.

References

Alpert, P., and B. Ziv (1989), The sharav cyclone - observations and some theoretical considerations, *J. Geophys. Res.*, *94*, 18,495–18,514.

Alpert, P., B. I. Neeman, and Y. Shay-el (1990), Climatological analysis of Mediterranean cyclones using ECMWF data, *Tellus*, *42A*, 65–77.

Banta, R., Y. L. Pichugina, and R. K. Newsom (2003), Realtionship between Low-Level Jet Properties and Turbulence Kinetic Energy in the Nocturnal Stable Boundary Layer, *J. Atmos. Sci.*, *60*, 2549–2555.

Banta, R. M., R. K. Newsom, J. K. Lundquist, Y. L. Pichugina, R. L. Coulter, and L. J. Mahrt (2002), Nocturnal low-level jet characteristics over Kansas during CASES-99, *Bound.-Layer Meteor.*, *105*, 221–252.

Banta, R. M., Y. L. Pichugina, and W. A. Brewer (2006), Turbulent Velocity-Variance Profiles in the Stable Boundary Layer Generated by a Nocturnal Low-Level Jet, *J. Atmos. Sci.*, *63*, 2700–2719.

Barkan, J., P. Alpert, H. Kutiel, and P. Kishcha (2005), Synoptics of dust transportation day from Africa toward Italy and central Europe, *J. Geophys. Res.*, *110*, D07,208, doi: 10.1029/2004JD005222.

Blackadar, A. K. (1957), Boundary Layer Wind Maxima and Their Significance for the Growth of Nocturnal Inversion, *Bull. Amer. Meteor. Soc.*, *38*(5), 283–290.

Bou Karam, D., C. Flamant, P. Knippertz, O. Reitebuch, J. Pelon, M. Chong, and A. Dabas (2008), Dust emission over the Sahel associated with the West African Monsoon inter-tropical discontinuity region: a representative case study, *Quart. J. R. Met. Soc.*, *134*(632), 621–634, doi:10.1002/qj.244.

Brooks, N., and M. Legrand (2000), Dust variability over northern Africa and rainfall in the Sahel, in *Linking Climate Change to Landsurface Change*, edited by S. J. McLaren and D. Kniveton, pp. 1–25, Kluwer Academic Publishers, Dordecht, The Netherlands.

Charba, J. (1974), Application of Gravity Current Model to Analysis of Suall-Line Gust Front, *Mon. Wea. Rev.*, *102*, 140–156.

Claquin, T., M. Schulz, and Y. J. Balkanski (1999), Modeling the mineralogy of atmospheric dust sources, *J. Geophys. Res.*, *104*(D18), 22,243–22,256.

Davis, P. A. (2000), Development and mechanisms of the nocturnal jet, *Meteorol. Appl.*, *7*(3), 239–246.

Dayan, U., J. Heffter, J. Miller, and G. Gutman (1991), Dust Intrusion into the Mediterranean Basin, *J. Appl. Meteor.*, *30*, 1185–1199.

Droegemeier, K. K., and R. B. Wilhelmso (1987), Numerical Simulation of Thunderstom Outflow Dynamics. Part I: Outflow Sensitivity Experiments and Turbulence Dynamics, *J. Atmos. Sci.*, *44*(8), 1180–1210.

Egger, J., P. Alpert, A. Tafferner, and B. Ziv (1995), Numerical experiments on the genesis of Sharav cyclones: idealized simulations, *Tellus*, *47A*(2), 162–174.

Engelstaedter, S., I. Tegen, and R. Washington (2006), North African dust emission and transport, *Earth-Science Reviews*, *79*, 73–100, doi:10.1016/j.erscirev.2006.06.004.

Flamant, C., J.-P. Chaboureau, D. J. Parker, C. M. Taylor, J.-P. Cammas, O. Bock, F. Timouk, and J. Pelon (2007), Airborne observations of the impact of a convective system on the planetary boundary layer thermodynamics and aerosol distsribution in the inter-tropical discontinuity region of the West African Monsoon, *Quart. J. R. Met. Soc.*, *133*, 1175–1189, doi:10.1002/qj.97.

Fung, I., S. Meyn, I. Tegen, S. C. Doney, J. John, and J. K. B. Bishop (2000), Iron supply and demond in the upper ocean, *Global Biogeochem. Cycles*, *14*, 281–296.

Garratt, J. R. (1992), *The atmospheric boundary layer*, Cambridge University Press.

Ginoux, P., M. Chin, I. Tegen, J. M. Prospero, B. Holben, O. Dubovik, and S.-J. Lin (2001), Sources and distributions of dust aerosols simulated with the GOCART model, *J. Geophys. Res.*, *106*(D17), 20,255–20,273.

Goudie, A. S., and N. J. Middleton (2001), Saharan dust storms: nature and consequences, *Earth-Science Rev.*, *56*, 179–204.

Heinold, B., J. Helmert, O. Hellmuth, R. Wolke, A. Ansmann, B. Marticorena, B. Laurent, and I. Tegen (2007), Regional Modeling of Saharan Dust Events using LM-MUSCAT: Model Description and Case Studies, *J. Geophys. Res.*, *112*, D11,204, doi: 10.1029/2006JD007443.

Heinold, B., , I. Tegen, M. Esselborn, K. Kandler, P. Knippertz, D. Müller, A. Schladitz, M. Tesche, B. Weinzierl, A. Ansmann, D. Althausen, B. Laurent, A. Massling, T. Müller, A. Petzhold, K. Schepanski, and A. Wiedensohler (2009), Regional Saharan Dust Modelling during the SAMUM 2006 Campaign, *Tellus*, *61B*(1), doi:10.1111/j.1600-0889.2008.00387.x.

Herman, J. R., P. K. Bhartia, O. Torres, C. Hsu, C. Seftor, and E. Celarier (1997), Global distribution of UV-absorbing aerosols from Nimbus 7/TOMS data, *J. Geophys. Res.*, *102*(D14), 16,922–16,922.

Holton, J. R. (1967), The diurnal boundary layer wind oscillation above sloping terrain, *Tellus*, *19*(2), 199–205.

Horvath, K., L. Fita, R. Romero, and B. Ivančan-Picek (2006), A numerical study of the first phase of a deep Mediterranean cyclone: Cyclogenesis in the lee of the Atlas Mountains, *Meteor. Z.*, *15*(2), 133–146, doi:10.1127/0941-2948/2006/0113.

Hoxit, L. R. (1975), Diurnal Variations in Planetary Boundary-Layer Winds over Land, *Bound.-Layer Meteor.*, *8*, 21–38.

Hsu, N. C., S. C. Tsay, M. D. King, and J. R. Herman (2004), Aerosol Properties Over Bright-Reflecting Source Regions, *IEEE Trans. Geosci. Remote Sens.*, *42*(3), 557–569.

Idso, S. B., R. S. Ingram, and J. M. Pritchard (1972), An American Haboob, *Bull. Amer. Meteor. Soc.*, *53*(10), 930–935.

IPCC (2007), *Climate Change 2007: The Physical Science Basis.*, Contribution of Working Group I to the Forth Assessment Report of the Intergovernmental Panel on Climate Change, edited by S. Solomon and D. Quin and M. Manning and Z. Chen and M. Marquis and K.B. Averyt and M. Tignor and H.L. Miller, Cambridge, United Kingdom and New York, NY, USA.

Jickells, T. D., Z. S. An, K. K. Andersen, A. R. Baker, G. Bergametti, N. Brooks, J. J. Cao, P. W. Boyd, R. A. Duce, K. A. Hunter, H. Kawahata, N. Kubilay, J. LaRoche, P. S. Liss, N. Mahowald, J. M. Prospero, A. J. Ridgwell, I. Tegen, and R. Torres (2005), Global Iron Connections Between Desert Dust, Ocean Biogeochemistry, and Climate, *Science*, *308*(5718), 67–71.

Knippertz, P., and J. E. Martin (2005), Tropical plumes and extreme precipitation in subtropical and tropical West Africa, *Quart. J. R. Met. Soc.*, *112*, 2337–2776.

Knippertz, P., C. Deutscher, K. Kandler, K. Müller, T. Schulz, and L. Schütz (2007), Dust mobilization due to density currents in the atlas region: Observations from the SAMUM 2006 field campaign, *J. Geophys. Res.*, *112*, D21,109, doi:10.1029/2007JG008774.

Knippertz, P., A. Ansmann, D. Althausen, D. Müller, M. Tesche, E. Bierwirth, T. Dinter, T. Müller, W. von Hoyningen-Huene, K. Schepanski, M. Wendisch, B. Heinold, K. Kandler, A. Petzold, L. Schütz, and I. Tegen (2009), Dust Mobilization and Transport in the Northern Sahara during SAMUM 2006 - A Meteorological Overview, *Tellus*, *61B*(1), doi:10.1111/j.1600-0889.2008.00380.x.

Kraus, H. J., J. Malcher, and E. Schaller (1985), Nocturnal low-level jet during PUKK, *Bound.-Layer Meteor.*, *38*, 1–22.

Laurent, B., B. Marticorena, G. Bergametti, J. F. Léon, and N. M. Mahowald (2008), Modeling mineral dust emissions from the Sahara desert using new surface properties and soil database, *J. Geophys. Res.*, *113*, D14,218, doi:10.1029/2007JD00948.

Lenschow, D. H., and B. Stankov (1979), The Rapid Morning Boundary-Layer Transition, *J. Atmos. Sci.*, *36*, 2108–2124.

Mahowald, N., R. G. Bryant, J. del Corral, and L. Steinberger (2003), Ephemeral lakes and desert dust sources, *Geophys. Res. Lett.*, *30*(2), 1074, doi:10.1029/2002GL016041.

Mahowald, N. M., A. R. Baker, G. Bergametti, N. Brooks, R. A. Duce, T. D. Jickells, N. Kubilay, J. M. Prospero, and I. Tegen (2005), Atmospheric global dust cycle and iron inputs to the ocean, *Global Biogeochem. Cycles*, *19*, GB4025, doi:10.1029/2004GB002402.

Mahrt, L. (1999), Stratified Atmospheric Boundary Layers, *Bound.-Layer Meteor.*, *90*, 375–396.

Marticorena, B., and G. Bergametti (1995), Modeling the atmospheric dust cycle: 1. Design of a soil-derived dust emission scheme, *J. Geophys. Res.*, *100*(D8), 16,415–16,430.

Mauritsen, T., and G. Svensson (2007), Observations of Stably Stratified Shear-Driven Atmospheric Turbulence at Low and High Richardson Numbers, *J. Atmos. Sci.*, *64*(2), 645–655, doi:10.1175/JAS3856.1.

May, P. T. (1995), The Australian nocturnal jet and diurnal variations of boundary-layer winds over Mt. Isa in north-eastern Australia, *Quart. J. R. Met. Soc.*, *121*, 987–1003.

Middleton, N. J., and A. S. Goudie (2001), Saharan dust: sources and trajectories, *Trans. Inst. Br. Geogr.*, *26*, 165–181.

Miller, R., and I. Tegen (1999), Radiative Forcing of a Tropical Direct Circulation by Soil Dust Aerosols, *J. Atmos. Sci.*, *56*, 2403–3433.

Milton, S. F., G. Greed, M. E. Brooks, J. Haywood, B. Johnson, R. P. Allan, A. Slingo, and W. M. F. Grey (2008), Modeled and observed atmospheric radiation balance during the West African dry season: Role of mineral dust, biomass burning aerosol, and surface albedo, *J. Geophys. Res.*, *113*, D00C02, doi:10.1029/2007JD009741.

Nappo, C. J. (1991), Sporadic Breakdowns of Stability in the PBL over Simple and Complex Terrain, *Bound.-Layer Meteor.*, *54*, 69–87.

Nicholson, S. E. (2000), The nature of rainfall variability over Africa on times scales of decades to millenia, *Global and Planetary Change*, *26*, 137–158.

Parker, D. J., R. R. Burton, A. Diongue-Niang, R. J. Ellis, M. Felton, C. M. Taylor, C. D. Thorncroft, P. Bessemoulin, and A. M. Tompkins (2005), Thei diurnal cycle of the West African monsoon circulation, *Quart. J. R. Met. Soc.*, *131*, 2839–2860, doi: 10.1256/qj.04.52.

Pedgley, D. E. (1972), Desert Depresssion over North-East Africa, *Meteor. Mag.*, *101*, 228–244.

Peters, M., and G. Tetzlaff (1988), The Structure of West African Squall Lines and Their Environmental Moisture Budget, *Meteorol. Atmos. Phys.*, *39*, 74–84.

Prezerakos, N. G., S. C. Michaelides, and A. S. Vlassi (1990), Atmospheric synoptic conditions associated with the initiation of north-west African depression, *Int. J. Climatol.*, *10*, 711–729.

Prospero, J. M., P. Ginoux, O. Torres, S. E. Nicholson, and T. E. Gill (2002), Environmental characterization of global sources of atmospheric soil dust identified with the Nimbus 7 Total Ozone Mapping Spectrometer (TOMS) absorbing aerosol product, *Rev. Geophys.*, *40*(1), 1002, doi:10.1029/2000RG000095.

Reiter, E. R., and R. F. Lester (1968), Richardson's Number in the Free Atmosphere, *Arch. Met. Geoph. Biokl., Ser. A*, *17*, 1–7.

Schepanski, K., I. Tegen, B. Laurent, B. Heinold, and A. Macke (2007), A new Saharan dust source activation frequency map derived from MSG-SEVIRI IR-channels, *Geophys. Res. Lett.*, *34*, L18,803, doi:10.1029/2007GL030168.

Schmetz, J., P. Pili, S. Tjemkes, D. Just, J. Kerkmann, S. Rota, and A. Ratier (2002), An introduction to Meteosat Second Generation (MSG), *Bull. Amer. Meteor. Soc.*, *83*, 977–992.

Smith, R. K., and M. J. Reeder (1988), On the Movement and Low-Level Structure of Cold Fronts, *Mon. Wea. Rev.*, *116*, 1927–1943.

Sokolik, I. N., and O. B. Toon (1996), Direct radiative forcing by anthropogenic mineral aerosols, *Nature*, *381*, 681–683.

Sorbjan, Z. (2006), local Structure of Turbulence in Stably Stratified Boundary Layers, *J. Atmos. Sci.*, *63*, 1526–1537.

Steppler, J., G. Doms, U. Schättler, H. W. Bitzer, A. Gassmann, U. Damrath, and G. Gregoric (2003), Meso-gamma scale forecast using the nonhydrostatic model LM, *Meteor. Atmos. Phys.*, *82*, 75–96.

Sutton, L. J. (1925), Haboobs, *Quart. J. R. Met. Soc.*, *51*(213), 25–30.

Tegen, I., and A. A. Lacis (1996), Modeling of particle size distribution and its influence on the radiative properties of mineral dust aerosol, *J. Geophys. Res.*, *101*(D14), 19,237–19,244.

Tegen, I., S. P. Harrison, K. Kohfeld, and I. C. Prentice (2002), Impact of vegetation and preferential source areas on global dust aerosol: Results from a model study, *J. Geophys. Res.*, *107*(D21), 4576, doi:10.1029/2001JD000963.

Thorncroft, C. D., and H. A. Flocas (1997), A Case Study of Saharan Cyclogenesis, *Mon. Wea. Rev.*, *125*, 1147–1165.

Thorpe, A. J., and T. H. Guymer (1977), The nocturnal jet, *Quart. J. R. Met. Soc.*, *103*, 633–653.

Tiedtke, M. (1989), A comprehensive mass flux scheme for cumulus parameterisation in large-scale models, *Mon. Wea. Rev.*, *117*, 1779–1799.

Todd, M. C., R. Washington, S. Raghavan, G. Lizcano, and P. Knippertz (2008), Regional Model Simulations of the Bodélé Low-level Jet of Northern Chad dudring the Bodélé Dust Experiment (BoDEx 2005), *J. Climate*, *21*, 995–1012, doi: 10.1175/2007JCLI1766.1.

Torres, O., A. Tanskanen, B. Veihelmann, C. Ahn, R. Braak, P. K. Bhartia, P. Veefkind, and P. Levelt (2007), Aerosols and surface UV products from Ozone Monitoring Instrument observations: An overview, *J. Geophys. Res.*, *112*, D24S47, doi: 10.1029/2007JD008809.

Trigo, I. F., G. R. Bigg, and T. D. Davies (2002), Climatology of Cyclogenesis Mechanisms in the Mediterranean, *Mon. Wea. Rev.*, *130*, 549–569.

Tulet, P., M. Mallet, V. Pont, J. Pelon, and A. Boone (2008), The 7-13 March 2006 dust strom over West Africa: Generation, transport, and vertical stratification, *J. Geophys. Res.*, *113*, D00C08, doi:10.1029/2008JD009871.

Uppala, S., P. Kallberg, A. Simmons, U. Andrae, V. da Costa Bechtold, M. Fiorino, J. Gibson, J. Haseler, A. Hernandez, G. Kelly, X. Li, K. Onogi, S. Saarinen, N. Sokka, R. Allan, E. Andersson, K. Arpe, M. Balmaseda, A. Beljaars, L. van de Berg, J. Bidlot, N. Bormann, S. Caires, F. Chevallier, A. Dethof, M. Dragosavac, M. Fisher, M. Fuentes, S. Hagemann, E. Holm, B. Hoskins, L. Isaksen, P. Janssen, R. Jenne, A. McNally, J.-F.

Mahfouf, J.-J. Morcrette, N. Rayner, R. Saunders, P. Simon, A. Sterl, K. Trenberth, A. Untch, D. Vasiljevic, P. Viterbo, and J. Woollen (2005), The era-40 re-analysis, *Quart. J. Roy. Meteor. Soc.*, *131*, 2961–3012.

Washington, R., and M. C. Todd (2005), Atmospheric contronls on mineral dust emission from the Bodélé Depression, Chad: The role of the low level jet, *Geophys. Res. Lett.*, *32*, L17,701, doi:10.1029/2005GL023597.

Washington, R., M. Todd, N. J. Middleton, and A. S. Goudie (2003), Dust-Storm Source Areas Determined by the Total Ozone Monitoring Spectrometer and Surface Observations, *Annals of the Association of American Geographers*, *93*(2), 297–313.

Washington, R., M. C. Todd, G. Lizcano, I. Tegen, C. Flamant, I. Koren, P. Ginoux, S. Engelstaedter, C. S. Bristow, C. S. Zender, A. S. Goudie, A. Warren, and J. M. Prospero (2006), Links between topography, wind, deflation, lakes and dust: The case of the Bodele depression, Chad, *J. Geophys. Res.*, *33*, L09,401, doi:10.1029/2006GL025827.

Westphal, D. L., O. B. Toon, and T. N. Calson (1988), A Case Study of Mobilization and Transport of Saharan Dust, *J. Atmos. Sci.*, *45*(15), 2145–2175.

Wolke, R., O. Hellmuth, O. Knoth, O. Schröder, and E. Renner (2004a), The parallel model system LM-MUSCAT for chemistry-transport simulations: Coupling scheme, parallelization and application, *Parallel Computing: Software Technology, Algorithms, Architectures, and Applications*, pp. 363–370.

Wolke, R., O. Hellmuth, O. Knoth, W. Schröder, B. Heinrich, and E. Renner (2004b), The chemistry-transport modeling system LM-MUSCAT: Description and CityDelta applications, in *Air Polution Modeling and Its Aplication XVI*, edited by C. Borrego and S. Incecik, Proceedings of twenty-sixth NATO/CCMS international technical meeting on air polution modeling and its application.

Yang, G.-Y., and J. Slingo (2001), The diurnal cycle of the tropics, *Mon. Wea. Rev.*, *129*, 784–801.

Zender, C. S., and D. Newman (2003), Spatial heterogeneity in aeolian erodibility: Uniform, topographic, geomorphic, and hydrologic hypotheses, *J. Geophys. Res.*, *108*(D17), 4543, doi:10.1029/2002JD003039.

Manuscript prepared for J. Name
with version 1.3 of the LaTeX class copernicus.cls.
Date: 20 January 2009

Saharan Dust Transport and Deposition towards the Tropical Northern Atlantic

Atmospheric Chemistry and Physics, submitted

K. Schepanski[1, 2], **I. Tegen**[1], **and A. Macke**[2]

[1]Leibniz Institute for Tropospheric Research, Leipzig, Germany
[2]Leibniz-Institute of Marine Sciences, IFM-GEOMAR, Kiel, Germany

Abstract. We present a study of Saharan dust export towards the tropical North Atlantic using the regional dust emission, transport and deposition model LM-MUSCAT. Horizontal and vertical distribution of dust optical thickness, concentration, and dry and wet deposition rates are used to describe seasonality of dust export and deposition towards the eastern Atlantic for three typical months in different seasons. Deposition rates strongly depend on the vertical dust distribution, which differs with seasons. Furthermore the contribution of dust originating from the Bodélé Depression to Saharan dust over the Atlantic is investigated. A maximum contribution of Bodélé dust transported towards the Cape Verde islands is evident in winter when the Bodélé source area is most active and dominant with regard activation frequency and dust emission. Limitations of using satellite retrievals to estimate dust deposition are highlighted.

1 Introduction

The Sahara as the World's most important dust source adjoins directly to the Atlantic ocean (e.g. Prospero et al., 2002, Middleton and Goudie, 2001, Goudie and Middleton, 2001, Washington et al., 2003). A major part of the Saharan mineral dust is exported towards the northern tropical Atlantic (e.g. Romero et al., 1999). Mineral dust consists of small soil particles with regionally specific mineralogical, chemical, physical, and optical properties. Besides the interactions with solar and thermal radiation as well as clouds during transport, mineral dust deposited onto soil or ocean surfaces acts as nutrient for terrestrial and oceanic ecosystems (e.g. Mahowald et al., 2005). The bio-availability of micro-nutrients in mineral dust particles depends on their mineralogical and chemical properties that depend on source area mineralogy, and processes on the particle surfaces during transport in dry or aqueous phases (Goudie and Middleton, 2001, Luo et al., 2003, Journet et al., 2008). The Earth's surface contains around 4 % of iron (Wedepohl, 1995) and consequently soil-derived mineral dust can be considered as transport medium for iron from soil surface into ocean regions (Fung et al., 2000, Sarthou et al., 2003, Jickells et al., 2005). Iron in its role as micro-nutrient for ocean-ecosystems acts as controlling factor for life in high-nitrate, low chlorophyll (HNLC) regions, e.g. for phytoplankton growth (Neuer et al., 2004, Mahowald et al., 2005, Moore et al., 2006, Sarthou et al., 2007). In the tropical Atlantic, iron delivered by dust particles may enhance nitrogen fixation. By these processes dust deposition may be coupled to the CO_2 budget and climate system (Gao et al., 2001 and references therein).
Remote sensing retrievals have been used to determine dust fluxes into the North Atlantic, assuming that the ratio of atmospheric dust load within a column and the corresponding aerosol optical thickness (AOT) can be described by a fixed value (e.g Kaufman et al., 2005). Based on such analyses of satellite retrievals, the Bodélé Depression was claimed to be the major source for dust transport to the Amazon (Koren et al., 2006).
Oceanic dust deposition has also been estimated from global dust models (e.g. Zender and Newman, 2003, Mahowald et al., 2005). Regional models are suitable to investigate dust conditions for specific meteorological situations and are expected to provide better vertical resolution of dust layers compared to global-scale models, which is an important control of dust deposition.
This paper aims to show for three case studies the characteristics as well as the differences of dust transport concerning e.g. direction, height, and amount, and dust deposition towards the eastern tropical North Atlantic in different seasons. The contribution of dust emitted over the Bodélé Depression to the total exported Saharan dust will be estimated. Furthermore the relation of AOT of dust (in the following referred

---

Correspondence to: Kerstin Schepanski,
(kerstin.schepanski@tropos.de)

to as AOT) and atmospheric dust column load and deposition fluxes is discussed. This addresses the question whether it is possible to determine dust deposition from AOTs retrievals based on space-borne measurements provided by e.g. MODIS or SeaWiFS.

2 Regional Model System LM-MUSCAT

To characterise Saharan dust transport and deposition towards the tropical North Atlantic, we use the dust transport model system LM-MUSCAT (Heinold et al., 2007). It consists of the regional scale meteorological model LM (provided by the Deutscher Wetterdienst, Steppler et al. (2003)) and the MUlti-Scale Chemical Aerosol Transport Model (MUSCAT, Wolke et al. (2004a), Wolke et al. (2004b)). The dust transport model includes a dust emission scheme based on Tegen et al. (2002). Meteorological and hydrological fields used for the simulation of dust emission, transport and deposition, are computed by the LM and updated in MUSCAT at every advection time step chosen to be 80 s. Local wind systems, clouds, precipitation, and meso-scale convection depend on topography. For simulation of subgrid scale moist convection the parameterisation following Tiedtke (1989) is used in the LM. Dust emission is modified by surface properties like vegetation, surface roughness, soil texture and soil moisture content. In addition to soil properties, wind shear stress at the ground is the major limiting factor for soil erosion. The wind shear stress τ is related to the air density ρ_a and the friction velocity u_*, by $\tau = \rho_a u_*^2$. Dust emission occurs if the friction velocity exceeds a local, soil-dependent threshold u_{*t} for dust mobilisation. Surface roughness elements like rocks and stones but also vegetation and the soil texture impact on the required momentum to mobilise soil particles. Here a parametrisation for u_{*t} based on Iversen and White (1982) is used, modified by Marticorena and Bergametti (1995). The simulation of dust emission is allowed for areas, which have been observed to be dust sources at least two times during 2006/03-2007/02 using Meteosat Second Generation (MSG) infra-red dust index imagery (Schepanski et al., 2007). The size distribution of particles during emission depends on the actual wind velocity and local soil characteristics (Tegen et al., 2006).

Airborne dust is transported as passive tracer in five independent size bins (radius limits at: 0.1 μm, 0.3 μm, 0.9 μm, 2.6 μm, 8 μm and 24 μm). For each size bin spherical dust particles following a log-normal size distribution are assumed. Dust deposition is parametrised as dry and wet deposition. The parametrisation of dry deposition depends on particle size, density and meteorological conditions affecting the behaviour of dust particles. In detail the parametrisation considers turbulent transfer, Brownian diffusion, impaction, interception, gravitational settling, and particle rebound (Heinold et al., 2007). Dry deposition of dust particles is controlled mainly by gravitational settling, which is dominant for particles larger than 2 μm, and the impact of aerodynamic (R_a) and surface resistance (R_s). Gravitational settling, commonly described by the gravitational settling velocity v_d is based on the Stoke's equation describing the equilibrium of gravitation and buoyancy:

$$v_g = \frac{(\rho_p - \rho_a) g D_p^2 C_c}{18\nu} \tag{1}$$

with particle diameter D_p, air density ρ_a, particle density $\rho_p = 2.65\ g/cm^3$, the gravitational constant g, the dynamic viscosity of air ν, and the Cunningham correction factor C_c. The Cunningham correction takes into account that the Stoke's law considers the velocity of the air surrounding the particle's surface relative to the particle itself as zero. This assumption is correct in continuum but not for particle larger than the mean free path λ of air molecules. The Cunningham correction factor C_c is used to take this into account and is described by

$$C_c = 1 + \frac{2\lambda}{D_p}\left[1.142 + 0.558 exp\left(-\frac{0.4995 D_p}{\lambda}\right)\right]. \tag{2}$$

For particles smaller than 2 μm, the gravitational settling velocity v_g is adjusted by the aerodynamic and surface resistance R_a and R_s to account for turbulent mix-out:

$$v_d = \frac{1}{R_a + R_s + R_a R_s v_g} + v_g. \tag{3}$$

Beside dry deposition, especially over the North Atlantic, wet deposition, e.g. by rain-out, has a strong influence on particle removal. In MUSCAT, the parametrisation follows Berge (1997) and Jacobson et al. (1997) and bases on the parametrisation used in the EMEP MSC-W Eulerian model by Tsyro and Erdman (2000). Wet deposition is controlled by the precipitation rate p and the scavenging coefficient λ,

$$Dep\_rate = -\lambda \cdot p, \tag{4}$$

with

$$\lambda = \frac{A \cdot E}{v_{dr}}, \tag{5}$$

related to an empirical coefficient $A = 5.2\ m^3/kg\ s$ due to Marshall-Palmer size distribution assumed for rain drops, to the mean collection efficiency E, averaged over all rain drop sizes and to the rain drop fall velocity v_{dr}, here $v_{dr} = 5 m/s$. For the computation of AOT at 550 nm, dust concentrations of the five size bins (dust mode, j) are used. The dust particles are assumed to be spherical particles with a density of quartz ($\rho_p = 2.65 g/cm^3$):

$$\tau = \sum_j \sum_k \left(\frac{3}{4}\frac{Q_{ext,550}(j)}{r_{eff}(j)\rho_p(j)} c_{dust}(j,k)\Delta z(k)\right), \tag{6}$$

with the extinction efficiency $Q_{ext,550} = (1.677, 3.179, 2.356, 2.144, 2.071, 2.034, 2.016, 2.008)$ for each size bin (derived from Mie-theory, following

Sinyuk et al. (2003)), effective radius of dust particle $r_{eff}(j)$, dust concentration $c_{dust}(j,k)$ at vertical level k, and the vertical increment of each vertical level $\Delta z(k)$. In the calculation of AOD from the model size distribution and refractive index information we use Mie-theory, i.e. a spherical shape of the dust particle is assumed, whereas the AERONET retrieval takes spheroidal dust particle shapes into account. However, our simplification only affects the calculation of the extinction efficiency, which is not very sensitive to particle shape at the dust size parameters in the solar spectral range.

For this study of dust transport and deposition towards the tropical North Atlantic, we run the model system on a 28 km horizontal grid resolution and 40 $\sigma - p$ levels up to 12 km height, whereby the LM itself simulates the atmosphere up to 24 km. The first level is centred around 38 m above ground level (agl). There is a spin-up period of 24 hours for the LM part, after this period the MUSCAT is coupled to the LM. Every 6 hours, meteorological boundary conditions are updated with analysis fields from GME (global weather forecast model of the DWD). After 24 hours of LM-MUSCAT computations, the meteorological fields are reinitialised. Three case studies of one month periods, in different seasons have been computed: March 2006, July 2006 and 20 December 2006 to 20 January 2007 (hereafter referred to as January 2007).

3 Dust transport and deposition towards the tropical North Atlantic

The Sahara and Sahel region over North Africa contains several potential dust source areas, mostly located in the foothills of the mountain areas where endorheic drainage systems (systems formed by flowing water), and wadis opening to fluvial fans provide a large amount of sediment available for aeolian erosion (e.g. Washington et al., 2003, Schepanski et al., 2007). Each dust source area is characterised by seasonal and annual changes in frequency of dust source activation (Schepanski et al., 2008). Consequently, seasonal changes in spatio-temporal dust source activity are related to seasonal changes in local meteorological conditions providing atmospheric conditions for dust mobilisation. Here, potential dust emission areas are limited to areas which have been observed to be dust sources (Schepanski et al., 2007). Seasonal changes in active dust source areas are not prescribed as the simulated atmospheric conditions should be able to reproduce seasonal changing conditions fulfilling and inhibiting dust emission, respectively. However, as local meteorological conditions are influenced by regional and mesoscale meteorological systems, dust transport is affected regarding amount, height of transport layer, and dry and wet deposition rates respectively.

To investigate typical transport and deposition patterns of Saharan dust in different seasons, three modelling studies for one month periods (March 2006, July 2006 and January 2007) representing different seasons (north hemispheric spring, summer and winter) have been performed using the regional model system LM-MUSCAT.

3.1 Characteristics of Saharan dust transport

To describe the horizontal distribution of atmospheric dust load, we have to distinguish between near-source area, areas affected by dust transport over the African continent and over the ocean. The atmospheric dust concentration over the near source area is mainly characterised by the dust source activity, the wind direction and speed, and atmospheric stability (Kalu, 1979). The dust particle sizes are larger close to the source region and decrease with distance due to gravitational settling (e.g. Westphal et al. (1987)). Dust is mixed up by turbulent mixing within the boundary layer (BL), transported within the regional wind flow or removed from the atmosphere by either dry or wet deposition. During transport, the dust plume can remain near the surface and be observed as dust storm, or can be transported as elevated layer. Within the daytime BL, dust concentration can be homogeneously distributed over the entire BL depth (Tesche et al., 2009). In the evening, mixing activity within the BL ceases and a significantly shallower nocturnal BL remains (Garratt, 1992). However, airborne dust can be still present in the residual layer. During night, the air layer does not change its height and will be re-mixed to the developing daytime BL (Blackadar, 1957, Lenschow and Stankov, 1979, Kalu, 1979). Alternatively, air masses above the nocturnal BL can be accelerated due to geostrophy caused by pressure gradient forces between the Saharan heat low and the surrounding higher air pressure and the Coriolis force. During day time, surface friction decelerates geostrophic air flows to sub-geostrophic wind velocities. During night, surface friction does not act on the air flow at levels above the decoupling inversion on top of the shallower nocturnal BL and the wind accelerates. As the BL depth shrinks relatively fast after sunset, the geostrophic equilibrium over-accelerates the wind flow to super-geostrophic wind velocities and a wind speed maximum develops, also termed as nocturnal low-level jet (LLJ) (e.g. Nappo, 1991, Banta et al., 2006, Schepanski et al., 2008). So the elevated air mass with its dust content is transported relatively fast away from the source area (Kalu, 1979; Westphal et al., 1987). Transported dust layers during night within a low-level jet might be mixed into the developing BL the next day and might lead to decreasing horizontal visibilities, which have been observed during the build-up phase of the daytime BL (Kalu, 1979).

Atmospheric dust layers that are transported away from the sources can be elevated to higher levels compared to dust near its source. The elevation of dust layers depends on the season (see Fig. 1).

During winter, the dust layers over the West African continent are situated at lower levels than during summer (Kalu,

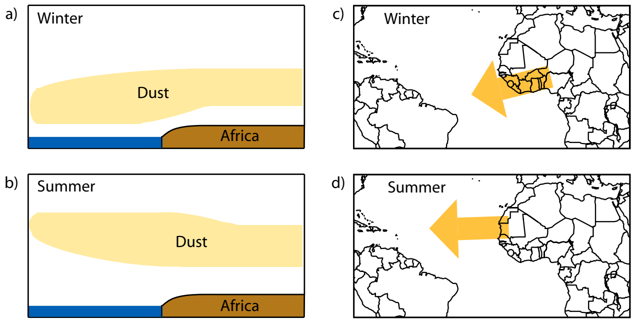

Fig. 1. Schematic diagram of vertical and horizontal dust export from North Africa towards the tropical East Atlantic for northern hemisphere winter (a, c) and summer (b, d). After Kalu (1979)

1979). In winter months, transported Saharan dust is observed at near-surface layers, while in summer the dust layer is elevated. This is due to seasonally different meteorological regimes especially over the Sahel and the Western Sahara. Due to northward shift of the ITD (inner-tropical discontinuity, marking the meeting of dusty desert air and tropical moist air) and higher insolation leading to a larger surface heating the BL is deeper during summer which results in a higher upward-mixing of dust. During night the West African Monsoon (WAM) circulation forces the development of high geostrophic wind speeds in the decoupled, elevated air layer (e.g. Parker et al., 2005). Dust can be mixed up high into troposphere and be transported rapidly during night. Additionally, dust layers within the mid-troposphere overlay the moist and denser monsoon air and reaches higher transport levels in summer than in winter when the dust layer is transported within the trade winds (Kalu, 1979). The location of the ITD is father south in winter, so the high vertical mixing of dusty air occurs further south over the South Sahel. In summer this strong mixing occurs further north over the Sahel/South Sahara due to northward shift of the Hadley circulation. Over the ocean, the Saharan dust layer is transported above the trade winds inversion (up to 5-7 km above sea level) (Kalu, 1979, Chiapello et al., 1997, Dunion and Velden, 2004, Karyampudi et al., 1999) in north hemispheric summer (Fig. 1). In winter the dust is transported within the trade wind layer at altitudes below 1.5-3 km (Chiapello et al., 1997, Barkan et al., 2004).

3.2 Horizontal Distribution of AOT

Horizontal dust transport paths can be tracked considering the distribution of AOT, e.g. provided for remote areas by satellite products (Figure 2). Furthermore, satellite products are often used and are well suitable for model validation as they provide information on a larger spatial scale compared to station measurements. Several satellite products from different instruments are available, e.g. MODIS (MOderate resolution Imaging Spectrometer) on-board the polar orbiting satellites Aqua and Terra and OMI (Ozone Monitoring Instrument) onboard the Aura satellite. Here, three satellite products applied to measurements at different ranges of wavelength provided by those satellite platforms are used to validate the models ability to reproduce horizontal aerosol distribution on a monthly time scale. For MODIS, two AOT products are available: MODIS AOT applied to measurements at visible wavelength and DeepBlue AOT (Hsu et al., 2004) applied to the deep-blue part of the visible spectrum. The MODIS AOT product is limited to dark surfaces like the Ocean or high vegetated land surfaces. Here it is used to validate the monthly mean AOT values over the Atlantic. The usage of measurements at deep-blue wavelengths (412 nm, 490 nm and 670 nm) situated in the high-frequency part of the visible spectrum allow AOT retrieval over bright surfaces due to low surface reflectance at this part of the spectrum. DeepBlue AOT is used here to validate monthly mean AOT over land surfaces. Both AOT retrievals do not only consider dust, also aerosol particles like sea-salt and soot add to the AOT values. The third index used here for validation aspects is the OMI Absorbing Aerosol Index (AI, Herman et al. (1997)). This index is applied to measurements at ultra-violet (UV) wavelength. At UV wavelength the surface reflectivity is low (Eck et al., 1987) and so UV absorbing aerosol like mineral dust (and also biomass burning aerosol) can be detected due to spectral different back-scattering effects (Veihelmann et al., 2007). The AI provides a qualitative indicator for the presence of dust. Compared to AOT retrievals, the AI values are not affected by the presence of sea-salt particles (Torres et al., 2002). The AI values are sensitive to the height of the aerosol layer (Israelevich et al., 2002).

Figure 2 shows monthly means of three different aerosol products in comparison to the modelled dust distribution for the same time period based on noon-time AOT values. Missing values (e.g. due to clouds) for the satellite products are taken into account. Depending on the wavelengths to which the retrieval algorithm is applied, information on the atmospheric dust content indicated by AOT and AI, respectively, are available for different underlying surfaces. The comparison highlights that retrievals applied to different wavelengths may show different features in terms of high index values. For July 2006, the OMI AI indicate high mean index values over Mali and Mauritania, the DeepBlue AOT shows a maximum pattern over the Bodélé Depression area. Different retrievals show different sensitivities concerning e.g. particle characteristics, which have to be considered. Furthermore, the AI detects aerosol due to biomass burning as well as dust which becomes important especially in boreal winter. Soot contributes to the maximum AI pattern shown in Fig. 2 for January 2007, which is also true for MODIS AOT and DeepBlue AOT. As the model only accounts for mineral dust aerosol, no other aerosol types contribute to the model based AOT. Remote sensing products for mineral dust are used to validate the horizontal distribution of simulated dust.

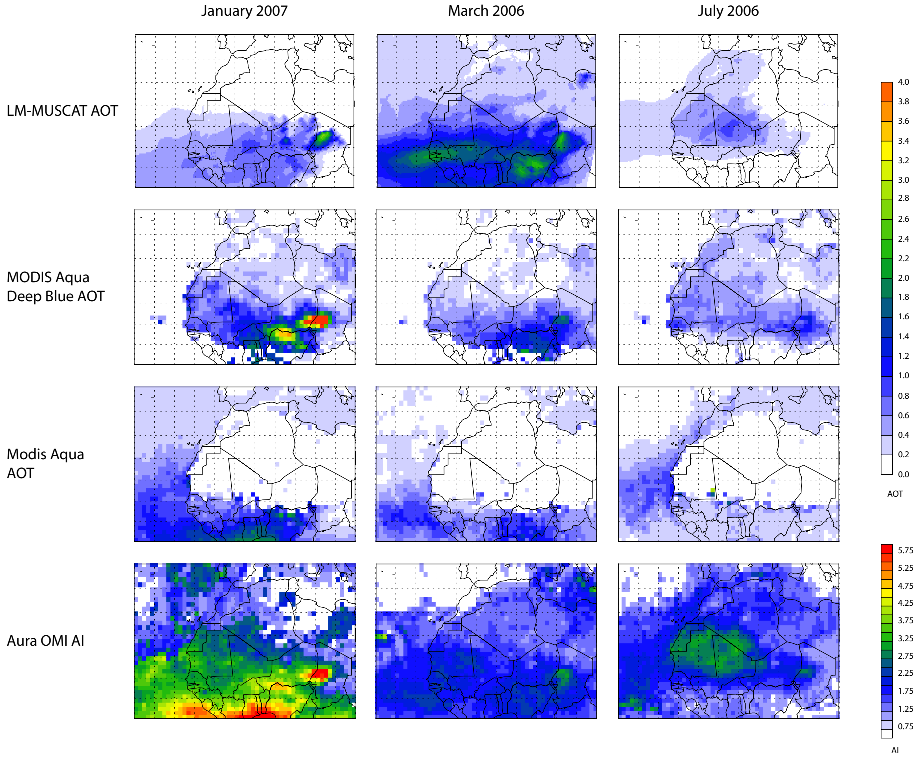

Fig. 2. Monthly mean AOT retrieved from model simulations and satellite observations done by MODIS and OMI instruments for January 2007, March 2006 and July 2006. Differences are due to model shortcomings and the sensitivities of the satellite retrievals. OMI AI values give a semi-quantitative information on atmospheric dust content.

For January, high AOT values are simulated over the Bodélé Depression, Niger and western Mali by LM-MUSCAT. The plume spread out in westward direction with an axis which can be drawn crossing Mali and Guinea. Similar patterns are evident in the remote sensing products. The MODIS AOT product shows a similar northward extent of the dust plume over the Atlantic, but with slightly higher AOT values compared to the model. This is especially evident over the tropical Ocean, where the contribution of biomass burning aerosol increases the observed AOT. OMI AI shows similar pattern of airborne dust distribution. Over land surfaces, the AOT patterns of the model simulation agree in general with the remotely sensed patterns, but they disagree in detail: The maximum mean AOT values simulated over the Bodélé Depression is around 2.8, measurement retrievals indicate AOTs up to 5 by the DeepBlue product. Furthermore, the satellite products point towards a second aerosol hot spot north of the Highlands of Jos (Nigeria) which is not represented in the model mean values, but may be due to biomass burning aerosol. Also, over the continent the simulated AOT values are slightly lower compared to the satellite retrieval. The horizontal distribution of simulated mean AOT for March 2006 agrees well compared to the satellite retrievals. The position of the dust plume entering towards the tropical Atlantic agrees well in LM-MUSCAT simulations and MODIS AOT retrievals, whereby in March the modelled AOT values are higher than AOT from remote sensing. LM-MUSCAT AOT, OMI AI and DeepBlue AOT, agree well regarding pattern distribution, but also over land the simulated AOT values are higher than the retrieval. The summer case (July 2006) agrees well concerning the range of mean AOT values over the continent, but again some differences are evident regarding the location of hot spot patterns: The simulations show a maximum mean AOT located over central Mali in agreement with OMI AI whereby the AI maximum is shifted to the west. DeepBlue AOT pattern indicate higher values over this areas, but show a maximum over the Bodélé which is not represented by the model. Outside of “hot spot” areas the OMI AI and DeepBlue AOT show similar patterns. In summary, monthly mean AOT distributions are in good agreement with satellite AOT retrievals concerning their horizontal patterns and the range of values. The model simulated AOTs over the Atlantic are lower compared to the satellite data in summer.

The atmospheric dust content is a result of dust emission, transport and deposition. So the comparison of horizontal distribution of dust load, here indicated by the AOT, shows implicitly the accuracy of the treatment of dust emission, transport and deposition, each requiring a correct reproduction of meteorological conditions. To account for the importance of accurate treatment of the meteorological conditions for this regional model system, especially the wind distribution as limiting factor for dust emission, we refer to the studies of Heinold et al. (2007), Laurent et al. (2008) and Reinfried et al. (2008). Furthermore, Schepanski et al. (2008) investigate the ability of LM-MUSCAT to reproduce the occurrence of nocturnal LLJs, which has been identified to be an important feature for Saharan dust mobilisation.

Besides the validation of the model's horizontal distribution of atmospheric dust loads, seasonal characteristics of extent and strength of North African dust plumes are evident. In summer, transport direction of the main plume is in westward direction, in winter its direction is in southwestward direction, which is in agreement with long-term observations (e.g. Romero et al. (1999)).

3.3 Monthly Distribution of Dry and Wet Dust Deposition

Airborne dust can be removed from the atmosphere by dry or wet deposition. Deposition measurements are sparse, so here the discussion bases on the assumption that a reliable field of AOT implicitly includes a correct treatment of deposition fluxes. The reliability of the model's dust fields are validated using horizontal distributions of monthly mean AOTs (Section 3.2), temporal evolution of single dust plumes at measurement sites provided by AERONET (Section 3.4) and the particle size distribution observed at these stations (Section 3.5).

The relative importance of dry or wet deposition processes differs regionally and changes with seasons (Fig. 3). During winter (January 2007, Fig. 3a), wet deposition is negligible over nearly the entire North African domain, while dry deposition is very dominant and represents the pattern of mean AOT. High dry deposition rates over Tunisia, the western foothills of the Hoggar Massif and western Algeria in the presence of relative low mean AOT values (Fig. 2) indicate near-source deposition and short residence time of dust within the atmosphere. Wet deposition occurs mainly over the Atlantic related to moist convection within the tropical convergence zone and low pressure disturbances further north. Over the tropical East Atlantic, the Saharan Air layer (SAL), a very dry, warm and dusty air mass originating from the desert, is characterised by negligible wet deposition (lower than 0.01 g/m^{2}month), high dry deposition (up to 1 g/m^{2}month) rates compared to other Atlantic regions and high mean AOT (Fig. 2 and 3). During March 2006 (not shown) representing a spring month, the same features as described for January 2007 can be found. The domain of high dry deposition rates and negligible wet deposition rates is centred further north due to northward shift of Hadley circulation. In summer, moist convection occurs especially over the mountains and the monsoon region. Thus wet deposition occurs especially over the West Sahara, the Sahel and the Atlas Mountains. Dominance of wet deposition is indicated by high deposition rates (up to 10 g/m^{2}month over the Atlas and up to 5 g/m^{2}month over the West Sahara) in these areas. High dry deposition rates are also found over the West and Central Sahara (up to 10 g/m^{2}month). The coincidence of both, dry and wet deposition in this region characterise summer months and point towards the varying weather character of the monsoon period.

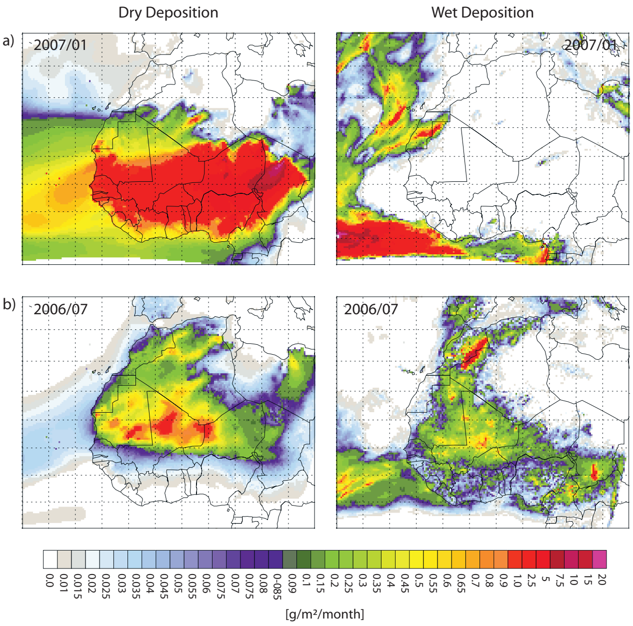

Fig. 3. Monthly dust dry and wet deposition fluxes for January 2007 (a) and July 2006 (b), computed by the regional model LM-MUSCAT.

In summer, the dusty Saharan air is elevated above the marine boundary layer and the dust concentration at near-surface levels decreases (e.g. Karyampudi et al. (1999)). Fields of dry deposition simulated by LM-MUSCAT indicate an elevation of the Saharan dust layer and thereby a decrease of dust load at the lowest level as shown for the Cape Verde Islands in Figure 4, but a too strong decrease of total deposition fluxes is evident following the shape of the coastline. This effect causes also the lower AOT compared to DeepBlue and will be investigated in future studies.

3.4 Temporal Evolution of the Dust Concentration

Beside the horizontal distribution of the atmospheric dust load (shown as monthly mean values, Figure 2), the temporal evolution of AOT values is compared. Sun-photometer measurements performed in the framework of AERONET (AErosol RObotic NETwork, Holben et al. (1998)) are used to characterise the temporal evolution of dust plumes for measurement sites located in North Africa.

Dust emission does not occur continuously in space and time. The spatial distribution of active dust sources changes

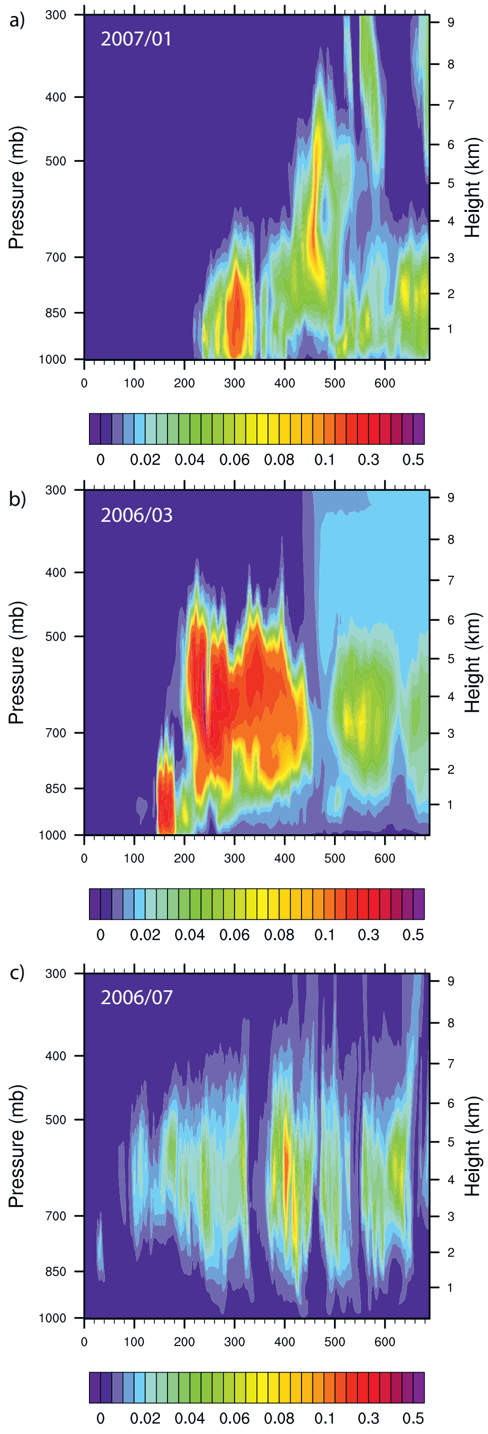

Fig. 4. Temporal evolution of the vertical dust concentration [g/cm^3] distribution over Sal, Cape Verde (16° N; 22° W) for January 2007 (a), March 2006 (b) and July 2006 (c).

within the day, from day to day and season to season (Schepanski et al., 2007). In remote areas where the dust transport is affected by the atmospheric flow pattern, the pulsed characteristic of dust emission is smoothed depending on atmospheric situation (e.g. clouds, precipitation) during transport. Cloud-free level-2 AOT sun-photometer measurements at AERONET sites located more closely to source areas and those located in the far-field dust transport path are chosen to evaluate the simulated dust export to the Atlantic ocean at different seasons (Figure 5). The AOT measurements do not distinguish between aerosol types like mineral dust and soot, but consider a mixture of spherical and non-spherical components (Dubovik et al., 2006). Over the Sahel and tropical North Africa the contribution of soot to the measured AOT might be high, especially in winter when biomass burning is a frequent phenomenon over this area. To ensure that the fraction of dust to the measured AOT is the dominant, only those AOT retrievals are considered, where the AOT ≥ 0.3 and the Angstrm coefficient $\alpha \leq 0.6$ following Dubovik et al. (2002). The sites are chosen with regard to obtain an overview of Saharan dust export at different latitudes.

During March 2006, an extra-ordinary dust storm occurred (Tulet et al., 2008) starting on March 05 in the Atlas Mountains initiated by a upper-level trough and crossing southward to the Sahel and the tropical Atlantic ocean. This strong event is dominant at all sites located in the remote transport path. At Tamanrasset this event is not evident as this site is not situated in the dust transport path. Comparing AOT measurements to the model simulation, the character of the month is well reproduced, but the strength of the extra-ordinary event during the beginning of the month is overestimated by the model at all stations.

In July 2006, the range of observed and simulated AOT values is significantly lower than during spring (March 2006). The temporal evolution of dust plumes is well represented regarding onset and AOT range for Tenerife over the whole month. At most other stations, crossing dust plumes during the first half of the month are underestimated by the model, but in general representing the onset and offset of observed dust plumes. During the second half of the month, dust occurrence is well represented regarding the strength of the dust plume and its temporal evolution.

January 2007 shows similar characteristics as March 2006. The range of observed and modelled AOT values is higher than during summer, which is also evident in seasonal differences shown in Fig. 2. The characteristics of the AOT evolution is well represented at all stations, but the second simulated dust plume (around January 12) arrives about 1-2 days too fast at Tenerife and Cap Verde. The earlier onset is also evident at the Sahelian observation sites Banizoumbou, Cinzana, Ilorin and Ouagadougou. Strong dust events as during January 3-5 at Cape Verde and during January 11-13 at Tenerife are overestimated by the model, whereby the maximum AOT values are well reproduced at Sahelian sites (Ouagadougou, Ilorin, Cinzana, Banizoumbou).

In general, the model is able to capture the seasonal differences of the atmospheric dust cycle comprising emission,

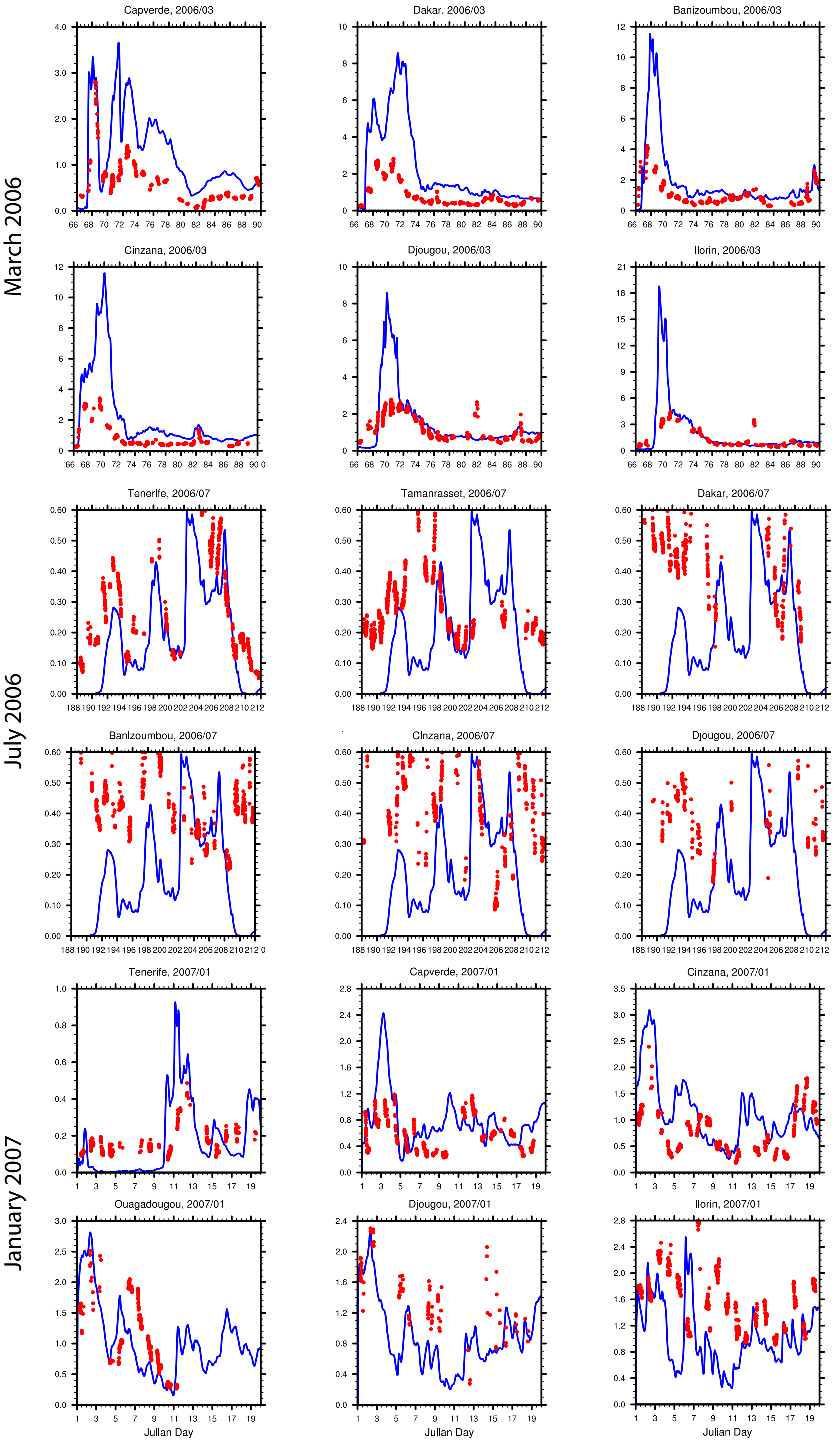

Fig. 5. Comparison of simulated and by sun-photometer observed AOT at North African stations (Santa Cruz de Tenerife 28.5° N 16.3° W, Tamanrasset 22.8° N 5.5° E, Cape Verde 16.7° N 22.9° W, Dakar 14.4° N 17.0° W, Cinzana 13.3° N 6.0° W, Banizoumbou 13.5° N 2.7° E, Ouagadougou 12.2° N 1.4° W, Djougou 9.8° N 1.6° E, Ilorin 8.3° N 4.3° E) situated in different transport directions of upwind dust source areas for March 2006 (top two rows), July 2006 (middle two rows) and January 2007 (lower two rows). The stations are sorted according their geographical location, starting with the northern most station. Red dots represent sun-photometer observations (at 440 nm), the blue solid line represents the AOT values computed from the model results (at 550 nm). Observations are provided by AERONET, http://aeronet.gsfc.nasa.gov.

transport and deposition in its extent but also in its temporal evolution. For July 2006, difficulties in simulating the observed level of dust concentration are evident.

The AOT as a measure for total dust concentration within the atmospheric column above the reference point does not give any information about the vertical distribution of the dust concentration. The regional model LM-MUSCAT provides information about the vertical dust distribution in addition to the column load or AOT. Figure 4 shows the modelled temporal evolution of vertical dust concentration over the Cape Verde at 16° N; 22° W for January 2007, and March and July 2006 representing the characteristics of the different seasons. During winter, the dust transport layer is situated at lower tropospheric levels with maximum dust concentrations up to around 2 km on most days. Frequently the dust layer extends down to (near-)surface layers (Fig. 4). In summer, the dust transport layer is the Saharan Air Layer (SAL), which is aloft in heights around 4-5 km and does not extend to the ground levels (See also Section 3.1 and Fig. 4c). This vertical layering is also described by Karyampudi et al. (1999). During spring, the dust transport layer can be found in lower tropospheric layers (up to around 2 km) as well as in higher levels (around 4 km height). Dust transport in spring is characterised by a transition from lower (winter) transport heights to high (summer) transport heights (Fig. 4b).

Comparing both, the AOT and vertical dust concentration distributions, it is obvious that high AOT do not necessarily indicate high surface dust concentrations. However, high dust concentrations at surface levels are coincident with high deposition rates. The relation between these three measures are strongly impacted by the height of the dust layer. In winter when the dust layer is situated within the lower troposphere or near the surface within the trade wind layer, high dust deposition rates coincide with high dust concentrations and high AOT values. In summer, this coincidence is not evident due to the dust transport occurring in an elevated layer above the trade winds inversion. However, dust deposition at a specific location is not closely linked to the AOT. Dust deposition depends rather on the vertical distribution of dust concentrations for which the AOT does not take account. However, to retrieve deposition rates from satellite observations, assumptions on the level-height of the dust layer have to be made.

3.5 Dust Size Distribution

Besides the monthly mean of the spatial distribution of AOT over the entire domain (Section 3.2) and the validation of the temporal evolution of single dust events at AERONET measurement sites (Section 3.4), the comparison of retrieved dust size distribution from sun-photometer measurements (available at http://aeronet.gsfc.nasa.gov) to modelled dust size distributions are a good possibility to validate the integrated effect of emission, transport and deposition processes, which result in the local dust concentration and soil size distribution. To consider the measured particle size distribution of dust aerosol, the criterion $\alpha \leq 0.6$ has to be fulfilled (Dubovik et al., 2002) to select periods with dominant mineral dust fraction. Dust particle size distribution is observed to change with distance from its source due to gravitational settling (e.g. Westphal et al., 1987). As no long-term measurements at active dust source areas are available, the size distribution at emission is still an unknown parameter for most model grid points and has to be estimated from e.g. wind tunnel and field experiments (e.g. Gillette (1979); Shao et al. (1996)). Here, measurements of size distributions at several stations located in the transport field are compared to the modelled size distribution, whereby the stations can be separated into three categories: 1) stations off the coast (Cape Verde and Tenerife), 2) stations in southwestward and westward transport direction like Sahelian stations (Banizoumbou, Cinzana, Ilorin, Ouagadougou, Djougou) and a West African station (Dakar), and 3) a station over the Central Sahara (Tamanrasset). The comparison is shown for typical days of each simulated season to account for seasonal effects impacting on the dust size distribution (Figure 6).

The observed maximum of the size distribution in the fine mode size range (around 0.1 μm) can be considered as artifact due to the inversion algorithm (Dubovik et al., 2006). In general, the maximum and the shape of the observed size distribution for coarse mode aerosol are in good agreement at most stations at different distances to source areas. The model shows a larger fraction of particles larger than 10μm compared to the AERONET product. Differences in size distributions are evident for stations located in the Central Sahara (Tamanrasset), located in the Sahelian band (Cinzana, Ilorin, Banizoumbou, Ouagadougou), located off the coast (Cape Verde, Tenerife), and located in between (Dakar) (Figure 6). With increasing transport distance, the distribution becomes narrower, compared to near-source sites.

During summer (July 2006), the observed size distribution is underestimated by the model for stations situated in the transport path, whereby the position of the maxima agree. This is consistent with the too low simulated AOT values over these areas (Figure 2). Nevertheless, the comparison of model size distribution to observed values shows good agreement although the model size distribution is shifted towards large particles compared to the observed distribution. The general agreement for the different sites and seasons supports the assumption that the model is able to simulate emission, transport and deposition processes realistically.

3.6 Zonal Dust Flux

Besides the horizontal distribution of AOT, dust concentration and dust deposition, zonal dust fluxes can be used to describe dust transport. In case of the Saharan dust export towards the North Atlantic, zonal fluxes can be used to estimate

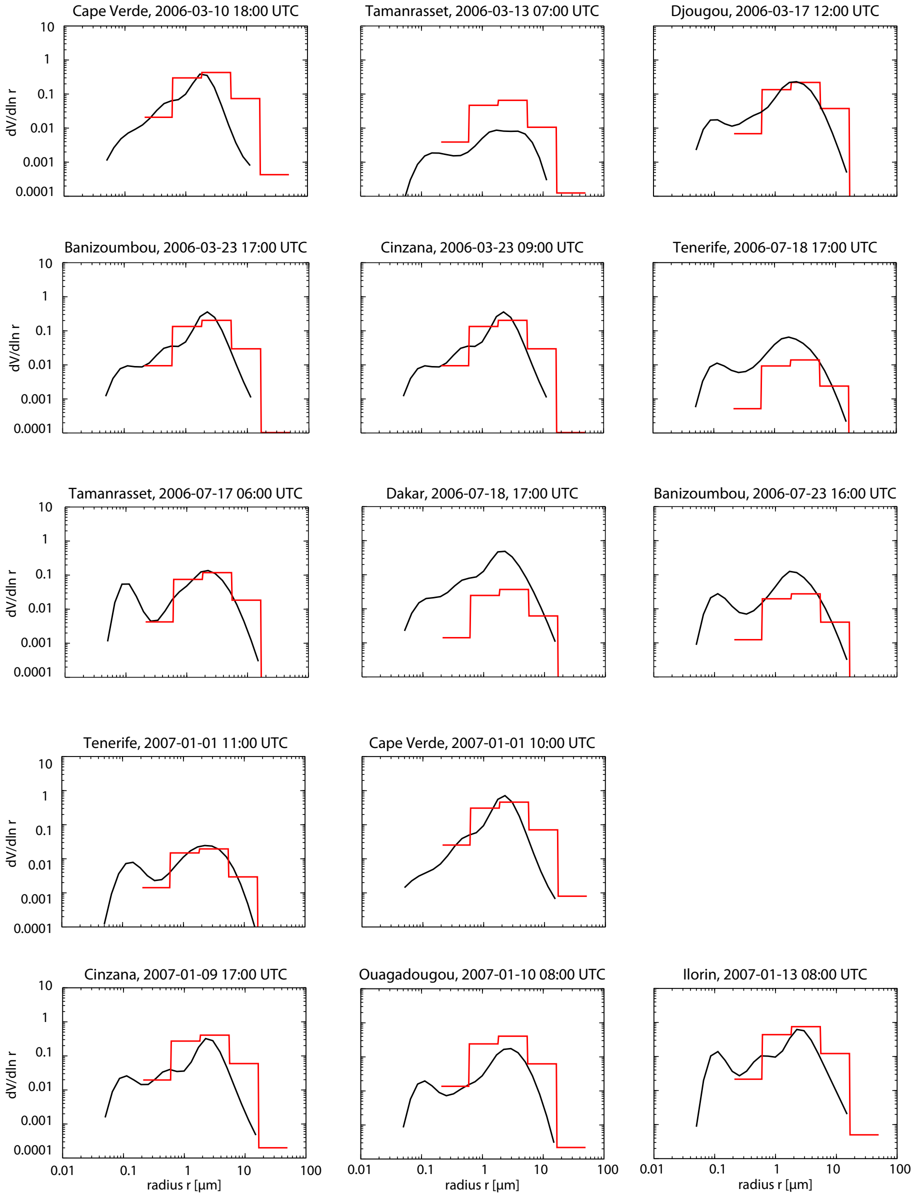

Fig. 6. Comparison of particle size distributions for the model and AERONET observations at stations located in different transport directions regarding upwind dust emission and different distances to the source area (Santa Cruz de Tenerife 28.5° N 16.3° W, Tamanrasset 22.8° N 5.5° E, Cape Verde 16.7° N 22.9° W, Dakar 14.4° N 17.0° W, Cinzana 13.3° N 6.0° W, Banizoumbou 13.5° N 2.7° E, Ouagadougou 12.2° N 1.4° W, Djougou 9.8° N 1.6° E, Ilorin 8.3° N 4.3° E). The upper two rows show chosen distributions in March 2006, the middle two rows for July 2006 and the lower two rows for January 2007. The stations are sorted following their geographical position, starting with the northern most station. Size distribution of the model are given by the red line, those based on sun-photometer observations are given in black.

Saharan dust export due to the dominant zonal wind direction in all seasons (e.g. Kaufman et al. (2005)). Here we computed monthly zonal dust fluxes at 10° W, 15° W and 20° W using the results from the regional dust emission and transport model (Fig. 7). Zonal dust fluxes F_{dust} are calculated using zonal wind speed u and dust concentration M_{dust}:

$$F_{dust} = M_{dust} \cdot u. \tag{7}$$

The 10° W meridian crosses the Western Sahara, so the western-most Saharan dust sources will be missed but dust export over the Gulf of Guinea and the Canary Islands will be captured close to the coast. Furthermore, this meridian accounts for atmospheric conditions changing seasonally due to the dominant West African Monsoon circulation in summer and the Harmattan in winter, both impacting strongly on the dust transport path. The 20° W meridian is located

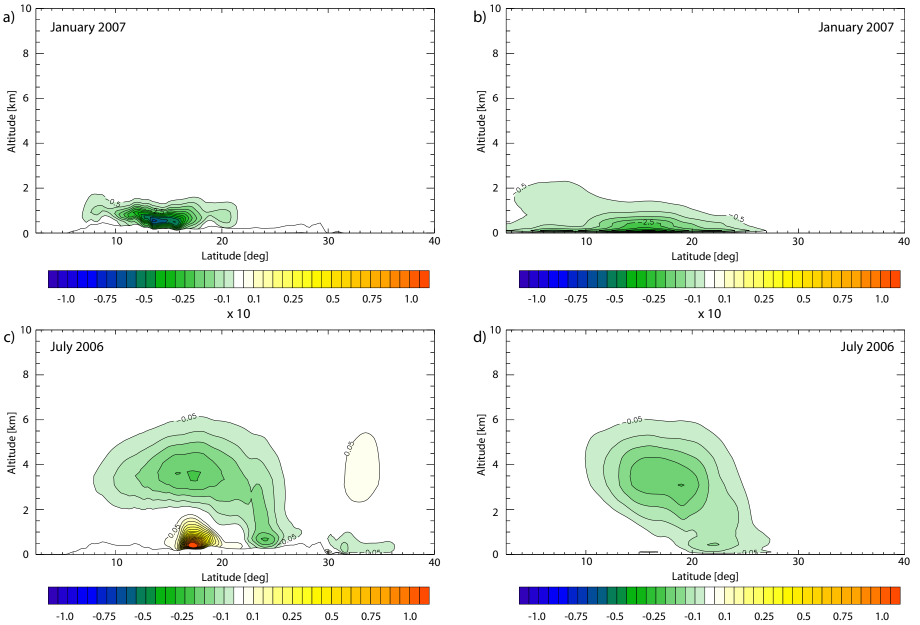

Fig. 7. Vertical distribution of the monthly zonal dust transport [Mg/month] at 10° W (a and c) and 20° W (b and d) for winter (January 2007) and summer (July 2006). Eastward fluxes are positive, westward fluxes are negative corresponding to the common definition of wind vectors.

over the Atlantic and thereby impacted by the marine boundary layer. Both meridional transects start at 2.5° N and end at 40° N, limited by the domain of the regional model LM-MUSCAT. The vertical structure of monthly zonal dust export for winter (January 2007) and summer (July 2006) is shown in Fig. 7. In winter, most of the dust is transported within the lower tropospheric layers (up to 2-3 km height), peaking between 12° N and 16° N with a maximum westward dust flux of 6 Mg/month. The backward dust transport to the African continent is relatively low with 0.2 Mg/month. Due to dust removal from the atmosphere by deposition and spreading of the dust plume into meridional direction, dust flux at 20° W is lower compared to 10° W. But also at 20° W the maximum dust export is located at lower levels and embedded within the trade wind layer. So the maximum of dust export is shifted further northward and peaking at around 17° N with a maximum of 4 Mg/month. A backward transport of 0.06 Mg/month occurs over subtropical latitudes and can be explained by the wind fields related to upper-level trough systems. In summer, a two-layer structure is evident. At levels up to 2 km height, the southwest monsoon is dominant at latitudes up to 20° N. The monsoon air is characterised by moist air masses advected from the Gulf of Guinea northward, whereby the Saharan heat low as part of the low pressure trough of the Hadley circulation is a driving factor. As the moist monsoon air is denser than the dry Saharan air mass, the Saharan air including atmospheric dust overlays the monsoon air and thereby it becomes situated above the trade wind inversion at the top of the monsoon air. Thus westward dust export is evident for the elevated layer, which is often termed Saharan Air Layer (SAL). North of the monsoon air, the Saharan air and thereby the dust layer is situated at lower levels, so westward dust export occurs also at levels below 2 km (Harmattan). Dust sinking downwards from the SAL is enclosed in the trade wind layer and transported back to the African continent. Subtropical dust plumes transported to the Atlantic Ocean might become affected by the anti-cyclonic circulation of the Azores high. The two-layer structure is dominant at 10° W due to the strong impact of the WAM, at 20°W the SAL transporting Saharan dust over the Atlantic as an elevated layer (maximum at around 4 km height) above the trade wind inversion is evident.

The Hadley circulation describes the dominant general atmospheric circulation over the North African continent and the adjacent Atlantic Ocean. Due to seasonal solar inclination, the heat trough as part of the circulation changes locally and thereby the centre of the circulation. This explains the dominance of the dust transport at lower tropospheric levels within the northeast trade wind layer, the so called Harmattan. In summer, the southwest trade wind circulation, which causes the monsoon circulation, replaces the Harmattan over at tropical latitudes and forces the elevated SAL. However, the dust export depends strongly on the latitude. Latitudes up to around 25° N are dominated by westward dust transport, controlled by the trade wind circulation, and by an eastward dust transport at latitudes north of 25° N (Figure 8).

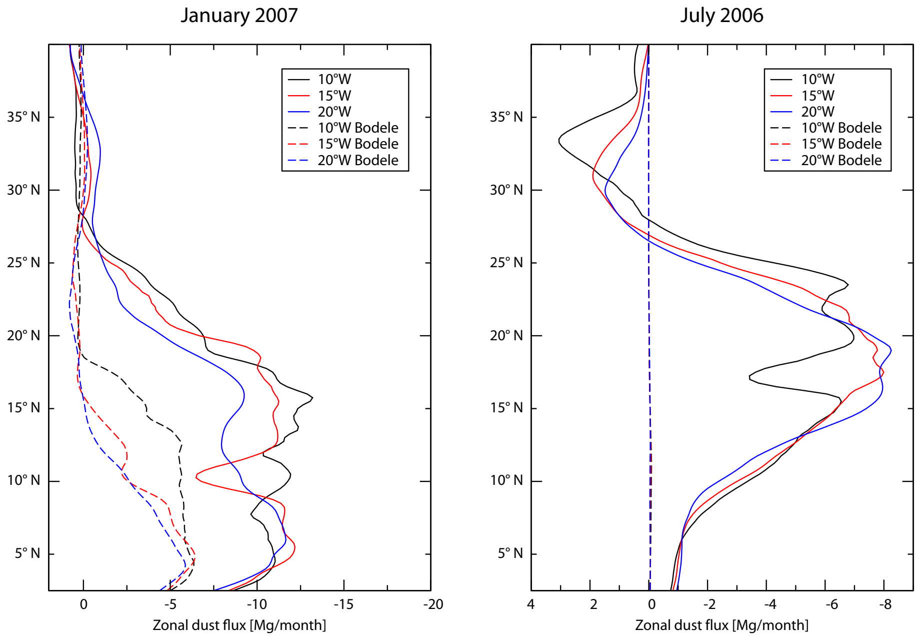

Fig. 8. Zonal dust export [g/month] as function of the latitude, shown for 10° W (black), 15° W (red) and 20° W (blue). Solid lines represent the zonal dust flux related to dust emissions over the entire model domain, dashed lines only contribute to dust emissions over the Bodélé Depression. Seasonal differences regarding latitude of main dust export and changing transport directions are evident comparing (a) winter and (b) summer.

The westward transport is stronger in winter than in summer, which is also affected by lower modelled dust concentrations during summer by LM-MUSCAT. Comparing the eastward (backward) dust transport, in summer higher fluxes occur than in winter. However, beside seasonal changes regarding transport path, the amounts of total column dust fluxes change with the seasons regarding latitude and amount.

3.7 Bodélé Dust

The Bodélé depression is the single most active dust source area of the world (e.g. Prospero et al., 2002) and is characterised by a maximum activity in winter and minimum during summer months (Schepanski et al., 2008). The Bodélé, now located in a hyper-arid zone, was a fresh-water lake about 6,000 years ago (Lake Mega-Chad,Washington et al. (2003)). Today, a hard crust of diatomite covers the former lake floor and provides a large amount of dust by aeolian erosion (Washington et al., 2003). It has been claimed that the diatomite-rich dust originating from the Bodélé Depression has an important fertilising impact on the Amazonian Rain forest in South America (e.g. Koren et al., 2006). Here we use the regional model LM-MUSCAT to evaluate the fraction of Bodélé dust over North Africa and the adjacent East Atlantic (Fig. 9 and 10). Due to changing source activity with the seasons, the contribution of Bodélé dust to the total dust load and deposition changes with seasons as well. During winter, the Bodélé Depression is the most active source regarding the number of active days over the entire Sahara and Sahel domain (Schepanski et al., 2008) and consequently the contribution of Bodélé dust is highest during this season. The present modelling study indicates a fraction of dust originating from the Bodélé of up to 50 % over the Cape Verde archipelago. During summer, when the dust source activity in the Bodélé Depression reaches minimum (Washington and Todd, 2005, Schepanski et al., 2008), its contribution to the atmospheric dust content is low (up to 14 % over the Cape Verde Islands). Beside the low source activity in the Bodélé, other source areas show a high activation frequency and are dominant (Schepanski et al., 2008). Over the northern Sahara and the extra-tropical Atlantic, the contribution of dust originating from the Bodélé is significantly lower than over the Sahel and tropical Atlantic.

The zonal flux of dust originating from the Bodélé indicates a strong seasonal dependence to Bodélé dust mobilisation activity and wind regime determining transport direction (Figs. 9 and 8). In winter, maximum dust export from the Bodélé occurs at up to 1.5 km height within the trade wind layer dominated by the Harmattan winds, peaking at 11-16° N with a westward dust export of -1.4 Mg/month at 10° W and -0.9 Mg/month at 20° W. In summer, the Bodélé dust export is in eastward direction at levels up to 2 km height following the southwest monsoon flow. At levels above the southwest monsoon air, dust transport shows a westward di-

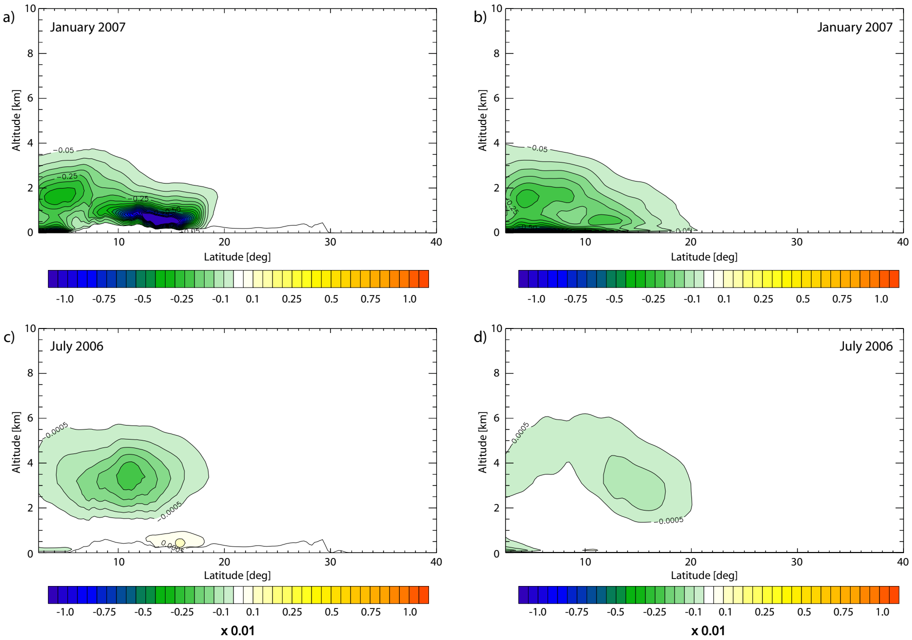

Fig. 9. Vertical distribution of the monthly zonal transport [Mg/month] of dust originating from the Bodélé Depression at 10° W (a and c) and 20° W (b and d) for winter (January 2007) and summer (July 2006). Eastward fluxes are positive, westward fluxes are negative corresponding to the common definition of wind vectors.

rection following the atmospheric circulation as described by the Hadley cell. As the Bodélé is located at around 16° N and northward transport of dust from this region is not dominant at monthly time scales, the atmospheric contribution of dust originating from the Bodélé is not significant at subtropical latitudes.

The export of dust originating from the Bodélé is significantly lower in summer than in winter (Fig. 8) which can be explained by the significantly lower dust source activity during summer months (Schepanski et al., 2008). However, mineral dust from the Bodélé Depression is able to reach higher tropospheric levels (Fig. 9) which is a precondition for long distance transport as crossing the Atlantic. For transport to South America, two preconditions are fulfilled during winter: wind regimes over the tropical Atlantic have a southwestward component and the Bodélé is most active during this season.

3.8 Relationship of AOT, dust column load and deposition

In Section 3.6 the dust flux from North Africa towards the tropical and subtropical Atlantic is described using the regional dust emission and transport model LM-MUSCAT. Kaufman et al. (2005) propose a method to determine dust concentrations as well as dust fluxes and dust deposition from space-borne measurements. The authors used AOT based on MODIS observations to derive dust column concentrations assuming a constant ratio between atmospheric column dust load M_{dust} and AOT τ_{dust}:

$$\frac{M_{dust}}{\tau_{dust}} = 1.33\rho_p \frac{R_{eff}}{Q} = 2.7 \pm 0.4\ g/m^2, \tag{8}$$

with the density of dust particle ρ_p, the effective radius of dust particle R_{eff} and the light extinction efficiency Q. Results from the regional model LM-MUSCAT show a lower M_{dust}/τ_{dust}-ratio of 1 g/m^2 (Fig. 11) instead of 2.7 g/m^2 assumed by Kaufman et al. (2005). The model ratio estimated by averaging the ratio over meridional transects. No differences in this ratio pointing towards a seasonal or regional dependence can be found for the three simulated months but the distribution suggests that local errors will occur in using the average relation. Kaufman et al. (2005) derive the AOT from the satellite measured radiance by using look-up tables for fine-mode aerosol (0.1μm $\leq R_{eff} \leq$ 0.25μm) and coarse-mode aerosol (1μm $\leq R_{eff} \leq$ 2.5μm). Differences for the M_{dust}/τ_{dust}-ratio derived from LM-MUSCAT model results using five independent size bins (radius limits at: 0.1 μm, 0.3 μm, 0.9 μm, 2.6 μm, 8 μm and 24 μm) and the ratio proposed by Kaufman et al. (2005) are likely caused by different size distributions of the atmospheric dust load. The size distributions of dust computed by LM-MUSCAT have been compared with near source measurements (Heinold et al., 2009) and AERONET size distributions (Section 3.5) as well, yielding good agreement. Differences to earlier cases may be related to differences in the considered atmospheric situation.

Kaufman et al. (2005) determine northern Atlantic dust de-

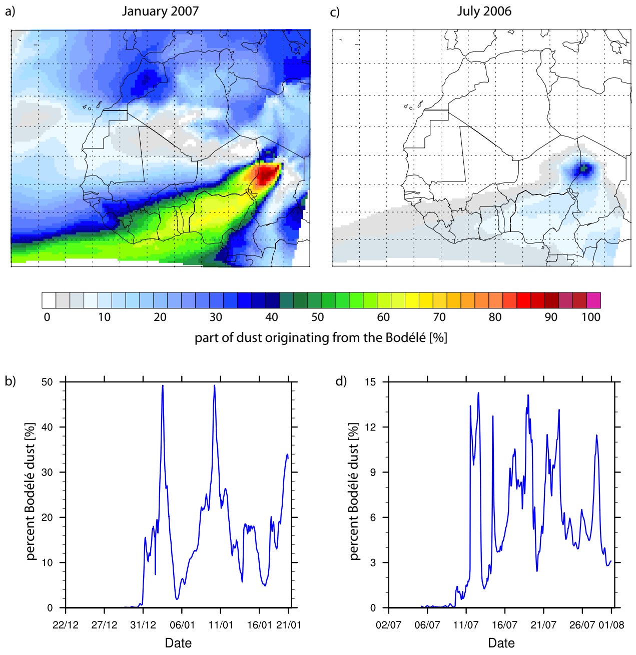

Fig. 10. Percentage of dust concentration originating from the Bodélé Depression source region compared to total dust. (a) and (c) show the horizontal distribution of the contribution of Bodélé, (b) and (d) the part of Bodélé dust over the Cape Verde Islands (16° N; 22° W). (a) and (b) winter (January 2007), (c) and (d) summer (July 2006).

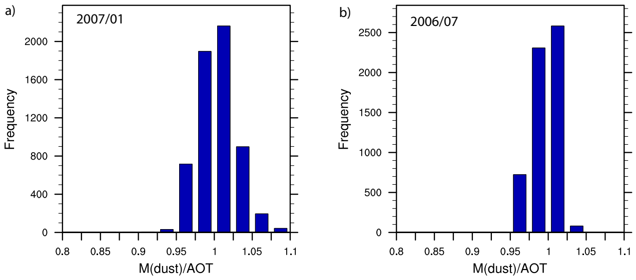

Fig. 11. Frequency distribution of ratio of column dust concentration and AOT for (a) January 2007 and (b) July 2006 following a transect at 16.7° N from 30° W west of the Cape Verde archipelago to 20° E east of the Bodélé Depression.

position fluxes by assuming that the gradient of AOT between two points is related to the atmospheric removal of dust. To test, whether the derivation of mass fluxes from dust column concentrations based on AOT values is realistic, we compute dust fluxes through a meridional transect over the Atlantic along 15° W and 20° W using two different approaches: dust flux computed using Equation 6 at each level (case 1), using Equation 6 but using total dust column concentration and zonal wind speed at a fixed height (800 hPa in winter, 700 hPa in summer) (case 2) assuming that the dust layer is contained at this height, so that the dust transport is related to wind speeds occurring at this height. Kaufman et al. (2005) found a high correlations of dust concentrations and wind velocities at this level, motivating this assumption. But the authors also state that this correlations are not evident for seasons and locations (e.g. Cape Verde in winter), when the dust layer is at lower levels. Comparing to dust fluxes computed directly from dust concentrations at each height level, differences concerning the transported dust amount can be found for case 1 and 2 for winter, when the height of maximum dust concentration does not correlate with the assumed wind layer to account for dust transport. For summer, the assumed relation between height of the dust layer and vertical wind distribution is evident, leading to low differences between case 1 and 2. Figure 12 shows the relation between dust deposition rates and changes in zonal dust transport between 15° W and 20° W for 10°-latitude bands covering the longitudes of main transport region off the North African coast towards the Atlantic. The whole latitudinal region is subdivided as the atmospheric zonal circulation pattern is not similar for each latitudinal band. The atmospheric flow between 10° N-20° N is dominated by the WAM circulation in summer (eastward transport within the trade wind layer (up to 2 km) and westward transport above the trade wind layer (SAL)) and the Harmattan (westward dust transport within the trade wind layer). The region between 20° N and 30° N is characterised by the Harmattan leading to a dominant westward air flow. Strong dust outbreaks might also show an eastward transport of dust due to eddy development. Farther north, between 30° N and 40° N, the anticyclonic flow of the Azores high gain influence on the atmospheric circulation. However, the relation of changes in zonal dust fluxes and deposition requires the assumption, that meridional dust fluxes are negligible. Comparing case 1 and case 2 small differences in the pattern are evident for 10° N-20° N, which are mainly due to the different consideration of the assumption made for the level of transport for case 2. Figure 7 indicates a two layer structure concerning transport direction, representing the impact of the WAM circulation. For case 2, the zonal dust flux is related to winds at a 700 hPa in summer and consequently does not account for the eastward transport within the trade wind layer. At latitudes farther north, the relations between dust deposition and fluxes at the different latitude bands agree for case 1 and case 2.

For satellite based retrievals of dust fluxes, a correct a-priory information on the dust transport height is required. Especially in winter, when transport height might change for individual locations (e.g. over the Cape Verde as shown in Figure 4a) height information on sub-monthly time scales are necessary for accurate estimations of the zonal flux. In general, assuming constant heights of dust transport levels leads to good results for seasons and latitudes, but only where a stationary and mono-modal circulation pattern concerning zonal dust flux can be assumed and meridional dust fluxes

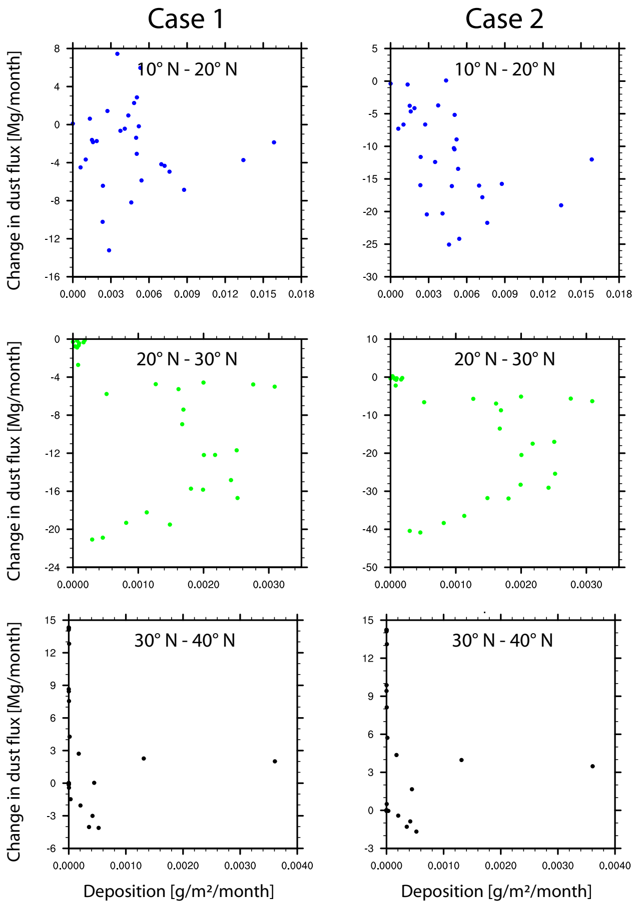

Fig. 12. Scatterplot relating the change of zonal dust flux between 15° W and 20° W (15° W-20° W) to the deposition rates for three different latitudinal bands (10-20° N, 20-30° N and 30-40° N) for case 1 and case 2 for July 2006.

are negligible.

4 Conclusions

The study on Saharan dust export towards the North Atlantic presented here uses results of the regional model system LM-MUSCAT to describe seasonal characteristics of horizontal and vertical dust distributions and their evolution exemplary for three case studies each covering a one-month period in different seasons. Transport of Saharan dust is characterised by the vertical and horizontal distribution of atmospheric dust concentrations, dry and wet deposition, and zonal dust fluxes. As airborne dust is an aerosol affected by meteorological features like wind, rain and turbulence changing with seasons, emission, transport, and deposition show seasonal characteristics.

In these case studies, summer and winter are the most dissimilar seasons with regard to Saharan dust transport. In winter, dust concentration has its maximum in near-surface layers over the tropical latitudes. In summer, dust is transported above the trade winds inversion with a maximum westward transport at the lower subtropic latitudes. The vertical distribution of the zonal dust export clearly shows the relation of meridional dust export with general circulation pattern that is mainly controlled by the Hadley circulation.

Considering the dust source activity controlling the atmospheric dust concentration, the Bodélé is most active during winter. Consequently the contribution of Bodélé dust to the Saharan dust load is maximum in winter months. Considering long-range transport as towards the Amazonian rain forest, preconditions are the best during winter months.

As expected, the modelled ratios of AOTs and deposition rates depends strongly on the height of the dust layer. The relation of dust deposition and AOT is evident for dust transported within the near-surface levels dust deposition is directly related to dust deposition, but this is not the case for elevated dust layers. In general, dust deposition rates cannot be derived directly from AOT measurements which agrees with a finding by a comparing modelling/remote-sensing study by Mahowald et al. (2003).

Zonal dust fluxes have been computed using three different approaches by taking the vertical inhomogeneity of the distribution of dust concentration and wind velocity into account. Gradients of dust fluxes between 15° W and 20° W have been compared to modelled deposition rates pointing towards the role of zonal dust transport especially in case of strong dust plumes, and the transport height.

Regional models provide a comprehensive data set in horizontal and vertical resolution and are able to capture local-scale features. Visual comparisons with the Cloud-Aerosol Lidar and Infrared Pathfinder Satellite Observation instrument (CALIPSO) show promising agreements between modelled vertical distribution of aerosol dust and distributions inferred from attenuated backscatter measurements. A more detailed comparison will be performed in a future study. Model deficiencies of the LM-MUSCAT are evident for July 2006 for which modelled dust optical thickness are too low compared to AOT retrievals and the temporal evolution of dust AOT at some locations was not matched well with AERONET sun-photometer measurements - although at this locations the magnitude of AOT between measurements and model results agree in general. The results for this month indicate a possible overestimation of wet deposition of dust. Too low dust AOT indicates that the modelling of moist convective events which are relevant for dust mobilising processes in this region is deficient. Consequently detailed investigations on dust emission during meteorological summer conditions are required.

Acknowledgements. We thank the Deutscher Wetterdienst (DWD) for good cooperation and support. We also thank D. Tanré, P. Goloub, B. Chatenet, R. T. Pinker, B. Mougenot, O. Hagolle, B. Duchemin, E. Cuevas, J. Cuesta and R. Wagner for his effort in establishing and maintaining AERONET observation sites. The

MODIS and OMI satellite data used in this study were acquired using the GES-DISC Interactive Online Visualization ANd aNalysis Infrastructure (Giovanni) as part of the NASA's Goddard Earth Sciences (GES) Data and Information Services Center (DISC). Furthermore, many thanks to the reviewers comments, especially to R. Miller whose comments and suggestions have been a great help to improve the manuscript.

References

Banta, R. M., Pichugina, Y. L., and a. Brewer, W.: Turbulent Velocity-Variance Profiles in the Stable Boundary Layer Generated by a Nocturnal Low-Level Jet, J. Atmos. Sci., 63, 2700–2719, 2006.

Barkan, J., Kutiel, H., Alpert, P., and Kishcha, P.: Synoptics of dust intrusion days from the African continent into the Atlantic Ocean, J. Geophys. Res., 109, D08 201, doi:10.1029/2003JD004416, 2004.

Berge, E.: Transboundary air pollution in Europe, MSC-W Status Rep. 1997, Part 1 and 2, EMEP/MSC-W Rep. 1/97, norwegian Meteorol. Inst. Oslo, Norway, 1997.

Blackadar, A. K.: Boundary Layer Wind Maxima and Their Significance for the Growth of Nocturnal Inversion, Bulletin of the American Meteorological Society, 38, 283–290, 1957.

Chiapello, I., Bergametti, G., Chatenet, B., Bousquet, P., Dulac, F., and Soares, E. S.: Origins of African dust transported over the northeastern tropical Atlantic, J. Geophys. Res., 102, 13,701–13,709, 1997.

Dubovik, O., Holben, B., Eck, T. F., Smirnov, A., Kaufman, Y. J., King, M. D., Tanre, D., and Slutsker, I.: Variability of Absorption and Optical Properties of Key Aerosol Types Observed in Worldwide Locations, J. Atmos. Sci., 59, 590–608, 2002.

Dubovik, O., Sinyuk, A., Lapyonok, T., Holben, B. N., Mihchenko, M., Yang, P., Eck, T. F., volten, H., Munoz, O., Veihelmann, B., van der Zande, W. J., Leon, J.-F., Sorokin, M., and Slutsker, I.: Application of spheroid models to account for aerosol particle nonsphericity in remote sensing of desert dust, J. Geophys. Res., 111, D11 208, doi:10.1029/2005JD006619, 2006.

Dunion, J. P. and Velden, C. S.: The Impact of the Saharan Air Layer on Atlantic Tropical Cyclone Activity, Bull. Amer. Meteor. Soc., pp. 353–365, 2004.

Eck, T. F., Bhartia, P. K., Hwang, P. H., and Stowe, L. L.: Reflectivity of the Earth's surface and clouds in ultraviolet from satellite observations, J. Geophys. Res., 92, 4287–5296, 1987.

Fung, I., Meyn, S., Tegen, I., Doney, S. C., John, J., and Bishop, J. K. B.: Iron supply and demond in the upper ocean, Global Biogeochem. Cycles, 14, 281–296, 2000.

Gao, Y., Kaufman, Y. J., Tanré, D., Kolber, D., and Falkowski, P. G.: Seasonal Distribution of Aeolian Iron Fluxes to the Global Ocean, Geophys. Res. Lett., 28, 29–32, 2001.

Garratt, J. R.: The atmospheric boundary layer, Cambridge University Press, 1992.

Gillette, D. A.: Saharan Dust, chap. Environmental factors affecting dust emission by wind erosion, pp. 71–94, John Wiley, New York, 1979.

Goudie, A. S. and Middleton, N. J.: Saharan dust storms: nature and consequences, Earth-Science Rev., 56, 179–204, 2001.

Heinold, B., Helmert, J., Hellmuth, O., Wolke, R., Ansmann, A., Marticorena, B., Laurent, B., and Tegen, I.: Regional Modeling of Saharan Dust Events using LM-MUSCAT: Model Description and Case Studies, J. Geophys. Res., 112, D11 204, doi:10.1029/2006JD007443, 2007.

Heinold, B., , Tegen, I., Esselborn, M., Kandler, K., Knippertz, P., Müller, D., Schladitz, A., Tesche, M., Weinzierl, B., Ansmann, A., Althausen, D., Laurent, B., Massling, A., Müller, T., Petzhold, A., Schepanski, K., and Wiedensohler, A.: Regional Saharan Dust Modelling during the SAMUM 2006 Campaign, Tellus, 61B, in press, 2009.

Herman, J. R., Bhartia, P. K., Torres, O., Hsu, C., Seftor, C., and Celarier, E.: Global distribution of UV-absorbing aerosols from Nimbus 7/TOMS data, J. Geophys. Res., 102, 16,922–16,922, 1997.

Holben, B. N., Eck, T. F., Slutsker, I., Tanre, D., Buis, J. P., Setzer, A., Vermote, E., Reagan, J. A., Kaufman, Y. J., Nakajima, T., Lavenu, F., Jankowiak, I., and Smirnov, A.: AERONET - A Federated Instrument Network and Data Archive for Aerosol Characterization, Remote Sens. Environ., 66, 1–16, 1998.

Hsu, N. C., Tsay, S. C., King, M. D., and Herman, J. R.: Aerosol Properties Over Bright-Reflecting Source Regions, IEEE Trans. Geosci. Remote Sens., 42, 557–569, 2004.

Israelevich, P. L., Levin, Z., Joseph, J. H., and Ganor, E.: Desert aerosol transport in the Mediterranean region as inferred from the TOMS aerosol index, J. Geophys. Res., 107, 4572, doi:10.1029/2001JD002011, 2002.

Iversen, J. D. and White, B. R.: Saltation threshold on Earth, Mars and Venus, Sedimentology, 29, 111–119, 1982.

Jacobson, H. A., Jonson, J. E., and Berge, E.: The multi-layer Eulerian model: Model description and evaluation of transboundary fluxes of sulphur and nitrogen species for one year, EMEP/MSC-W Note 2/97, Norwegian Meteorol. Inst., Oslo, Norway, 1997.

Jickells, T. D., An, Z. S., Andersen, K. K., Baker, A. R., Bergametti, G., Brooks, N., Cao, J. J., Boyd, P. W., Duce, R. A., Hunter, K. A., Kawahata, H., Kubilay, N., LaRoche, J., Liss, P. S., Mahowald, N., Prospero, J. M., Ridgwell, A. J., Tegen, I., and Torres, R.: Global Iron Connections Between Desert Dust, Ocean Biogeochemistry, and Climate, Science, 308, 67–71, 2005.

Journet, E., Desboeufs, K. V., Caquineau, S., and Colin, J.-L.: Mineralogy as a critical factor of dust iron solubility, Geophys. Res. Lett., 35, L07 805, doi:10.1029/2007GL031589, 2008.

Kalu, A. E.: The African dust plume: Its characteristics and propagation across west Africa in winter, SCOPE, 14, 95–118, 1979.

Karyampudi, V. M., Palm, S. P., Reagen, J. A., Fang, H., Grant, W. B., Hoff, R. M., Moulin, C., Pierce, H. F., Torres, O., Browell, E. V., and Melfi, S. H.: Validation of the Saharan Dust Plume comceptual Model Using Lidar, Meteosat, and ECMWF Data, Bulletin of the American Meteorological Society, 80, 1045–1075, 1999.

Kaufman, Y. J., Koren, I., Remer, L. A., Tanré, D., Ginoux, P., and Fan, S.: Dust transport and deposition observed from the Terra-Moderate Resolution Imaging Spectroradiometer (MODIS) spacecraft over the Atlantic Ocean, J. Geophys. Res., 110, D10S12, 2005.

Koren, I., Kaufman, Y., Washington, R., Todd, M. C., Rudich, Y., Martins, J. V., and Rosenfeld, D.: The Bodélé depression: a single spot in the Sahara that provides most of the mineral dust to the Amazon forest, Environ. Res. Lett., 1, 014 005, doi:10.1088/1748-9326/1/1/014005, 2006.

Laurent, B., Heinold, B., Tegen, I., Bouet, C., and Cautenet, G.: Surface wind accuracy for modeling mineral dust emission: Comparing two regional models in a Bodélé case study, Geophys. Res. Lett., 35, L09 804, doi:10.1029/2008GL033654, 2008.

Lenschow, D. H. and Stankov, B.: The Rapid Morning Boundary-Layer Transition, J. Atmos. Sci., 36, 2108–2124, 1979.

Luo, C., Mahowald, N., and del Corral, J.: Sensitivity study of meteorological parameters on mineral aerosol mobilization, transport, and distribution, J. Geophys. Res., 108, 4447, doi: 10.1029/2003JD003483, 2003.

Mahowald, N., Bryant, R. G., del Corral, J., and Steinberger, L.: Ephemeral lakes and desert dust sources, Geophys. Res. Lett., 30, 1074, doi:10.1029/2002GL016041, 2003.

Mahowald, N. M., Baker, A. R., Bergametti, G., Brooks, N., Duce, R. A., Jickells, T. D., Kubilay, N., Prospero, J. M., and Tegen, I.: Atmospheric global dust cycle and iron inputs to the ocean, Global Biogeochem. Cycles, 19, GB4025, doi: 10.1029/2004GB002402, 2005.

Marticorena, B. and Bergametti, G.: Modeling the atmospheric dust cycle: 1. Design of a soil-derived dust emission scheme, J. Geophys. Res., 100, 16,415–16,430, 1995.

Middleton, N. J. and Goudie, A. S.: Saharan dust: sources and trajectories, Trans. Inst. Br. Geogr., 26, 165–181, 2001.

Moore, C. M., Mills, M. M., Milne, A., Langlois, R., Achterberg, E. P., Lochte, K., Geider, R. J., and Roche, J. L.: Iron limits primary productivity during spring bloom development in the central North Atlantic, Global Change Biology, 12, 626–634, doi: 10.1111/j.1365-2486.2006.01122.x, 2006.

Nappo, C. J.: Sporadic Breakdowns of Stability in the PBL over Simple and Complex Terrain, Bound.-Layer Meteor., 54, 69–87, 1991.

Neuer, S., Torres-Padrón, M. E., Gelado-Caballero, M. D., Rueda, M. J., Hernández-Brito, J., Davenport, R., and Wefer, G.: Dust deposition pulses to the eastern subtropical North Atlantic gyre: Does ocean's biogeochemistry respond?, Global Biogeochem. Cycles, 18, GB4020, doi:10.1029/2004GB00228, 2004.

Parker, D. J., Burton, R. R., Diongue-Niang, A., Ellis, R. J., Felton, M., Taylor, C. M., Thorncroft, C. D., Bessemoulin, P., and Tompkins, A. M.: Thei diurnal cycle of the West African monsoon circulation, Quart. J. R. Met. Soc., 131, 2839–2860, doi: 10.1256/qj.04.52, 2005.

Prospero, J. M., Ginoux, P., Torres, O., Nicholson, S. E., and Gill, T. E.: Environmental characterization of global sources of atmospheric soil dust identified with the Nimbus 7 Total Ozone Mapping Spectrometer (TOMS) absorbing aerosol product, Rev. Geophys., 40, 1002, doi:10.1029/2000RG000095, 2002.

Reinfried, F., Tegen, I., Heinold, B., Hellmuth, O., Schepanski, K., Cubasch, U., Huebener, H., and Knippertz, P.: Simulations of convectively-driven density currents in the Atlas region using a regional model: Impacts on dust emission and sensitivty to horizontal resolution and convective schemes, J. Geophys. Res., submitted, 2008.

Romero, O. E., Lange, C. B., Swap, R., and Wefer, G.: Eolian-transported freshwater diatoms and phytoliths across the equatorial Atlantic: Temporal changes in Saharan dust transport patterns, J. Geophys. Res., 104, 3211–3222, 1999.

Sarthou, G., Baker, A. R., Blain, S., Achterberg, E. P., Boye, M., Bowie, A. R., Croot, P., Laan, P., de Baar, H. J. W., Jickells, T. D., and Worsfold, P. J.: Atmospheric iron deposition and sea-surface dissolved iron concentrations in the eastern Atlantic Ocean, Deep-Sea Research Part I, 50, 1339–1352, doi: 10.1016/S0967-0637(03)00126-2, 2003.

Sarthou, G., Baker, A. R., Kramer, J., Laan, P., Laës, A., Ussher, S., Achterberg, E. P., de Baar, J. H. W., Timmermans, K. R., and Blain, S.: Influence of atmospheric inputs on the iron distribution in the subtropical North-East Atlantic Ocean, Mar. Chem., 104, 186–202, doi:10.106/j.marchem.2006.11.004, 2007.

Schepanski, K., Tegen, I., Laurent, B., Heinold, B., and Macke, A.: A new Saharan dust source activation frequency map derived from MSG-SEVIRI IR-channels, Geophys. Res. Lett., 34, L18 803, doi:10.1029/2007GL030168, 2007.

Schepanski, K., Tegen, I., Todd, M. C., Heinold, B., Bönisch, G., Laurent, B., and Macke, A.: Meteorological processes forcing Saharan dust emission inferred from MSG-SEVIRI observations of sub-daily dust source activation, J. Geophys. Res., submitted, 2008.

Shao, Y., Raupach, M. R., and Leys, J. F.: A model for predicting aeolian sand ddrift and dust entrainment on scales from paddock to region, Aust. J. Soil Res., 34, 309–342, 1996.

Sinyuk, A., Torres, O., and Dubovik, O.: Combined use of satellite and surface observations to infer the imaginary part of refractive index of Saharan dust, J. Geophys. Res., 30, 1081, doi:10.1029/2002GL016189, 2003.

Steppler, J., Doms, G., Schättler, U., Bitzer, H. W., Gassmann, A., Damrath, U., and Gregoric, G.: Meso-gamma scale forecast using the nonhydrostatic model LM, Meteor. Atmos. Phys., 82, 75–96, 2003.

Tegen, I., Harrison, S. P., Kohfeld, K., and Prentice, I. C.: Impact of vegetation and preferential source areas on global dust aerosol: Results from a model study, J. Geophys. Res., 107, 4576, doi: 10.1029/2001JD000963, 2002.

Tegen, I., Heinold, B., Todd, M., Helmert, J., Washington, R., and Dubovik, O.: Modelling soil dust aerosol in the Bodele depression during the BoDEx campaign, ACPs, 6, 4345–4339, 2006.

Tesche, M., Ansmann, A., Müller, D., Althausen, D., Mattis, I., Heese, B., Freudenthaler, V., Wiegner, M., Esselborn, M., Pisani, G., and Knippertz, P.: Vertical profiling of Saharan dust with Raman lidars and airborne HSRL in southern Morocco during SAMUM, Tellus, 61B, in press, 2009.

Tiedtke, M.: A comprehensive mass flux scheme for cumulus parameterisation in large-scale models, Mon. Wea. Rev., 117, 1779–1799, 1989.

Torres, O., Bhartia, T. K., Herman, J. R., Sinyuk, A., Ginoux, P., and Holben, B.: A long-term record of aerosol optical depth from TOMS observations and comparison to AERONET measurements, J. Atmos. Sci., 59, 398–413, 2002.

Tsyro, S. and Erdman, L.: Parameterisation of aerosol deposition processes in EMEP MSC-E and MSC-W transport models, EMEP/MSC-W Note 7/00, Norwegian Meteorol. Inst., Oslo, Norway, 2000.

Tulet, P., Mallet, M., Pont, V., Pelon, J., and Boone, A.: The 7-13 March 2006 dust storm over West Africa: Generation, transport, and vertical stratification, JoGRs, 113, D00D08, doi: 10.1029/2008JD009871, 2008.

Veihelmann, B., Levelt, P. F., Stammes, P., and Veefkind, J. P.: Simulation study of the aerosol information content in OMI spectral reflectance measurements, Atmos. Chem. Phys., 7, 3115–3127, 2007.

Washington, R. and Todd, M. C.: Atmospheric contronls on mineral dust emission from the Bodélé Depression, Chad: The role of the low level jet, Geophys. Res. Lett., 32, L17 701, doi:10.1029/2005GL023597, 2005.

Washington, R., Todd, M., Middleton, N. J., and Goudie, A. S.: Dust-Storm Source Areas Determined by the Total Ozone Monitoring Spectrometer and Surface Observations, Annals of the Association of American Geographers, 93, 297–313, 2003.

Wedepohl, K. H.: The composition of the continental crust, Geochemica et Cosmochimica Acta, 59, 1217–1232, 1995.

Westphal, D. L., Toon, O. B., and Carlson, T. N.: A Two-Dimensional Numerical Investigation of the Dynamics and Microphysics of Saharan Dust Storms, J. Geophys. Res., 92, 3027–3049, 1987.

Wolke, R., Hellmuth, O., Knoth, O., Schröder, W., Heinrich, B., and Renner, E.: The chemistry-transport modeling system LM-MUSCAT: Description and CityDelta applications, in: Air Polution Modeling and Its Aplication XVI, edited by Borrego, C. and Incecik, S., Proceedings of twenty-sixth NATO/CCMS international technical meeting on air polution modeling and its application, 2004a.

Wolke, R., Hellmuth, O., Knoth, O., Schröder, W., and Renner, E.: The parallel model system LM-MUSCAT for chemistry-transport simulations: Coupling scheme, parallelization and application, Parallel Computing: Software Technology, Algorithms, Architectures, and Applications, pp. 363–370, 2004b.

Zender, C. S. and Newman, D.: Spatial heterogeneity in aeolian erodibility: Uniform, topographic, geomorphic, and hydrologic hypotheses, J. Geophys. Res., 108, 4543, doi:10.1029/2002JD003039, 2003.

Chapter 7

Outlook

The present work bases on observation data and model simulations. It is shown, that the usage of both leads to a more complete description of the Saharan dust cycle than each single dataset will give. The complementary usage of such datasets facilitate the improvement of the knowledge on atmospheric dust and its effects on the environment. Nevertheless, future studies have to be done.

Modelling studies are limited e.g. by the accuracy of parametrisations, input variables, and fields. To estimate the magnitude of errors made by necessary assumptions for parametrisation ensemble runs will be a good possibility. Thereby, several similar model runs but with slightly varying input parameters will be computed, approximating the most realistic case by the probability of occurrence of a specific evolution. In the case of dust modelling, e.g. several different particle characteristics concerning their optical properties and size distribution could be assumed. Dust particles act on the atmospheric conditions due to their direct and indirect radiative effect, that ensemble runs of different particle characteristics will improve the approximation of the real case. This ensembles for atmospheric models will also account for the effect of radiative feedback mechanisms on meteorological conditions and thereby allow for a feedback on processes forcing or limiting dust emission. This would not be possible with stand-alone radiative transport models.
Long-term observations of dust storm frequencies and dust optical thickness point towards strong interannual variability of atmospheric dust. The improvement of our knowledge of meteorological conditions responsible for dust emission, transport and deposition, but also teleconections to remote atmospheric and oceanic circulation pattern will help to understand interannual variability, also with regard to a changing environment. To address this question modelling studies as well as long-term observations (ground- and space-borne) are required.
Interactions of atmospheric dust and monsoon circulations as well as the development of tropical cyclones (up to Hurricanes and Typhoons) are the topic of recent modelling and measurement studies. Improved knowledge on the interaction of tropical atmospheric elements (e.g. African Easterly Jet, West African Monsoon circulation) and dust emission as well as interactions of dust particles and cloud development, convection or stability,

will help to improve forecasts and climate projections.
In the present work dust source activities over North Africa are investigated and characterised on a sub-daily scale. An extension of this study with such a comparably high temporal resolution to other hyper-arid, arid and semi-arid areas will be of interest. There, differences concerning geomorphology and atmospheric circulation are evident. Furthermore, the identification of individual source area and an improved knowledge of meteorological conditions during dust emission will help to understand dust feedback mechanisms which depend on the characteristics of dust source areas (e.g. mineralogy), transport path (e.g. chemical reactions on particle's surface) and the deposition fluxes (fertilisation of remote areas).
Besides the effect of mineral dust on the atmosphere, dust impacts on oceanic and terrestrial biosphere. Dust as transport medium for micro-nutrients act on the biological productivity of remote areas, and thereby on the atmospheric CO_2-cycle and the climate system. Furthermore, iron and phosphorous transported to the Ocean by mineral dust particles enhance nitrogen fixation, an important process for the global nitrogen cycle. The precise knowledge of dust source conditions may help to characterise the mineralogical and chemical composition of dust, providing improved estimates of their deposition fluxes. This may provide useful input for models describing microbiological processes in the surface ocean.

An improved knowledge on the spatio-temporal distribution of dust sources and its activation will help to give a more accurate estimation of interactions of mineral dust and the environment. Furthermore, an improved understanding of dust feedback mechanisms will help to describe the role of airborne dust for a changing environment.

List of Abbreviations

AEJ	African easterly jet
AERONET	AErosol RObotic NETwork
AEW	African easterly wave
AI	Absorbing Aerosol Index
AOT	Aerosol Optical Thickness
BL	Boundary Layer
BT	Brightness temperature
BTD	Brightness temperature difference
CALIPSO	Cloud-Aerosol Lidar and Infrared Pathfinder Satellite Observations
CCN	Cloud condensation nuclei
CH	Channel
DSA	Dust source activation
DSAF	Dust source activation frequency
DWD	Deutscher Wetterdienst, German Weather Service
ECMWF	European Center for Medium-Range Weather Forecast
ERA-40	ECMWF 45-year reanalysis data
EUMETSAT	European Organisation for the Exploitation of Meteorological Satellites
HNLC	High-nitrate, low chlorophyll
IDDI	Infrared Difference Dust Index
IR	Infrared, wavelength spectrum
ITCZ	Inter-tropical convergence zone
ITD	Inner-tropical discontinuity
LLJ	Low-level jet
LM	Lokalmodell, meso-scale model of German Weather Service (DWD)
MCS	Meso-scale convective system
MUSCAT	MUlti Scale Chemistry and Aerosol Transport Model
MSG	Meteosat Second Generation
NAO	North Atlantic Oscillation
NASA	National Aeronautics and Space Agency, United States
NBL	Nocturnal boundary layer
NIR	Near-infrared
OMI	Ozone Monitoring Instrument
SAL	Saharan Air Layer

SEVIRI	Spinning and Enhanced Visible and InfraRed Imager
TOMS	Total Ozone Mass Spectrometer
TRACES	Ocean – Atmosphere – Land Impacts on TRopical Atlantic EcoSystems
UTC	Universal time, coordinated
UV	Ultraviolet, wavelength spectrum
VIS	Visible
WV	Water vapour

Bibliography

Ackerman, S. A. (1997), Remote sensing aerosol using satellite infrared observations, *J. Geophys. Res.*, *102*(D14), 17,069–17,079.

Allen, M. D., and O. G. Raabe (1982), Re-evaluation of Millikan's oil drop data for the motion of small particles in air, *Journ. of Aerosol Sci.*, *13*(6), 537–547, doi:10.1016/0021-8502(82)90019-2.

Allen, M. D., and O. G. Raabe (1985), Slip correction measurements of spherical solid aerosol-particles in an improved Millikan apparatus, *Aerosol Science and Technology*, *4*(3), 269–286.

Alpert, P., and B. Ziv (1989), The Sharav Cyclone - observations and some theoretical considerations, *J. Geophys. Res.*, *94*, 18,495–18,514.

Alpert, P., B. I. Neeman, and Y. Shay-el (1990), Climatological analysis of Mediterranean cyclones using ECMWF data, *Tellus*, *42A*, 65–77.

Arimoto, R., B. J. Ray, N. F. Lewis, U. Tomaza, and R. A. Duce (1997), Mass particle size distribution of atmospheric dust and the dry deposition of dust to the remote ocean, *J. Geophys. Res.*, *102*, 15,867–15,874.

Avila, A., and J. Penuelas (1999), Increasing frequency of Saharan rains over northeastern Spain and its ecological consequences, *The Science of the Total Environment*, *228*(2-3), 153–156.

Bagnold, R. A. (1941), *The Physics of Blown Sand and Desert Dunes*, 265 pp., Methuen, New York.

Banta, R., Y. L. Pichugina, and R. K. Newsom (2003), Realtionship between Low-Level Jet Properties and Turbulence Kinetic Energy in the Nocturnal Stable Boundary Layer, *J. Atmos. Sci.*, *60*, 2549–2555.

Banta, R. M., R. K. Newsom, J. K. Lundquist, Y. L. Pichugina, R. L. Coulter, and L. J. Mahrt (2002), Nocturnal low-level jet characteristics over Kansas during CASES-99, *Bound.-Layer Meteor.*, *105*, 221–252.

Banta, R. M., Y. L. Pichugina, and W. A. Brewer (2006), Turbulent Velocity-Variance Profiles in the Stable Boundary Layer Generated by a Nocturnal Low-Level Jet, *J. Atmos. Sci.*, *63*, 2700–2719.

Barkan, J., H. Kutiel, P. Alpert, and P. Kishcha (2004), Synoptics of dust intrusion days from the African continent into the Atlantic Ocean, *J. Geophys. Res.*, *109*, D08,201, doi:10.1029/2003JD004416.

Barton, I. J., A. J. Prata, I. G. Watterson, and S. A. Young (1992), Identification of the mount Hudson volcanic cloud over SE Australia, *Geophys. Res. Lett.*, *19*(12), 1211–1214.

Bücher, A., and J. Dessens (1992), Saharan dust over France and England, 6-9 March 1991, *J. Meteor.*, *17*, 226–233.

Berge, E. (1997), Transboundary air pollution in Europe, *MSC-W Status Rep. 1997, Part 1 and 2, EMEP/MSC-W Rep. 1/97*, Norwegian Meteorol. Inst. Oslo, Norway.

Berkofsky, L. (1982), A heuristic investigation to evaluate the feasibility of developing a desert dust prediction model, *Mon. Wea. Rev.*, *110*, 2055–2062.

Berry, G., and C. Thorncroft (2005), Case study on an intense African easterly wave, *Mon. Wea. Rev.*, *133*, 752–766, doi:10.1175/MW2884.1.

Berry, G., C. Thorncroft, and T. Hewson (2007), African Easterly Waves during 2004 - Analysis Using Objective Techniques, *Mon. Wea. Rev.*, *135*, 1251–1267, doi: 10.1175/MWR3343.1.

Blackadar, A. K. (1957), Boundary Layer Wind Maxima and Their Significance for the Growth of Nocturnal Inversion, *Bull. Amer. Meteor. Soc.*, *38*(5), 283–290.

Bonner, W. D. (1968), Climatology of the Low Level Jet, *Mon. Wea. Rev.*, *96*(12), 833–850.

Bonner, W. D., and J. Paegle (1970), Diurnal Variations in Boundary Layer Winds over the South-Central United States in Summer, *Mon. Wea. Rev.*, *98*(10), 735–744.

Bouet, C., G. Cautenet, R. Washington, M. C. Todd, B. Laurent, B. Marticorena, and G. Bergametti (2007), Mesoscale modeling of aeolian dust emission during the BoDEx 2005 experiment, *Geophys. Res. Lett.*, *34*(7), L07,812, doi:10.1029/2006GL029184.

Boy, J., and W. Wilke (2008), Tropical Andean forest derives calcium and magnesium from Saharan dust, *Global Biogeochem. Cycles*, *22*, GB1027, doi:10.1029/2007GB002960.

Brooks, N., and M. Legrand (2000), Dust variability over northern Africa and rainfall in the Sahel, in *Linking Climate Change to Landsurface Change*, edited by S. J. McLaren and D. Kniveton, pp. 1–25, Kluwer Academic Publishers, Dordecht, The Netherlands.

Brost, R. A., and J. C. Wyngaard (1978), A Model Study of the Stably Stratified Planetary Boundary Layer, *J. Atmos. Sci.*, *35*(8), 1427–1440.

Browning, K. A., and G. W. Bryant (1975), An example of rainbands associated with stationary longitudinal circulations in the planetary boundary layer, *Quart. J. R. Met. Soc.*, *101*, 893–900.

Bullard, J., M. Baddock, G. McTainsh, and J. Leys (2008), Sub-basin scale dust source geomorphology detected using MODIS, *Geophys. Res. Lett.*, *35*(15), L15,404, doi: 10.1029/2008GL033928.

Burpee, R. W. (1972), The origin and structure of easterly waves in the lower troposphere of North Africa, *J. Atmos. Sci.*, *29*, 77–90.

Burpee, R. W. (1974), Characteristics of North African easterly waves during the summers of 1968 and 1969, *J. Atmos. Sci.*, *31*, 1556–1570.

Carlson, T. N. (1969), Some remarks on African disturbances and their progress over the tropical Atlantic, *Mon. Wea. Rev.*, *97*, 716–726.

Carlson, T. N. (1979), Atmospheric Turbidity in Saharan Dust Outbreaks as Determined by Analyses of Satellite Brightness Date, *Mon. Wea. Rev.*, *107*, 322–335.

Carlson, T. N., and J. M. Prospero (1972), The Large-Scale Movement of Saharan Air Outbreaks over the Northern Equatorial Atlantic, *J. Appl. Meteor.*, *11*, 283–297.

Cavazos, C., M. C. Todd, and K. Schepansi (2008), Numerical model simulation of the saharan dust event of march 2006, *J. Geophys. Res.*, revised.

Chesters, D., L. W. Uccellini, and W. D. Robinson (1983), Low-Level Water Vapor Fields from the VISSR Atmospheric Sounder (VAS) “Split Window” Channels, *J. Climate Appl. Meteor.*, *22*, 725–743.

Chiapello, I., and C. Moulin (2002), TOMS and METEOSAT satellite records of the variability of Saharan dust transport over the Atlantic during the last two decades (1979-1997), *Geophys. Res. Lett.*, *29*(8), L1176.

Chiapello, I., G. Bergametti, L. Gomes, B. Chatenet, F. Dulac, J. Pimenta, and E. S. Suares (1995), An additional low layer transport of Sahelian and Saharan dust over the North-Eastern Tropical Atlantic, *Geophys. Res. Lett.*, *22*(23), 3191–3194.

Chiapello, I., G. Bergametti, B. Chatenet, P. Bousquet, F. Dulac, and E. S. Soares (1997), Origins of African dust transported over the northeastern tropical Atlantic, *J. Geophys. Res.*, *102*(D12), 13,701–13,709.

Chiapello, I., C. Moulin, and J. M. Prospero (2005), Understanding the long-term variability of African dust transport across the Atlantic as recorded in both Barbados surface concentrations and large-scale Total Ozone Mapping Spectrometer (TOMS) optical thickness, *J. Geophys. Res.*, *110*, D18S10.

Chimonas, G. (2005), The Nighttime Accelerations of the Wind in the Boundary Layer, *Bound.-Layer Meteor.*, *116*, 519–531, doi:10.1007/s10546-005-0609-x.

Coen, M. C., E. Weingartner, D. Schaub, C. Hueglin, C. corrigan, S. Henning, M. Schwikowski, and U. Baltensperger (2004), Saharan dust events at the Jungfraujoch:

detection by wavelength dependence of the single scattering albedo and first climatology analysis, *Atmos. Chem. Phys.*, *4*, 2465–2480.

Cook, K. H. (1999), Generation of the African easterly jet and its role in determining West African precipitation, *J. Climate*, *12*, 1165–1184.

Criado, C., and P. Dorta (2003), An unusual "blood rain" over the Canary Islands (Spain). The storm of January 1999, *Journ. Arid Environm.*, *55*, 765–783.

D'Almeida, G. A. (1986), A Model for Saharan Dust Transport, *J. Climate Appl. Meteor.*, *25*, 903–916.

Davis, P. A. (2000), Development and mechanisms of the nocturnal jet, *Meteorol. Appl.*, *7*(3), 239–246.

DeMott, P. J., K. Sassen, M. R. Poellot, D. Baumgardner, D. C. Rogers, S. D. Brooks, A. J. Prenni, and S. M. Kreidenweis (2003), African dust aerosols as atmospheric cloud ice nuclei, *Geophys. Res. Lett.*, *30*(14), L1732.

Drobinski, P., B. Sultan, and S. Janicot (2005), Role of the Hoggar Masif in the West African monsoon onset, *Geophys. Res. Lett.*, *32*(1), L01,705, doi: 10.1029/2004GL020710.

Duce, R. A. (1995), Sources, Distributions, and Fluxes of Mineral Aerosols and Their Relationship to Climate, in *Dahlem Workshop on Aerosol Forcing of Climate*, edited by R. J. Charton and J. Heintzenberg, pp. 43–72, John Wiley, Chichester, U. K.

Dunion, J. P., and C. S. Velden (2004), The Impact of the Saharan Air Layer on Atlantic Tropical Cyclone Activity, *Bull. Amer. Meteor. Soc.*, pp. 353–365.

Eck, T. F., P. K. Bhartia, P. H. Hwang, and L. L. Stowe (1987), Reflectivity of the Earth's surface and clouds in ultraviolet from satellite observations, *J. Geophys. Res.*, *92*, 4287–4296.

Ellis, W. G., and J. T. Merrill (1995), Trajectories for Saharan dust transported to Barbados using Stokes Law to describe gravitational settling, *J. Appl. Meteor.*, *34*(7), 1716–1726.

Engelstaedter, S., and R. Washington (2007), Atmospheric controls on the annual cycle of North African dust, *J. Geophys. Res.*, *112*, D03,103.

Engelstaedter, S., I. Tegen, and R. Washington (2006), North African dust emission and transport, *Earth-Science Reviews*, *79*, 73–100, doi:10.1016/j.erscirev.2006.06.004.

Enger, L., D. Koračin, and X. Yang (1993), A Numerical Study of Boundary Layer Dynamics in a Mountain Valley, *Bound.-Layer Meteor.*, *66*, 357–394.

Erel, Y., U. Dayan, R. Rabi, Y. Rudich, and M. Stein (2006), Trans Boundary Transport of Pollutants by Atmospheric Mineral Dust, *Environ. Sci. Technol.*, *40*, 2996–3005.

Evan, A., A. K. Heidinger, and P. Knippertz (2006), Analysis of winter dust activity off the coast of West Africa using a new 24-year over-water advanced very high resolution radiometer satellite dust climatology, *J. Geophys. Res.*, *111*, D12,210, doi: 10.1029/2005JD006336.

Fan, S.-M., W. J. Moxim, and H. Levy (2006), Aeolian input of bioavailable iron to the ocean, *Geophys. Res. Lett.*, *33*(7), L07,602, doi:10.1029/2005GL024852.

Findlater, J. (1972), Aerial explorations of the low-level cross-equatorial current over Eastern Africa, *Quart. J. R. Met. Soc.*, *98*, 274–289.

Flamant, C., J.-P. Chaboureau, D. J. Parker, C. M. Taylor, J.-P. Cammas, O. Bock, F. Timouk, and J. Pelon (2007), Airborne observations of the impact of a convective system on the planetary boundary layer thermodynamics and aerosol distsribution in the inter-tropical discontinuity region of the West African Monsoon, *Quart. J. R. Met. Soc.*, *133*, 1175–1189, doi:10.1002/qj.97.

Franzen, L. G., J. O. Mattson, and U. Martensson (1994), Yellow snow over the Alps and sub-Arctic from dust storm in Africa, March 1991, *Ambio*, *23*(3), 233–235.

Fraser, Y. J. K. R. S. (1997), The effect of smoke particles on clouds and climate forcing, *Science*, *227*, 1573–1728.

Fung, I., S. Meyn, I. Tegen, S. C. Doney, J. John, and J. K. B. Bishop (2000), Iron supply and demand in the upper ocean, *Global Biogeochem. Cycles*, *14*, 281–296.

Ganor, E. (1994), The frequency of Saharan dust episodes over Tel Aviv, Israel, *Atmos. Environ.*, *28*(17), 2867–2871.

Gao, Y., Y. J. Kaufman, D. Tanré, D. Kolber, and P. G. Falkowski (2001), Seasonal Distribution of Aeolian Iron Fluxes to the Global Ocean, *Geophys. Res. Lett.*, *28*(1), 29–32.

Garratt, J. R. (1992), *The atmospheric boundary layer*, Cambridge University Press.

Gatz, D. F., and J. M. Prospero (1996), A large silicon-aluminium aerosol plume in central Illinois: North African desert dust?, *Atmos. Environ.*, *30*(22), 3789–3799.

Gillette, D. (1978), A wind tunnel simulation of the erosion of soil: Effect of soil texture, sandblasting, wind speed, and soil consolidation on dust production, *Atmos. Environ.*, *12*, 1735–1743.

Gillette, D. A. (1979), Environmental factors affecting dust emission by wind erosion, in *Saharan Dust*, edited by C. Morales, pp. 71–94, John Wiley, New York.

Ginoux, P., M. Chin, I. Tegen, J. M. Prospero, B. Holben, O. Dubovik, and S.-J. Lin (2001), Sources and distributions of dust aerosols simulated with the GOCART model, *J. Geophys. Res.*, *106*(D17), 20,255–20,273.

Ginoux, P., J. M. Prospero, O. Torres, and M. Chin (2004), Long-term simulation of global dust distribution with the GOCART model: correlation with North Atlantic Oscillation, *Environment Modelling & Software*, *19*(10.1016/S1364-8152(03)00114-2), 113–128.

Goudie, A. S., and N. J. Middleton (1992), The changing frequency of dust storms through time, *Clim. Change*, *20*, 197–225.

Goudie, A. S., and N. J. Middleton (2001), Saharan dust storms: nature and consequences, *Earth-Science Rev.*, *56*, 179–204.

Griffin, D. W., and C. A. Kellogg (2004), Dust Storms and Their Impact on Ocean and Human Health: Dust in Earth's Atmosphere, *EcoHealth*, *1*, 284–295.

Grini, A., C. S. Zender, and P. R. Colarco (2002), Saltation sandblasting behaviour during mineral dust aerosol production, *Geophys. Res. Lett.*, *29*(18), 1868, doi: 10.1029/2002GL015248.

Grini, A., G. Myhre, C. S. Zender, and I. S. A. Isaksen (2005), Model simulations of dust sources and transport in the global atmosphere: Effects of soil erodibility and wind speed variability, *J. Geophys. Res.*, *110*, D02,205, doi:10.1029/2004JD005037.

Guerzoni, S., E. Molinaroli, and R. Chester (1997), Saharan dust inputs to the western Mediterranean Sea: depositional patterns, geochemistry and sedimentological implications, *Deep-Sea Research II*, *44*(3-4), 631–654.

Ha, K.-J., and L. Mahrt (2001), Simple Inclusion of z-less Turbulence within and above the Modeled Nocturnal Boundary Layer, *Mon. Wea. Rev.*, *129*, 2136–2143.

Hamilton, R. A., and J. W. Warchbold (1945), Meteorology of Nigeria and adjacent territory, *Quart. J. R. Met. Soc.*, *71*, 231–265.

Haywood, J., P. Francis, S. Osborne, M. Glew, N. Loeb, E. Highwood, D. Tanré, G. Myhre, P. Formenti, and E. Hirst (2003), Radiative properties and direct radiative effect of Saharan dust measured by the C$-$130 aircraft during SHADE: 1. Solar spectrum, *J. Geophys. Res.*, *208*(D18), 8577, doi:10.1029/2002JD002687.

Heinold, B., J. Helmert, O. Hellmuth, R. Wolke, A. Ansmann, B. Marticorena, B. Laurent, and I. Tegen (2007), Regional Modeling of Saharan Dust Events using LM-MUSCAT: Model Description and Case Studies, *J. Geophys. Res.*, *112*, D11,204, doi: 10.1029/2006JD007443.

Heinold, B., I. Tegen, M. Esselborn, K. Kandler, P. Knippertz, D. Müller, A. Schladitz, M. Tesche, B. Weinzierl, A. Ansmann, D. Althausen, B. Laurent, A. Massling, T. Müller, A. Petzhold, K. Schepanski, and A. Wiedensohler (2008a), Regional Saharan Dust Modelling during the SAMUM 2006 Campaign, *Tellus*, *61B*, doi:10.1111/j.1600-0889.2008.00387.x.

Heinold, B., I. Tegen, K. Schepanski, and O. Hellmuth (2008b), Dust Radiative Feedback on Saharan Boundary Layer Dynamics and Dust Mobilization, *Geophys. Res. Lett.*, *35*, L20,817, doi:10.1029/2008GL035319.

Herman, J. R., P. K. Bhartia, O. Torres, C. Hsu, C. Seftor, and E. Celarier (1997), Global distribution of UV-absorbing aerosols from Nimbus 7/TOMS data, *J. Geophys. Res.*, *102*(D14), 16,922–16,922.

Holben, B. N., T. F. Eck, I. Slutsker, D. Tanre, J. P. Buis, A. Setzer, E. Vermote, J. A. Reagan, Y. J. Kaufman, T. Nakajima, F. Lavenu, I. Jankowiak, and A. Smirnov (1998), AERONET - A Federated Instrument Network and Data Archive for Aerosol Characterization, *Remote Sens. Environ.*, *66*, 1–16.

Holton, J. R. (1967), The diurnal boundary layer wind oscillation above sloping terrain, *Tellus*, *19*(2), 199–205.

Hoose, C., U. Lohmann, R. Erdin, and I. Tegen (2008), The global influence of dust mineralogical composition on heterogeneous ice nucleation in mixed-phase clouds, *Environ. Res. Lett.*, *3*(2), 025,003, doi:10.1088/1748-9326/3/2/025003.

Houze, R. A. J., S. A. Rutledge, B. F. Smull, and P. Doge (1990), Mesoscale organization of springtime rainstorms in Oklahoma, *Mon. Wea. Rev.*, *118*, 613–654.

Hoxit, L. R. (1975), Diurnal Variations in Planetary Boundary-Layer Winds over Land, *Bound.-Layer Meteor.*, *8*, 21–38.

Hsu, N. C., S. C. Tsay, M. D. King, and J. R. Herman (2004), Aerosol Properties Over Bright-Reflecting Source Regions, *IEEE Trans. Geosci. Remote Sens.*, *42*(3), 557–569.

Hurrell, J. W. (1995), Decadal trend in the North Atlantic Oscillation: Regional temperatures and precipitations, *Science*, *269*, 676–679.

IPCC (2007), *Climate Change 2007: The Physical Science Basis.*, Contribution of Working Group I to the Forth Assessment Report of the Intergovernmental Panel on Climate Change, edited by S. Solomon and D. Quin and M. Manning and Z. Chen and M. Marquis and K.B. Averyt and M. Tignor and H.L. Miller, Cambridge, United Kingdom and New York, NY, USA.

Israelevich, P. L., Z. Levin, J. H. Joseph, and E. Ganor (2002), Desert aerosol transport in the Mediterranean region as inferred from the TOMS aerosol index, *J. Geophys. Res.*, *107*(D21), 4572, doi:10.1029/2001JD002011.

Iversen, J. D., and B. R. White (1982), Saltation threshold on Earth, Mars and Venus, *Sedimentology*, *29*, 111–119.

Jacobson, H. A., J. E. Jonson, and E. Berge (1997), The multi-layer Eulerian model: Model description and evaluation of transboundary fluxes of sulphur and nitrogen species for one year, *EMEP/MSC-W Note 2/97*, Norwegian Meteorol. Inst., Oslo, Norway.

Jaffe, D., J. Snow, and O. Cooper (2003), the April 2001 Asian dust events: transport and substantial impact on surface particulate matter concentrations across the United States, *EOS transactions*.

Jickells, T. D., Z. S. An, K. K. Andersen, A. R. Baker, G. Bergametti, N. Brooks, J. J. Cao, P. W. Boyd, R. A. Duce, K. A. Hunter, H. Kawahata, N. Kubilay, J. LaRoche, P. S. Liss, N. Mahowald, J. M. Prospero, A. J. Ridgwell, I. Tegen, and O. Torres (2005), Global Iron Connections Between Desert Dust, Ocean Biogeochemistry, and Climate, *Science*, *308*(5718), 67–71.

Johansen, A. M., R. L. Siefert, and M. R. Hoffmann (2000), Chemical composition of aerosols collected over the tropical North Atlantic, *J. Geophys. Res.*, *105*(D12), 15,227–15,312.

Johnson, B. T., S. R. Osborne, and J. M. Haywood (2008), Aircraft measurements of biomass burning aerosol over West Africa during DABEX, *J. Geophys. Res.*, *113*(D00C06), doi:10.1029/2007JD009741.

Jones, C., N. Mahowald, and C. Luo (2003), The role of easterly waves on African desert dust transport, *J. Climate*, *16*(22), 3617–3628.

Jones, C., N. Mahowald, and C. Luo (2004), Observational evidence of African desert dust intensification of easterly waves, *Geophys. Res. Lett.*, *31*(17), 17,208.

Jones, P., T. Jünsson, and D. Wheeler (1997), Extension to the North Atlantic Oscillation using early instrumental pressure observations from Gribaltar and south-west Iceland, *Int. J. Climatol.*, *17*, 1433–1450.

Journet, E., K. V. Desboeufs, S. Caquineau, and J.-L. Colin (2008), Mineralogy as a critical factor of dust iron solubility, *Geophys. Res. Lett.*, *35*, L07,805, doi: 10.1029/2007GL031589.

Joussaume, S. (1990), Three-Dimensional Simulations of the Atmospheric Cycle of Desert Dust Particles Using a General Circulation Model, *J. Geophys. Res.*, *95*(D2), 1909–1941.

Kahn, R., W.-H. Li, C. Moroney, D. J. Diner, J. V. Martonchik, and E. Fishbein (2007), Aerosol source plume physical characteristics from space-based multiangle imaging, *J. Geophys. Res.*, *112*(D11), D11,205, doi:10.1029/2006JD007647.

Kalu, A. E. (1979), The African dust plume: Its characteristics and propagation across west Africa in winter, *SCOPE*, *14*, 95–118.

Kaplan, J. O. (2001), Geophysical applications of vegetation modeling, Ph.D. thesis, Dep. of Ecol., Lund Univ., Lund, Sweden.

Karyampudi, V. M., S. P. Palm, J. A. Reagen, H. Fang, W. B. Grant, R. M. Hoff, C. Moulin, H. F. Pierce, O. Torres, E. V. Browell, and S. H. Melfi (1999), Validation of the Saharan Dust Plume Conceptual Model Using Lidar, Meteosat, and ECMWF Data, *Bull. Amer. Meteor. Soc.*, *80*(6), 1045–1075.

Kidder, S. Q., and T. H. Vonder Haar (1995), *Satellite meteorology: an introduction*, Academic Press, San Diego, California.

King, M. D., Y. J. Kaufman, D. Tanre, and T. Nakajima (1999), Remote Sensing of Tropospheric Aerosol from Space: Past, Present, and Future, *Bull. Amer. Meteor. Soc.*, *80*(11), 2229–2259.

Knippertz, P., and A. H. Fink (2006), Synoptic and dynamic aspects of an extreme springtime Saharan dust outbreak, *Quart. J. R. Met. Soc.*, *132*, 1153–1177, doi: 10.1256/qj.05.109.

Knippertz, P., C. Deutscher, K. Kandler, K. Müller, T. Schulz, and L. Schütz (2007), Dust mobilization due to density currents in the Atlas region: Observations from the SAMUM 2006 field campaign, *J. Geophys. Res.*, *112*, D21,109, doi:10.1029/2007JG008774.

Knorr, W., and M. Heimann (1995), Impact of drought stress and other factors on seasonal land biosphere CO_2 exchange studied through and atmospheric tracer model, *Tellus, Ser. B*, *47*, 471–489.

Kohfeld, K. E., and S. E. Harrison (2001), DIRTMAP: the geological record of dust, *Earth-Science Rev.*, *54*(1-3).

Koren, I., Y. Kaufman, R. Washington, M. C. Todd, Y. Rudich, J. V. Martins, and D. Rosenfeld (2006), The Bodélé depression: a single spot in the Sahara that provides most of the mineral dust to the Amazon forest, *Environ. Res. Lett.*, *1*, 014,005, doi: 10.1088/1748-9326/1/1/014005.

Kraus, H. J., J. Malcher, and E. Schaller (1985), Nocturnal low-level jet during PUKK, *Bound.-Layer Meteor.*, *38*, 1–22.

Kubilay, N., S. Nickovic, C. Moulin, and F. Dulac (2000), An illustration of the transport and deposition of mineral dust onto the eastern Mediterranean, *Atmos. Environ.*, *34*(8), 1293–1303.

Laurent, H., N. D'Amato, and t. Lebel (1998), How important is the contribution of the mesoscale convective complexes to the Sahelian rainfall?, *Phys. Chem. Earth*, *23*, 629–633.

Lee, I. (1983), Simulation of transport and removal processes of Saharan dust, *J. Climate Appl. Meteor.*, *22*, 632–639.

Legrand, M., J. J. Nertrand, M. Desbois, L. Menenger, and Y. Fouquart (1989), The potential of infrared satellite data for the retrieval of Saharan dust optical depth over Africa, *J. Climate Appl. Meteor.*, *28*, 309–318.

Legrand, M., A. Plana-Fattori, and C. N'Doume (2001), Satellite detection of dust using the IR imagery of Meteosat 1. Infrared difference dust index, *J. Geophys. Res.*, *106*(D16), 18,251–18,274.

Lenschow, D. H., and B. Stankov (1979), The Rapid Morning Boundary-Layer Transition, *J. Atmos. Sci.*, *36*, 2108–2124.

Leroux, M. (1983), *Le climate de l'Afrique tropicale*, 633 pp., Editions Champion, Paris.

Levin, Z., E. Ganor, and V. Gladstein (1996), The Effects of Desert Particles Coated with Sulfate on Rain Formation in the Eastern Mediterranean, *J. Appl. Meteor.*, *35*, 1511–1523.

Littmann, T. (1991), Dust strom frequency in Asia: Climatic control and variablity, *Int. J. Climatol.*, *11*, 393–412.

Liu, D., Z. Wang, Z. Liu, D. Winker, and C. Trepte (2008), A height resolved global view of dust aerosols from the first year CALIPSO lidar measurement, *J. Geophys. Res.*, *113*(D14), D16,214, doi:10.1029/2007JD009776.

Liu, X., Z.-Y. Yin, X. Zhang, and Y. Yang (2004), Analyses of the spring dust storm frequency of northern china in relation to antecedent and current wind, precipitation, vegetation, and soil moisture conditions, *J. Geophys. Res.*, *109*, D16,210, doi: 10.1029/2004JD004615.

Lohmann, U. (2002), Possible aerosol effects on ice clouds via contact nucleation, *J. Atmos. Sci.*, *59*, 647–656.

Loosmore, G. A., and J. R. Hunt (2000), Below-threshold, non-abraded dust resuspension, *J. Geophys. Res.*, *105*, 20,663–20,671.

Luo, C., N. Mahowald, and J. del Corral (2003), Sensitivity study of meteorological parameters on mineral aerosol mobilization, transport, and distribution, *J. Geophys. Res.*, *108*(D15), 4447, doi:10.1029/2003JD003483.

Lyamani, H., F. J. Olmo, and L. Alados-Arboledas (2005), Saharan dust outbreak over southeastern Spain as detected by sun photometer, *Atmos. Environ.*, *39*(38), 7276–7284.

Mahowald, N., R. G. Bryant, J. del Corral, and L. Steinberger (2003), Ephemeral lakes and desert dust sources, *Geophys. Res. Lett.*, *30*(2), 1074, doi:10.1029/2002GL016041.

Mahowald, N. M., A. R. Baker, G. Bergametti, N. Brooks, R. A. Duce, T. D. Jickells, N. Kubilay, J. M. Prospero, and I. Tegen (2005), Atmospheric global dust cycle and iron inputs to the ocean, *Global Biogeochem. Cycles*, *19*, GB4025, doi: 10.1029/2004GB002402.

Mahowald, N. M., J. A. Ballantine, J. Feddema, and N. Ramankutty (2007), Global trends in visibility: implications for dust sources, *Atmos. Chem. Phys.*, *7*, 3309–3339.

Mahrt, L. (1985), Vertical Structure and Turbulence in the Very Stable Boundary Layer, *J. Atmos. Sci.*, *42*(22), 2333–2349.

Mahrt, L. (1999), Stratified Atmospheric Boundary Layers, *Bound.-Layer Meteor.*, *90*, 375–396.

Mahrt, L., J. Sun, W. Blumen, T. Delany, and S. Oncley (1998), Nocturnal Boundary-Layer Regimes, *Bound.-Layer Meteor.*, *88*, 255–278.

Marshall, J. S., and W. M. Palmer (1948), The distribution of raindrops with size, *J. Meteor.*, *5*, 165–166.

Marticorena, B., and G. Bergametti (1995), Modeling the atmospheric dust cycle: 1. Design of a soil-derived dust emission scheme, *J. Geophys. Res.*, *100*(D8), 16,415–16,430.

Marticorena, B., G. Bergametti, B. Aumont, Y. Callot, C. N'Doume, and M. Legrand (1997), Modeling the atmospheric dust cycle: 2. Simulation of Saharan dust sources, *J. Geophys. Res.*, *102*(D4), 4387.

Marticorena, B., P. Chazette, G. Bergametti, F. Dulac, and M. Legrand (2004), Mapping the aerodynamic roughness length of desert surface from the POLDER/ADEOS bi-directional reflectance product, *Int. J. Remote Sens.*, *25*(3), 603–626.

Mattsson, J. O., and T. Nihlen (1996), The transport of Saharan dust to southern Europe: a scenario., *Journal of Arid Environments*, *32*(2), 111–119.

Mauritsen, T., and G. Svensson (2007), Observations of Stably Stratified Shear-Driven Atmospheric Turbulence at Low and High Richardson Numbers, *J. Atmos. Sci.*, *64*(2), 645–655, doi:10.1175/JAS3856.1.

Mbourou, G. N., J. J. Bertrand, and S. E. Nicholson (1997), The Diurnal and Seasonal Cycles of Wind-Borne Dust over Africa North of the Equator, *J. Appl. Meteor.*, *36*, 868–882.

McConnell, C. L., E. J. Highwood, H. Coe, P. Formenti, B. Anderson, S. Osborne, S. Nava, K. Desboeufs, G. Chen, and M. A. J. Harrison (2008), Seasonal variations of the physical and optical characteristics of Saharan dust: results from the Dust Outflow and Deposition to the Ocean (DODO) experiment, *J. Geophys. Res.*, *113*(D14), D14S05, doi:10.1029/2007JD009606.

McKendry, I. G., J. P. Hacker, and R. Stull (2001), Long-range transport of asian dust to the Lower Fraser Valley, British Columbia, Canada, *J. Geophys. Res.*, *106*, 18,361–18,370.

McNider, R. T., and R. A. Pielke (1981), Diurnal Boundary-Layer Development over Sloping Terrain, *J. Atmos. Sci.*, *38*(10), 2198–2212.

McNider, R. T., M. Singh, and J. T. Lin (1993), Diurnal Wind-Structure Variations and Dispersion of Pollutants in the Boundary Layer, *Atmos. Environ.*, *27A*, 2199–2214.

Menut, L., G. Forêt, and G. Bergametti (2007), Sensitivity of mineral dust concentrations to the model size distribution accuracy, *J. Geophys. Res.*, *112*, D10,210, doi: 10.1029/2006JD007766.

Meskhidze, N., W. L. Chameides, A. Nenes, and G. Chen (2003), Iron mobilization in mineral dust: Can anthropogenic SO_2 emission affect ocean productivity?, *Geophys. Res. Lett.*, *30*(21), 2085, doi:10.1029/2003GL018035.

Meskhidze, N., W. L. Chameides, and A. Nenes (2005), Dust and pollution: A recipe for enhanced ocean fertilization?, *J. Geophys. Res.*, *110*(D3), D03,301, doi: 10.1029/2004JD005082.

Middleton, N. J., and A. S. Goudie (2001), Saharan dust: sources and trajectories, *Trans. Inst. Br. Geogr.*, *26*, 165–181.

Miller, R., and I. Tegen (1999), Radiative Forcing of a Tropical Direct Circulation by Soil Dust Aerosols, *J. Atmos. Sci.*, *56*, 2403–3433.

Moore, C. M., M. M. Mills, A. Milne, R. Langlois, E. P. Achterberg, K. Lochte, R. J. Geider, and J. L. Roche (2006), Iron limits primary productivity during spring bloom development in the central North Atlantic, *Global Change Biology*, *12*, 626–634, doi: 10.1111/j.1365-2486.2006.01122.x.

Moulin, C., C. E. Lambert, F. Dulac, and U. Dayan (1997), Control of atmospheric export of dust from North Africa by the North Atlantic oscillation, *Nature*, *387*(6634), 691–694.

Moulin, C., C. E. Lambert, U. Dayan, V. Masson, M. Ramonet, P. Bousquet, M. Legrand, Y. J. Balkanski, W. Guelle, B. Marticorena, G. Bergametti, and F. Dulac (1998), Satellite climatology of African dust transport in the Mediterranean atmosphere, *J. Geophys. Res.*, *103*(D11), 13,137–13,144.

Murphy, E. A., R. B. D'Agostino, and J. P. Noonan (1982), Patterns in the Occurrences of Richardson Numbers Less Than Unity in the Lower Atmosphere, *J. Appl. Meteor.*, *21*, 321–333.

Nappo, C. J. (1991), Sporadic Breakdowns of Stability in the PBL over Simple and Complex Terrain, *Bound.-Layer Meteor.*, *54*, 69–87.

Neuer, S., M. E. Torres-Padrón, M. D. Gelado-Caballero, M. J. Rueda, J. Hernández-Brito, R. Davenport, and G. Wefer (2004), Dust deposition pulses to the eastern subtropical North Atlantic gyre: Does ocean's biogeochemistry respond?, *Global Biogeochem. Cycles*, *18*, GB4020, doi:10.1029/2004GB00228.

Nickovic, S., G. Kallos, A. Papadopoulos, and O. Kakaliagou (2001), A model for prediction of desert dust cycle in the atmosphere, *J. Geophys. Res.*, *106*(D16), 18,113–18,129.

Ott, S. T., A. Ott, D. W. Martin, and J. A. Young (1991), Analysis of a trans-Atlantic Saharan dust outbreak based on satellite and GATE data, *Mon. Wea. Rev.*, *119*(8), 1832–1850.

Pacyna, J. M. (1995), *Sources, Particle Size Distribution and Transport of Aerosol*, Springer-Verlag, Berling, Heidelberg.

Parker, D. J., R. R. Burton, A. Diongue-Niang, R. J. Ellis, M. Felton, C. M. Taylor, C. D. Thorncroft, P. Bessemoulin, and A. M. Tompkins (2005), The diurnal cycle of the West African monsoon circulation, *Quart. J. R. Met. Soc.*, *131*, 2839–2860, doi: 10.1256/qj.04.52.

Parker, M. D., and R. H. Johnson (2000), Organizational modes of midlatitude mesoscale convective systems, *Mon. Wea. Rev.*, *128*(10), 3413–3436, doi:10.1256/qj.04.52.

Payne, S. W., and M. M. McGarry (1977), The relationship of satellite inferred convective activity to easterly waves over West Africa and the adjacent ocean during phase III of GATE, *Mon. Wea. Rev.*, *105*, 413–420.

Peagle, J., M. McCorcle, and E. Miller (1984), Diagnoses and numerical simulation of a low-lewel jet during ALPEX, *Contirb. Atmpos. Phys.*, *57*, 419–430.

Pérez, C., S. Nickovic, J. M. Baldasano, M. Sicard, and F. Rocadenbosch (2003), A long Saharan dust event over the western Mediterranean: Lidar, Sun photometer observations, and regional dust modeling, *J. Geophys. Res.*, *111*, D15,214.

Perlwitz, J., I. Tegen, and R. L. Miller (2001), Interactive soil dust aerosol model in the GISS GCM: 1. Sensitivity of the soil dust cycle to radiative properties of soil dust aerosols, *J. Geophys. Res.*, *106*, 18,167–18,192.

Perry, K. D., T. A. Cahill, R. A. Eldred, D. D. Dutcher, and T. E. Gill (1997), Long-range transport of North African dust to the eastern United States, *J. Geophys. Res.*, *102*(D10), 11,225–11,238.

Pinzon, J. (2002), Using HHT to Successfully Uncouple Seasonal and Interannual Components in Remotely Sensed Data, in *SCI 2002 Conference Proceedings July 14-18*, edited by N. Huang, SCI Int., Orlando, Florida.

Pinzon, J., M. E. Brown, and C. J. Tucker (2005), *Satellite time series correction of orbital drift artefacts using empirical mode decomposition*, pp. 167–186, World Sci., Tokyo.

Poulos, G. S., W. Blumen, D. C. Fritts, J. K. Lundquist, J. Sun, S. P. Burns, C. Nappo, R. Banta, R. Newsom, J. Cuyart, E. Terradellas, B. Balsley, and M. Jensen (2002), CASES-99: A comprehensive investigation of the stable nocturnal boundary layer, *Bull. Amer. Meteor. Soc.*, *88*, 555–581.

Prata, A. J. (1989), Observations of volcanic ash clouds in the 10-12 μm window using AVHRR/2 data, *Int. J. Remote Sens.*, *10*, 751–761.

Prigent, C., I. Tegen, F. Aires, B. Marticorena, and M. Zribi (2005), Estimation of the aerodynamic roughness length in arid and semi-arid regions over the globe with the ERS scatterometer, *J. Geophys. Res.*, *110*(D9), D09,205.

Prospero, J. M. (1999), Long-term measurements of the transport of African mineral dust to the southeastern United states: Implications for regional air quality, *J. Geophys. Res.*, *D13*, 15,917–15–927.

Prospero, J. M., and P. J. Lamb (2003), African droughts and dust transport to the Caribbean: climate change implications, *Science*, *302*(5647), 1024–1027.

Prospero, J. M., and R. T. Nees (1986), Impact of the North African Drought and El-Nino on mineral dust in the Barbados trade winds, *Nature*, *320*(6064), 735–738.

Prospero, J. M., R. A. Glaccum, and R. T. Nees (1981), Atmospheric transport of soil dust from Africa to South America, *Nature*, *289*, 570–572.

Prospero, J. M., K. Barrett, T. Church, F. Dentener, R. A. Duce, J. N. Galloway, H. Levy, J. Moody, and P. Quinn (1996), Atmospheric deposition of nutrients to the North Atlantic Basin, *Biogeochemistry*, *35*, 27–73.

Prospero, J. M., P. Ginoux, O. Torres, S. E. Nicholson, and T. E. Gill (2002), Environmental characterization of global sources of atmospheric soil dust identified with the Nimbus 7 Total Ozone Mapping Spectrometer (TOMS) absorbing aerosol product, *Rev. Geophys.*, *40*(1), 1002, doi:10.1029/2000RG000095.

Prospero, J. M., E. Blades, G. Mathison, and R. Naidu (2005), Interhemispheric transport of viable fungi and bacteria from Africa to the Caribbean with soil dust, *Aerobiologica*, *21*(1), 1–19.

Psenner, R. (1999), Living in a dusty world: airborne dust as a key factor for alpine lakes, *Water, Air and Soil Pollution*, *112*(3-4), 217–227.

Pye, K. (1987), *Aeolian Dust and Dust Deposits*, Academic Press London.

Qian, W. H., L. S. Quan, and S. Y. Shi (2002), Variations of the dust storm in Cina and its climatic control, *J. Clim.*, *15*(10), 1216–1229.

Ramel, R., H. Gallée, and C. Messager (2006), On the northward shift of the West African monsoon, *Clim. Dyn.*, *26*(4), 429–440.

Redelsperger, J.-L., C. D. Thorncroft, A. Diedhiou, T. Lebel, D. J. Parker, and J. Polcher (2006), African monsoon multidisciplinary analysis: An international research project and field campaign, *Bull. Amer. Meteor. Soc.*, *87*(12), 1739–1746, doi:10.1175/BAMS-87-12-1739.

Riemer, N., O. M. Doherty, and S. Hameed (2006), On the variability of African dust transport across the Atlantic, *Geophys. Res. Lett.*, *33*(13), L13,814, doi: 10.1029/2006GL026163.

Rogora, M., R. Mosello, and A. Marchetto (2004), Long-term trends in the chemistry of atmospheric deposition in Northwestern Italy: the role of increasing Saharan dust deposition, *Tellus*, *56B*(5), 426–434.

Rosenfeld, D., Y. Rudich, and R. Lahav (2001), Desert dust suppressing precipitation: A possible desertification feedback loop, *PNAS*, *98*(11), 5975–5980.

Ryall, D. B., R. G. Derwent, A. J. Manning, A. L. Redington, J. Corden, W. Millington, P. G. Simmonds, S. O'Doherty, N. Carslaw, and G. W. Fuller (2002), The origin of high particulate concentrations over the United Kingdom, March 2000, *Atmos. Environ.*, *36*(8), 1363–1378.

Sarthou, G., A. R. Baker, S. Blain, E. P. Achterberg, M. Boye, A. R. Bowie, P. Croot, P. Laan, H. J. W. de Baar, T. D. Jickells, and P. J. Worsfold (2003), Atmospheric iron deposition and sea-surface dissolved iron concentrations in the eastern Atlantic Ocean, *Deep-Sea Research Part I*, *50*, 1339–1352, doi:10.1016/S0967-0637(03)00126-2.

Sarthou, G., A. R. Baker, J. Kramer, P. Laan, A. Laës, S. Ussher, E. P. Achterberg, J. H. W. de Baar, K. R. Timmermans, and S. Blain (2007), Influence of atmospheric inputs on the iron distribution in the subtropical North-East Atlantic Ocean, *Mar. Chem.*, *104*, 186–202, doi:10.106/j.marchem.2006.11.004.

Sassen, K., P. J. DeMott, J. M. Prospero, and M. R. Poellot (2003), Saharan dust storms and indirect aerosol effects on clouds: CRYSTAL-FACE results, *Geophys. Res. Lett.*, *30*(12), L1633.

Schepanski, K., I. Tegen, B. Laurent, B. Heinold, and A. Macke (2007), A new Saharan dust source activation frequency map derived from MSG-SEVIRI IR-channels, *Geophys. Res. Lett.*, *34*(18), L18,803, doi:10.1029/2007GL030168.

Schepanski, K., I. Tegen, and A. Macke (2008a), Saharan Dust Transport and Deposition towards the Tropical Northern Atlantic, *Atmos. Chem. Phys. Discuss.*, *8*, 16,061–16,096.

Schepanski, K., I. Tegen, M. C. Todd, B. Heinold, G. Bönisch, B. Laurent, and A. Macke (2008b), Meteorological processes forcing Saharan dust emission inferred from MSG-SEVIRI observations of sub-daily dust source activation, *J. Geophys. Res.*, revised.

Schmetz, J., P. Pili, S. Tjemkes, D. Just, J. Kerkmann, S. Rota, and A. Ratier (2002), An introduction to Meteosat Second Generation (MSG), *Bull. Amer. Meteor. Soc.*, *83*, 977–992.

Schütz, L. (1980), Long range transport of desert dust with special emphasis on the Sahara, *Ann. N. Y. Acad. Sci.*, *338*, 515–532.

Schwikowski, M., P. Seibert, U. Baltensperger, and H. W. Gaggeler (1995), A study of an outstanding Saharan dust event at the high-Alpine Site Jungfraujoch, Switzerland, *Atmos. Environ.*, *29*(15), 1829–1842.

Shao, Y. (2000), *Physics and Modelling of Wind Erosion*, Kluwer Academic Publishers.

Shao, Y. (2001), A model for mineral dust emission, *J. Geophys. Res.*, *106*(D17), 20,239–20,254.

Shao, Y., M. R. Raupach, and P. A. Findlater (1993), The effect of saltation bombardment on the entrainment of dust by wind, *J. Geophys. Res.*, *98*, 12,719–12,726.

Shao, Y., M. R. Raupach, and J. F. Leys (1996), A model for predicting aeolian sand drift and dust entrainment on scales from paddock to region, *Aust. J. Soil Res.*, *34*, 309–342.

Shenk, W. E., and R. J. Curran (1974), The detection of dust storms over land and water with satellite visible and infrared measurements, *Mon. Wea. Rev.*, *102*, 830–837.

Sijikumar, S., P. Roucou, and B. Fontaine (2006), Monsoon onset over Sudan-Sahel: Simulation by the regional scale model MM5, *Geophys. Res. Lett.*, *33*, L03,814, doi: 10.1029/2005GL024819.

Skammarock, W. C., and J. B. Klemp (1992), The stability of time-split numerical methods for the hydrostatic and the non-hydrostatic elastic equations, *Mon. Wea. Rev.*, *120*, 2109–2127.

Sokolik, I. N. (2002), The spectral radiative signature of wind-blown mineral dust: Implications for remote sensing in the thermal IR region, *Geophys. Res. Lett.*, *29*(24), 2154, doi:10.1029/2002GLR015910.

Sokolik, I. N., and O. B. Toon (1996), Direct radiative forcing by anthropogenic mineral aerosols, *Nature*, *381*, 681–683.

Sokolik, I. N., D. M. Winker, G. Bergametti, G. D. A, G. Carmichael, Y. J. Kaufman, L. Gomes, L. Schuetz, and J. E. Penner (2001), Introduction to special section: Outstanding problems in quantifying the radiative impacts of mineral dust, *J. Geophys. Res.*, *106*(D16), 18,015–18,027.

Solot, S. B. (1959), General circulation over the Angolo-Egyptian Sudan and adjacent regions, *Bull. Amer. Meteor. Soc.*, *31*, 85–94.

Sorbjan, Z. (2006), Local Structure of Turbulence in Stably Stratified Boundary Layers, *J. Atmos. Sci.*, *63*, 1526–1537.

Stensrud, D. J. (1996), Importance of Low-Level Jets to Climate: A Review, *J. Climate*, *9*, 1698–1711.

Steppler, J., G. Doms, U. Schättler, H. W. Bitzer, A. Gassmann, U. Damrath, and G. Gregoric (2003), Meso-gamma scale forecasts using the nonhydrostatic model LM, *Meteor. Atmos. Phys.*, *82*, 75–96.

Stull, R. B. (1988), *An Introduction to Boundary Layer Meteorology*, NATO Asi Series. Series C, Mathematical and Physical Science, 680 pp., Springer Verlag.

Sultan, B., and S. Janicot (2003), The West African monsoon dynamics. Part II: The "Preonset" and "Onset" of the summer monsoon, *J. Climate*, *16*, 3407–3427.

Sultan, B., K. Labadi, J. F. Guegan, and S. Janicot (2005), Climate drives the meningitis epidemics onset in West Africa, *Plos Medicine*, *2*(1), 43–49.

Sultan, B., S. Janicot, and R. Drobinski (2006), Characterization of the Diurnal Cycle of the West African Monsoon around the Monsoon Onset, *J. Climate*, *20*, 4014–4032.

Swap, R., M. Garstang, S. Greco, R. Talbot, and P. Kallberg (1992), Saharan dust in the Amazon Basin, *Tellus B*, *44*, 133–149.

Tegen, I., and I. Fung (1994), Modeling of mineral dust in the atmosphere: Sources, transport, and optical thickness, *J. Geophys. Res.*, *99*(D11), 22,896–22,914.

Tegen, I., and A. A. Lacis (1996), Modeling of particle size distribution and its influence on the radiative properties of mineral dust aerosol, *J. Geophys. Res.*, *101*(D14), 19,237–19,244.

Tegen, I., S. P. Harrison, K. Kohfeld, and I. C. Prentice (2002), Impact of vegetation and preferential source areas on global dust aerosol: Results from a model study, *J. Geophys. Res.*, *107*(D21), 4576, doi:10.1029/2001JD000963.

Tegen, I., B. Heinold, M. Todd, J. Helmert, R. Washington, and O. Dubovik (2006), Modelling soil dust aerosol in the Bodélé depression during the BoDEx campaign, *Atmos. Chem. Phys.*, *6*, 4345–4339.

Thomas, F. G. (1982), Saharan dust-fall in Dover, Kent, *J. Meteor.*, *7*, 92–93.

Thorncroft, C., and K. Hodges (2001), African easterly wave variability and its relationship to Atlantic tropical cyclone activity, *J. Climate*, *14*(6), 1166–1179.

Thorncroft, C. D., and M. Blackburn (1999), Maintance of the African easterly jet, *Quart. J. R. Met. Soc.*, *125*, 763–786.

Thorpe, A. J., and T. H. Guymer (1977), The nocturnal jet, *Quart. J. R. Met. Soc.*, *103*, 633–653.

Tiedtke, M. (1989), A comprehensive mass flux scheme for cumulus parametrisation in large-scale models, *Mon. Wea. Rev.*, *117*, 1779–1799.

Todd, M., R. Washington, J. V. Martins, O. Dubovik, G. Lizcano, S. M'Baimayel, and S. Engelstaedter (2007), Mineral dust emission from the Bodélé Depression, nothern Chad, during BoDEx 2005, *J. Geophys. Res.*, *112*(D6), D06,207, doi: 10.1029/2006JD007170.

Todd, M. C., R. Washington, S. Raghavan, G. Lizcano, and P. Knippertz (2008), Regional Model Simulations of the Bodélé Low-level Jet of Northern Chad dudring the Bodélé Dust Experiment (BoDEx 2005), *J. Climate*, *21*, 995–1012, doi: 10.1175/2007JCLI1766.1.

Tsai, F., G. T.-J. Chen, T.-H. Liu, W.-D. Lin, and J.-Y. Tu (2008), Characterizing the transport pathways of Asian dust, *J. Geophys. Res.*, *113*, D17,311, doi: 10.1029/2007JD009674.

Tsyro, S., and L. Erdman (2000), Parameterisation of aerosol deposition processes in EMEP MSC-E and MSC-W transport models, *EMEP/MSC-W Note 7/00*, Norwegian Meteorol. Inst., Oslo, Norway.

Tucker, C. J., J. E. Pinzon, M. E. Brown, D. Slayback, E. W. Park, R. V. E. Mahoney, and N. El Saleous (2005), An extend AVHRR 8-km NDVI data set compatible with MODIS and SPOT vegetation NDVI data, *Int. J. Remote Sens.*, *26*(20), 4485–4498.

Tulet, P., M. Mallet, V. Pont, J. Pelon, and A. Boone (2008), The 7-13 March 2006 dust strom over West Africa: Generation, transport, and vertical stratification, *J. Geophys. Res.*, *113*, D00C08, doi:10.1029/2008JD009871.

Van de Wiel, B. J. H., A. F. Moene, O. K. Hartogensis, H. A. R. D. Bruin, and A. A. M. Holtslag (2003), Intermittent Turbulence in the Stable Boundary Layer over Land. Part III: A Classification for Observations during CASES-99, *J. Atmos. Sci.*, *60*, 2509–2522.

VanCuren, R. A. (2003), Asian aerosols in North America: Extractin the chemical composition and mass concentration of the Asian continental aerosol plume from long-term aerosol records in the western United States, *J. Geophys. Res.*, *108*(D20), 4623, doi: 10.1029/2003JD003459.

Veihelmann, B., P. F. Levelt, P. Stammes, and J. P. Veefkind (2007), Simulation study of the aerosol information content in OMI spectral reflectance measurements, *Atmos. Chem. Phys.*, *7*, 3115–3127.

Wald, A. E., Y. J. Kaufman, D. Tanre, and B.-C. Gao (1998), Daytime and nighttime detection of mineral dust over desert using infrared spectral contrast, *J. Geophys. Res.*, *103*(D24), 32,307–32,313.

Walker, H. O. (1958), The Monsoon in West Africa, *Note*, Ghana Met. Dept., Accra.

Washington, R., and M. C. Todd (2005), Atmospheric controls on mineral dust emission from the Bodélé Depression, Chad: The role of the low level jet, *Geophys. Res. Lett.*, *32*, L17,701, doi:10.1029/2005GL023597.

Washington, R., M. Todd, N. J. Middleton, and A. S. Goudie (2003), Dust-Storm Source Areas Determined by the Total Ozone Monitoring Spectrometer and Surface Observations, *Annals of the Association of American Geographers*, *93*(2), 297–313.

Washington, R., M. C. Todd, S. Engelstaedter, S. Mbainayel, and F. Mitchell (2006a), Dust and the low-level circulation over the Bodele Depression, Chad: Observations from BoDEx 2005, *J. Geophys. Res.*, *111*(D3), D03,201.

Washington, R., M. C. Todd, G. Lizcano, I. Tegen, C. Flamant, I. Koren, P. Ginoux, S. Engelstaedter, C. S. Bristow, C. S. Zender, A. S. Goudie, A. Warren, and J. M. Prospero (2006b), Links between topography, wind, deflation, lakes and dust: The case of the Bodele depression, Chad, *J. Geophys. Res.*, *33*, L09,401, doi:10.1029/2006GL025827.

Weaver, C. J., P. Ginoux, N. C. Hsu, M.-D. Chou, and J. Joiner (2001), Radiative Forcing of Saharan Dust: GOCART Model Simulations Compared with ERBE Data, *J. Atmos. Sci.*, *59*(3), 736–747.

Wedepohl, K. H. (1995), The composition of the continental crust, *Geochemica et Cosmochimica Acta*, *59*(7), 1217–1232.

Weischet, W., and W. Endlicher (2000), *Regional Klimatologie, Teil 2: Die alte Welt*, Teubner Verlag, Stuttgart.

Westphal, D., O. Toon, and T. Carlson (1987), A Two–Dimensional Numerical Investigation of the Dynamics and Microphysics of Saharan Dust Storms, *J. Geophys. Res.*, *92*(D3), 3027–3049.

Wilkening, K. E., L. A. Barrie, and M. Engle (2000), Trans-Pacific air pollution, *Science*, *290*, 65–67.

Wolke, R., O. Hellmuth, O. Knoth, W. Schröder, B. Heinrich, and E. Renner (2004a), The chemistry-transport modeling system LM-MUSCAT: Description and CityDelta applications, in *Air Pollution Modeling and Its Aplication XVI*, edited by C. Borrego and S. Incecik, pp. 427–437, Proceedings of twenty-sixth NATO/CCMS international technical meeting on air pollution modeling and its application.

Wolke, R., O. Hellmuth, O. Knoth, W. Schröder, and E. Renner (2004b), The parallel model system LM-MUSCAT for chemistry-transport simulations: Coupling scheme, parallelization and application, *Parallel Computing: Software Technology, Algorithms, Architectures, and Applications*, pp. 363–370.

Wurzler, S., T. G. Reisin, and Z. Levin (2000), Modification of mineral dust particles by cloud processing and subsequent effects on drop size distribution, *J. Geophys. Res.*, *105*, 4501–4512.

Zender, C. S., and D. Newman (2003), Spatial heterogeneity in aeolian erodibility: Uniform, topographic, geomorphic, and hydrologic hypotheses, *J. Geophys. Res.*, *108*(D17), 4543, doi:10.1029/2002JD003039.

Zender, C. S., H. Bian, and D. Newman (2003), Mineral Dust Entrainment And Deposition (DEAD) model: Description and 1990s dust climatology, *J. Geophys. Res.*, *108*(D14), 4416, doi:10.1029/2002JD002775.

Zhang, L., S. Gong, J. Padro, and L. Barrie (2001), A size-segregated particle dry deposition scheme for an atmospheric aerosol module, *Atmos. Environ.*, *35*, 549–560.

Zhang, P., N. Lu, X. Hu, and C. Dong (2006), Identification and physical retrieval of dust storm using three MODIS thermal IR channels, *Global and Planetary Change*, *52*, 197–206, doi:10.1016/jgloplacha.2006.02.014.

Zhang, X. Y., S. L. Gong, Z. X. Shen, F. M. Mei, X. X. Xi, L. c. Liu, Z. J. Zhou, D. Wang, Y. Q. Wang, and Y. Cheng (2003), Characterization of soil dust aerosol in China and its transport and distribution during 2001 ACE-Asia: 1. Network observations, *J. Geophys. Res.*, *108*(D9), 4261, doi:10.1029/2002JD002632.

Zhao, T. L., S. L. Gong, X. Y. Zhang, J.-P. Blanchet, I. G. McKendry, and Z. J. Zhou (2006), A Simulated Climatology of Asian Dust Aerosol and Its Trans-Pacific Transport. Part I: Mean Climate and Validation, *JoCys*, *19*, 88–103.

Zobler, L. (1986), A world soil file for global climate modeling, *NASA Tech. Memo.*, NASA, Washington, D.C.

Acknowledgement

First of all, I want to thank all those people, who accompanied me but are not mentioned explicitly.

Many thanks to Prof. Dr. A. Macke and Dr. I. Tegen for supporting the development of this thesis, advice and discussion.

Thanks to Dr. Benoit Laurent for reading and critical discussion.

Furthermore, thanks to all colleagues of the “Modelling Department” at the IfT in Leipzig and the “Maritime Meteorologie” at the IFM-GEOMAR in Kiel for support and computing environment. The collaboration of both institutes allowed for an interesting and interdisciplinary view on Saharan dust.

Finally, I would like to thank my parents for their assistance and encouragement.

This work was performed in the frame of the network project TRACES (Ocean–Atmosphere–Land Impacts on TRopical AtlantiC EcoSystems) funded by the Wissenschaftsgemeinschaft Gottfried Willhelm Leibniz.

Erklärung

Hiermit bestätige ich, dass ich die vorliegende Dissertation selbstständig verfasst und keine anderen als die angegebenen Quellen und Hilfsmittel verwendet habe.
Ich versichere, dass diese Arbeit noch nicht zur Erlangung eines Doktorgrades an anderer Stelle vorgelegen hat.
Ich erkläre, dass die vorliegende Arbeit gemäß der Grundsätze zur Sicherung guter wissenschaftlicher Praxis der Deutschen Forschungsgemeinschaft erstellt wurde.

Kiel, Dezember 2008

(Kerstin Schepanski)